UNIVERSITY OF SOUTHAMPTON

FACULTY OF PHYSICAL SCIENCES AND ENGINEERING

Optoelectronics Research Centre

Theoretical and Experimental Investigation of Novel Passive and Active Optical Microresonators

by

Shahab Bakhtiari Gorajoobi

Thesis for the degree of Doctor of Philosophy

November 2017

UNIVERSITY OF SOUTHAMPTON

ABSTRACT

FACULTY OF PHYSICAL SCIENCES AND ENGINEERING

Optoelectronics Research Centre

Doctor of Philosophy

Thesis for the Doctor of Philosophy

THEOETICAL AND EXPERIMENTAL INVESTIGATION OF NOVEL PASSIVE AND ACTIVE OPTICAL MICRORESONATORS

Shahab Bakhtiari Gorajoobi

The scope of this thesis is to develop and investigate novel "fiberised" microresonator lasers suitable for side/remote pumping and signal collection. Several resonator configurations (stub, bottle, rod and sphere) made from normal optical fibres are studied in detail towards development of all-in-fibre microlasers.

A theoretical model for tapered fibre-coupled microspheres based on general coupled mode theory is developed, describing the excitation of multimode WGMs. By precisely designing the taper coupling condition, excitation of specific mode or group of modes is possible. Simulations show coupling induced cross-coupling between frequency degenerate WGMs in a perfect microsphere, and provide their intra-cavity intensity distribution which is important in lasing and nonlinear applications. Lasing characteristics of Yb^{3+}-doped microbottle lasers are theoretically investigated. Along with the experiment, it is demonstrated that desired lasing characteristics for a specific WGM is achievable by precisely setting the taper-resonator coupling condition, intrinsic Q factors and dopant concentration. Yb^{3+}-doped MBLs are experimentally demonstrated to be promising devices in realization of selective WGM microlasers. Such cavities naturally exhibit multimode lasing. Precise, fast and low cost spectral cleaning methods are employed towards developing robust, stable and single mode lasers. It is observed that by further improving the quality factor of such resonators,

cascaded Stimulated Raman Scattering (SRS) lasing is enabled, that together with Yb^{3+}-lasing, extend the spectra beyond the emission band of Yb ions, well in the O-band of the telecom spectrum. It is also demonstrated that pumping and signal collection in such laser cavities can be achieved without the complex and sensitive tapered fibre coupling mechanism. In this study, microtaper-free side-pumped laser-milled microrod and microstub lasers are developed as robust, stand-alone and compact devices towards the realization of ultra-short all-in-fibre microlasers.

Table of Contents

List of Figures

DECLARATION OF AUTHORSHIP

I, Shahab Bakhtiari Gorajoobi, declare that this thesis, entitled "*Theoretical and Experimental Investigation of passive and Active Optical Microresonators,*" and the work presented in it are my own and has been generated by me as the result of my own original research.

I confirm that:

1. This work was done wholly or mainly while in candidature for a research degree at this University;
2. Where any part of this thesis has previously been submitted for a degree or any other qualification at this University or any other institution, this has been clearly stated;
3. Where I have consulted the published work of others, this is always clearly attributed;
4. Where I have quoted from the work of others, the source is always given. With the exception of such quotations, this thesis is entirely my own work;
5. I have acknowledged all main sources of help;
6. Where the thesis is based on work done by myself jointly with others, I have made clear exactly what was done by others and what I have contributed myself;
7. Parts of this work have been published as: [please see list of publications].

Signed: .....

Date: .....

Acknowledgements

First and foremost, I wish to express my sincere gratitude to my supervisors, Professor Michalis Zervas and Dr. Senthil Ganapathy for their endless support, motivation and patience during the course of my PhD. This thesis would have not been possible without their encouragement and support.

I would also like to thank all the members of the ORC family, especially those who kindly helped me in this research. Many, many thanks to Professor James Wilkinson and Integrated Photonic Devices group members for their kind support, ideas and all the discussions during the group meetings. I truly appreciate all the support from my lab mates Dr. Narizee Mohd Nasir, Dr. Armen Aghajani, Dr. Jonathan Butement, Dr. Vinita Mittal, Dr. David Rowe and Amy Tong. It has been a great learning experience working with all of you. I appreciate the kind help from members of the Advanced Laser Lab, especially, Dr. Christophe Codemard and Dr. Jaclyn Chan for fabrication of the active microstub resonator.

I would like to thank all my friends who are now my second family; Mehdi, Reza, Mohammad, Adel, Elham, Sara, Ali, Niloufar, Sarvenaz and little Lona. Thank you all for the infinite love and support you have given me, and making Southampton feel like home during the past four years.

Last but not least, my deepest gratitude goes to my family for their unconditional love and support throughout my life.

Nomenclature

2D	Two Dimensions
3D	Three Dimensions
ASE	Amplified Spontaneous Emission
CMT	Coupled-mode Theory
CQED	Cavity Quantum Electro-dynamics
CW	Continuous Wave
DFB	Distributed Feed-back
EDFA	Erbium-doped Fibre Amplifier
Er	Erbium
FBG	Fibre Bragg Grating
FIB	Focused Ion-Beam
FSR	Free Spectral Range
FWHM	Full Width at Half Maximum
FWM	Four-wave Mixing
LD	Laser Diode
LLP	Low Lasing Probability
LP	Linearly Polarized
MBL	Microbottle Laser
MBR	Microbottle Resonator
MMF	Multi-Mode Fibre
MRR	Microrod Resonator
MSR	Microstub Resonator
OC	Over-coupling
OSA	Optical Spectrum Analyser

PC	Polarisation Controller
PD	Photo Detector
Q	Quality
SBH	Spatial Hole Burning
SEM	Scanning Electron Microscope
SHG	Second Harmonic Generation
SMF	Single Mode Fibre
SNR	Signal to Noise Ratio
SRS	Stimulated Raman Scattering
TE	Transverse Electric
THG	Third Harmonic Generation
TLS	Tuneable Laser Source
TM	Transverse Magnetic
TMM	Transfer Matrix Method
UV	Ultra Violet
V	Mode Volume
WGM	Whispering gallery mode
Yb	Ytterbium

To my dear father, and the loving memory of my mother

Chapter 1 Introduction

1.1 Optical whispering-gallery mode microcavities

Definition

Optical cavities are generally comprised of a set of two or more mirrors that reflect a light beam within a closed path providing circumnavigation of light, bouncing back and forth between the mirrors. A class of cavities called Whispering Gallery Mode (WGM) resonators have been used extensively over the years as high quality and robust optical microcavities. WGM resonators are usually designed in convex shapes such as micropillars [1, 2], microcylinders [3, 4], microrings [5, 6], microdisks [7-9], microtoroides [10], microspheres [11] and microbottles [12-14].

Circulation of light inside the resonator is achieved due to the total internal reflection from the boundary of the resonator material with the surrounding material. High quality factor (Q) of such resonators provides highly-confined optical modes in the resonator, such that, in each round-trip, only a tiny amount of light power is lost due to the surface scattering and material losses. This makes WGM resonators perform as long photon lifetime cavities. WGM resonators with Q factors as high as 10^9 have been reported [15]. In addition, WGM microresonators exhibit large internal powers confined in a very small volume. The amount of the light confinement in a cavity can be quantified by Q/V, where V denotes the mode volume. High Q/V provides strong light matter interactions, and such microcavities are excellent devices for nonlinear optics and lasers.

Fabrication

Fabrication of microspheres and Micro Bottle Resonators (MBR), which will be extensively investigated in this thesis, is mostly based on thermal processes or sol-gel chemistry. The thermal glass processing are carried out by either directly melting the solid glass or using a glass powder by crushing and then applying heat [16-18] to form microspheres. The simplest and most effective method to fabricate microspheres is by melting a fibre tip. Oxygen-butane torch, CO_2 laser or electrical arcs can provide the heat source for the reflow process. This method is cheap and allows good control of the

microsphere diameter. In the sol-gel process, a thin film of sol-gel is usually used to coat a previously formed microsphere [19] which provides high purity materials.

Light coupling

Various methods are developed for efficient light coupling into the resonators, especially for spherical type of microresonators. The most commonly used coupling mechanisms are tapered fibre [20, 21], prism [22], integrated waveguide [23], free-space coupling [24, 25] and angle polished fibre [26]. Most of these methods suffer from low coupling efficiency (except tapered fibres), difficulty in collecting the transmitted light from the resonator and large dimensions which affect the performance of resonator-coupler system. In order to efficiently couple into a WGM resonator, enough overlap between the propagating mode of the excitation waveguide and the resonator mode is necessary. Equally important, such coupling depends on the phase-matching (synchronisation) between resonator and excitation modes, which is determined by their effective indices. The effective index of the excitation mode is determined by the waveguide structure and material. Thus, for excitation of a particular mode with desired internal and output power, selection of a proper coupling system is important. Among aforementioned coupling systems, tapered fibres show very high efficiency and high controllability in coupling light into microresonators [20].

Nonlinear cavities

As it was mentioned, WGM resonators, are a great platform for investigation of nonlinear optical processes, due to providing strong light-matter interactions. In this case, the coupling efficiency is an important factor in determining the internal power of WGMs, and great care should be taken to have adequate modal overlap and phase-matching. Crystalline microresonators exhibit low losses and are transparent over a broad range. They have the smallest absorption for OH^- and water, thus, enable ultra-high Q factors. In [27] a CaF_2 crystalline WGM resonator with $Q > 2\times10^{10}$ at 1319nm wavelength fabricated by mechanical polishing is demonstrated. On the other hand, ultimate Q for fused-silica microspheres is demonstrated to be around 10^{10} [28]. Owing to such high Q factors, frequency combs [29-32], second [33] and third harmonic generation, and third order sum-frequency generation have been recently achieved in WGM microresonators coupled to tapered fibres [34]. Such devices are based on stimulated Raman scattering [35-37], stimulated Brillouin scattering [38-40] and four wave mixing [41-43].

Sensing

WGM resonance wavelength depends on the geometry of the resonator and the refractive indices of the resonator and the surrounding medium. The WGM evanescent tail of a typical silica resonator extends into the surrounding air up to few hundreds of nanometer. This property of WGMs enables a large variety of sensing applications. Several works are reported on incorporation of WGM resonators in biomedical [44-46], mechanical [47, 48] and temperature sensing [49, 50]. These sensors operate based on either the perturbations due to the ambient medium, or the changes of the refractive index by temperature variations, and/or applying mechanical forces resulting in change of refractive index and cavity deformations.

1.2 WGM Microlasers

A laser is generally characterised by the lasing wavelength, pump threshold and linewidth of the lasing peak. These fundamental parameters are determined by the laser cavity providing a feedback for the laser, determined by the Q factor, and the mode volume (V). Larger Q factor implies longer photon life time, and smaller V indicates stronger light confinement. Hence, a high Q/V results in a possible low threshold and narrow line width laser. WGM microresonators are excellent candidates for realization of high Q/V [11, 15, 28, 51-55].

In order to maximize the pumping efficiency, one should couple pump light resonantly in the form of WGM. Strong light confinement within a small volume of the gain medium can enable very low threshold lasing. The internal power enhancement factor (η) in a WGM resonator can be defined as the ratio of stored power (P_c) in the resonator to the input power (P_{in}). Let us define τ_r and $\Delta\omega$ as the round-trip photon life time and the frequency detuning from the WGM resonance $\underline{\omega_c}$, respectively. Then, η is given by [15, 56]

$$\eta = \frac{P_c}{P_{in}} = \frac{1}{\tau_r} \frac{4\kappa_{ext}}{4\Delta\omega^2 + \left(\kappa_{ext} + \kappa_0\right)^2} \qquad (1.1)$$

where $\kappa_0 = \omega_c / Q_0$ determines the intrinsic cavity loss, corresponding to the intrinsic quality factor Q_0, and the coupling loss can be evaluated by $\kappa_{ext} = \omega_c / Q_{ext}$ where Q_{ext} is the external (extrinsic) quality factor. Critical coupling is achieved when $\kappa_0 = \kappa_{ext}$. This will be examined in detail in Chapter 2. At resonance $\Delta\omega = 0$, and the power enhancement factor becomes $\eta = Q_0 / \tau_r \omega_c$. This means, if we have a WGM with high Q (typically 10^8), for small amount of input light (e.g. 1mW) we can build up a substantially larger

amount of internal circulating power in the resonator (~300W for a silica microsphere with radius of 50μm). On the other hand, this amount of energy is confined in a very small V (few hundreds of μm^3), indicating the potential of WGM microlasers for low threshold microlasers.

Types of microlasers

Rare-earth ions, such as Er^{3+}, Yb^{3+}, Nd^{3+}, Tm^{3+} and Sm^{3+}, are the most common dopants for solid-state microlasers. They are widely employed owing to their high efficiency, long upper-level life time and wide emission spectrum. The first WGM microlaser demonstration refers back to the year 1961, where light from stimulated emission scattering from the surface of a Sm^{3+}-doped CaF_2 microsphere with 1-2 mm diameter was observed [11]. Later, stimulated emission in other media such as rhodamine 6G dye (as the gain medium) in ethanol solvent droplets with diameter of 60μm as the WGM resonator was demonstrated [57]. Then, in a pioneering work in 1996, a 56μm-diameter Nd^{3+}-doped glass microsphere with Q factor exceeding 10^8 was demonstrated to have a threshold (absorbed) pump power as low as 200nW [22]. Four years later, Vahala's group reported a low threshold pump power of 60μW at 1.5μm wavelength in an Er:Yb phosphate glass microsphere coupled to a tapered fibre [21]. Afterwards, several types of WGM microlasers have been developed which can be categorized and described briefly as below:

Liquid droplets

Liquid droplets were basically generated by means of vibrating-orifices in which surface tension enforce the formation of spherical droplets [58]. The liquid droplets usually have very low surface roughness, hence, small scattering losses. Q factors of order of 10^8 were reported in CS_2 microdroplets [59]. Their diameter depend on the orifice aperture and are usually of the order of tens of microns. These droplets are basically floating in a stream of liquid solution or are brought in contact with a substrate [56]. The size of the droplets can be controlled by varying the orifice aperture [60] or applying lateral gas flow [61]. Gain media can be added to the liquid before formation of the droplet [58]. Then, the total internal reflection by the droplet internal surface provides the propagation of WGMs inside the droplet. Using a T-junction is another method to form microdroplets [62, 63]. In this approach, a microfluidic channel containing a stream of the carrier fluid interferes with the dye solution at the T-junction. As shown in Figure 1-1 for a two-coloured microfluidic laser [63], this results in microdroplets of

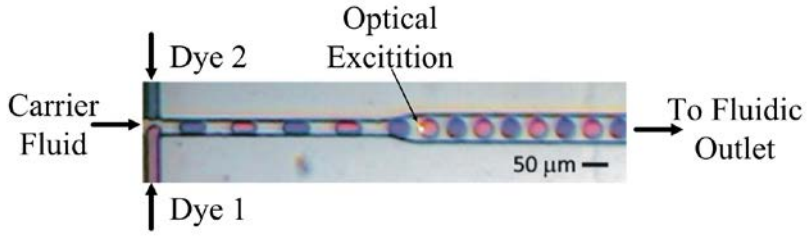

Figure 1-1 Two-colour droplet laser generated by incorporating a T-junction micro fluidic channel [56].

the dye solution separated by the carrier fluid. The droplet size is controlled by the flow rate, channel width and viscosity of the involving liquids [64]. Liquid droplet lasers are good candidates for tunable sensing applications on opto-fluidic chips. However, these chip-based microlasers suffer from issues such as low light coupling efficiency, mechanical instability, and requirement of complex characterisation setups [56, 62, 64, 65].

Microspheres and microtoroids

Fused quartz microspheres with diameter between 40µm and 400µm were the first reported ultra-high Q factor (>10^8) WGM resonators, fabricated by melting or sol-gel processes [54]. The dimensions of a microsphere are related to the tip size of the stem fibre, and the reported surface qualities are in order of 1nm roughness enabling high Q factor WGM resonances. Microtoroids, on the other hand, are chip-based versions of spherical WGM resonators [10, 66]. Using lithographic methods microdisks are patterned on an oxidised silicon wafer followed by dry etching. The underneath silicon layer is etched down to form a post supporting the silica disk in the air. Then, by surface reflow using a CO_2 laser beam and melting the silica edges of the micro disk, a microtoroid-like ring forms along the circumference of the disk. Their major diameters are typically between 10µm to 100µm, and the minor ones are of the order of a few microns. The observed quality factors (>10^8) are comparable to the ones of microspheres. Microtoroids are usually resonators characterised by small mode volumes and a small number of resonant modes [67], due to the confinement of light mostly in radial and polar directions (in telecom wavelengths).

To fabricate active microresonators based on microspheres and microtoroids, numerous methods have been developed. Such methods are based on fabrication of microresonators from doped materials [21-23], coating the resonator with light emitters [19, 68] and using ion implantation to dope the resonator [68]. The silica microsphere laser in [22] was formed by heating, directly from the tip of a Nd^{3+}-doped silica fibre. Later, a coated silica microsphere with Er^{3+}-doped silica sol-gel films was reported [19].

They demonstrated a lasing threshold of 28μW and a single-mode laser emission up to 10μW of power. Moreover, lower threshold powers as low as 65nW were reported in Nd^{3+}-doped gadolinium oxide nanocrystal silica microspheres [69] for a single mode lasing at 1088.2nm wavelength.

Various lasing actions have been reported in rare-earth ion doped microtoroid resonators. Due to the reduced mode numbers and high Q factors in microtoroids, single mode lasing is enabled. The threshold power in microtoroids is reported to be in order of few to hundreds of microwatts, and generally depends on the cavity Q factor, dopant concentration and optical mode size [56]. If the pump power is coupled into a WGM of the resonator the active medium can be excited more efficiently, and lasing threshold can be significantly reduced. The pump spectrum is usually selected to be broadband to ensure efficient coupling to at least one of the WGM resonances of the resonator. In [70], a microlaser with three organic dyes coated on a micro cavity is demonstrated without coupling in pump WGMs. In this device, three different dyes are selected such that the emission of one layer matches the absorption peak of the next one. Hence, this significantly increased the pumping efficiency such that the pumping was done by direct-illumination without extra need to couple in pump WGM.

Furthermore, cylindrical resonators, especially microtubes, are a promising platform for realization of WGM microlasers. The WGMs propagate close to the outer surface of the capillary, and if its thickness is kept sufficiently small, the optical mode will have efficient overlap with the medium inside. Therefore, such devices are excellent candidates for laser-based biochemical and chemical sensing [56].

Microdisks

Microdisks, usually referred as 2D WGM resonators, exhibit light confinement in radial and azimuthal directions due to their small thickness, and are widely used to realize chip-based microlasers [71]. A pioneering work on Er^{3+}-doped silica microdisk resonator with Q factor of ~10^6 is reported in [72]. Lasing at 1550nm wavelength with pump threshold power of 43μW is observed. Integrated microdisk and microcylinder lasers are developed based on semiconductor fabrication processes in materials such as GaAs/AlGaAs, InP/InGaAsP, and GaN/InGaN. Due to the large refractive index, and hence, strong light confinement, semiconductor resonators can be miniaturized with few-micron radii [73, 74]. Active media are incorporated in the disk material or deposited as a layer on top of the resonator. One advantage of these microlasers is that they can be electrically pumped. But, due to the surface roughness of the side-walls,

induced by the etching processes, they suffer from low Q factor, and hence large threshold powers.

1.3 Motivation

The ability of optical WGM resonators to store energy in a very small volume for a long time enables their use in practical applications requiring strong intra-cavity energy densities. One big problem with WGM resonators is the coupling light in and out of the resonator, especially for microlasers where the output light power is also an important factor. Coupling light in or out the resonator with conventional methods (such as tapered fibres, integrated waveguides or prisms) need precise alignment, and due to the strong confinement of light (small evanescent field), extracting light out of the resonator is a challenge. To maximize out-coupling of light, ways such as embedding a defect at the boundary of the resonator [75, 76] such as a tab or grating, or deformed microcavities [77, 78] are investigated, which mostly come with the cost of degradation in the Q factor.

Microtapers provide an effective coupling mechanism which can be easily tuned by its diameter and the air gap with the resonator, and has been dominantly employed with WGM microresonators. Therefore, understanding taper-coupled resonators is important for their effective operation. On the other hand, tapered fibres are delicate devices, require extra fabrication steps and degrade fast under normal operating conditions. Therefore, providing a platform where the excitation and collection of light along with the WGM laser cavity itself are all integrated as a stand-alone device, would be a major step towards the development of fully functional ultra-low threshold lasers.

Furthermore, owing to the high Q factor, WGM resonators make excellent sensors. Integration of microspheres in sensing systems such as stress sensors is difficult. A new class of devices such as microbottle (or microbubble) resonators overcome this issue with naturally having two stems attached to their sides, which enables handling and mechanical tuning of the resonator. Moreover, in the case of active cavity, due to the ultra-narrow linewidth of the laser, sensitivity of the device becomes higher than the passive counterpart, opening windows for label-free single molecule detection [45, 46, 79, 80]. Additionally, well-developed Yb/Er fibre lasers and amplifier technology has shown great promise in providing a commercially viable, low cost and high gain active platform. Such capability together with high Q and flexibility of microbottle resonators can offer inexpensive, tunable and low threshold single frequency microlasers.

Additionally, nonlinear optical processes do not need any additional dopant and can be enhanced only by optimisation of the resonator. The excitation threshold of such processes depends highly on the Q factor. Thus, enhancing the Q of the rare-earth doped WGM resonators can boost the internal power of the generated signal, and through cascaded processes can provide lasing lines well beyond the emission spectrum of used dopants.

Fabrication of such resonators is based on thermal, or chemical glass processing. Most of these methods do not have precise control on the size of the resonator or are not reproducible. Therefore, other methods such as material processing by light, would be a great step towards more controllable, single-step and mass fabrication of WGMs.

Key contributions of this thesis

In this thesis, I have tried to address the above issues in passive and active fibre-based WGM microcavies. The main contributions of this work are as follows:

- Development of a systematic general model for multimode propagation of WGMs in passive microresonators coupled to tapered fibres based on coupled mode theory. A phase matching map for coupling to specific WGMs in microspheres in terms of the cavity intrinsic losses and taper dimensions is produced.

- Modelling and analysis of Yb^{3+}-doped microbottle resonators. Investigation of effects of the cavity parameters such as intrinsic Q, dopant concentration and coupling condition on lasing characteristics.

- Demonstration of lasing in taper coupled Yb^{3+}-doped microbottle resonators fabricated directly from large core Yb^{3+}-doped silica fibres. Investigating the effects of coupling condition on tuning the lasing wavelength, efficiency and threshold. Achieving single mode lasing using spectra clean-up methods.

- Passive and active characterisation of new fiberized microstub resonators where the pumping of the microstub lasers and signal collection are realized through the stem fibres without usage of extra tapers.

- Study of a new type of pulsed CO_2 laser-milled WGM microrod lasers fabricated directly from Yb^{3+}-doped silica fibres. Characteristics of such resonator lasers are investigated in terms of lasing wavelength, and threshold. Generation of WGMs by side-pumping and side-signal-collection are demonstrated, providing a unified, robust and fully fiberized WGM laser.

- Demonstration of cascaded stimulated Raman scattering in passive microbottle and microstub resonators, and cooperative Yb-Raman lasing in super-polished microbottle and microsphere lasers, achieving lasing up to and above 1300nm wavelength by 976nm pumping.

Chapter 2 Basics of spherical whispering gallery modes

2.1 Introduction

Spherical resonators are among the fundamental resonator structures from which the concept of optical WGMs originated [11, 81, 82]. Their shape is simple, and exist naturally in the form of liquid droplets, bubbles and biological microparticles [44, 64, 83, 84]. In addition, straightforward fabrication methods have been developed to controllably fabricate microspheres from common optical telecom devices and materials. Hence, the study of such structures is especially important. Furthermore, the most experimentally common and efficient way to couple light in and out of such resonators is using tapered fibres [20]. Thus, a systematic study of tapered fibre-coupled resonators is of interest from a practical point of view.

In this chapter, the performance and characteristics of tapered fibre-coupled microsphere resonator are studied. From [85], first, an analytical model for spherical waves by solving wave equation is introduced, and then, a simple analytical solution for derivation of tapered fibre modes is given. Considering the general Coupled Mode Theory (CMT) for asymmetric couplers and transfer matrix method, used extensively in Fibre Bragg Gratings (FBGs), a general model for derivation of transmission spectra and internal power for phase-mismatched resonator-fibre modes is derived.

The ability of precisely controlling the coupling in microresonators is extremely important in both Cavity Quantum Electrodynamic (CQED), and linear/nonlinear photonics. On the other hand, given the experimental conditions, in most cases, it is preferred to bring the tapered fibre in contact to the resonator which makes the fundamental mode operate usually in the over-coupling regime where the taper-induced losses are dominant, and consequently, the internal power is lower. Hence, in nonlinear processes where higher intensity is required, excitation of higher order modes that are less affected by the cavity loading may be more efficient. On the other hand, proper selection or suppression of specific modes, is extremely important in designing WGM microlaser systems. Since, multimode lasing, gain competition and temporal instability are major ongoing problems with WGM microlasers.

I show that the loaded cavity Q factor not only is determined by the amount of the modal overlap but also phase-matching condition can play a significant role. This helps with

excitation of the close-to-fundamental-order modes for which the loaded Q is low due to high modal overlap when the taper diameter is small. Hence, phase mismatching can be beneficial as it increases the loaded Q and thus can provide higher internal power. In [20], it is hinted that using tapered fibres, excitation of different radial order WGMs of microspheres is possible. In general, higher radial order WGMs have larger effective refractive index differences (with the microtapered fibre mode), and for such modes changing the field overlap may affect significantly their excitation. In perfect microspheres, on the other hand, angular modes with the same azimuthal order have small effective index differences (due to slightly-different effective propagation radii), and this can be problematic if excitation of a certain mode is desired.

In this Chapter, I discuss extensively the effects of the tapered fibre and the intrinsic microcavity losses on the critical coupling condition to different (degenerate) angular order modes. This provides a parametric map, which can be used to selectively excite/collect specific WGMs in microspheres. Moreover, using general CMT, a systematic approach to calculate the total transmission spectra of taper-resonator system considering multimode excitation is provided. I focus on the influence of the taper diameter on the excitation of different radial and angular order WGMs. It is shown that by selecting the taper diameter, desired spectral response can be achieved for a specific resonator with given intrinsic losses.

To the best of my knowledge, there has not been any study about total internal field of microsphere resonators considering degenerate multimodal internal field excitation. All the experimental and theoretical reports so far consider deformed microspheres to map the internal non-degenerate fields [86, 87]. Due to broken degeneracy in prolate/oblate spheroidal resonators, WGMs are separated in frequency, hence, well-defined single spherical harmonics have been observed using taper-fibre-axial-scanning of transmission spectra [87] or collection through sharp fibre tips [86, 88]. In this Chapter, the total internal field in terms of taper diameter and the simultaneous excitation of degenerate WGMs is studied. It is demonstrated that depending on the taper fibre loading, specific WGMs or combination of various WGMs may exist, distorting the transmission spectra from a Fano-line shape. I conducted 3D FDTD simulations to prove the fact that the actual intra-cavity field in a perfect microsphere is a combination of degenerate fields depending on the coupling conditions.

This chapter contains the following new results:

- Transmission spectra model of taper-resonator system considering multimodal WGM propagation
- Phase-matching map for under-, over- and critically-coupled conditions to a desired degenerate spherical modes as a function of the excitation taper diameter and intrinsic microsphere losses.
- Theoretical model of total internal field of the micro resonator in the presence of degenerate angular modes, and the first demonstration of multimodal propagation of WGMs in microspheres using 3D FDTD modelling.

2.2 Fields of Microsphere

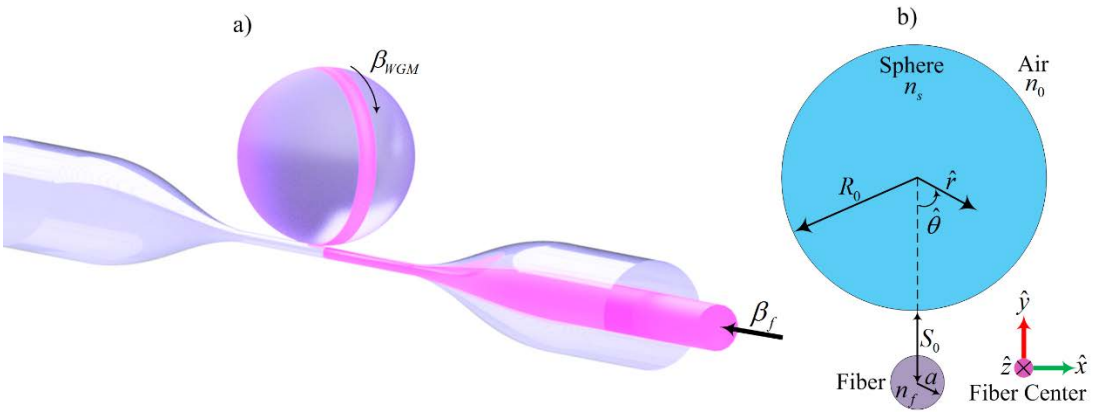

Figure 2-1 a) Schematic of optical microsphere resonator coupled to a tapered optical fibre, b) Cross-sectional view of the coupled tapered fibre and microsphere.

Figure 2-1 (a) illustrates a microsphere coupled to a tapered optical fibre, and (b) shows a cross-sectional view of the coupled tapered fibre and microsphere. The sphere and fibre have radii of R_0 and a, respectively. The centre of the fibre is off-set by S_0 from the sphere surface, and θ is the deviation angle from the equator line of the microsphere cross-section. The refractive indices of the dielectric microsphere, tapered fibre and the surrounding air are assumed to be n_s, n_f and n_0, respectively. The microsphere is described in spherical coordinate system by unit vectors $(\hat{r},\hat{\varphi},\hat{\theta})$ in radial, azimuthal and polar directions. $(\hat{x},\hat{y},\hat{z})$ describe the unit vectors in Cartesian system which are fixed at the fibre centre.

The Helmholtz equation in spherical coordinate system can describe the optical fields in the microsphere which results in the well-known Spherical Bessel functions and Spherical Harmonics for radial and angular field components, respectively. The fields of a microsphere can be derived as [85]

$$\Psi_{\ell,m,n}(r,\theta,\phi) = N_s \varphi_r(r)\varphi_\theta(\theta)\varphi_\phi(\phi) \tag{2-1}$$

where the field components are given by

$$\varphi_\phi(\phi) = \exp(\pm jm\phi) \tag{2-2}$$

$$\varphi_\theta(\theta) = \exp\left(-\frac{m}{2}\theta^2\right) H_N\left(\sqrt{m}\theta\right) \tag{2-3}$$

$$\varphi_r(r) = \begin{cases} j_\ell(kn_s r) & r \le R_0 \\ j_\ell(kn_s R_0)\exp\{-\alpha_s(r-R_0)\} & r > R_0 \end{cases}. \tag{2-4}$$

The coefficients are analytically evaluated as

$$N_s = \left\{ \sqrt{\frac{\pi}{m}} 2^{N-1} N! R_0^2 \left[\left(1 + \frac{1}{\alpha_s R_0} \right) j_\ell^2 \left(k n_s R_0 \right) - j_{\ell-1} \left(k n_s R_0 \right) j_{\ell+1} \left(k n_s R_0 \right) \right] \right\}^{-1/2}$$

$$\alpha_s = \sqrt{\beta_\ell^2 - k^2 n_0^2},$$

$$\beta_\ell = \frac{\sqrt{\ell(\ell+1)}}{R_0}, \qquad 2\text{-}5$$

$$N = \ell - m,$$

$$k = \frac{2\pi}{\lambda}.$$

The polar mode number, m, spans the values for $|m| \leq \ell$, where both m and the azimuthal mode number, ℓ are chosen large enough to minimize the errors due to approximations considered in solving the Helmholtz equation. α_s is the field decay coefficient along radial coordinate outside of the sphere, and β_ℓ is the propagation constant parallel to the surface of the sphere. The projection of β_ℓ along the equator on the sphere surface is evaluated as $\beta_m = m/R_0$. N_s is the normalization constant evaluated by taking the volume integral of $\Psi_{\ell,m,n}^2$ over all space divided by one equatorial path length $2\pi R_0$, which should be unity.

By matching the tangential electric and magnetic fields at $r = R_0$, the characteristic equation which relates the resonance wavelength and spherical eigennumbers, ℓ, m, n, can be obtained

$$\left(\eta_s \alpha_s + \frac{\ell}{R_0} \right) j_\ell \left(k n_s R_0 \right) - k n_s j_{\ell+1} \left(k n_s R_0 \right) = 0$$

$$\eta_s = \begin{cases} 1 & \text{TE mode} \\ \left(\dfrac{n_s}{n_0} \right)^2 & \text{TM mode} \end{cases} \qquad 2\text{-}6$$

For TE (TM) modes, the electric (magnetic) field is parallel to the surface and $\vec{E} = \hat{\theta} E_\theta = \hat{\theta} \Psi_{\ell,n,m}, \overrightarrow{E_\phi} = \overrightarrow{E_r} = 0$ ($\vec{H} = \hat{\theta} H_\theta = \hat{\theta} \Psi_{\ell,n,m}$, $\overrightarrow{H_\phi} = \overrightarrow{H_r} = 0$). The resonance wavelength is dependent on the azimuthal and radial mode numbers, ℓ and n, and the number of field maxima along the polar direction is determined by the value of N+1. At a specific wavelength, different m numbers correspond to different paths of modes, which have different inclination angles with respect to the equatorial plane that results in different propagation constants denoted by β_m for each mode. For the fundamental mode $\ell = m$, and decreasing the value of m will result in spreading the modes out of the equatorial

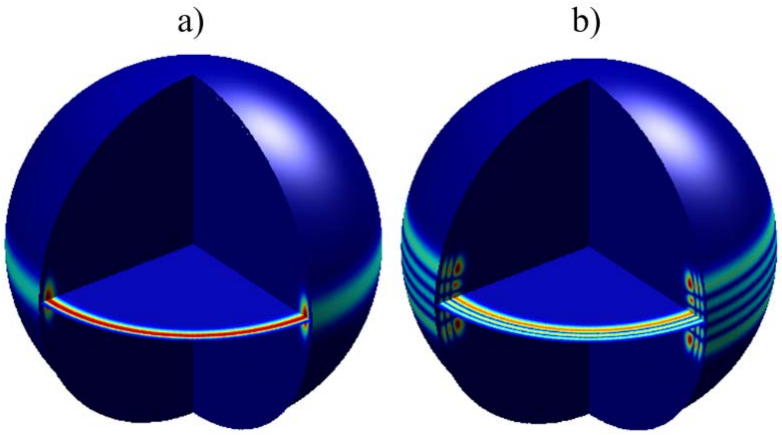

Figure 2-2 Spherical field intensity corresponding to a) fundamental mode ($\ell = m$, $n = 1$), and b) $N+1 = \ell-m+1 = 5$ and $n = 3$ mode numbers.

plane as well as increasing their inclination angle. Since, for all m's with the same value of ℓ, the resonance wavelength is constant (wavelength degeneracy), the higher order modes with higher N number (smaller m) will spread out from the equatorial plane which experience a shorter round-trip. Figure 2-2 (a) and (b) illustrate examples of spherical fields for the fundamental mode and a mode with $N+1 = \ell-m+1 = 5$ and $n = 3$, respectively.

2.3 Fields of Tapered Fibre

A tapered fibre with radius of a, core and cladding index of n_f and n_0, respectively, is schematically illustrated in Figure 2-1 (b). The linearly polarized mode fields of the fibre can be written analytically as [85]

$$F_o(\rho) = N_f \begin{cases} J_0^{-1}(k_f a) J_0(k_f \rho) & \rho \le a \\ \exp\{-\gamma_f(\rho - a)\} & \rho > a \end{cases}$$

$$N_f = \frac{\alpha_f J_0(k_f a)}{V_f \sqrt{\pi} J_1(k_f a)}, \quad k_f = \sqrt{k^2 n_f^2 - \beta_f^2}, \qquad 2\text{-}7$$

$$\alpha_f = \sqrt{\beta_f^2 - k^2 n_0^2}, \quad \gamma_f = \alpha_f \frac{K_1(\alpha_f a)}{K_0(\alpha_f a)}, \quad V_f = ka\sqrt{n_f^2 - n_0^2}$$

where J_0 and J_1 are the Bessel functions of zero and first orders, respectively, and K_0 and K_1 denote the modified Hankel functions of zero and first orders, accordingly. N_f is the fibre normalization constant which is obtained by integrating $F_o(\rho)$ over the transverse plane of the fibre cross-section. Propagation constant of the fibre can be evaluated from the characteristic equation given by

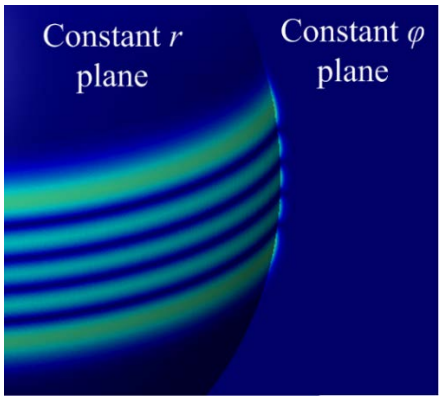

Figure 2-3 Typical high-angular-mode order spherical WGM shown at $r = R_0$ plane with evanescent wave tail on an arbitrary plane normal to $\hat{\varphi}$.

$$k_f \frac{J_1(k_f a)}{J_0(k_f a)} - \alpha_f \frac{K_1(\alpha_f a)}{K_0(\alpha_f a)} = 0. \qquad 2\text{-}8$$

2.4 Coupling between Tapered Fibre and Microsphere

From the characteristics equations 1.6 and 1.8, the resonance wavelengths and the propagation constant of the WGMs and the fibre modes can be obtained. Then, using Coupled Mode Theory (CMT) [89] the interaction strength of the normalized spherical and fibre fields at the minimum separation value of S_0 can be calculated by

$$\kappa_{sf}(S_0) = \frac{k^2}{2\beta_s} \iint_{(on\ sphere)} \left(n_s^2 - n_0^2\right) F_o \Psi_{l,m,n} dxdy$$
$$\kappa_{fs}(S_0) = \frac{k^2}{2\beta_f} \iint_{(on\ fiber)} \left(n_f^2 - n_0^2\right) F_o \Psi_{l,m,n} dxdy \qquad 2\text{-}9$$

where β_s is the propagation constant of the WGM. Integration over the microsphere cross-section gives $\kappa_{sf}(S_0)$ which shows the rate of increase of the sphere mode power at distance S_0 due to the fibre mode coupling. Similarly, if the overlap integral is calculated over the fibre cross-section, we obtain $\kappa_{fs}(S_0)$ which gives the rate of increase of the fibre mode power at distance S_0 due to the sphere mode coupling out and tunnelling into the fibre mode. Figure 2-3 shows a typical high angular WGM field from which the evanescent field extends out of the resonator boundaries into the air cladding.

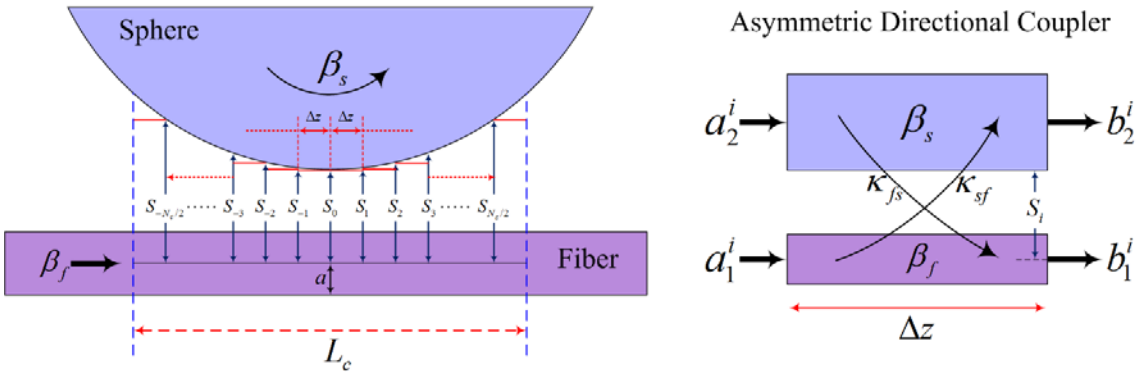

Figure 2-4 Schematic illustration of coupled sphere-fibre system showing the coupling region is tapered to N_c small directional coupler sections.

In order to evaluate the total coupling between the fibre and the sphere, the region where fibre mode has strong interaction with the WGM is considered as the coupler length denoted by L_c (see Figure 2-4). The coupler length is divided into N_c sections with fixed length of Δz and the separation is assumed constant along the coupler subsections defined by S_i (where $|i| \le N_c/2$). The solution of general coupled mode equation for an asymmetric directional coupler assuming weak coupling condition is given as [90]

$$\begin{bmatrix} b_1^i \\ b_2^i \end{bmatrix} = T_i \begin{bmatrix} a_1^i \\ a_2^i \end{bmatrix} = \begin{bmatrix} T_{11}^i & T_{12}^i \\ T_{21}^i & T_{22}^i \end{bmatrix} \begin{bmatrix} a_1^i \\ a_2^i \end{bmatrix} \tag{2-10}$$

where (a_1^i, a_2^i) and (b_1^i, b_2^i) are the input and output modes of coupler i as shown in Figure 2-4, and for a lossless coupler, entries of transfer matrix T_i are given as

$$\begin{aligned} T_{11}^i &= \left[\cos(\gamma_i \Delta z) + j\frac{\Delta\beta}{\gamma_i}\sin(\gamma_i \Delta z)\right]\exp\left\{j(\beta_f - \Delta\beta)\Delta z\right\} \\ T_{12}^i &= j\frac{\kappa_{fs}(S_i)}{\gamma_i}\sin(\gamma_i \Delta z)\exp\left\{j(\beta_f - \Delta\beta)\Delta z\right\} \\ T_{21}^i &= j\frac{\kappa_{sf}(S_i)}{\gamma_i}\sin(\gamma_i \Delta z)\exp\left\{j(\beta_s + \Delta\beta)\Delta z\right\} \\ T_{22}^i &= \left[\cos(\gamma_i \Delta z) - j\frac{\Delta\beta}{\gamma_i}\sin(\gamma_i \Delta z)\right]\exp\left\{j(\beta_s + \Delta\beta)\Delta z\right\} \end{aligned} \tag{2-11}$$

where

$$\begin{aligned} \Delta\beta &= \frac{\beta_f - \beta_s}{2} \\ \gamma_i &= \left(\Delta\beta^2 + \kappa_{sf}(S_i)\kappa_{fs}(S_i)\right)^{\frac{1}{2}}. \end{aligned} \tag{2-12}$$

Then, the total transfer matrix of the coupler is calculated by

$$T = \begin{bmatrix} T_{11} & T_{12} \\ T_{21} & T_{22} \end{bmatrix} = \prod_{i=-N_c/2}^{N_c/2} T_i \ . \qquad 2\text{-}13$$

In order to derive the total transmission of the coupled-fibre-sphere system, we assume that the optical mode circulating in the resonator experiences transformation T_{FB} due to feedback, hence

$$\begin{aligned} a_2 &= T_{FB} b_2 \\ &= \exp\left(-\left(2\pi R_0 - L_c\right)\alpha_{\text{int}} + j\varphi_{rt}\right) b_2 \\ \varphi_{rt} &= 2\pi R_0 \beta_s - \varphi_c \end{aligned} \qquad 2\text{-}14$$

φ_{rt} is the total round-trip phase change experienced by the WGM, φ_c denotes the phase shift due to the coupler, and α_{int} is the total intrinsic loss coefficient per unit length due to scattering losses such as Rayleigh (residual surface inhomogeneity) and radiation (due to curvature). The intrinsic loss per unit length is related to the intrinsic Q factor by

$$\alpha_{\text{int}} = \frac{1}{\tau_{\text{int}}} \cdot \frac{n_{eff}}{c} = \frac{\omega}{Q_{\text{int}}} \cdot \frac{n_{eff}}{c} = \frac{2\pi n_{eff}}{Q_{\text{int}} \lambda} \qquad 2\text{-}15$$

where τ_{int} is the photon lifetime considering only intrinsic losses in one round-trip, c is the speed of light, ω is the angular frequency of the optical mode, n_{eff} is the effective index of the optical mode, λ is the wavelength and Q_{int} is the intrinsic quality factor.

The transmitted power of the resonator can be written such that

$$P_{out} = \left| T_{11} + \frac{T_{12} T_{21}}{\frac{1}{T_{FB}} - T_{22}} \right|^2 P_{in} \qquad 2\text{-}16$$

where P_{in} is the input power. The intra-cavity power in terms of the input power and entries of the transfer matrix is

$$P_{intra} = \left| \frac{T_{21}}{1 - T_{FB} T_{22}} \right|^2 P_{in} . \qquad 2\text{-}17$$

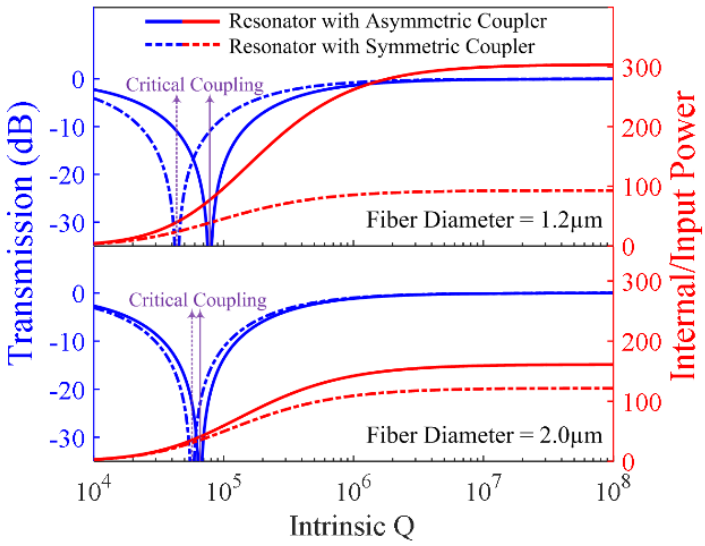

Figure 2-5 Transmission and internal power of fibre taper coupled resonator as function of intrinsic Q for taper diameters of 1.2μm and 2 μm considering both symmetric and asymmetric coupler model (for fundamental taper and resonator modes).

In order to understand the importance of the asymmetric coupler model incorporated in our design, let us first evaluate the model of the taper-resonator system considering two cases with symmetric and asymmetric coupler model. For the symmetric coupler model, the coupling coefficient from resonator to taper is taken identical to the one from taper to resonator such that $\kappa_{sf} = \kappa_{fs}$. Assuming the fundamental WGM and LP_{01} fibre mode, the transmission and internal-to-input power ratio for two different taper diameters (1.2μm and 2μm) coupled to a microsphere with $R_0 = 30\mu m$ are shown in Figure 2-5. The critical coupling point (where transmission is zero) determined by the κ_{fs} and intrinsic losses, happens at smaller loss values in the case of symmetric coupler. This is due to higher power coupled from the resonator to the fibre when considering symmetric coupler, while in the case of asymmetric one, the internal power couples out by a smaller rate. The internal/input power ratio shows the fact that in asymmetric coupler case due to smaller out-coupling rate the power inside the resonator is accumulated to higher levels. This is important when nonlinear and lasing effects are analysed, as the internal power defines the nonlinearity strength and the gain saturation. As the taper diameter increases the effect of symmetry in the coupling coefficients decreases due to the larger cross section area of the taper and smaller evanescent field overlaps.

2.5 WGM Phase-matching and Q Factor

In this section parameters affecting the coupling, transmission and internal power of coupled taper/sphere system will be studied. We consider a microsphere with $R_0 = 30\mu m$ and refractive indices of $n_s = n_f = 1.45$.

Solving the characteristics equation for spherical modes (Eq. 2-6) gives all the possible resonance wavelengths for a sphere with certain optical and geometrical parameters at a given azimuthal mode number (ℓ). The Transverse Electric (TE) resonance wavelengths in 1530-1580nm range for a 30μm-radius sphere at each angular mode number, m, down to the third radial order (n = 1, 2, 3), are illustrated in Figure 2-6 (a). Here, we consider the first 15 angular modes for each group of same azimuthal order. The resonance wavelengths are not dependent to the angular mode number. Hence, each set of points, which have equal azimuthal mode number (ℓ) and resonance wavelength, represents all the degenerate modes with different m mode numbers. The first angular mode number for each set of degenerate modes with the same azimuthal order is called the fundamental mode for which $m = \ell$.

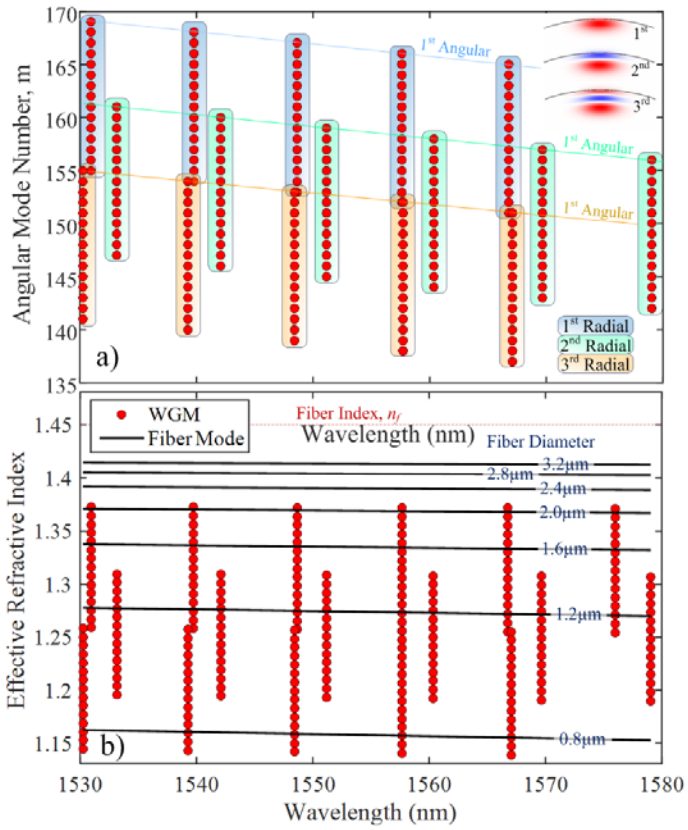

Figure 2-6 a) Spectra of TE resonances of a 30μm-radius sphere for various angular mode numbers ($N \leq 14$) for the first three radial order ($n \leq 3$) WGMs, and b) corresponding effective refractive indices of WGMs, and tapered fibres with various diameters.

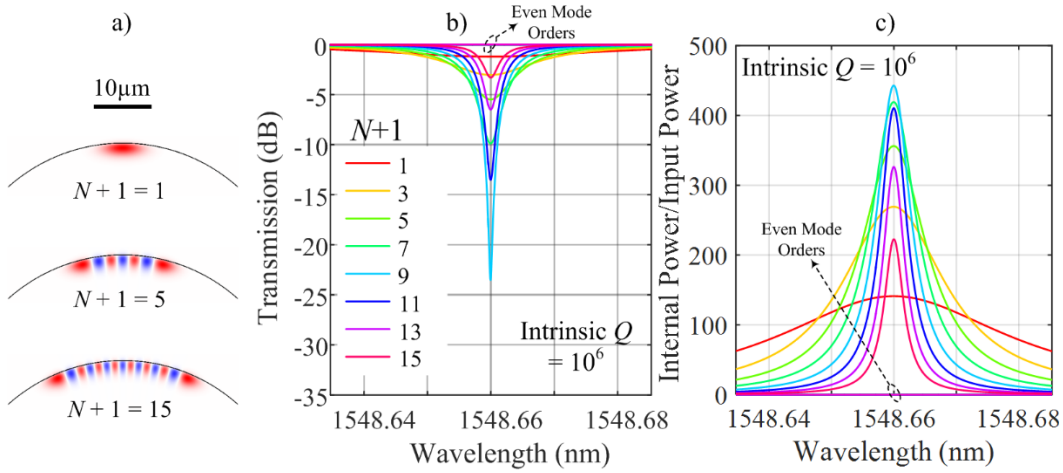

Figure 2-7 Calculated a) first order radial mode fields with various angular orders, b) transmission and c) internal power spectra of the first 15 angular mode orders.

Figure 2-6 (b) shows the calculated effective refractive index of each WGM as well as the effective refractive index of the tapered fibre with various diameters. The effective refractive index of each WGM is given by β_m/k. Propagation constant of the fibre with a fixed diameter is only dependent on the wavelength, and the propagation constant of the WGM circulating in the microsphere is proportional to the angular mode number, m. Therefore, the phase mismatch between the propagating fibre mode and the WGM is a function of both wavelength and angular mode number. By decreasing the m value, or in other words, increasing the number of maxima in angular direction ($N + 1 = \ell - m + 1$), the phase mismatch increases or decreases depending on the effective refractive index of the tapered fibre which is a function of the taper diameter. Figure 2-6 (b) is important in designing suitable tapered fibre-resonator system in order to phase-match to a desired set of modes. This provides a map from which conditions to couple to different WGMs can be satisfied, by precisely controlling the taper diameter.

In section 2.4, the total transmission for a coupled-taper-sphere was derived. Assuming that the effective refractive index of WGMs does not change significantly around the resonance wavelength, the propagation constant of a resonance mode can be evaluated at various wavelengths such that $\beta_{WGM}(m, \lambda) = 2\pi n_{eff,WGM} / \lambda$, where the dependence on m comes from the fact that distinct angular WGMs have different n_{eff}.

Figure 2-7 (a) shows examples of calculated first order radial mode fields with varying angular orders. The calculated transmission spectra and the intra-cavity power for the fundamental mode of the taper (LP_{01}) corresponding to each WGM is plotted in Figure 2-7 (b). The taper diameter is chosen to be 2μm and touching the resonator surface from the top (zero air gap), and the intrinsic Q for all the modes is fixed at 10^6. Results show that for the modes with even N+1 value, the internal power is very low such that the

input power is transmitted with no coupling. This is due to the symmetry of WGM fields at the centre where the total fibre-resonator mode overlap integral is close to zero.

The strength of resonance for each specific mode depends on the phase-matching and coupling condition to that mode which is determined by the cavity loading induced by the taper coupling and intrinsic losses. Loading of the tapered fibre can be evaluated in terms of the external Q factor which is defined by the ratio of the stored energy over the lost energy per cycle such that

$$\begin{aligned} Q_{ext} &= \omega \frac{\text{Stored Energy}}{\text{Dissipated Energy per Cycle}} \\ &= 2\pi \frac{c}{\lambda} \frac{P_{intra}(n_{eff} L_{cavity} / c)}{|T_{12}|^2 P_{intra}} \\ &= \frac{2\pi m}{|T_{12}|^2} \end{aligned} \qquad 2\text{-}18$$

where $L_{cavity} = 2\pi R_0$ denotes the cavity length, and $|T_{12}|^2 P_{intra}$ determines the power loss due to resonator-to-fibre out-coupling per round-trip. Eq. 2-18 is derived considering only forward propagating wave. The backward waves are neglected since the intra-cavity back-reflections are considered zero. The external Q calculated from [6] in which both forward and backward waves are considered, is half of the above value. It should also be noted that T_{12} is calculated from Eq. 2-13, and includes the phase matching information between WGM and fibre mode.

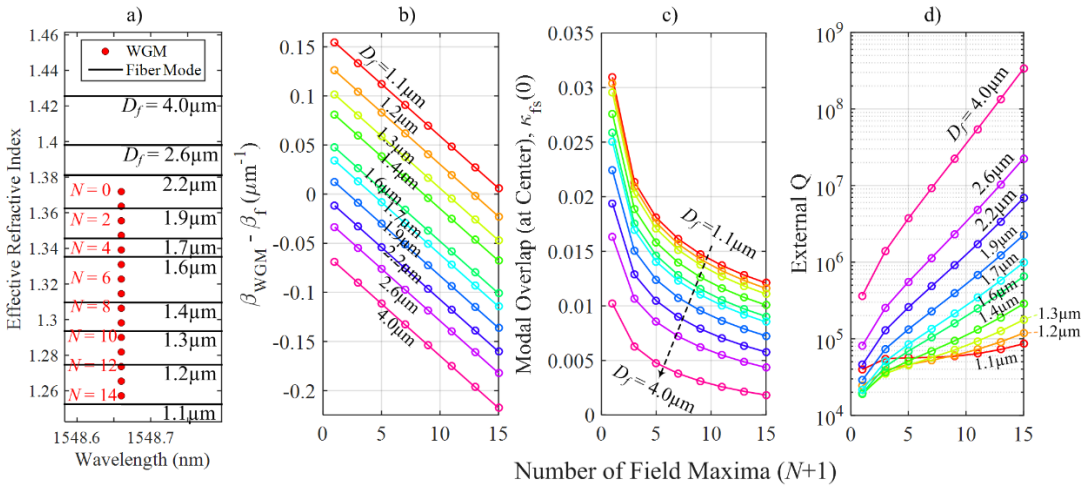

Figure 2-8 a) Effective refractive index spectra of resonator and fibre modes of various diameters, b) phase mismatch, c) fibre-WGM modal overlap at S_0 = 0, and d) calculated total external Q, for the first radial order (n=1) WGMs as function of number of field maxima (N+1).

Figure 2-8 (a) shows the calculated effective index for the first radial order WGMs ($n = 1$) at ~1548.65nm wavelength, with the ones calculated for different taper diameters. As the taper diameter varies depending on the angular order of the WGM the phase mismatch value decreases or increases (Figure 2-8 (b)) due to the difference between the effective indices. As the number of field maxima ($N + 1$) of the WGMs increases (or m decreases) the modal field extends further into the air surrounding, and hence, experiences a smaller effective index. Similarly, decreasing the taper diameter expands the mode into the air cladding, and lowers the effective index of the fibre mode. Combination of these two effects determines the modal overlap between the WGMs and the fibre mode. Figure 2-8 (c) plots the modal overlap evaluated from the overlap integral in Eq. 2-9 at the centre of the resonator in contact with the tapered fibre for the LP_{01} mode of different fibre diameters and WGMs with increasing N number. As the taper diameter increases, the evanescent tail of the fibre mode drops, which decreases the fibre and WGM interaction. In addition, expansion of higher angular order WGMs along the resonator, decreases the evanescent field amplitude, and hence, lowers the modal overlap strength. The cavity loading (external Q factor) due to the fibre coupling is shown in Figure 2-8 (d) as a function of WGM number ($N + 1$). The results show that for large taper diameters as well as high angular orders the external Q is high due to small modal overlaps. While, at small taper diameters, when the angular order of the WGMs is small the phase-mismatch between the fibre mode and WGM significantly affects the external Q.

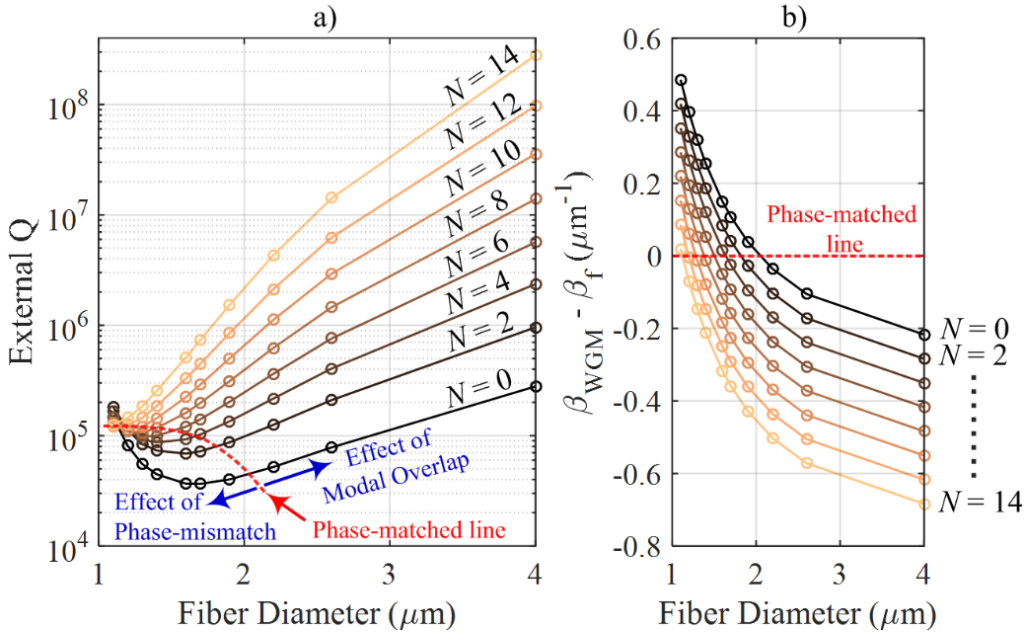

Figure 2-9 Calculated a) external Q and b) WGM-fibre-mode phase-mismatch as function of taper diameter for the first order radial WGMs with various angular orders.

In order to discriminate the effects of phase-mismatch and modal overlap, the external Q as a function of taper diameter for fixed angular mode numbers is plotted in Figure 2-9 (a). For small taper diameters where there is large phase-mismatch (see Figure 2-9 (b)), the effect of the taper diameter on the WGM is small, and increases the external Q factor. While, by gradually enlarging the taper diameter, phase-mismatch decreases and the external Q drops. For large N's the effect of modal overlap is dominant since the WGM intensity is lower comparing to WGMs with small N. The phase-matched line in Figure 2-9 (a) and (b) shows where the phase-matching happens for a specific WGM order. Note that, the external Q increases in an exponential fashion above the phase-matched line, due to the dominant effect of the modal overlap and the exponential drop of the evanescent field.

2.6 WGM Transmission and Internal Power

Transmitted power due to coupling to a cavity resonance is a function of the intrinsic and external Q's. Such parameters determine the coupling states under which a WGM operates such that:

1) If $Q_{ext} > Q_0$ then the resonance is in 'Under-coupling' regime, and $0 < Transmission < 1$.
2) If $Q_{ext} = Q_0$ then the resonance is in 'Critical-coupling' regime, and $Transmission = 0$.
3) If $Q_{ext} < Q_0$ then the resonance is in 'Over-coupling' regime, and $0 < Transmission < 1$.

An important parameter in excitation of WGMs is the critical coupling point where the total intrinsic losses is equal to the external losses induced by the coupling. At this point the transmitted power at the taper output is equal to zero.

Let us consider the aforementioned set of first radial order mode group ($n = 1$) at 1548.65nm wavelength. We will investigate the effect of angular order (m) of WGMs and the condition of excitation/collection of such modes in terms of the taper diameter and the intrinsic Q factor of the resonator. Figure 2-10 (a) depicts the transmission of the taper-resonator system as a function of intrinsic Q for each angular order of WGMs at various taper diameters. The critical Q for each WGM is dependent on the chosen taper diameter such that for small diameters due to high external loading, all the WGMs have fairly similar critical Q. As the taper diameter increases, the critical-coupling condition for higher order modes shifts to larger intrinsic Q values, due to the lower external loading (high external Q) of such modes. Figure 2-10 (b) shows the critical Q value for all the WGMs as a function of the fibre diameter. Each constant-N

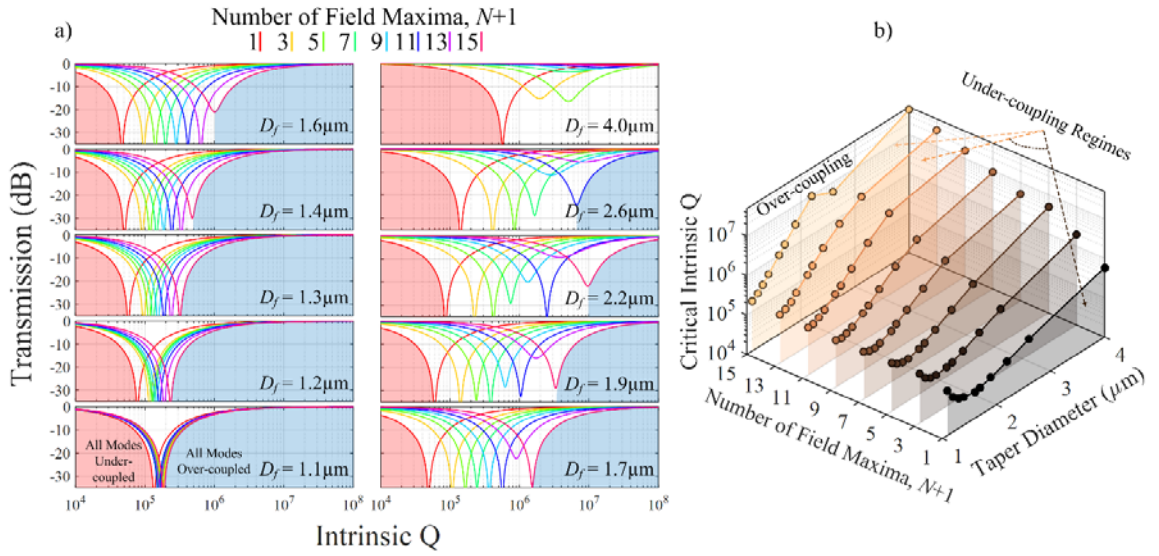

Figure 2-10 a) Transmission of the taper-resonator system at resonance wavelength as function of intrinsic Q for each angular order of WGMs at various taper diameters, and b) critical Q as function of fibre diameter and number of mode field maxima ($N + 1$), showing various coupling regimes under which a WGM operates.

curve gives information about the critical-coupling condition to that specific WGM. Below and above the critical-coupling curve, taper-resonator system operates in under-coupling and over-coupling regimes, respectively. This gives a figure of merit to selectively-excite/collect a specific WGM with a given intrinsic Q by only changing the taper diameter. Taper diameter can be experimentally varied by translating the resonator along the taper length and this method will be used later to selectively-excite/collect WGM lasing lines in microbottle laser chapter (Chapter 5). Furthermore, access to selective-WGM-excitation is significantly important in nonlinear optical processes where the spatial distribution and power intensity of the mode determines the nonlinear gain/loss of the system.

Figure 2-11 shows the calculated internal-to-input power-ratio at the resonance wavelength as function of intrinsic Q factor for each individual angular mode order with various taper diameters. For each considered taper diameter, the total "weighted" internal fields, b_T's, at three different intrinsic Q's is estimated using the following relation

$$b_T = \sum_{m=m_1}^{m_2} \frac{P_{intra}^m}{\sum_{i=m_1}^{m_2} P_{intra}^i} b_m \qquad 2\text{-}19$$

where P_{intra}^m is the internal power of the mode with angular order of m calculated from Eq. 2-17, b_m is the internal field from Eq. 2-10, and $P_{intra}^m / \sum_{i=m_1}^{m_2} P_{intra}^i$ is the contribution of

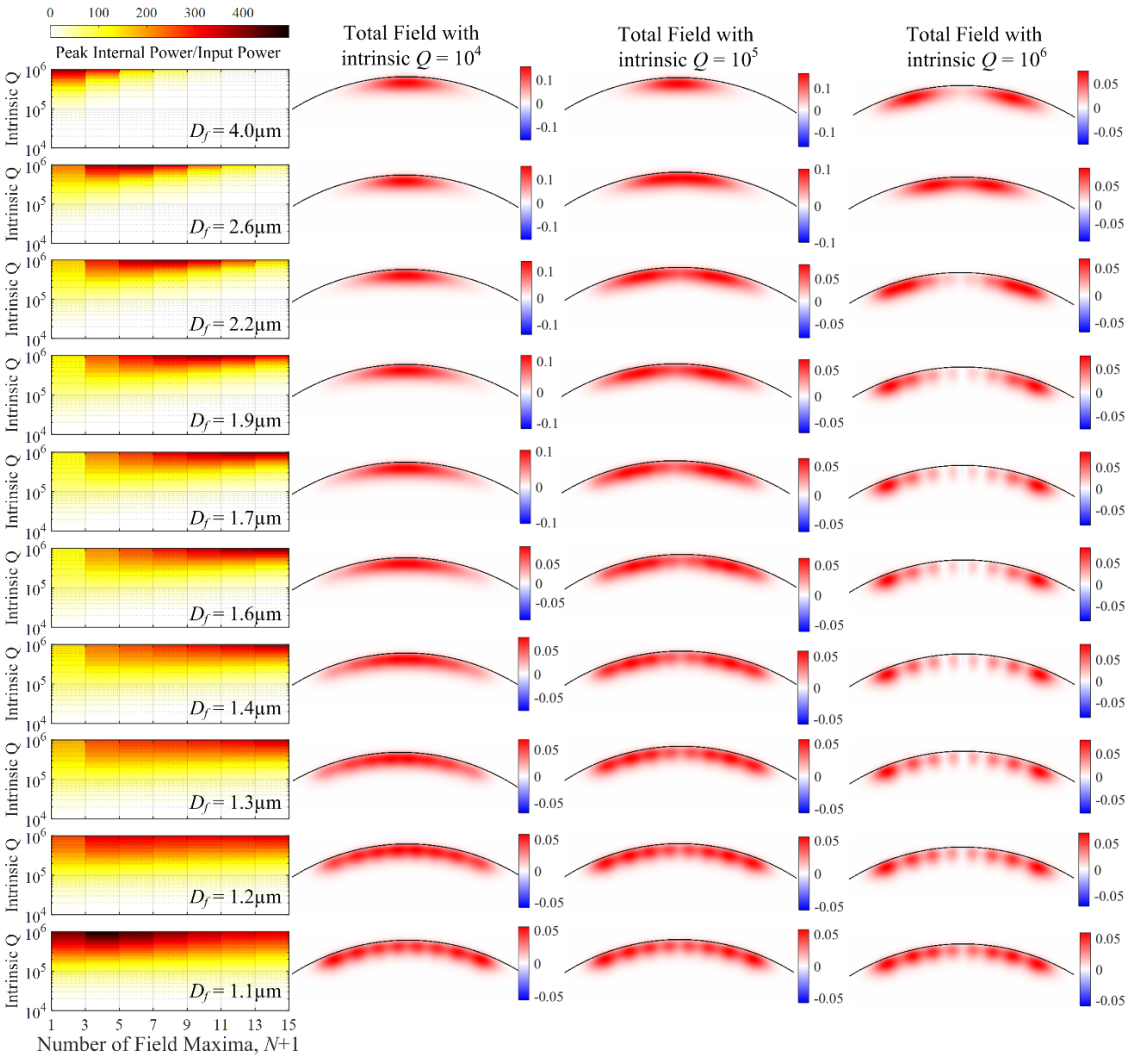

Figure 2-11 Calculated internal-to-input power-ratio at resonance wavelength as function of intrinsic Q factor for each individual angular mode order with various taper diameters, as well as, the corresponding total weighted internal field profiles with intrinsic Q's of 10^4, 10^5 and 10^6.

mode m to the total accumulated internal power of distinct WGMs (with angular mode numbers between m_1 and m_2). Modes with even m are not plotted in Figure 2-11, since they have close to zero internal power due to symmetry of the field profile around the centre of the microsphere resonator. For large taper diameters where the external Q factor is relatively high, the total internal field is mostly constructed by the WGMs with small N order. Only by increasing the intrinsic Q factor higher order modes will be closer to critical coupling, and hence, their internal power increases. Whereas, at small taper diameters, the internal power can be distributed between various higher order modes. At very small taper diameters, most of the modes are in the over-coupling regime, and the modes that have closer Q to critical coupling will be predominantly excited.

Figure 2-12 (a) depicts the condition required for excitation of a WGM with specific angular order for a given intrinsic resonator Q factor. If the intrinsic Q of the resonator is too low (i.e. $Q_{int} = 10^4$) all modes are in under-coupling regime. The maximum power

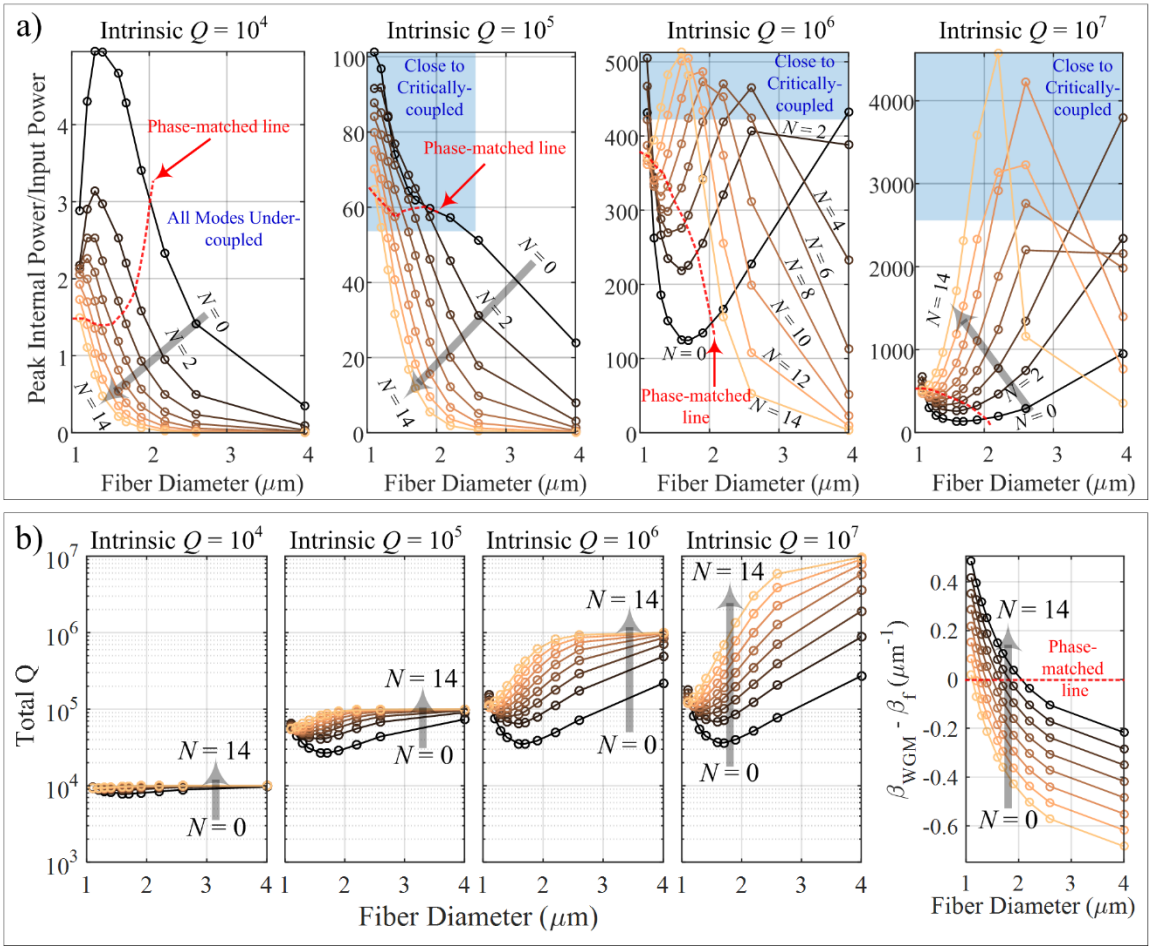

Figure 2-12 a) Internal power or various angular mode orders as function of taper diameter at different intrinsic Q's, and b) corresponding total Q and WGM-fibre mode phase matching map.

for a particular angular order mode happens at a taper diameter that has the smallest distance to the $Q_{int} = Q_{ext}$ line. Furthermore, the internal power at small intrinsic Q's for the taper diameters below the phase-matched line is a function of both phase-matching and modal overlap. While, at large taper diameters, since the coupling efficiency is dominant, the internal power drops dramatically. As the intrinsic Q factor gradually increases, the taper diameter corresponding to the dominantly-excited mode can be shifted to larger values. At $Q_{int} = 10^5$, most of the modes operate close to under-coupling regime, hence, the maximum achievable internal power is at very small taper diameters. Further increasing Q_{int} will force the WGMs to go from under-coupling to critically-coupling and over-coupling regimes. For instance, at $Q_{int} = 10^6$ for $N = 0$ and 2, regardless of taper diameter, the WGM operates at under-coupling regime, while for $N > 2$ depending on the taper diameter, a particular WGM may operate in either of the three aforementioned coupling regimes. At $Q_{int} = 10^7$, WGMs close to $Q_{int} = Q_{ext}$ line which have high N orders see a significant power rise, when compared to lower order modes as well as those at small taper diameters, which are dramatically under-coupled.

It should be noted that, the maximum internal power for each WGM is determined by the total Q factor (Q_T) determined by $1/Q_T = 1/Q_{int} + 1/Q_{ext}$. Figure 2-12 (b) shows the calculated total Q as a function of fibre diameter corresponding to the intrinsic Q's studied in Figure 2-12 (a). For large taper diameters where the external Q is much higher than the intrinsic one, the total Q clamps to the intrinsic Q. At the clamping region where the total losses are constant, further increasing the taper diameter will decrease the amount of input power into the resonator due to the low coupling efficiency. This drops the internal power as the taper diameter increases, while the total loss is dominated by the intrinsic losses and no longer depends on the taper diameter.

The findings shown in Figure 2-11 and Figure 2-12 can be used to define to large extent the criteria for selecting the dimensions of fibre microtapers in microsphere based lasers and nonlinear elements, since they can be used to define the pumping and active mode characteristics for optimum performance.

In order to show that simultaneous excitation of degenerate WGMs in perfect microspheres is possible, 3D Finite Difference Time Domain (FDTD) simulations of Maxwell's equations are conducted (in RSOFT, fullwave). In this model, due to hardware limitations, a microsphere with 12μm diameter and spatial computational grid-size of $100\times100\times100nm^3$ is chosen. Since the purpose of these simulations is to demonstrate the possibility of existing such degenerate WGMs, the accuracy of the calculated transmission spectra and field values is not important here. However, it is tried to keep the grid-size ~1/10 of the width of the smallest part in the design. Figure 2-13 (a) shows the calculated transmission spectra of the coupled-taper-resonator system for various taper diameters ($0.8\mu m \leq D_f \leq 1.5\mu m$). The transmission spectra are calculated from the impulse response of the resonator by taking the spectral ratio of the input LP_{01} fibre mode and the output of the fibre at the other side of the coupling region. Simulation is carried out temporally long enough (~27 round-trips) so that the output power is stabilized. The transmission spectra show dips separated in the wavelength range matching the FSR of the resonator (i.e. $\lambda^2/2\pi nR_0$). The off-resonance drop in the transmission is mostly due to light scattering into the microsphere owing to the strong index perturbation at the coupling point. As the taper diameter decreases the amount of off-resonance power loss increases since the fibre mode has stronger overlap with the resonator. This effect is experimentally shown in [91] for microbottle resonators. Here, the material losses are considered zero, therefore, the radiation losses due to curvature and index perturbation are the only loss mechanisms.

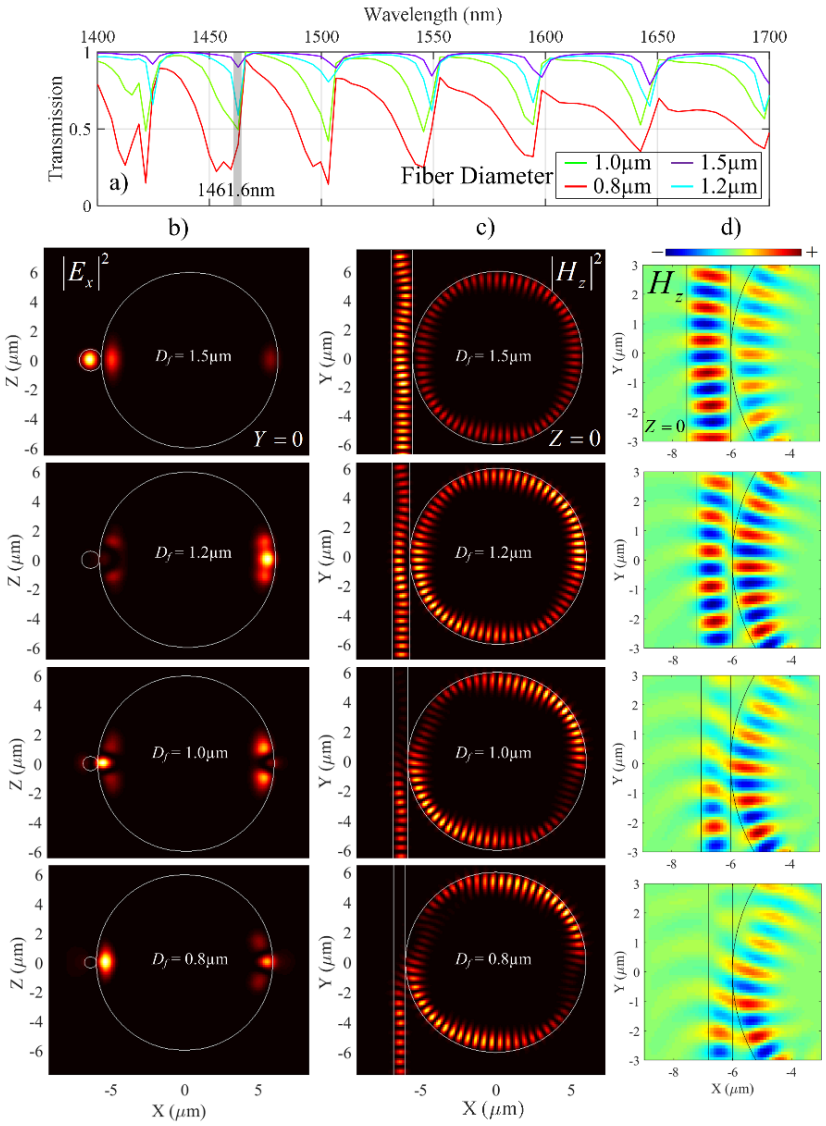

Figure 2-13 FDTD simulations showing a) transmission spectra, and resonance field intensities at 1461.6nm for various taper diameters in a) X-Z, b) X-Y planes, and c) magnetic field around the coupling region showing phase-matching conditions.

The E_x intensity of the system at the wavelength of 1461.6nm is depicted in Figure 2-13 (b) for various taper diameters. The results show that for taper diameter of 1.5µm only the fundamental (N = 0) WGM is excited. As the taper diameter is decreased, the next angular order (N = 1) WGM starts building up inside the resonator. At taper diameter 0.8µm, it is clearly shown that the total intra-cavity electric field intensity is constructed by both the first and the second order WGMs, which due to different propagation constant interfere along the resonator length. Figure 2-13 (c) and (d) plot the H_z intensity and value for each taper diameter. At larger taper diameters (i.e 1.5µm) for which only the fundamental WGM is excited, it is clear that the fibre mode and the WGM are totally out of phase over the coupling region. This shows that due to large diameter of the fibre and hence smaller evanescent field, only the fundamental mode have adequate overlap with the fibre mode to be excited/collected. By gradually

decreasing the fibre diameter, the total intra-cavity field at coupling region starts to phase-match and synchronise with the fibre mode. At 0.8μm fibre diameter, two distinct WGMs are shown to be beating along the resonator.

It is worth mentioning that, at larger taper diameters the fibre mode seems to be repelled away from the resonator. This is owing to slight excitation of LP_{11} fibre mode, in addition to the LP_{01} fibre mode, in the outcoupling process [91, 92]. Further along the taper, two LP_{01} and LP_{11} modes beat together causing fluctuations in the fibre field intensity. At smaller taper diameters, higher order modes are cut-off, and not excited.

2.7 Total Transmission of Multimode Microsphere Resonator

In order to evaluate the total transmission of the taper-microsphere system, I adopt the vector form of CMT [89, 93, 94]. Let us assume all the modes propagating along the coupler illustrated in Figure 2-4 as a vector denoted by $a(z) = [a_f(z)\ a_0(z)\ \ a_1(z)\ \ \ldots\ a_N(z)]^t$ where $a_f(z)$ and $a_i(z)$ (with $0 \le i \le N$) are respectively the electric field amplitude of the fibre mode and WGM of order i at position z. Then, the CMT formulation for the coupling region is given by

$$\frac{d}{dz}a(z) = jM(z)a(z) \qquad 2\text{-}20$$

where $M = B + C^{-1}K$ represents an effective coupling matrix, and B denotes the diagonal propagation constant matrix given as $B = diag\ (\beta_f, \beta_0, \beta_1, \ldots, \beta_N)$. Elements of matrices C and K are given by

$$K_{ij} = \frac{k^2}{2\beta_i} \iint_{\text{Over Guide } i} \left(n_i^2 - n_0^2\right) E_i^* E_j \, dxdy$$
$$C_{ij} = \iint_{\text{Over All Space}} E_i^* E_j \, dxdy \qquad 2\text{-}21$$

where K_{ij} is the coupling coefficient of mode j with E-field of Ej to mode i with E-field of E_i. It should be noted that, in a microsphere eigenmodes are orthonormal (i.e. $C_{ii} = 1$), hence, coupling coefficients between distinct WGMs are zero. The solution of 2-20 is given by $b(z) = e^{jMz}a(0)$ where $a(0)$ is the initial value, and $b(z) = [b_f(z)\ b_0(z)\ \ b_1(z) \ldots b_N(z)]^t$. Value of e^{jMz} can be evaluated from the eigenvalue solutions of matrix M. Note that, Eq. 2-11 was an analytical solution of the coupled-mode relation for a system of two modes (single fibre and single WGM).

The coupled-mode solution can be calculated for each section of the coupler with length of Δz (as demonstrated in Figure 2-4). Thus, the total transfer matrix of the coupler is $\Lambda = e^{jM_{N_c}\Delta z} e^{jM_{N_c-1}\Delta z} \cdots e^{jM_1\Delta z}$. Let us signify the internal amplitudes of the resonator WGMs at the beginning and end of the coupler region by $a_{wgm}(0) = [a_0(0)\ a_1(0)\ \ldots\ a_N(0)]^t$ and $b_{wgm}(L_c) = [b_0(L_c)\ \ b_1(L_c)\ \ \ldots\ b_N(L_c)]^t$, respectively. Similar to the case of two-mode-coupler, $a_{wgm}(0)$ and $b_{wgm}(L_c)$ are related through the propagation of WGMs in the resonator, given by a diagonal transformation matrix T_F such that $a_{wgm}(0) = T_F\, b_{wgm}(L_c)$ where $T_F = diag\,(T_{FB(0)}, T_{FB(1)}, \ldots, T_{FB(N)})$. Each round-trip transformation element is given by $T_{FB(i)} = exp[(2\pi R_0 - L_c)\alpha_{int(i)} + j\varphi_{rt(i)}]$ where $\alpha_{int(i)}$ is the intrinsic loss parameter (per unit of length) of mode i. The round-trip phase shift, $\varphi_{rt(i)}$, can be calculated from the modified resonance condition for mode i such that

$$\varphi_{rt(i)} + \Delta\varphi_{c(i)} = 2\pi m \qquad 2\text{-}22$$

where the coupler-induced-phase-shift on mode i is calculated from the diagonals of transfer matrix of the coupler by $\Delta\varphi_{c(i)} = \arg\{\Lambda_{ii}\}$. Let us define matrices V_1, V_2 and V_3 from Λ such that

$$\Lambda = \left[\Lambda_{ij}\right] = \begin{bmatrix} \overbrace{\begin{bmatrix} \Lambda_{11} & \Lambda_{12} & \cdots & \Lambda_{1(N+1)} \end{bmatrix}}^{V_1} \\ \underbrace{\begin{bmatrix} \Lambda_{21} \\ \vdots \\ \Lambda_{(N+1)1} \end{bmatrix}}_{[V_2]^t} & \underbrace{\begin{bmatrix} \Lambda_{22} & \cdots & \Lambda_{2(N+1)} \\ \vdots & \ddots & \vdots \\ \Lambda_{(N+1)1} & \cdots & \Lambda_{(N+1)(N+1)} \end{bmatrix}}_{V_3} \end{bmatrix} \qquad 2\text{-}23$$

and write the coupler relation in the form of $[b_f(L_c)\ b_{wgm}(L_c)] = \Lambda[a_f(0)\ a_{wgm}(0)]$. Then, by simple matrix manipulations, the output of the tapered fibre, $b_f(L_c)$, and the internal field amplitudes, $a_{wgm}(0)$, can be written as a function of input fibre mode, $a_f(0)$, such that

$$\begin{aligned} a_{wgm}(0) &= \left(\left[T_F{}^{-1} - V_3\right]^{-1} V_2\right) a_f(0) \\ b_{wgm}(L_c) &= V_1 \begin{bmatrix} 1 \\ a_{wgm}(0) \end{bmatrix} a_f(0) \end{aligned} \qquad 2\text{-}24$$

Accordingly, the power transmission of the system is given by scalar $|b_{wgm}(L_c)/a_f(0)|^2$ and the ratio of the internal power to the input power of all WGMs can be evaluated by vector $|a_{wgm}(0)/a_f(0)|^2$.

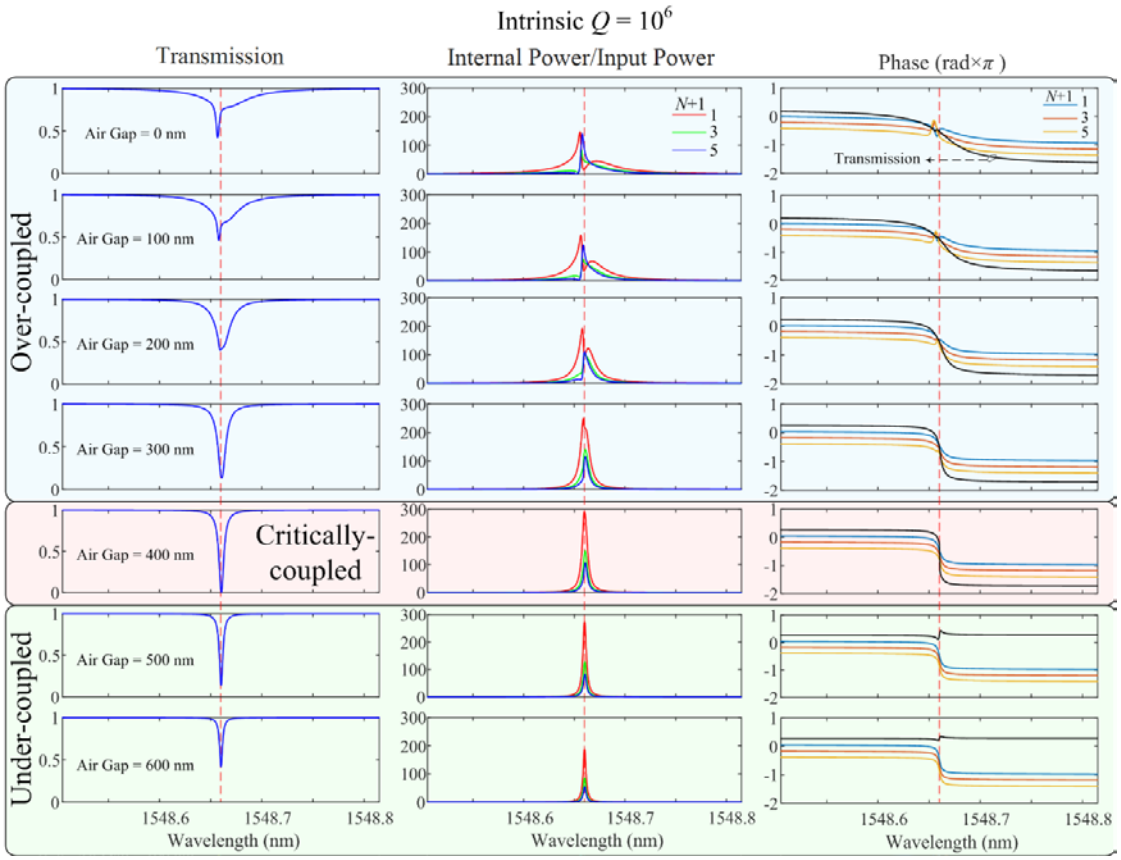

Figure 2-14 Spectra of transmission, internal power enhancement and phase of tapered fibre coupled microsphere considering degenerate modes of 1st, 3rd and 5th order modes as a function of fibre-to-sphere air gap. The intrinsic Q of all modes is set to 10^6 and the tapered fibre diameter is 2μm (dashed lines show the position of the isolated microsphere resonance wavelength).

Figure 2-14 shows the calculated transmission, internal/output power and phase spectra of the system for a taper diameter of 2μm as function of air gap between the taper and microsphere. The intrinsic Q of the WGMs is considered to be 10^6, and for the sake of simplicity, only the first five degenerate modes (N = 0-4) of the first radial order at 1548.66nm are considered. Even (N+1) mode orders are not considered due to zero coupling coefficient to such WGMs, and hence, save computational time and memory. The simulations show that, at very small air gaps, symmetric Lorentzian shape of the transmission spectrum is distorted. The internal-to-input-power ratios of WGMs at zero air gap show a Fano-like line shape. This is due to the interference of the degenerate modes owing to the strong coupling between the tapered fibre and the resonator WGMs. The phase spectra of the internal mode amplitudes show that, at very small air gaps, coupling-induced phase changes on individual modes give rise to destructive interference between the modes. Therefore, the phase of the total transmission shows a non-monotonic transition as the wavelength increases. Accordingly, the power transmission spectrum shows slight frequency shift with respect to the uncoupled resonator resonance frequency.

On the other hand, as the air gap between the taper and microsphere increases, phase perturbations due to effect of the fibre coupling on WGMs, progressively diminish. Subsequently, the transmission spectrum becomes closer to a Lorentzian line shape. At air gaps larger than 300nm, the fundamental WGM is dominantly excited owing to its higher total Q factor comparing to small air gaps, and exhibiting greater modal overlap than the higher order WGMs. Hence, the effect of the higher order WGMs on the total output field is not anymore significant. The resonator exhibits critical-coupling at air gap of 400nm below and above which transmission is non-zero due to over- and under-coupling, respectively. Additionally, internal power of the excited WGMs show less deterioration (due to modal interference), comparing to Lorentzian line-shape, by widening the air gap, which indicates lower impact of the tapered fibre on the WGM coupling-induced phase-shift.

The resonance condition set by Eq. 2-22 implies that the resonance frequency of a particular WGM is always set to the uncoupled cavity resonance frequency. Since, the round-trip phase shift is always compensated for by the effect of fibre-coupling induced phase shift. Cavity index perturbation due to coupler is shown to shift the cavity resonance depending on the air gap between the excitation coupler (e.g. tapered fibre, waveguide, etc.) and the resonator, as well as, relative sizes of the resonator and coupler [95-98]. In contrast, the complex transmission spectra of the current analysis is owing to the modal interference between degenerate WGMs due to the coupling system. It

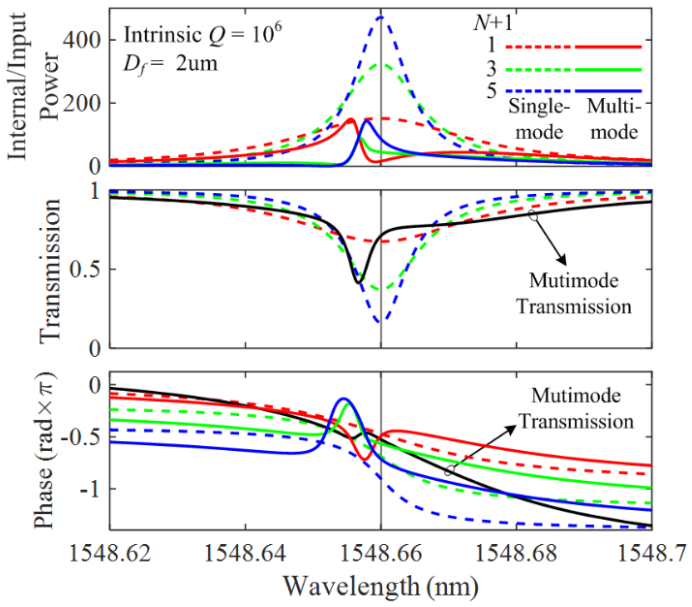

Figure 2-15 Internal power enhancement, transmission and phase spectra of tapered fibre-coupled microsphere with zero air gap, taper diameter of 2μm and intrinsic Q of 10^6. Results are shown for N+1 = 1, 3 and 5 modes when the cavity operates in single mode (dashed lines) or multimode (solid lines).

should be noted that, solving the coupled equations given in Eq. 2-20 for the asymmetric taper-microsphere coupler, generally, results in an asymmetric matrix Λ, with nonzero off-diagonal elements. The first row and column show the coupling between fibre and WGMs, while the rest of the off-diagonal elements correspond to energy transfer between WGMs due to coupling.

Figure 2-15 shows simulations for the microsphere coupled to a taper with 2μm diameter at zero air gap. The results are shown for both cases when cavity operates in single-mode or multimode conditions. The multimode transmission of the resonator shows the effect of modal cross-coupling between the WGMs in presence of fibre coupling. The response of each isolated WGM shows a generic Lorentzian line shape with a 2π phase shift around the resonance frequency. In the presence of simultaneous excitation of degenerate WGMs, phases of the internal mode amplitudes are affected by the amount of WGM cross-couplings. Such interference between the modes deforms the internal power variation to a Fano-like shape.

The modal interference between the degenerate WGMs depends on the coupling condition under which each mode is excited. It is worth noting that, the coupled-mode formulation does not enforce any limitation on the number of considered modes. Figure 2-16 plots the transmission and amount of internal power enhancement when the intrinsic Q of the cavity is varied for fixed taper diameter and air gap of 2μm and zero, respectively. The first 15 degenerate modes with radial order of one are considered. For very low intrinsic Q's (i.e. 5×10^4) most of the modes are under-coupled, hence, the dominant excited mode correspond to the fundamental mode (which is close to critical-coupling) owing to its high overlap with the fibre mode. As the intrinsic Q factor gradually increases, the fundamental mode is over-coupled and the higher order modes reach critical-coupling condition. The relatively higher internal power of high order WGMs increases the modal interference between the modes. At very high intrinsic Q's, WGMs get into over-coupling regime, such that at Q's above 10^7, the fundamental and $N+1 = 3$ modes are significantly suppressed compared to higher order WGMs.

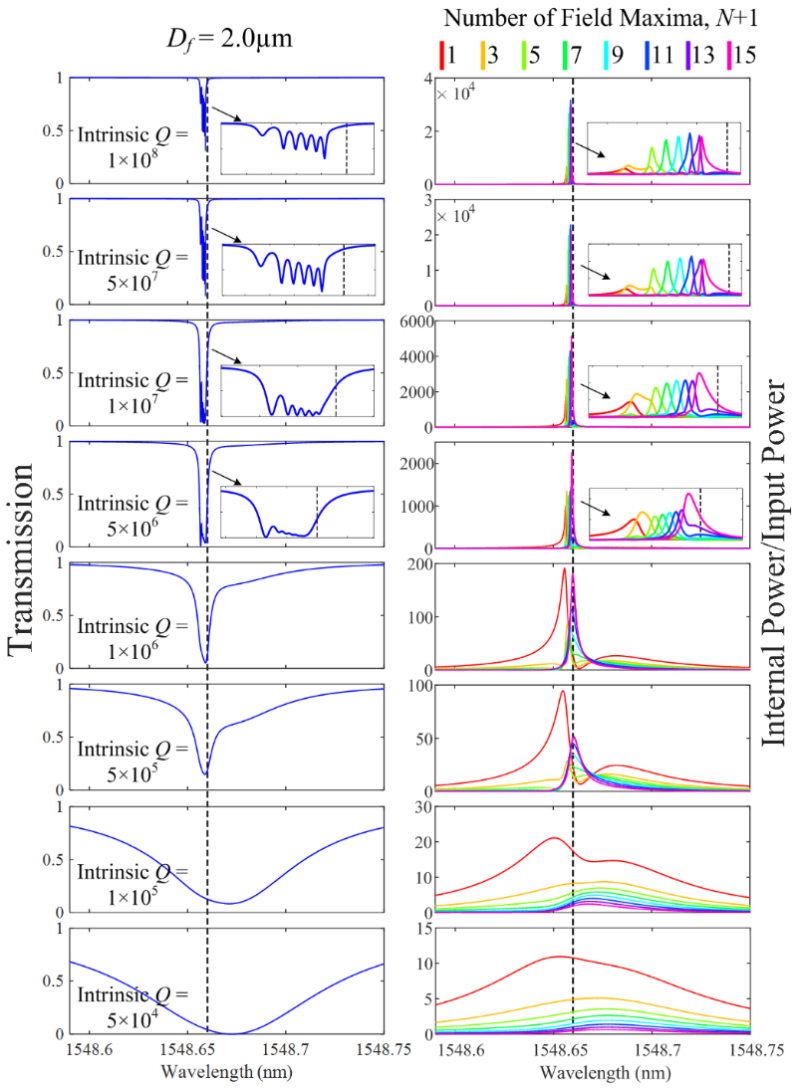

Figure 2-16 Transmission and internal/input power spectra of the microsphere coupled to a taper diameter with diameter of 2μm at zero air gap when the intrinsic Q of the modes varies from 5×10^4 to 1×10^8 (dashed lines show the position of the isolated microsphere resonance wavelength).

On the other hand, cross-coupling between degenerate WGMs depend on the fibre diameter, as it determines the amount of fibre mode coupling and phase-matching to WGMs. Figure 2-17 shows the simulations when the taper diameter is varied between 1.2μm and 9.2μm at a fixed air gap of zero and intrinsic Q of 10^6. At very small taper diameters (i.e. 1.2μm), WGMs are over-coupled due to high modal overlap between the fibre and WGMs. Despite the close-to-90% transmission of the system at D_f = 1.2μm, the internal powers of WGMs are not significantly dampened. The interference between WGMs is relatively high at small taper diameters, since due to high coupling coefficients between WGMs, resulting off-diagonal elements of matrix Λ, corresponding to WGM cross-couplings are greater. As the taper diameter increases, the interaction between WGMs decreases and the distorted line-shape of the resonance transmission develops again into a well-defined Lorentzian shape. At very large taper diameters, the

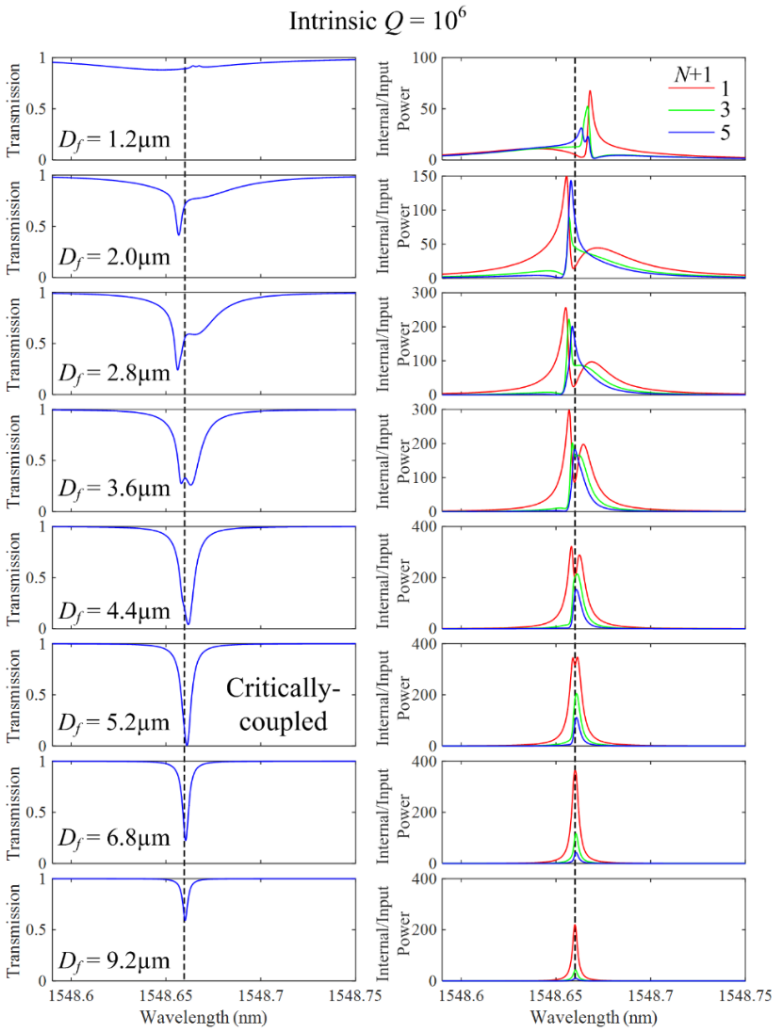

Figure 2-17 Transmission and internal/input power spectra of the microsphere with a fixed intrinsic Q of 10^6 coupled to a tapered fibre at zero air gap when the taper diameter varies from 1.2μm to 9.2μm (dashed lines show the position of the isolated microsphere resonance wavelength).

fundamental mode is dominantly excited due to its lower phase-mismatch to the fibre mode comparing to higher order WGMs.

Experimental determination of degenerate WGMs is difficult, since any index perturbation on the cavity breaks the degeneracy, and WGMs shift in frequency depending on the strength of the perturbation and the WGM numbers [99-102]. However, two or multiple WGMs, with different polarisation states or radial orders, can be brought very close to each other in frequency, due to such perturbations. Therefore, simultaneous excitation of WGMs is common, especially in sizable microresonators which support larger number of modes. On the other hand, any deformation on a microsphere results in breaking the degeneracy of angular modes [47, 103]. Next, I use the developed CMT to further elucidate the effects of frequency degeneracy breaking in taper-coupled microsphere resonators.

Frequency shift between same radial order WGMs with consecutive angular orders is proportionally related to the amount of eccentricity defined by $\varepsilon = 1 - R_{minor}/R_{major}$ where R_{minor} and R_{major} respectively signify the length of the minor and major axes in a spheroid.

Frequency shift ($\Delta\nu$) between pairs of WGMs for the group of angular modes studied in this section, considering an oblate spheroid with R_{minor}= 30μm, as a function of eccentricity, is calculated (from theory given in [47]) to be $\Delta\nu \simeq 435\varepsilon$ (GHz). Figure 2-18 (a) plots the simulation results for the first three odd WGM orders considering eccentricities of 0, 0.5, 1.1 and 2 percent. As previously discussed, when degenerate modes (i.e. $\varepsilon = 0\%$) are excited, modal interference distorts the transmission and internal power spectra from their Lorentzian line-shape. As a small eccentricity is introduced to the microsphere, WGMs are split in spectra varying the amount of modal

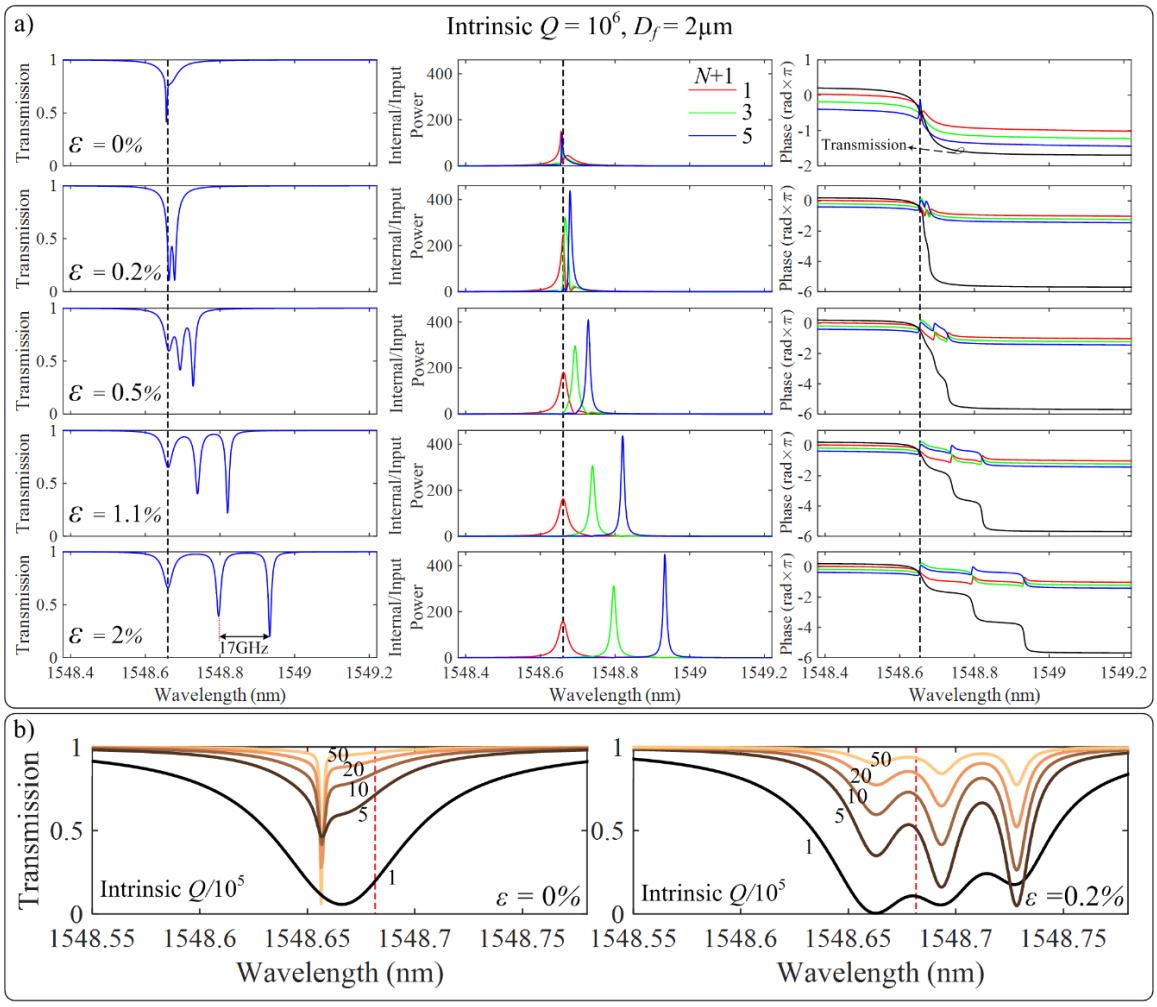

Figure 2-18 a) Transmission, internal/input power and phase spectra of microsphere with a fixed intrinsic Q of 10^6 as a function of eccentricity showing various amount of WGM interactions, and b) transmission spectra corresponding to eccentricities of zero and 0.2% as function of intrinsic Q factor (Q = 1, 5, 10, 20 and 50 × 10^5), coupled to a tapered fibre at zero air gap with diameter of 2μm (dashed lines show the position of the isolated perfect microsphere resonance wavelength).

interactions between distinct modes. Further increasing the eccentricity, decreases the cross-coupling between WGMs. At ε = 2%, independent modal operation is enabled. The amount of WGM interactions is manifested in the phase spectra such that, slight eccentricity-induced-frequency-shift between modes, breaks their destructive phase interaction. Thereby, phase of the total transmission spectra is constructively built-up (~2π per mode) such that at ~0.2% a close-to-critical-coupling is achieved.

Note that, as an example, 0.5% eccentricity for a microsphere with 30μm radius implies a difference of about 150nm between major and minor radii. For bigger microspheres, the sensitivity of frequency degeneracy breaking to structural deformations is smaller. Nevertheless, small frequency shifts can be produced due to index perturbations by submicron sized particles [100]. Figure 2-18 (b) shows the sensitivity of modal interference and the amount of visibility of frequency splitting as a function of Q factor for perfect (i.e. ε = 0%) and slightly-eccentric (i.e. ε = 0.2%) microspheres. As previously stated, at relatively small Qs (Q = 10^5), the modal interference is not strong enough due to low internal power of the modes. Hence, a perfect microsphere does not exhibit strong deterioration in its transmission spectra compared to a Fano-line shape. Deformed microsphere, on the other hand, shows small ripples in the transmission owing to close resonances with low total Q's. As the Q factor increases, a perfect sphere shows strong modal interference, while, the deformed one maintain well-defined split resonances. Of course, the strength of WGM excitation depends on the coupling condition under which a mode is excited/collected. Such well-defined and clear single mode operation is important in CQED applications where interaction of a single atom with a single optical mode (preferably the fundamental one due to its high surface intensity) is prefered. The eccentricity of a microsphere is shown to be controllably set by applying CO_2 laser pulses to a perfect microsphere without Q degradation [104, 105]. On the other hand, transition between perfect and deformed microspheres with various levels of deformations can be dynamically achieved by applying mechanical strain [106-108].

2.8 Summary and Conclusion

In this chapter, first, I adopted an analytical model for evaluation of the spherical WGMs and taper fibre modes. Then, using CMT, the coupling efficiency coefficient between various WGMs and fibre mode is calculated. The coupling coefficient is then used to calculate the internal and output modes of the taper-resonator system. In this model, the general asymmetric CMT for directional couplers is used. The effect of the tapered fibre on the transmission and internal power of WGMs, is investigated in terms

of external Q factor and phase-mismatch between fibre and resonator modes. The excitation condition can be determined by the regime in which the WGM is excited. Depending on the fibre diameter, specific WGMs can be forced to operate in either under-, or over-coupling regimes, as well as, under critical-coupling regime were a complete power drop happens for the fibre mode at the output. It is also shown that due to small differences in the effective refractive index of degenerate WGMs with distinct angular orders, depending on the coupling efficiency and phase-matching to such modes, a combination of WGMs contribute to the actual total transmission spectra and the internal field accumulation. I showed that, by precisely varying the taper diameter, critical coupling condition to such modes can be well-discriminated. This helps in designing a cavity system where specific modes are desired to be present. Performing 3D FDTD simulations shows that such simultaneous excitation of degenerate WGMs exists, and varying the taper diameter provides a degree of freedom to selectively excite/collect such different order modes.

Although the analyses in this chapter are performed on the microsphere resonator as a general and well-known cavity structure to scientific community, the same approach can be applied to other types of whispering gallery resonators. Due to the dense spectra of typical (bottle, eccentric sphere, stub, rod, etc) microresonators, WGMs that are close in frequency with distinct spatial orders, polarizations, and/or propagation directions may be excited and interact with each other. Thus, such formulation is applicable to any multimode cavity. Further, these analyses are very useful in designing lasers and resonators for nonlinear light generation, in which intensity and spatial distribution of optical fields are important factors in determining the gain/loss of the system. On the other hand, due to experimental difficulties in accurate positioning of reflective mirrors in Fabry-Perot microcavities, and the fact that WGMs can provide ultra-high Q factors, such resonators are great candidates for CQED applications. Our approach can be employed to precisely and selectively design cavity-atom systems that provide sufficient intra-cavity fields by critical coupling to a specific WGM.

Chapter 3 CO_2 Laser-fabrication, Mode Stripping and Polarized Transmission of Passive Microresonators

3.1 Introduction

In this thesis, a number of methods have been developed to fabricate different WGM microresonators. Most of the devices rely on fibre-tip melting [109-111] or splicing of small fibre stubs [112], and to a large extent they are not controllable and/or reproducible. Material processing with CO_2 laser has been of great interest in recent years. Continuous wave lasers have been employed to fabricate microspheres [110, 113, 114], microbottles [37, 115], microrods [116] and to surface-reflow microtoroids [10] in order to achieve ultra-high Q's. These processes rely on melting and softening of materials by heat. Here, I use a pulsed CO_2 laser in order to achieve controlled ablation of the fibre surface and form a WGM microcavity, similar to microstub resonators [112], without the need though of extra laborious splicing steps. In this method, precise control of the cavity length and sub-micron ablation depth in a very short fabrication time, as a simplified one-step process, are achievable. High Q and control on the cavity geometry, which are essential parameters in microlasers, can be achieved by additional fire-polishing. MBRs are fabricated using "soften and compress" technique [117], and methods such as tapering, laser and FIB-milling are investigated to clean-up the dense and complex transmission spectra. Finally, the polarisation dependent transmission in cleaned-up MBRs is studied and cavity-induced polarisation cross-coupling in a tapered fibre coupled resonator is demonstrated.

3.2 CO_2 Laser-milled-microresonators

Fabrication Method

A modulated CO_2 laser (Coherent G100) at 9.6μm wavelength with ~100W output power and controllable pulse width is focused onto the fibre using optical lenses. The position of the fibre with respect to the laser beam waist is controlled using an XYZ stage, and the fibre axis can be continuously tilted at the pivot point for precise alignment (see Figure 3-1 (a)). A DC motor provides rotation around fibre axis with a controllable speed between zero and 3000rpm. A sequence of pulses with varying width

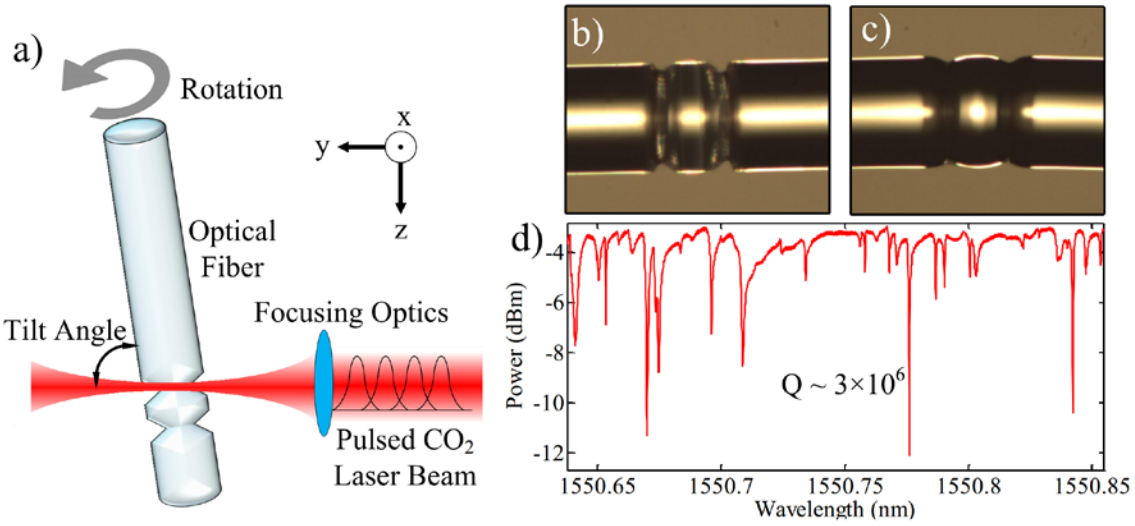

Figure 3-1 a) Pulsed CO_2 laser fabrication setup. CO_2 laser-milled microrod resonator b) before and c) after fire-polishing, and d) Resonance spectrum of the microresonator after fire-polishing at 1550nm wavelength.

duration (8-500µs) and repetition rate (1Hz-10kHz) is applied on the fibre surface with a certain tilt angle to achieve the desired ablation depth. The fibre tilting helps to control the angle of the side edges of the microrod resonators. In order to improve the surface quality of the milled edges, the structure is fire-polished, using a standard splicer, by applying controlled electrical arcs. In addition, thermally-induced surface tensions smoothen the surface roughness, and improve the optical quality of the microrod resonator edges. A typical milled microrod resonator fabricated on a 240µm-diameter silica fibre before and after fire-polishing is shown in Figure 3-1 (b) and (c), respectively. The transmission spectrum of the fire-polished microrod resonator at 1550nm wavelength is plotted in Figure 3-1 (d). The transmission response is obtained by coupling a 2µm-diameter tapered fibre with zero air gap at the centre of the resonator. Fire-polishing resulted in a maximum Q-factor improvement of more than an order of magnitude (from ~10^5 to ~3×10^6).

Q-enhancement (Polishing)

In order to investigate the effects of fire-polishing on the Q factor, resonators with triangular cross-section are fabricated. Therefore, WGMs have considerable overlap with the surface of the sidewalls. This pronounces the effect of the fabrication-imposed surface roughnesses compared to the initial roughness of the fibre. Figure 3-2 (a) and (b) show the fabricated resonator before and after fire-polishing with 40 consequent electrical arcs having 20% of maximum (available) power using a standard fusion splicer (FITEL S153A). The arc power is kept low in order to avoid any significant thermally-induced deformations in the shape of the resonator. Then, the resonator is excited using a 2µm-diameter tapered silica fibre evanescently coupled to the resonator at the centre with a zero air gap. The spectra of the resonator after applying each electrical arc are plotted in Figure 3-2 (c). The spectra generally get denser by applying more arcs. This is due to the smoother surface and lower scattering experienced by the optical WGMs. Hence, larger number of WGM modes can survive and propagate along

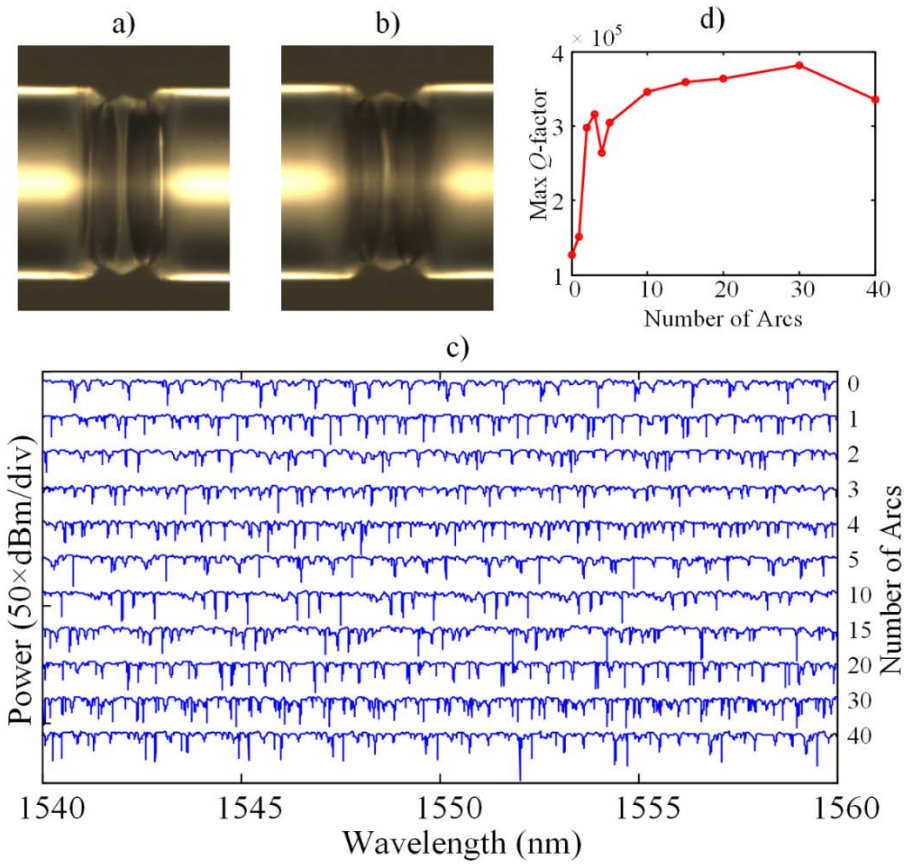

Figure 3-2 Optical image of WGM resonator a) before and b) after fire-polishing with 40 electrical arcs having a power of 20%, c) transmission spectra of the resonator as a function of number of electrical arcs, and d) max measured Q factor of WGMs for an 8nm wavelength window around 1550nm.

the circumference of the resonator. The theoretical azimuthal Free Spectral Range (FSR) of WGMs is approximated [118] by $\lambda^2/(2\pi n_{eff}R)$ where λ, and n_{eff} are wavelength and effective refractive index of the optical mode, respectively, and R is the radius of the resonator. The FSR is measured to be ~2.2nm which agrees well with the theory. The maximum Q factor within 8nm-wavelength range around 1550nm, large enough to cover three FSRs, is calculated from the spectra by fitting Lorentzian curves to the transmission dips. Figure 3-2 (d) shows that the maximum Q factor increases more than three times comparing to the unpolished resonator by applying 30 arcs. Further increasing the number of applied arcs above ten does not significantly improve the measured Q- factor. This is primarily due to the excessive loading applied by the tapered fibre. One may increase the power of the electrical arcs for further improvements with compromising the shape of the resonator.

3.3 Milled Microbottle Resonators

CO_2 laser-milling mode reduction

Nowadays, owing to the availability of cheap glass fibre processing systems, fabrication of microbottle resonators is very fast and easy, whereas fabrication of symmetric ones can be a complex process. The simplest method, called "soften and compress" [115, 117, 119], includes applying electrical arcs (or a laser beam) directly onto the middle of a fibre while pressurized from both stems. Due to possible misalignments, formation of asymmetric plasma (or non-uniform laser beam) around the fibre and/or fibre bending, the profile of the created MBR may vary from the ideal quasi-harmonic profile. Steps of a modified version of the "soften and compress" method is illustrated in Figure 3-3 where two flat cleaved fibre ends are pushed towards each other while applying an electrical arc. Using flat cleaved facets improves the uniformity of the applied force, and, hence results in a more symmetric MBR.

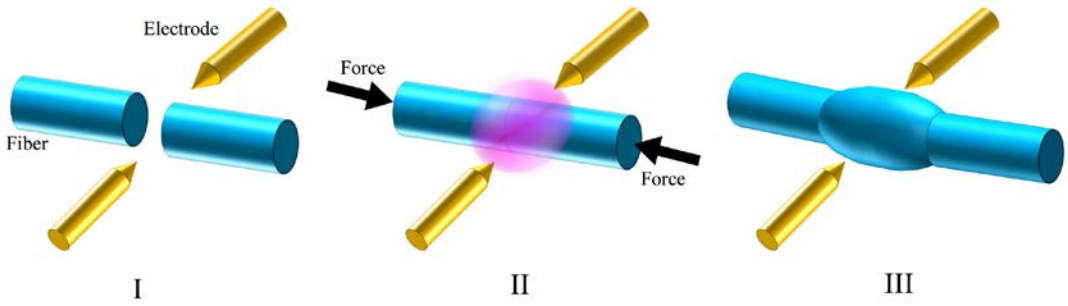

Figure 3-3 steps involved in fabrication of MBRs using "soften and compress" method.

Although MBRs are well-defined and easy-to-fabricate resonators, they typically support large number of WGMs due to the broken degeneracy of axial modes compared to microspheres. This makes them complex devices when used, for example, as a sensor. Scattering methods including high index micro-droplets [12], prisms [120] and FIB milling [121] were previously used to clean-up the spectrum. Additionally, reducing the dimensions of the resonator can result in fewer number of WGMs. Figure 3-4 plots the spectra of four different MBRs fabricated using regular and tapered fibres. The diameter of the tapered MBR is almost four times smaller than the regular one, and exhibits fewer excited WGMs. Nevertheless, the obtained spectra are still dense. It should be noted that, the length of the resonator is ~300μm, and hence, it should still include a large number of axial WGMs. On the other hand, due to the smaller diameter (longer FSR), and hence, increased radiation losses (due to curvatures), tapered MBR exhibit lower number of WGMs compared to regular ones, as expected.

Mode stripping using microgrooves milled on the surface of microresonator, is also used in order to increase the scattering losses on high axial-order WGMs. A microgroove is milled on top of the resonator using pulsed CO_2 laser. As shown in Figure 3-4 the number of resonant modes is significantly reduced. Observed WGMs in the spectra show a dramatic degradation in terms of Q factor. To compensate for the losses induced by the sidewalls, the resonator is fire-polished by applying electrical arcs. As plotted in Figure 3-4 for the fire-polished CO_2-laser-milled MBR, although the Q factors of the modes are significantly improved, the spectrum becomes again extremely dense. Furthermore, owing to the large wavelength of the CO_2 laser, and hence, large spot size

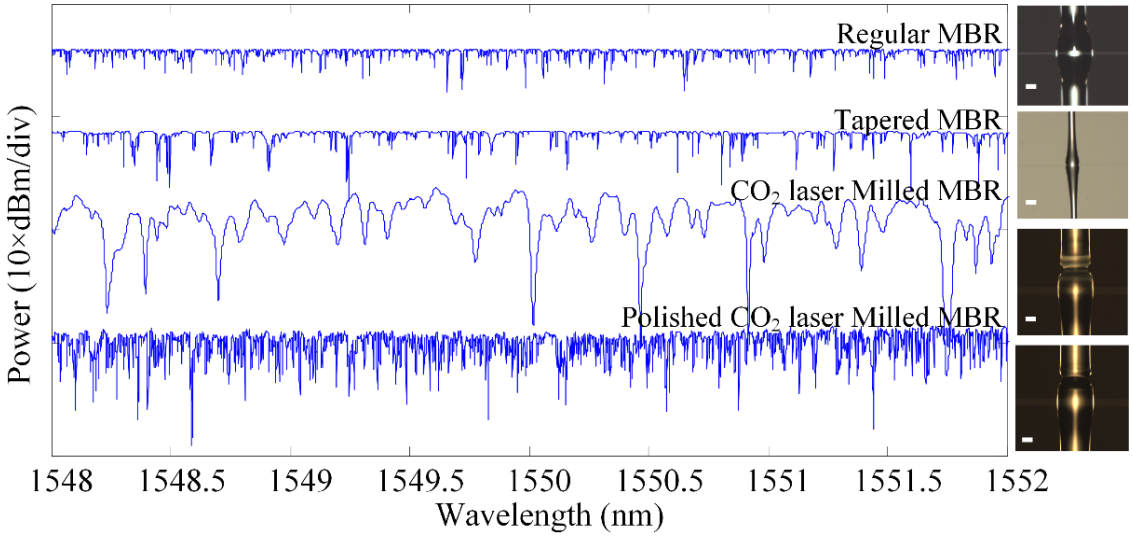

Figure 3-4 Transmission spectra of regular, tapered, laser-milled and polished laser-milled MBRs fabricated using normal SMF. Optical micrographs show the corresponding fabricated devices (scale bar is 50μm).

of the laser beam, the minimum possible micro-machined groove length is in 10-15μm range. This reduces the accuracy and resolution of the milling. However, FIB-milling will be shown to be a more accurate and controllable method in cleaning-up the transmission spectra.

Focused ion beam milled microresonators (fabrication and polarised transmission)

Figure 3-5 (a) shows two rectangular grooves fabricated on a gold coated MBR. Microgrooves are 3μm×20μm separated by 20μm distance and are equidistant from the centre of the MBR along the axis of the stem fibre. The residues around the microgrooves correspond to the ablated silica and gold. The voltage and current of the FIB are set to 30kV and 2.7nA, respectively. A tilted view of the cross-sectional structure of a fabricated microgroove is illustrated in Figure 3-5 (b). The grooves exhibit a V shape, which comes from the conical shape of the ion beam such that as the depth increases the amount of ions colliding with the material decreases. This effect can be overcome by enlarging the groove width. The effective depth of the fabricated grooves is about 5μm. Figure 3-5 (c) shows the gold particles on the MBR after etching the coated gold layer from the surface of the resonator. The gold particles are then removed by applying very low power electrical arcs (see Figure 3-5 (d)). Such weak fire-polishing will also remove the unwanted surface roughness created during FIB focussing and maintain the high Q of the WGMs.

Figure 3-6 (a) shows the polarisation resolved setup for characterisation of microresonators. Output of a tunable laser is passed through a polarisation controller and couples into a tapered fibre with 2μm diameter. The tapered fibre is then evanescently coupled to the microresonator, and the output fibre is cleaved and fixed

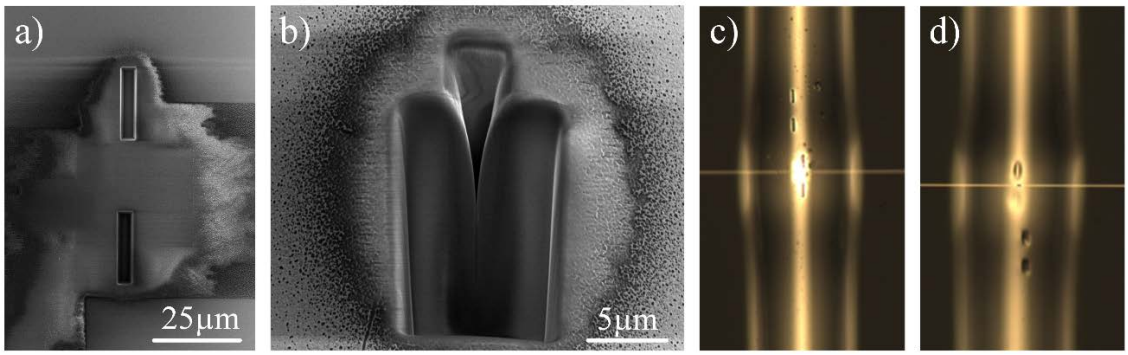

Figure 3-5 a) SEM of micro grooves created on top of gold coated MBR, b) top view of the cross-section of a fabricated microgroove. Optical image of the coupled tapered fibre and the FIB milled MBR c) after gold removal, and d) after cleaning.

straight in order to avoid any polarisation variations. The output light is focused into a multimode fibre after passing through a polariser, and monitored by an InGaAs photo detector. A TE or TM field can be defined with respect to the microresonator axes. As illustrated in Figure 3-6 (b), a TE (TM) WGM is defined with electric (magnetic) field parallel to the radial axis of the resonator. Let us assume a pure TE or TM input field to the tapered fibre with power P_f. This mode will couple into the resonator WGM with a mixed polarisation state (due to the coupler) corresponding to WGMs with total P_m power. Then, after one round-trip, the internal cavity modes (with power of P_m), will couple back into the fibre mode with a mixed polarisation shown by $P_{TE} + P_{TM}$. The output mode is a linear combination of the uncoupled input mode (in the case of non-critical resonance) and the out-coupled WGMs. For an uncoupled taper-resonator, the polarisation of the input light at 1150nm is varied until a discrimination of about 15dBm (highest value I obtained) between the TE and TM modes at the output is observed. In other words, for a pure TE (TM) input light, the power of the output TM (TE) mode after the polariser should be zero. Then, the tapered fibre is coupled to

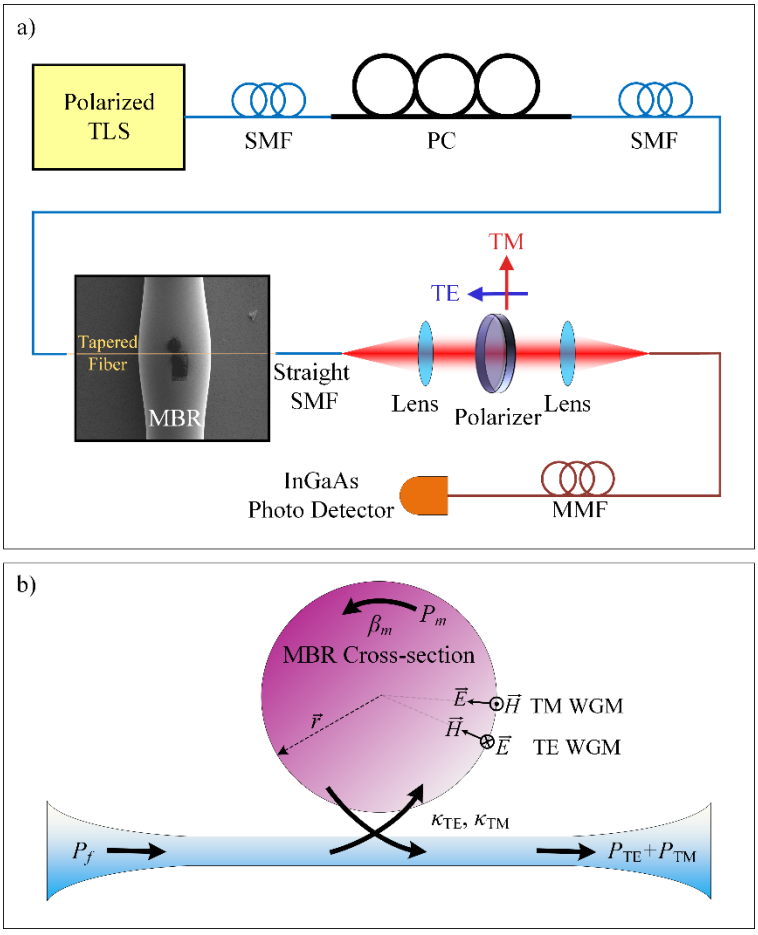

Figure 3-6 a) Polarisation resolved characterisation setup (TLS: Tunable Laser Source, SMF: Single Mode Fibre, PC: Polarisation Controller, MMF: Multi Mode Fibre), and b) Electric field direction of two state of polarisations with respect to the MBR cross-section and the direction of WGM propagation.

the resonator and the spectra is measured for both TE and TM input lights.

Figure 3-7 (a) and (b) shows the transmission spectra of the MBR for both TE and TM input modes when the polariser is set to TE and TM transmission angles. The tapered fibre is placed at the centre of the FIB-milled MBR between the two grooves with no air gap. The results show, firstly, that there is a significant reduction in the number of resonances observed in the transmission spectra, compared to the regular MBR shown in Figure 3-4 with similar dimensions. No significant Q-factor degradation due to FIB-milling is seen. Secondly, for an input light at resonance wavelength with a specific orthogonal polarisation, the output light power is a mixture of both polarisations. This implies that, polarisation cross-coupling occurs due to the presence of the microresonator. An *s*-to-*p*-polarisation conversion efficiency, $\eta_{s\to p}$, can be defined and denoted by $\eta_{s\to p} = P_p / P_s$ where P_p is the power of cross-coupled polarisation *p*, and P_s is the output power of the polarisation *s* at off-resonance wavelength. For the WGMs shown in green region of Figure 3-7 around 1550nm wavelength, polarisation conversion efficiencies of $\eta_{TE\to TM} \sim 25\%$ and $\eta_{TM\to TE} \sim 15\%$ are calculated.

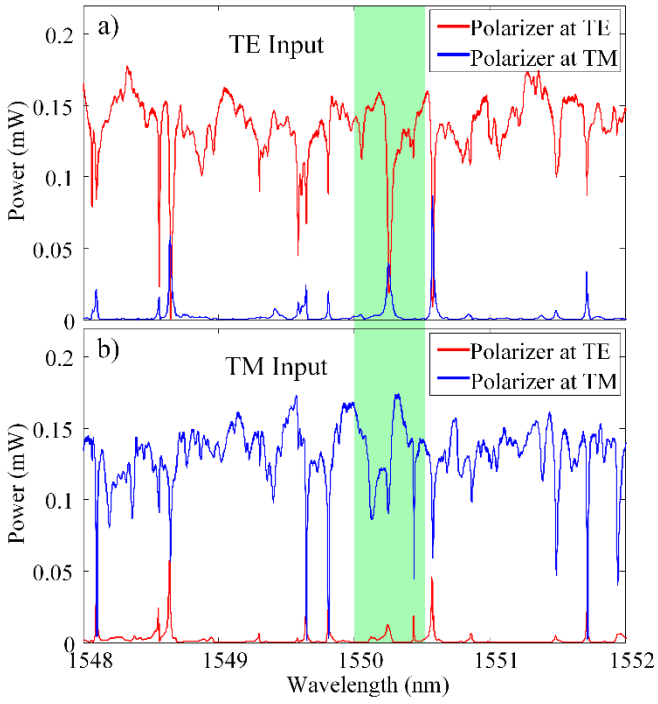

Figure 3-7 Transmission and polarisation cross-coupling spectra for a) TE, and b) TM tapered fibre input mode for output polariser at both TE and TM polarisation states.

3.4 Summary and Conclusion

In this chapter, I presented fabrication techniques of high Q factor microrod resonators using modulated CO_2 laser-milling. This fabrication method is based on material ablation, and hence, allows milling on microstructures without significant thermal effects on the rest of the device. With this technique microrod resonators with Q-factors of ~10^5 are fabricated. Further, fire-polishing using electrical arcs in standard splicers results in Q-factors in excess of 10^6.

Fabrication of high Q microbottle resonators using a “soften and compress” technique is discussed, and different methods are employed in order to clean-up the spectra; Shrinking the dimensions of the microbottle does not significantly reduce the number of modes, and CO_2 laser-milling on the resonator surface deteriorates the Q factor. On the other hand, FIB-milling shows the most precise and effective way in order to selectively ”kill” WGMs and clean-up spectra. Microgrooves with few microns offset from the resonator centre are accurately fabricated along the MBR. A significant reduction in the number of supported WGMs is observed while preserving the Q factors. A polarisation resolved setup established in order to investigate the polarisation conversion in FIB-milled MBRs. A maximum polarisation cross-coupling between TE and TM modes of about 25%, due to the coupling to the resonator, was measured.

Chapter 4 Rare-earth WGM Microlasers: Theory

4.1 Introduction

Owing to their high quality factor (Q), WGM microresonators have been widely recognised as miniature micron-scale devices, which can sustain high internal optical powers. Such capability along with small mode volume (V) of these structures, provide enormous amount of optical intensities. This quality is highly favoured in applications where efficient light-matter interactions are required such as nonlinear optics, Cavity Quantum Electrodynamics (CQED) and lasers. Devices based on nonlinear phenomena such as continuesly-pumped Kerr frequency combs, Brillouin and Raman lasers are implemented with ultra-high Q WGM resonators. Further, the dynamic behaviour of atoms in presence of high intensity and long duration optical modes is of importance for CQED studies, for which WGMs have shown to be a powerful platform to provide such strong coupling. On the other hand, several studies have been reported on development of integrated and fibre-based rare-earth doped microlasers which shows the importance of such compact devices. WGM microresonators have played an essential role in developing the field of photonics, and as new low loss materials emerge, these devices are employed for light generation not only in the conventional telecom wavelengths, but also further into the mid-IR.

WGM resonators are also great candidates for realization of low threshold and narrow line-width microlasers, since they can exhibit high quality factors and small mode volumes (high Q/V). Among various configurations proposed, recently, a new type of resonators called Microbottle Resonators (MBRs) show great prospects for sensing, telecom, lasing and CQED applications. Due to their quasi-harmonic profile, the supported axial modes in the same radial order family show broken frequency degeneracy, in contrast with microsphere resonators. This property of MBRs can be proven advantageous in CQED applications where the interaction of atom with single optical mode at single frequency is desired. Moreover, in sensing applications it is extremely important to have high Q single resonances well-separated in frequency, in order to have high sensitivity, as well as, adequate sensing range. I later show that single mode operation is possible using microbottle resonator lasers, which naturally provide high sensitivities. Therefore, understanding MBRs and especially their performance as laser cavities is important given their broad range of possible applications.

On the other hand, thanks to the well-developed Yb and Er-doped fibre amplifier and laser technology, such rare-earth materials have shown significant advantages in realization of high gain, high power and low noise active devices in near-IR wavelengths. The fabrication of Yb/Er doped silica fibres is well established making them commercially available at low cost. Hence, combination of such rare-earth dopants with high Q WGM resonators opens up a new platform for the realization of high Q, high relative power and single frequency microlasers.

In this chapter, following the approach presented in [122], I adopt a model to analyse the behaviour of Yb-doped microresonators using the well-known theory of quasi-three-level laser systems, which is used frequently in fibre amplifiers and lasers. Then, the developed model is employed to analyse the tapered fibre-coupled microbottle lasers.

First, the upper-state population inversion in a general microcavity is given in terms of the Giles parameters and the cavity Q factors. Then, the lasing condition (threshold condition) as a function of the signal Q's is derived. The minimum condition for lasing as function of intrinsic Q's, dopant concentration and signal wavelengths is studied. Then, relations of the internal signal and p ump powers, threshold input pump power and lasing slope efficiency, for a tapered fibre-couple microbottle resonator are derived. Afterwards, the developed theory is employed to analyse lasing of the fundamental pump and signal modes of a typical microbottle laser. Such analyses include the effects of fibre-resonator coupling condition, intrinsic Q of both pump and signal modes, dopant concentration and the signal wavelength on the laser performance.

4.2 Gain/loss and Rate Equations in Yb^{3+}:silica Material

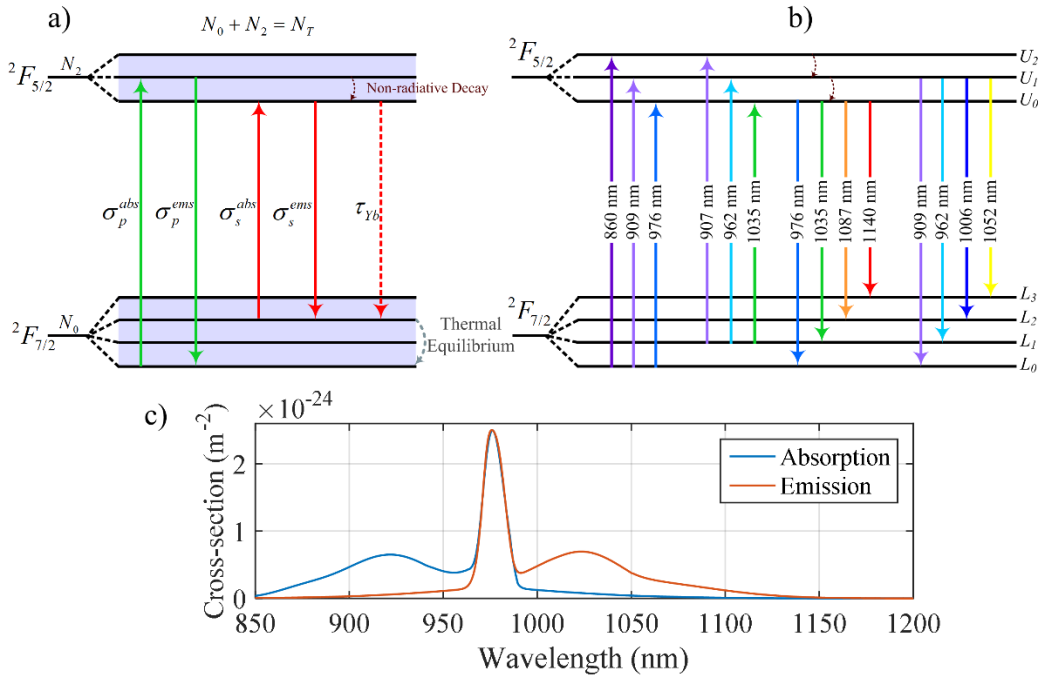

Figure 4-1 a) Schematic diagram of a quasi-three level laser model ,b) energy level structure, and c) absorption and emission cross-section spectra of Yb^{3+} ions.

Yb-doped fibre lasers are wide-spread due to their broad gain bandwidth, high efficiency and great pump absorption, resulting in high output powers and ultrafast pulse operation. In a rare-earth-doped material, a seed signal within the emission spectral range can be amplified through the stimulated emission process. Figure 4-1 (a) and (b) show the energy level structure of Yb^{3+} ions [123] consisting of two manifolds, namely ground state ($^2F_{7/2}$) with Stark levels of $L_0 - L_3$, and excited state ($^2F_{5/2}$) including $U_0 - U_2$ Stark levels. In the active medium, propagating pump (signal) photons are absorbed and emitted with cross-sections of $\sigma_{p(s)}^{abs}$ [m^{-2}] and $\sigma_{p(s)}^{ems}$ [m^{-2}], respectively. Absorption and emission cross-sections of Yb^{3+}-doped silica glass fibres are dependent to wavelength [123]. In Figure 4-1 (c), there are three important transition points. First, 976nm wavelength range, where the absorption and emission cross-sections are equal and correspond to energy transfer between the lowest energy levels in ground and excited states ($L_0 \leftrightarrow U_0$). Second, 920nm wavelength range, which corresponds to energy transfer from the L_0 Stark level of ground state to either U_1 or U_2 levels in excited state. Finally, 1030nm range, where the emission and absorption cross-sections have maximum difference and is preferred for signal amplification (energy transfer between L_1 and U_1). Owing to the broad absorption and emission cross-sections of Yb^{3+}, signal wavelength can be designed to be anywhere in the range between 976-1200nm, and

pump wavelength can lie in a broad range of 900-980nm based on the requirements of the specific application.

Let's assume ground and excited state populations per unit volume are denoted as N_0 and N_2, respectively. Then, the total population of Yb^{3+} ions is equal to $N_T = N_0 + N_2$. Originated from the modelling of Er-doped Fibre Amplifiers (EDFAs), the absorption and emission coefficients named as Giles parameters, for both pump and signal, per unit length, are respectively defined as [124]

$$\begin{aligned} \alpha_{s,p} &\equiv \Gamma_{s,p} N_T \sigma_{s,p}^{abs} \\ g_{s,p}^{*} &\equiv \Gamma_{s,p} N_T \sigma_{s,p}^{ems} \end{aligned} \qquad 4\text{-}1$$

where $\Gamma_{s,p}$ is the ratio of the signal (pump) modal overlap with the active medium such that $0 \le \Gamma_{s,p} \le 1$, with $\Gamma_{s,p} = 1$ representing the complete mode-active-medium overlap. Ignoring the Amplified Spontaneous Emission (ASE) at signal wavelength, without any loss of generality, the intensity variation of the pump and signal ($dI_{s,p}$) along the length of dz can be written as

$$\frac{dI_{s,p}}{dz} = \left(g_{s,p}^{*} \bar{N}_2 - \alpha_{s,p} \bar{N}_0 - \alpha_{s,p}^{passive} \right) I_{s,p} . \qquad 4\text{-}2$$

$\bar{N}_0$ and $\bar{N}_2$ are the normalized ground and upper-state populations to N_T. The total passive losses that pump and signal undergo due to scattering, material absorption, bending, etc are denoted as $\alpha_{s,p}^{passive}$.

Furthermore, the time-dependent rate equation corresponding to both upper and ground state populations, considering all the propagating signal and pump modes, can be written in the form of

$$\frac{dN_0}{dt} = \sum_i \frac{I_{s_i}}{h\nu_{s_i}} \left(g_{s_i}^{*} \bar{N}_2 - \alpha_{s,p} \bar{N}_0 \right) + \sum_i \frac{I_{p_i}}{h\nu_{p_i}} \left(g_{p_i}^{*} \bar{N}_2 - \alpha_{p_i} \bar{N}_0 \right) + \bar{N}_2 \frac{N_T}{\tau_{Yb}} \qquad 4\text{-}3$$

where $\nu_{p_i}(\nu_{s_i})$ is the pump (signal) optical frequency of mode i, h is the Plank's constant and τ_{Yb} is the relaxation rate of Yb^{3+} ions from the upper state to ground state. Eq. 4-3 shows that the decay rate of N_0 is determined by the amount of photon energy flux from the ground state to upper state due to pump i, and from upper state to the ground one induced by signal i. It should be noted that because of constant total ion population $dN_0 / dt = - dN_2 / dt$. Considering a 3D medium, the mode intensity is driven from optical modal power per unit volume [125] by $I_{s,p} = |a_{s,p}|^2 / V_{s,p}$ where $a_{s,p}$ is the complex signal

(pump) mode field value, and $V_{s,p}$ is the corresponding quantum mode volume, which for a given electric field of $\vec{E}_m(\vec{r})$, is calculated by definition[126] from

$$V_m = \frac{\int_{V_Q} \varepsilon(\vec{r}) \left|\vec{E}_m(\vec{r})\right|^2 d^3\vec{r}}{\left(\max\left\{\varepsilon(\vec{r})\left|\vec{E}_m(\vec{r})\right|\right\}\right)^2} \qquad 4\text{-}4$$

where $\vec{r}$ is the vector indicating the coordinates of each space point, and the integral is taken over V_Q defined as the total volume of the medium. $\varepsilon(\vec{r})$ is the relative permittivity of the dielectric such that $\varepsilon(\vec{r}) = n^2(\vec{r})$.

At the steady state, the amount of ground and upper state populations remain constant such that $dN_0 / dt = -dN_2 / dt = 0$, hence, using Eq. 4-3, the normalized upper-state population inversion of ions in terms of the modal powers, can be derived such that

$$\bar{N}_2 = \frac{\sum_i \frac{\alpha_{s_i}\left|a_{s_i}\right|^2}{h\nu_{s_i} n_{s_i} V_{s_i}} + \sum_i \frac{\alpha_{p_i}\left|a_{p_i}\right|^2}{h\nu_{p_i} n_{p_i} V_{s_i}}}{\sum_i \frac{\left(\alpha_{s_i} + g^*_{s_i}\right)\left|a_{s_i}\right|^2}{h\nu_{s_i} n_{s_i} V_{s_i}} + \sum_i \frac{\left(\alpha_{p_i} + g^*_{p_i}\right)\left|a_{p_i}\right|^2}{h\nu_{p_i} n_{p_i} V_{p_i}} + \frac{N_T}{\tau_{Yb}}}. \qquad 4\text{-}5$$

where n_{si} and n_{pi} are the refractive indices at signal and pump wavelengths, respectively. Moreover, from Eq. 4-2 the signal gain (g_s) and pump loss (l_p) per unit length can be obtained from the Giles parameters and upper-state population inversion such that

$$\begin{aligned} g_s &= \bar{N}_2\left(\alpha_s + g^*_s\right) - \alpha_s \\ l_p &= \alpha_p - \bar{N}_2\left(\alpha_p + g^*_p\right) \end{aligned}. \qquad 4\text{-}6$$

Figure 4-2 plots the calculated gain per unit length for Yb^{3+}:silica material with $N_T = 1.16 \times 10^{26} m^{-3}$ concentration as the upper-state population inversion percentage increases. The chosen concentration is the estimated value from our actual experimental results which will be used in the next chapters. The calculated gain spectra reveals two important phenomena in Yb^{3+}:silica active medium. First, if the pump wavelength is chosen at 976nm wavelength where the maximum absorption of Yb^{3+} happens, the upper-state population cannot exceed ~50%, since the absorption and emission cross-sections are identical at this wavelength. Hence, in order to achieve inversions greater than 50%, the pump wavelength should be designed at ~920nm band where the absorption is less than the one at 976nm, but the emission is very low (see Figure 4-2 right top graph). Second, the peak gain wavelength depends on the inversion level. At high inversions, the peak gain happens at ~1030nm, while as the inversion

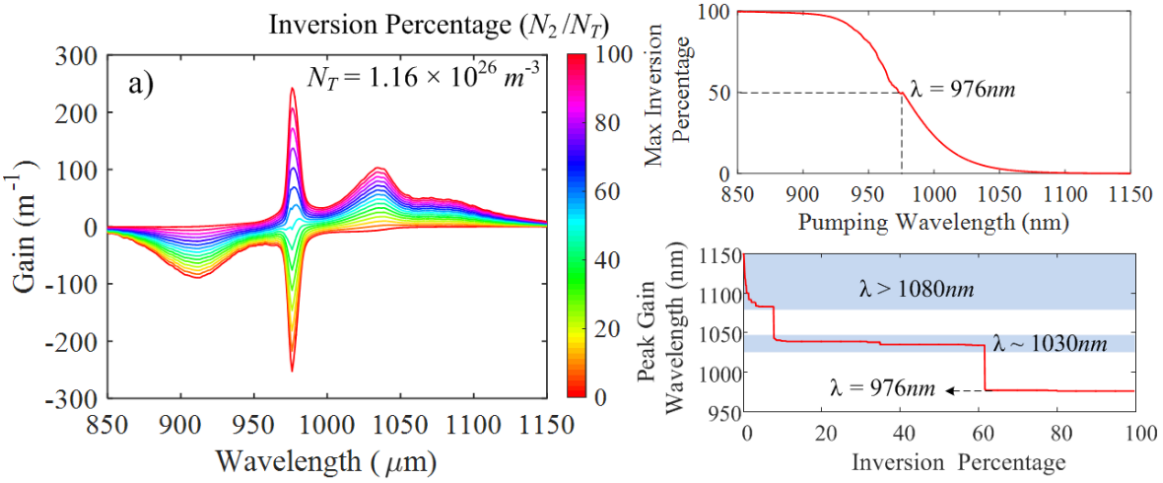

Figure 4-2 Left: calculated gain per unit length for Yb^{3+}:silica material as the upper-state population inversion percentage increases. Top right: obtained maximum inversion percentage from the gain spectra. Bottom right: peak of the gain spectra as a function of inversion level.

level decreases the maximum gain red-shifts. At very low inversions, since the absorption is high, signal undergoes loss (negative gain) at ~1030nm, while due to small emission and almost zero absorption, signal experiences gain at wavelengths above ~1080nm (see Figure 4-2 right bottom graph).

4.3 Population Inversion, Signal and Pump Qs in Microcavity Lasers

In a generic passive microcavity, the optical losses will be mainly due to either intrinsic losses including absorptions from material impurities, Rayleigh scattering, surface inhomogeneity scattering, radiation losses caused by the device curvature, or the external losses induced by the coupling mechanism by which the optical power is out-coupled. On the other hand, in the case of doped cavities, the effects of dopant absorption and emission should be considered in order to determine the total losses of both pump and signal. For this purpose, let us consider the time evolution of the signal mode with effective refractive index of n_s inside the active cavity as

$$\frac{da_s}{dt} = -\left(\frac{1}{\tau_{0(s)}} + \frac{1}{\tau_{ext(s)}}\right)a_s + \frac{c}{n_s}g_s a_s \qquad 4\text{-}7$$

where $\tau_{0(s)}$, $\tau_{ext(s)}$ and $\tau_{Yb(s)}$ are the decay rates of signal power due to intrinsic losses, out-coupling and dopant absorption, respectively as demonstrated in Figure 4-3. The speed of light and signal gain are accordingly denoted by c and g_s. At steady state where the signal power does not change with time, $da_s / dt = 0$, and the above equation reduces to

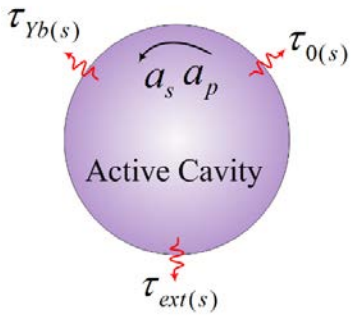

Figure 4-3 General loss mechanisms contributing in an active cavity.

$$g_s = \frac{n_s}{c}\left(\frac{1}{\tau_{0(s)}} + \frac{1}{\tau_{ext(s)}}\right). \tag{4-8}$$

This relation leads to the well-known threshold condition, where the signal gain is equal to the total losses. On the other hand, the total losses of the signal per unit length (α_s^T) can be determined in terms of the Q factors. Let us denote the intrinsic, external (due to out-coupling loss) and Yb absorption Q's of the signal by $Q_{0(s)}$, $Q_{ext(s)}$ and $Q_{Yb(s)}$, respectively. By assuming the total passive Q of the signal to be $Q^T_{passive(s)}$, then, the total signal loss, $\alpha^T_{pasive(s)}$, is given by

$$\begin{aligned}\alpha^T_{passive(s)} &= \frac{\omega_s}{Q^T_{passive(s)}}\cdot\frac{n_s}{c} = \frac{2\pi n_s}{Q^T_{passive(s)}\lambda_s} \\ &= \frac{2\pi n_s}{\lambda_s}\left(\frac{1}{Q_{0(s)}} + \frac{1}{Q_{ext(s)}}\right)\end{aligned} \tag{4-9}$$

where ω_s is the optical angular frequency of the signal with wavelength λ_s. It should be noted that $Q_{Yb(s)}$ is the Q factor induced by Yb^{3+} dopants absorption or emission indicated by $\alpha_{Yb(s)}$ per unit length, and are related by

$$\begin{aligned}\frac{1}{Q_{Yb(s)}} &= \frac{\lambda_s}{2\pi n_s}\alpha_{Yb(s)} = \frac{\lambda_s}{2\pi n_s}\left[\alpha_s - \bar{N}_2\left(\alpha_s + g_s^*\right)\right] = -\frac{\lambda_s}{2\pi n_s}\alpha^T_{passive(s)} \\ &= -\frac{1}{Q^T_{passive(s)}}.\end{aligned} \tag{4-10}$$

Equation 4-10 indicates that total $1/Q$ of the signal is equal to $1/Q^T_{passive(s)} + 1/Q_{Yb(s)} = 0$, which means that signal experiences an infinite Q factor at threshold (as there is signal output without signal input). In reality, this does not happen, and generated Amplified Spontaneous Emission (ASE) is responsible for broadening the lasing linewidth and keeping the total Q finite.

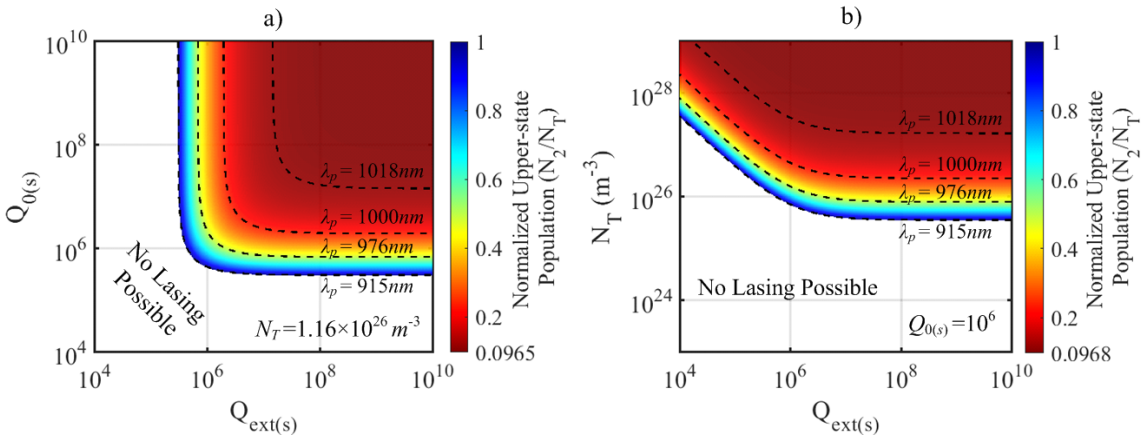

Figure 4-4 Required normalized upper-state population inversion for lasing (at λ_s = 1068nm) as function of external signal $Q_{ext(s)}$ for various a) intrinsic $Q_{0(s)}$'s, and b) dopant concentration N_T. Dashed lines translate the normalized inversion into pump wavelength above which the corresponding inversion is not achievable.

Moreover, from the gain relation given in Eq. 4-6, the normalized population inversion at and above lasing threshold can be determined as

$$\bar{N}_2 = \frac{\alpha_s + \frac{2\pi n_s}{\lambda_s}\cdot\frac{1}{Q^T_{passive(s)}}}{\alpha_s + g^*_s} = \frac{\alpha_s + \frac{2\pi n_s}{\lambda_s}\cdot\left(\frac{1}{Q_{0(s)}} + \frac{1}{Q_{ext(s)}}\right)}{\alpha_s + g^*_s}. \qquad 4\text{-}11$$

Equation 4-11 is an important relation as it gives the minimum required conditions for signal generation at threshold. Let us consider a signal at wavelength λ_s = 1068nm with Yb^{3+} concentration of $N_T = 1.16 \times 10^{26} m^{-3}$. These values closely relate to the fundamental mode of a microbottle resonator which I will be using in experiments in the next chapters. Figure 4-4 (a) and (b) show the normalized upper-state population as function of intrinsic $Q_{0(s)}$, external $Q_{ext(s)}$ and dopant concentration of N_T. The results demonstrate that the required normalised upper-state population is symmetric about the $Q_{0(s)} = Q_{ext(s)}$ line as the total Q is dominated by the smaller one of the $Q_{0(s)}$ or $Q_{ext(s)}$. On the other hand, as expected, as the total Q increases, the minimum normalized required inversion for lasing lowers.

The minimum required inversion for lasing is also dependent on the dopant concentration. As depicted in Figure 4-4 (b), for given intrinsic losses (fixed $Q_{0(s)}$), the lasing possibility can be enhanced by increasing the dopant concentration. For low external Q's ($Q_{ext(s)} < Q_{0(s)}$), lasing is possible only with increased dopant concentration. For $Q_{ext(s)} > Q_{0(s)}$, on the other hand, the behaviour is dominated by the intrinsic Q and the required dopant concentration is fixed. At very high total Q and/or high dopant concentration, as Eq. 4-11 indicates, the minimum required upper-state population

inversion for lasing is independent from $Q^{T}_{passive(s)}$ and N_T, and is only a function of signal wavelength. In these cases, the inversion is clamped at the value of $\alpha_s / (\alpha_s + g_s^*)$. For λ_s = 1068nm, the normalized inversion clamps at ~9.7%. In addition, Q factors and dopant concentration values below which no lasing can occur is indicated as "No Lasing Possible" regions in Figure 4-4.

Additionally, such population inversion-microcavity Q map (shown in Figure 4-4) can be translated into pump wavelength requirements. The illustrated dashed contour lines correspond to the maximum inversion achievable by each λ_p. In other words, lasing can be achieved everywhere in the coloured region, but it will require different pump wavelengths. It is shown that the λ_p = 915nm pump wavelength can cover the widest combination of dopant concentrations and microcavity external Q factors.

From Eq. 4-6, it can be easily deduced that at threshold, where the signal power is much smaller than the pump power, the maximum upper-state population is limited by

$$\frac{N_2}{N_T} \le \frac{\alpha_p}{\alpha_p + g_p^*}. \qquad 4\text{-}12$$

In order to set the minimum requirement to achieve lasing for a given dopant concentration, by substituting Eq. 4-11 in inequality 4-12, it can be derived that

$$\frac{1}{N_T}\left(\frac{1}{Q_{0(s)}} + \frac{1}{Q_{ext(s)}}\right) \le \frac{\Gamma_s \lambda_s}{2\pi n_s}\left[\frac{\sigma_p^{abs}}{\sigma_p^{abs} + \sigma_p^{ems}} \cdot \left(\sigma_s^{abs} + \sigma_s^{ems}\right) - \sigma_s^{abs}\right] = M\left(\lambda_p, \lambda_s\right) \qquad 4\text{-}13$$

where $M(\lambda_p, \lambda_s)$ is only dependent on the doped material parameters at pump and signal wavelengths. Let us define $\min\{Q_{0(s)}\}$ ($\min\{Q_{ext(s)}\}$) as the minimum intrinsic (external) Q of signal required for lasing obtained when $Q_{ext(s)} \gg Q_{0(s)}$ ($Q_{0(s)} \gg Q_{ext(s)}$), then, $\min\{Q_{0(s)}\} = \min\{Q_{ext(s)}\} = [N_T . M(\lambda_p, \lambda_s)]^{-1}$. Figure 4-5 (a) shows the boundary curves indicating the required $Q_{0(s)}$ and $Q_{ext(s)}$ in order to achieve normalized population inversion 0.5 (deduced from Eq. 4-12), corresponding to pump wavelength of 976nm, for various dopant concentrations. The signal wavelength is 1068nm. When the dopant concentration decreases, lasing happens only at high Qs corresponding to smaller intrinsic and coupling losses. Moreover, each curve is characterised by an important "knee" point for which

$$Q_{0(s)}\Big|_{Knee} = Q_{ext(s)}\Big|_{Knee} = 2\min\{Q_{0(s)}\} = 2\min\{Q_{ext(s)}\}. \qquad 4\text{-}14$$

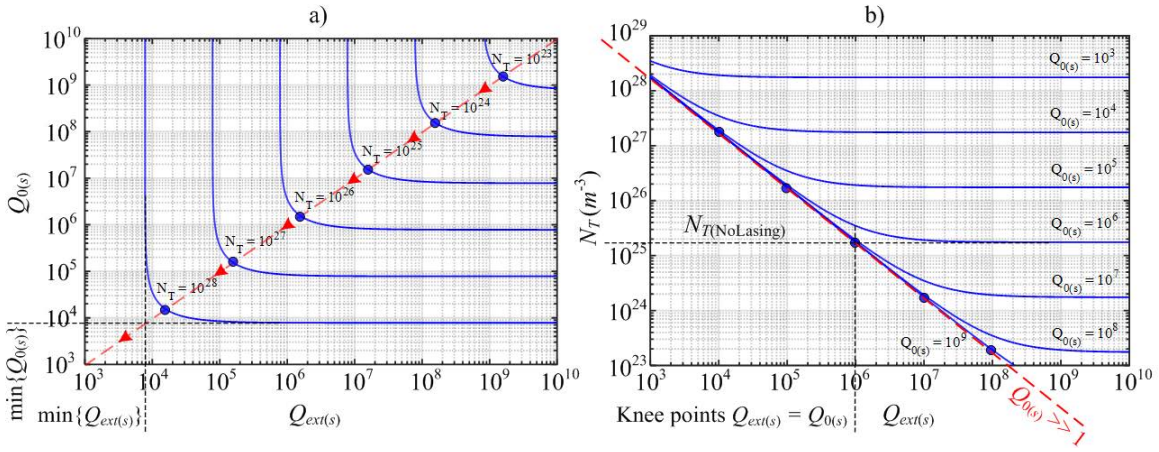

Figure 4-5 Boundary curves indicating the required a) $Q_{0(s)}$ for various dopant concentrations, and b) N_T for different intrinsic Q factors, as a function of external Q factors ($Q_{ext(s)}$), in order to achieve $\bar{N}_2 = 0.5$, corresponding to λ_p = 976nm (λ_s = 1068nm).

This point corresponds to the critical coupling point in which the external losses are equal to the intrinsic ones.

On the other hand, a lower bound on dopant concentration can be deduced using Eq. 4-13. The minimum required dopant concentration, $N_{T(\text{NoLasing})}$, for a given signal and pump wavelengths, can be evaluated by assuming $Q_{ext(s)} \gg Q_{0(s)}$. Then, for a fixed intrinsic Q factor of $Q_{0(s)}$ imposed by fabrication process, $N_{T(\text{NoLasing})} = [Q_{0(s)}.\, M\,(\lambda_p, \lambda_s)]^{-1}$. To clarify, $N_{T(\text{NoLasing})}$ is the smallest value of dopant concentration when there is no external out-coupling loss induced on the signal. Figure 4-5 (b) shows the required dopant concentration N_T for signal and pump wavelengths of respectively 1068nm and 976nm as a function of the external Q factors ($Q_{ext(s)}$), for different intrinsic Q factors ($Q_{0(s)}$). It is also shown that the lower bound, $N_{T(\text{NoLasing})}$, increases as $Q_{0(s)}$ decreases.

It should be noted that Eq. 4-13 is dependent on both pump and signal wavelengths through the emission and absorption cross-section spectra. Here, considering the experimental conditions, the pump wavelength, in most cases, is fixed at 976nm, which can be provided by conventional solid-state laser diodes, while, due to the broad emission of Yb^{3+}, the signal wavelength can lie anywhere in the 1020-1200nm range. Using Eq. 4-13, Figure 4-6 plots the minimum required intrinsic Q to achieve lasing for signal at critical coupling condition (the so-called "knee" point), as a function of dopant concentration and signal wavelength. The pump wavelength is chosen to be 976nm. The results show that at shorter signal wavelengths (i.e. ~1030nm), due to high gain value, the minimum Q required for lasing is smaller than the one at longer wavelengths. This implies that, in order to have lasing at longer wavelengths, the cavity quality should be improved by lowering the intrinsic losses. Figure 4-6 is important from the

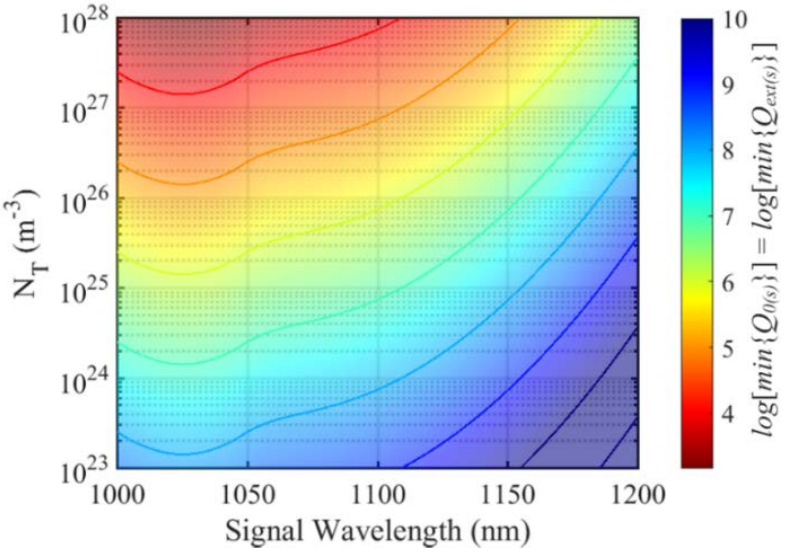

Figure 4-6 Minimum required intrinsic Q to achieve lasing for signal critical coupling (knee point), as function of dopant concentration and lasing wavelength. Pump wavelength at 976nm.

experimental perspective, since it provides a quick criterion on choosing the suitable cavity design in order to achieve lasing at a desired wavelength. We, later in the experimental chapters, use such useful $Q-\lambda$ map to expand lasing to longer wavelengths.

Furthermore, similarly to Eq. 4-2, the variation of pump power ($|a_p|^2$) along length dz in terms of the passive losses ($\alpha_p^{passive}$) and losses due to Yb^{3+} absorption (l_p) is given by

$$\begin{aligned}\frac{d\left|a_p\right|^2}{dz} &= -\left(\alpha_p - \bar{N}_2\left(g_p^* + \alpha_p\right)\right)\left|a_p\right|^2 - \alpha_p^{passive}\left|a_p\right|^2 \\ &= -\left(l_p + \alpha_p^{passive}\right)\left|a_p\right|^2\end{aligned} \qquad 4\text{-}15$$

where $\alpha_p^{passive} = 2\pi n_p / (Q_{0(p)}\lambda_p)$ in which n_p, $Q_{0(p)}$ and λ_p are effective refractive index, intrinsic Q and wavelength of pump mode, respectively. In a microcavity structure, the total Q of pump (Q_p^T) can be derived from the Q's due to Yb^{3+} absorption/emission ($Q_{Yb(p)}$) and the total passive losses on the pump mode ($Q_{passive(p)}^T$), hence

$$\begin{aligned}\frac{1}{Q_p^T} &= \frac{1}{Q_{Yb(p)}} + \frac{1}{Q_{passive(p)}^T} \\ &= \frac{1}{Q_{Yb(p)}} + \frac{1}{Q_{0(p)}} + \frac{1}{Q_{ext(p)}}\end{aligned} \qquad 4\text{-}16$$

where $Q_{ext(p)}$ is the Q factor corresponding to losses on pump mode caused by out coupling, and $Q_{Yb(p)}$ can be evaluated from

$$\frac{1}{Q_{(Yb)p}} = \frac{\lambda_p}{2\pi n_p} l_p = \frac{\lambda_p}{2\pi n_p}\left[\alpha_p - \bar{N}_2\left(\alpha_p + g_p^*\right)\right]. \qquad 4\text{-}17$$

Equations 4-16 and 4-17 suggest that if the dopant concentration is kept low, then, the total Q is not significantly affected by the Yb^{3+} absorption, and total pump Q follows closely the passive one. If the dopant concentration is very high and the inversion level is low, the effect of Yb-absorption becomes important, such that at low inversion levels, the $Q_{Yb(p)}$ will be dominant. Whereas, as the inversion increases, due to increase in the emission of Yb^{3+}, the loss caused by dopant absorption decreases resulting in enhanced $Q_{Yb(p)}$. Hence in this case, the total Q of the pump mode will be dominated by the total passive Q.

4.4 Pump and Signal Powers, Lasing Threshold and Efficiency

Equation4-5 gives the normalized upper-state population inversion in terms of intra-cavity pump and signal mode powers. On the other hand, from the threshold condition given in Eq. 4-11, the upper-state population inversion can be evaluated as function of signal losses and the emission/absorption cross-sections. Thus, if we know the internal pump power, the signal power can be determined accordingly. Let us consider the tapered fibre coupled resonator configuration illustrated in Figure 4-7 (a), where as an example, an active microbottle resonator is considered. Input pump mode is coupled into the resonator from one side of the tapered fibre, and pump and signal WGMs are excited inside the resonator. The excited pump and generated signal modes are coupled out into the tapered fibre due to the evanescent field overlap and photon tunnelling between the resonator and the fibre modes. It should be noted that due to

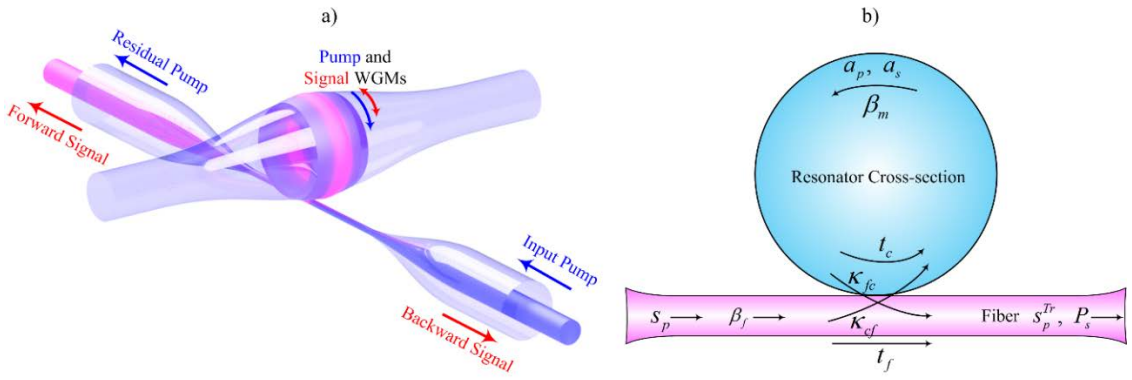

Figure 4-7 a) Schematic 3D demonstration, and b) cross-section of tapered fibre-coupled microbottle laser.

multi-directional emission of Yb^{3+} ions, in reality, both forward and backward signal WGMs are excited, and coupled out into the tapered fibre.

Following the same transfer matrix method developed in Chapter 2, the intra-cavity pump WGM power, $|a_p|^2$, in terms of input pump power, s_p, is evaluated as

$$\left|a_p\right|^2 = \left| e^{-j\beta_c L_c} \frac{j\kappa_{cf(p)}}{1 - t_{c(p)} e^{-\left(l_p + \alpha_p^{passive}\right) L_{rt}} e^{-j(\varphi_{rt} - \beta_c L_c)}} \right|^2 s_p \qquad 4\text{-}18$$

where β_c is the light propagation constant in the coupling region, and L_c is the coupler length. $\kappa_{cf(p)}$ is the coupling efficiency of tunnelling pump fibre mode to the cavity pump WGM, and $t_{c(p)}$ is the transmission coefficient of the pump WGM inside the cavity, and is approximately calculated from the power conservation relation such that $|t_{c(p)}|^2 + |\kappa_{fc(p)}|^2 = 1$, where $\kappa_{fc(p)}$ is the pump coupling efficiency from the cavity into the fibre. φ_{rt} is the round-trip phase shift of pump mode evaluated from $\varphi_{rt} = \beta_p L_{rt} = (2\pi / \lambda_p) n_{eff(p)} (2\pi R_0)$, in which L_{rt} is the round-trip cavity length ($2\pi R_0$), and $n_{eff(p)}$ signifies the effective refractive index of pump WGM. Without loss of generality, in order to simplify the calculations, the total coupling coefficient along the cavity curvature is calculated by the approximation given in [85] such that

$$\kappa_{ij}^2 = \kappa_{ij}^2(S_0) \frac{\pi R_0}{\gamma_f} \exp\left\{ -R_0 \frac{(\beta_i - \beta_j)^2}{2\gamma_f} \right\} \qquad 4\text{-}19$$

where $\kappa_{ij}^2(S_0)$ is calculated from the overlap integrals given in Eq. 2-9, β denotes the propagation constant, i and j correspond to either fibre or cavity. R_0 and r_f are the centre of microbottle and fibre radii, respectively, and $\gamma_f = \alpha_f K_1(\alpha_f r_f) / K_0(\alpha_f r_f)$, where $\alpha_f = (\beta_f{}^2 - k^2 n_0^2)^{1/2}$, in which k is the free space wave-number, and n_0 denotes the index of the cladding. K_0 and K_1 are the modified Hankel functions of the zero and first orders, respectively. The output pump power, s_p^{Tr}, can be calculated from the interference of the uncoupled transmitted pump power with the out-coupled intra-cavity mode, such that

$$s_p^{Tr} = \left| e^{-j\beta_c L_c} \left(t_{f(p)} + \frac{\kappa_{cf(p)} \kappa_{fc(p)}}{t_{f(p)} - e^{\left(l_p + \alpha_p^{passive}\right) L_{rt}} e^{j(\varphi_{rt} - \beta_c L_c)}} \right) \right|^2 s_p \qquad 4\text{-}20$$

where $t_{f(p)}$ is the transmission coefficient of the fibre pump mode. Considering the regime where only a single pump and single signal mode propagate inside the cavity, then, using Eq. 4-5, the signal power can be derived as

$$\left|a_s\right|^2 = \frac{\frac{1}{n_p h\nu_p V_p}\left[\alpha_p - \bar{N}_2\left(\alpha_p + g_p^*\right)\right]\left|a_p\right|^2 + \bar{N}_2\frac{N_T}{\tau_{Yb}}}{\frac{1}{n_s h\nu_s V_s}\left[\bar{N}_2\left(\alpha_s + g_s^*\right) - \alpha_s\right]}. \qquad 4\text{-}21$$

It is important to realize that Eq. 4-21 evaluates the internal signal power in terms of the pump power and the upper-state population level at a given wavelength. Subsequently, the output signal power P_s, is the amount of its intra-cavity power which couples out of the cavity, i.e. $P_s = \kappa_{fc\,(s)}^2 \left|a_s\right|^2$.

The threshold input pump power can be calculated from the fact that the intra-cavity signal power is zero at threshold ($\left|a_s\right|^2 = 0$). Therefore, by combining Eq.s 4-18 and 4-214-18 the threshold pump power is derived as

$$\left|s_p^{th}\right|^2 = \frac{n_p h\nu_p V_p \bar{N}_2 N_T \left|1 - t_{(c)p} e^{-\left(l_p + \alpha_p^{passive}\right)L_{rt}} e^{-j\left(\varphi_{rt} - \beta_c L_c\right)}\right|^2}{\tau_{Yb}\kappa_{cf\,(p)}^2\left[\bar{N}_2\left(\alpha_p + g_p^*\right) - \alpha_p\right]}. \qquad 4\text{-}22$$

It is worth mentioning that the last relation gives a minimum value for the threshold input pump power, since, the upper-level population inversion is calculated from the assumption of the threshold condition given in Eq. 4-8. The slope efficiency can be obtained, by definition, from the ratio of the increase rate of the output signal power to the one of the input pump power, as

$$\eta \equiv \frac{dP_s}{d\left|s_p\right|^2} = \left(\kappa_{fc(s)}^2 \kappa_{cf\,(p)}^2\right)\frac{n_s v_s V_s}{n_p v_p V_p}\frac{\left[\alpha_p - \bar{N}_2\left(\alpha_p + g_p^*\right)\right]}{\left[\bar{N}_2\left(\alpha_s + g_s^*\right) - \alpha_s\right]} \cdot \frac{1}{\left|1 - t_{c(p)} e^{-\left(l_p + \alpha_p^{passive}\right)L_{rt}} e^{-j\left(\varphi_{rt} - \beta_c L_c\right)}\right|^2}. \qquad 4\text{-}23$$

In the next section, such relations will be applied to the microbottle resonator lasers, which will be studied in the next chapters.

4.5 Analysis of Yb^{3+}-doped Microbottle Resonator Lasers (MBLs)

Let us consider the system of microbottle resonator coupled to a tapered fibre schematically shown in Figure 4-7. As previously described, the pump launching and signal collection are done through the same tapered fibre. Unlike perfect microsphere cavities where different axial (angular) modes belonging to the same radial order, are frequency degenerate, microbottle resonators exhibit broken frequency degeneracy for all the families of axial modes having a fixed radial order. Figure 4-8 (a) shows the intensity profile of the first five axial modes with radial order of one for a typical microbottle resonator at 1070±2nm wavelength band. The dimensions of the microbottle resonator is as depicted in Figure 4-8 (b) corresponding to the device which will be studied experimentally in the next chapter. The modes profile of the resonator are calculated using general Transfer Matrix Method (TMM) [127]. The evanescent field modal profile of a typical microbottle WGM outside the resonator varies in an exponential fashion in the radial direction. This is known to provide a degree of freedom in controlling the coupling to a WGM. Coupling can be achieved by gradually changing the air gap between the resonator and the excitation tapered fibre. In practical conditions, such air gap should not exceed few hundreds of nanometres in order to have an efficient coupling. In microspheres, varying the resonator-taper air gap is the only way to control the coupling coefficient of the system. This requires complex and

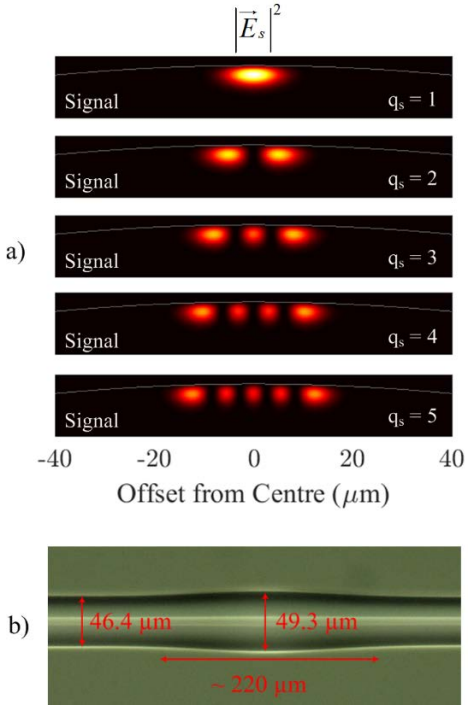

Figure 4-8 a) Intensity profile of the first five axial modes with radial order of one at 1070±2nm wavelength band corresponding to fabricated microbottle resonator shown in b with given dimensions.

expensive experimental apparatus, as for small air gaps (below 100nm) static forces between the taper and the resonator makes it very hard to control the position of the tapered fibre. On the other hand, changing the fibre position in nanometer scales requires precise alignment equipment, and due to the sharp decay of the evanescent field of WGMs into the air cladding, the coupling coefficient will be very sensitive to the fluctuations in the air gap width.

At the same time, microbottle resonators present another way of tuning coupling condition between the tapered fibre and the resonator. Due to the tapered quasi-harmonic profile of the microbottles, it is possible to couple in various orders of WGMs by axially translating the tapered fibre along the curvature of the resonator profile. Microbottles with typical dimensions used in our experiments, support fundamental modes with size of more than ten microns in the axial direction. This is an important property of such resonators which provides the possibility of tuning the coupling in micron scale, even when the tapered fibre is in contact with the resonator surface. The system would be more mechanically stable compared to the case where tapered fibre freely floats in the air.

Moreover, in perfect microspheres, WGMs always propagate along the circumference closest to the taper, regardless of the taper position. Thus, the mode profile in axial (angular) direction is always symmetric with respect to the point where the fibre is coupled. While, in microbottles, which can be considered as extremely deformed microspheres, due to the tapered quasi-harmonic profile of the resonator, the WGMs will always have fixed "turning points" which are axially symmetric with respect to the centre of the resonator. Hence, it is possible to change the coupling coefficient (modal overlap) to WGMs by changing the tapered fibre position along the resonator profile. The external Q factor of the pump and signal can be calculated in terms of the coupling coefficient using the following relation

$$Q_{ext(wgm)} = \frac{m_{wgm}\pi}{\left|\kappa_{fc(wgm)}\right|^2}. \qquad 4\text{-}24$$

where m_{wgm} is the azimuthal mode number of the corresponding WGM.

Effects of intrinsic modal Q factors on MBL characteristics

In this section, I investigate the effect of intrinsic Q factor and tapered fibre offset on the main optical characteristics of MBLs, such as signal and pump extrinsic Qs, internal and output powers, threshold pump power and laser efficiency. Figure 4-9 (a) plots the calculated external Q factors of both pump and signal fundamental modes as a function of the taper offset from the resonator centre. The pump wavelength is chosen to be at ~976nm corresponding to maximum absorption of Yb^{3+} and signal wavelength is at ~1068nm. The external Q factors of pump and signal modes follow closely the

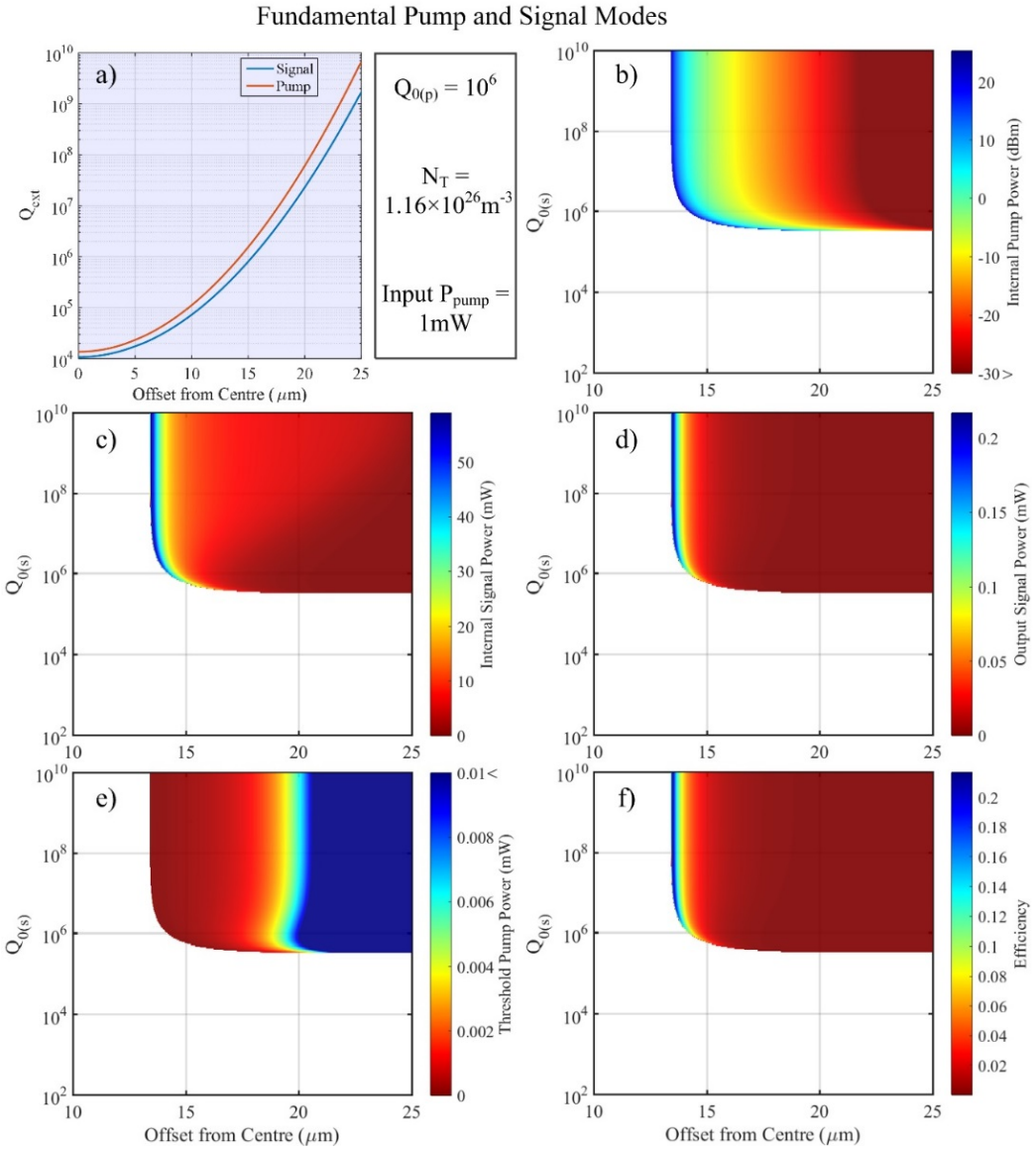

Figure 4-9 a) calculated external Q factor of fundamental pump and signal modes, internal b) pump and c) signal, d) Output signal powers, e) threshold input pump power, and f) slope efficiency, as a function of taper offset from the resonator centre and intrinsic signal Q. The intrinsic pump Q is 10^6, the dopant concentration $N_T = 1.16\times10^{26}m^{-3}$ and the input pump power is 1mW.

shape of the mode profile along the axial axis. The pump Q is slightly higher than the signal one since the mode size at the pump wavelength is smaller, which decreases the strength of the evanescent WGM field. Thus, smaller modal overlap between the WGM and the fibre mode results in smaller coupling coefficient leading to higher Q factor.

Internal pump power is an important parameter, as it largely defines the lasing threshold and other nonlinear effects, and it is plotted in Figure 4-9 (b). If we intentionally improve the intrinsic Q of the signal, the internal pump power does not change significantly since the pump power is limited by its intrinsic Q factor at a fixed offset. The maximum internal pump power is achieved for a tapered fibre offset of ~14μm. As shown in Figure 4-9 (a), this offset corresponds to a pump external Q of $\sim 10^6$ and, therefore, critical pump coupling. For smaller offsets there is no lasing due to pump overcoupling. For the offset of 14μm the corresponding signal external Q is $\sim 5\times 10^5$ (see Figure 4-9 (a)) and as a result there is no lasing for signal external Q factors below that value, this time due to signal overcoupling.

On the other hand, as plotted in Figure 4-9 (c) and (d), the internal and output signal power is highest for tapered fibre offset of ~14μm and critical pump coupling, as well as, intrinsic signal Qs larger than the corresponding critical value of $\sim 5\times 10^5$. This is due to high pump power inside the resonator, which implies high level of upper-state population. As the offset increases, the internal and output signal power decreases since the population inversion and consequently the gain decrease. At fixed offsets, increasing the intrinsic signal Q does not significantly change the internal and output signal power as the total Q, and hence, the losses are limited by the external Q factor and the level of inversion which are determined by the taper offset. It should be noted that the internal signal and pump powers are connected through the population inversion set by the fibre offset. Interesting observation about the relation between internal and output signal powers is that, although the internal signal power is not zero at larger offsets (e.g. at 18μm), the output signal power is close to zero. This is due to the fact that the pump and the signal modes exhibit slightly different coupling coefficients along the resonator owing to different mode sizes and external Q's. It should be noted that the coupling efficiency from the fibre into the resonator is usually smaller than the one from the resonator to the fibre. This shows that the rate of power coupling into the resonator is not necessarily identical to the out-coupling one, as it depends on the coupling regime (over-, under- or critical- coupling) under which the resonator-taper system operates. The effect of these phenomena is more pronounced for higher order modes, which I will investigate in more detail in the experimental Chapter 5.

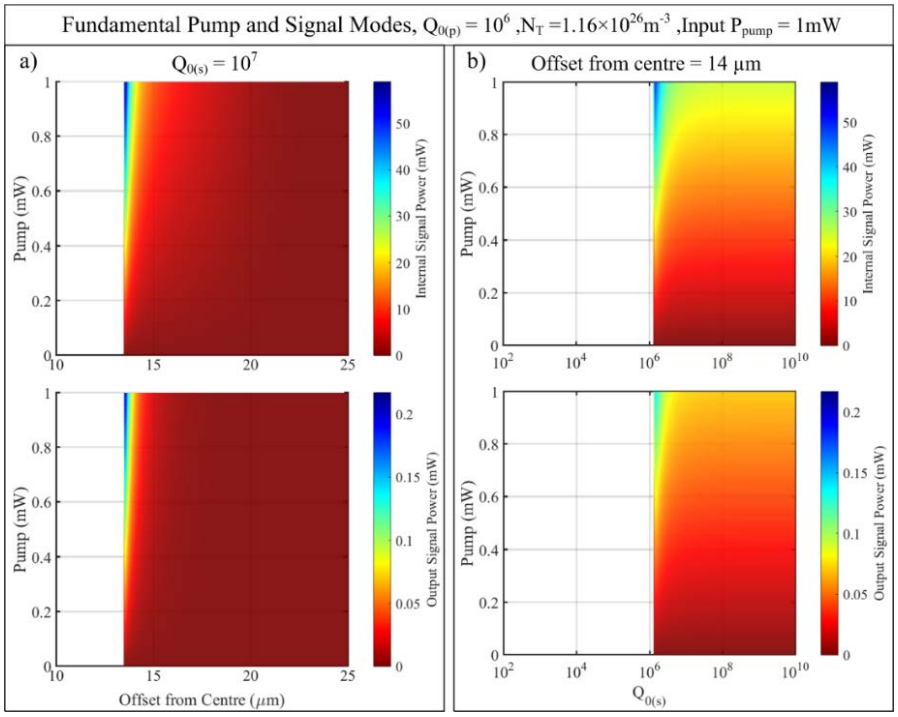

Figure 4-10 Internal and output signal powers as a function of input pump power for a) fixed signal intrinsic Q of 10^7 at various offsets, and b) fixed offset of 14µm at various intrinsic signal Q's.

The calculated input pump power threshold and the lasing efficiency are plotted in Figure 4-9 (e) and (f). As expected, the pump threshold is to large extend inversely proportional to the internal (c.f. Figure 4-9 (b) and (e)) and the overall efficiency follows the output signal variation. For the current case of pump and signal fundamental mode excitation and the parameters of Figure 4-9, optical efficiencies in excess of 20% are calculated under conditions of critical pump coupling.

Furthermore, the internal and output signal powers can be calculated from Eq. 4-21 as a function of the input pump power. The results at constant signal intrinsic Q of 10^7 and offset of 14µm are respectively plotted in Figure 4-10 (a) and (b). When the intrinsic Q of the signal is fixed, the loss on the signal is determined by the level of the inversion and the external losses which are determined by the taper offset (see Figure 4-10 (a)). On the other hand, at fixed taper offset (Figure 4-10 (b)), the internal signal power is maximum where the intrinsic Q of signal provides critical coupling.

An important parameter in determining the MBL characteristics is the intrinsic Q factor of the pump mode. Figure 1-11 plots the internal and output signal powers for the case of intrinsic pump Q factor of $Q_{0\,(p)} = 10^5$, for input pump power of 1mW. When compared to $Q_{0\,(p)} = 10^6$ (see Figure 4-9) the overall efficiency is dropped from 20% to ~3%.

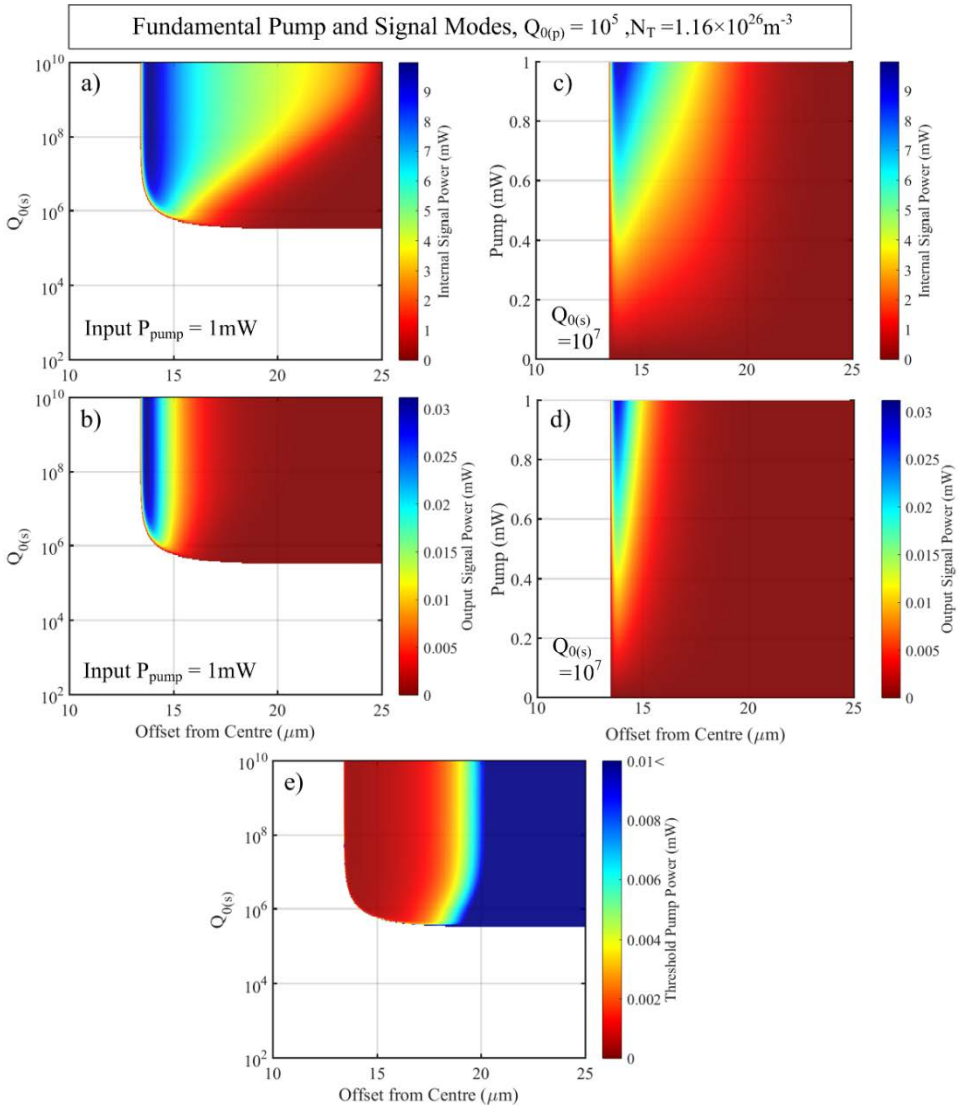

Figure 4-11 a) Internal and b) output signal powers as a function intrinsic signal Q and offset. c) Internal and d) output signal powers as a of input pump power and offset for fixed intrinsic signal Q of 10^7, and e) the corresponding threshold pump power.

Effects of dopant concentration on MBLs

Another important factor in designing microcavity lasers is the concentration of the active dopants in the host material, which is determined largely by the fabrication process. The bulk material gain and loss given by the Giles parameters in Eq. 4-1 are directly proportional to the total dopant concentration. Hence, the level of the upper-state population inversion can be significantly altered by the dopant concentration. The total passive Q of the fundamental pump and signal WGM corresponding to the MBL of Figure 4-8 are calculated from $1/Q^{T}_{passive} = 1/Q_0 + 1/Q_{ext}$ relation and plotted in Figure 4-12 (a). For the sake of simplicity, the intrinsic Q of both signal and pump are assumed to be identical (which is a valid assumption) and equal to 10^6. Obviously, the total passive Q at very high external Q's (large offsets) clamps to the intrinsic one. Figure 4-12 (b-d) plot the internal pump, internal signal and optical efficiency, respectively, in terms of the Yb^{3+} concentration and the fibre offset from the MBL centre. The white region in the plots correspond to the "no lasing regime", where as previously discussed, the total losses (internal + out-coupling) on the signal mode are large and prohibit

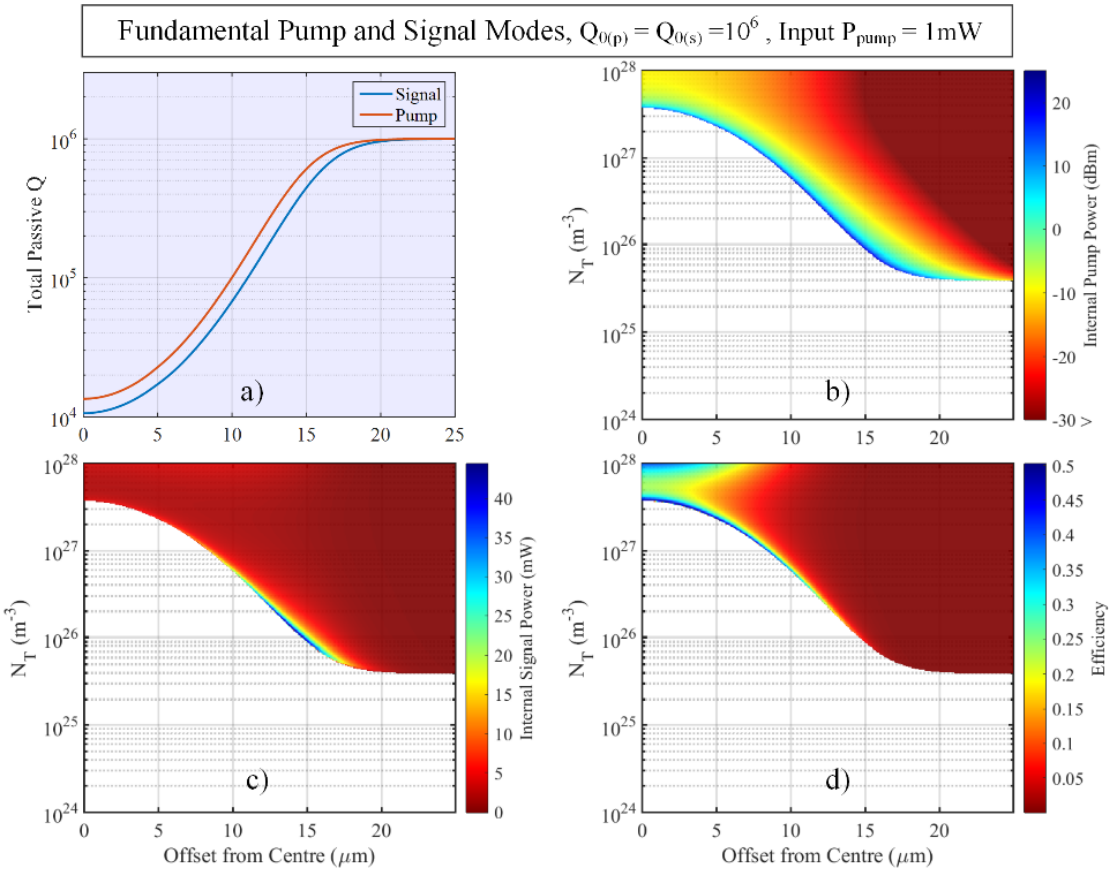

Figure 4-12 a) Total passive Q of the fundamental pump and signal modes as function of offset, internal b) pump Q and c) signal powers, and d) slope efficiency as a function of dopant concentration and offset from the resonator centre.

lasing. For all dopant concentrations, the internal pump power (Figure 4-12 (b)) is highest where the conditions for pump mode critical coupling are met. As the tapered fibre offset and/or the dopant concentration increase beyond the critical coupling values, the internal pump power level decreases due to lower mode coupling and high internal pump power absorption, respectively. In Figure 4-12 (c) it is shown that the maximum internal signal power (~45mW) occurs for tapered fibre offsets of ~14μm and dopant concentration of ~$10^{26}m^{-3}$. However, as shown in Figure 4-12 (d), the highest output power and, therefore, the overall efficiency (~50%) occurs for small tapered fibre offsets (<5μm) and dopant concentration of >$3\times10^{27}m^{-3}$. This is due to the fact that the signal in-coupling and out-coupling coefficients are different resulting in different optimum conditions for signal storage and out-coupling. It should be mentioned that cooperative up-conversion due to ion pairing (which happens in highly doped fibres) are not considered here, in order to keep the analysis simple. Concentration quenching could be easily taken into account in a simplified manner through the lifetime shortening of Yb ions.

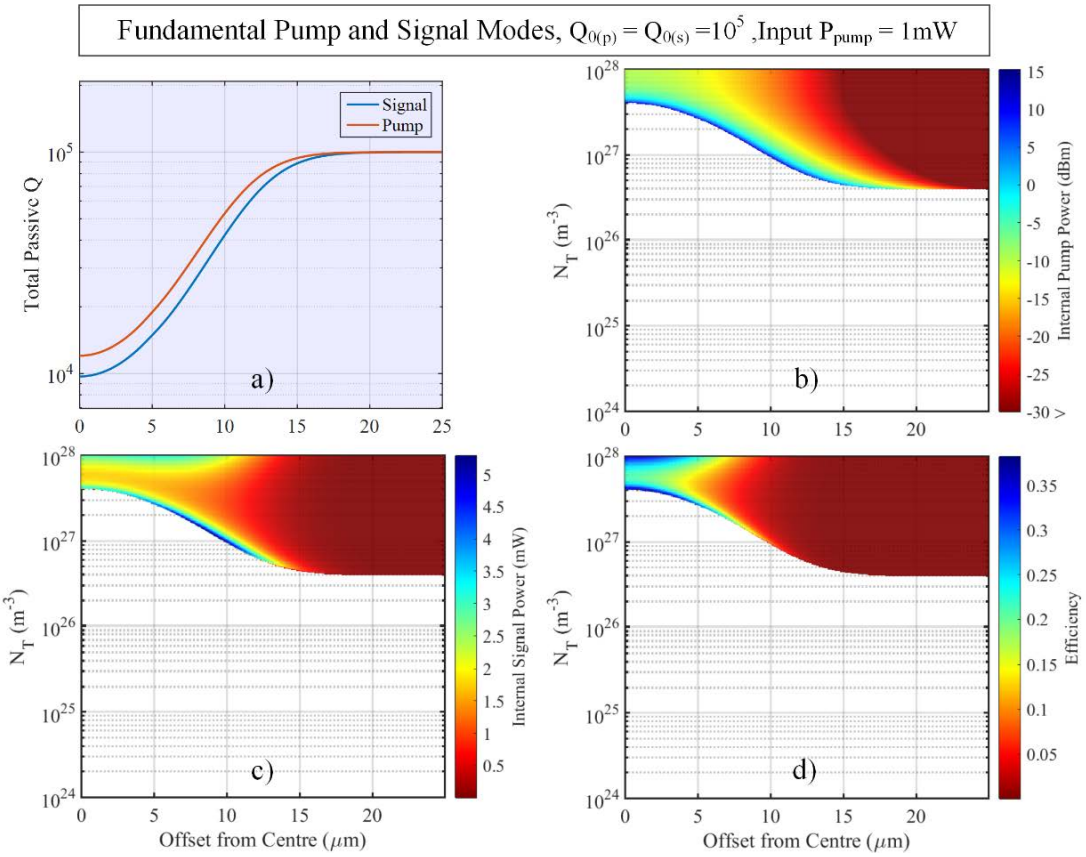

Figure 4-13 a) Total pasive Q of signal and pump modes as a function of taper offset, Internal b) pump and c) signal powers, and d) slope efficiency as a function of dopant concentration and taper offset from the resonator centre for intrinsic Q's of 10^5.

Furthermore, as previously discussed, the minimum dopant concentration to achieve lasing is highly dependent on the value of the modal intrinsic Q's. Figure 4-13 plots the same MBL characteristics as in Figure 4-12, for intrinsic Q of both the signal and pump fundamental modes of 10^5. The maximum achievable internal pump and signal powers are significantly decreased owing to the higher intrinsic losses. At large taper offsets, the total passive Q's are obviously limited to power values by the higher intrinsic ones. The maximum achievable efficiency cannot exceed ~40% at the optimum N_T- offset combination.

Lasing conditions as a function of lasing wavelength

In this section, I describe the required conditions in order to achieve lasing in a MBL at desired signal wavelength for the fundamental pump and signal WGMs. The achievable gain for specific signal mode depends on the wavelength of the signal which determines the absorption and emission of Yb^{3+} at that particular wavelength. The absorption and emission cross sections determine the required level of the upper-state population in order to obtain net gain level at the signal wavelength.

I interpolated the mode volume and coupling coefficients at different wavelengths along the lasing spectra from few numerically calculated samples of the fundamental mode. As the wavelength of the signal increases, the corresponding mode size increases monotonically. Figure 4-14 (a) plots the variation of the effective mode volume of the fundamental modes over the emission band of Yb^{3+}. The effective mode volume increases in a linear fashion with respect to wavelength. On the other hand, the out-coupling efficiency which is a function of mode size, increases monotonically with wavelength. The variation of the coupling efficiency for the fundamnetal mode is plotted in Figure 4-14 (b), which demonstrates that, at a fixed fibre offset the coupling efficiency

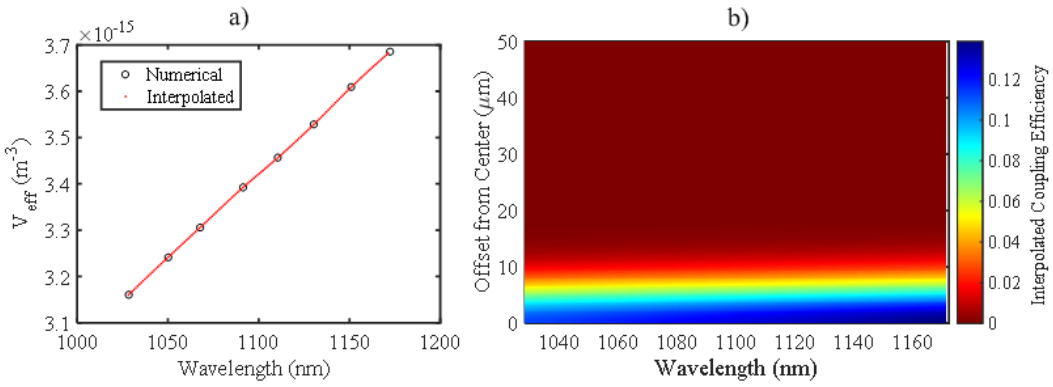

Figure 4-14 Spectra of a) numerical and estimated values of the effective mode volume, and b) interpolated coupling efficiency, for the fundamental mode of the MBL.

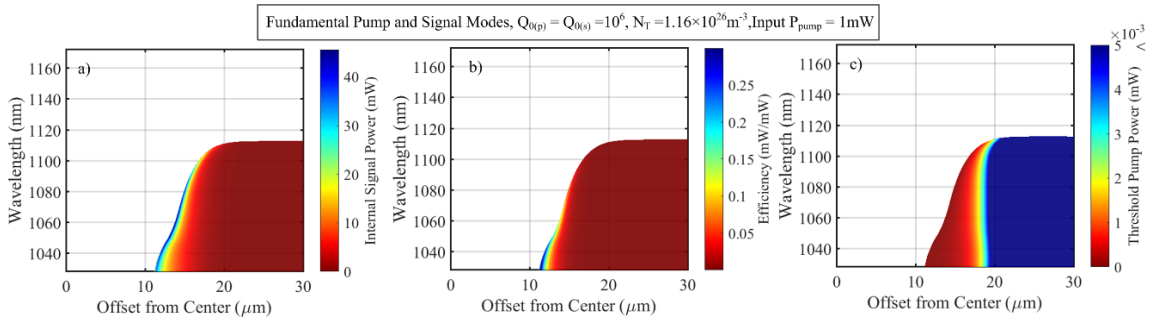

Figure 4-15 a) internal signal power, b) slope efficiency, and c) threshold pump power as function of signal wavelength and taper offset from resonator centre.

increases with wavelength. This is important since the external Q factor is determined by the coupling coefficient, which in turn affects the required inversion level, and hence, the signal gain.

Figure 4-15 (a) shows the internal signal power for 1mW input pump power as a function of signal wavelength and tapered fibre offset from the resonator centre. The intrinsic Q's of both signal and pump are assumed to be 10^6 and the dopant concentration is fixed at $1.16\times10^{26}\,m^{-3}$. No lasing is observed for offsets smaller than ~12μm and signal wavelength longer than ~1110mn, primarily due to excessive signal out-coupling. For the given conditions, the maximum internal signal power happens around 1060nm, while the maximum efficiency (output signal power) occurs at ~1030nm, as shown in Figure 4-15 (b). Additionally, the input pump power threshold (Figure 4-15 (c)) increases as the wavelength of the signal increases. These results imply that it is more likely to achieve lasing at longer wavelengths if the tapered fibre offset from the centre is increased. While, due to higher gain, and hence, lower total signal losses at short wavelengths (i.e. ~1030nm), lasing is possible with smaller tapered fibre offsets.

One way to expand the lasing possibility to longer wavelengths is improving the intrinsic Q of the pump and signal WGMs. This can be experimentally achieved by further thermal-polishing of the resonator surface, or controlling the purity of the host material during the fabrication. Figure 4-16 shows the calculated achievable threshold pump power and lasing efficiency of the fundamental pump and signal WGMs of MBL at various intrinsic Q's. Such results illustrate two different phenomena: 1) for the given dopant concentration, no lasing is possible for offsets below ~11μm (this offset is set by the value of the external Q factors), and 2) Lasing at longer wavelengths is possible if and only if for given dopant concentration the intrinsic losses are lowered. It should also be noted that the maximum achievable lasing slope efficiency is

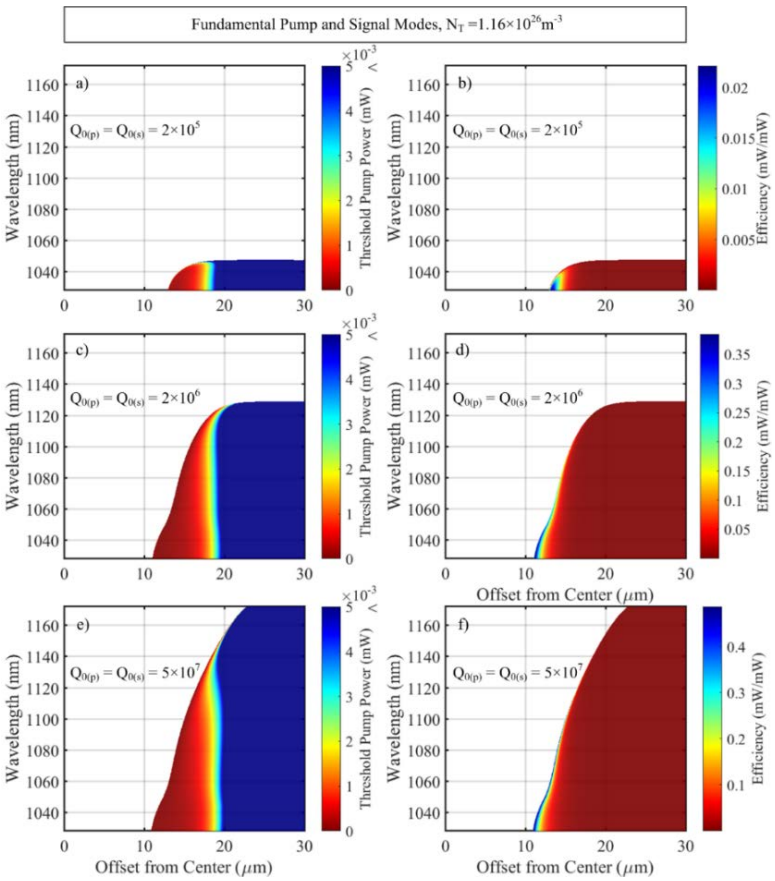

Figure 4-16 Threshold pump power and slope efficiency as function of lasing wavelength and taper offset from resonator centre, for equal intrinsic Q of signal and pump of a, b) 2×10^5, c, d) 2×10^6, e, and f) 5×10^7.

significantly increased with higher intrinsic Q's. For instance, the maximum slope efficiency from 2% at intrinsic Q of 2×10^5 increases to ~50% at Q of 5×10^7.

As we have seen previously, altering the intrinsic Q factor broadens the lasing possibility to longer wavelengths where due to low signal absorption and small modal overlap, the total Q of the signal is high and the threshold pump power is low. Otherwise, if the external signal Q is dominant, the lasing threshold will significantly increase due to very low total signal and pump Q.

Finally, as previously discussed, the overall lasing characteristics can be manipulated through the amount of dopant concentration. The input pump power threshold and efficiency of the MBL for fundamental pump and signal mode at intrinsic Q of 10^6 are plotted in Figure 4-17 for various dopant concentrations. The minimum taper offset in order to achieve lasing for the fundamental modes, can be decreased by increasing the dopant concertation. At very small offsets, due to over-coupling of the tapered fibre to the signal and pump modes, the upper-state population is very low for low concentrations (Figure 4-17 (a-d)) as no lasing is possible. As the dopant concentration increases the population inversion at fixed offsets increases, which in turn enhances

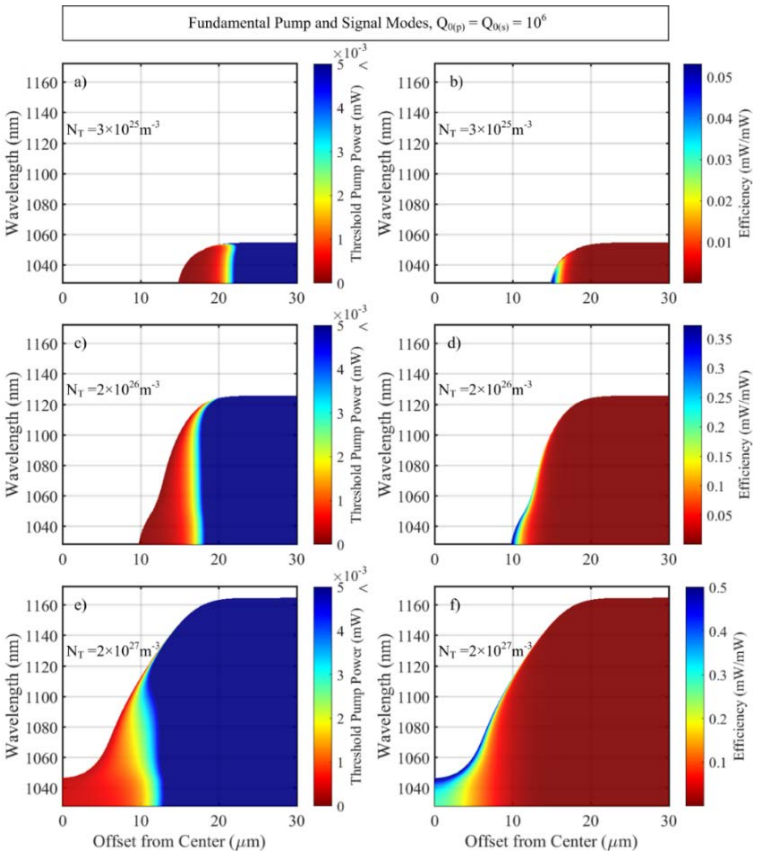

Figure 4-17 Threshold pump power and slope efficiency as function of lasing wavelength and taper offset from resonator centre, for various dopant concentrations of a, b) 3×10^{25} m^{-3}, c, d) 2×10^{26} m^{-3}, e, and f) 5×10^{27} m^{-3}.

the total signal gain. Hence, at higher dopant concentrations lasing becomes possible at shorter wavelengths (i.e. ~1030nm), and as the concentration is further increased, the lasing possibility for longer wavelengths increases even at smaller offsets.

These analyses are obviously dependent on the pump and signal mode profiles which determines the offset-dependent coupling coefficients as well as the effective mode volume. I will explore such effects on the lasing condition for higher order modes, which naturally exist in MBLs, in the next chapters along with experimental studies.

4.6 Summary and Conclusion

In this chapter, a unified and general approach to study the performance of rare-earth doped microcavity lasers is presented. Yb^{3+} as doping material, is specifically studied, due to its simple energy level and high gain. The gain and loss on both pump and signal modes are derived using the well-known two-level model theory. Then, using the threshold condition in microcavity lasers, the required inversion level in order to achieve lasing is derived in terms of signal losses and the Giles parameters (introduced in the EDFA modelling). Results show that the minimum upper-state population

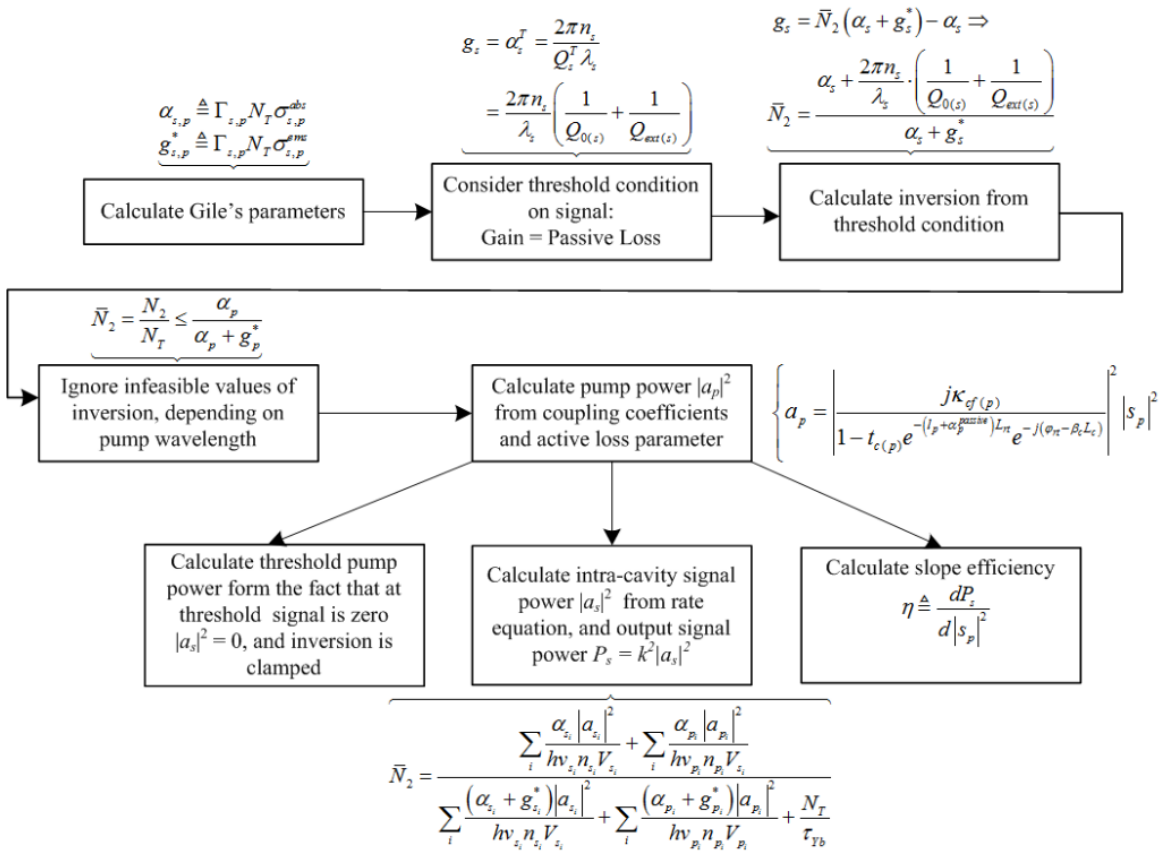

Figure 4-18 Flowchart of the steps in simulating rare-earth doped cavities used in this study.

inversion to achieve lasing for a particular signal mode is determined by the losses (intrinsic and loading) on the signal mode as well as dopant concentration. The pump Q factor is also dependent on the inversion level and coupling conditions, such that, if the concentration is high the total pump Q is always dominated by the excessive dopant absorption.

Moreover, the internal and transmitted pump power for typical microbottle lasers coupled to tapered fibres are derived in terms of coupling coefficients and intrinsic Q's, as well as the total losses induced by the active dopant. Then, signal power is calculated from the rate equations that relate the internal pump power to the inversion level, and consequently, the output signal lasing power can be calculated from the signal out-coupling coefficient. Furthermore, the threshold pump power is derived from the fact that at threshold, the intra-cavity signal power is zero. Then, the slope efficiency of the laser can be easily calculated from the ratio of the output signal power to the input pump power. Figure 4-18 briefly summarizes the steps employed in the simulations.

Thanks to the quasi-harmonic profile of MBRs, it is possible to achieve efficient coupling to a specific mode by translating the tapered fibre along the profile of the resonator. This method provides an accurate and mechanically stable way to couple to desired

WGMs. Having this in mind, the derived relations are then employed to analyse the lasing characteristics of the fundamental pump and signal modes of typical microbottle lasers depending on the coupling condition.

Results show that, for the fundamental pump and signal modes and given dopant concentration, at very small taper offsets from the resonator centre, the threshold is very high. This is due to the large cavity loading by the tapered fibre which has large overlap with signal and pump modes at offsets close to centre of the resonator. The output lasing signal power is maximum at the region where the pump and signal modes are close to critical coupling. On the other hand, the dopant concentration plays an important role in determining the gain and loss of pump and signal modes, and thus, changing the corresponding "knee" point that determines the regime under which the lasing signal operates. As the Yb^{3+} concentration increases the total Q of pump mode decreases due to higher absorptions. By increasing the taper offset from the resonator centre, the internal pump power increases due to lower loading losses, until it goes into the under-coupling regime, which decreases the internal pump power, and hence, results in lower inversions. Therefore, the maximum internal signal power happens where, first, the internal pump is high, and second, taper loading is low. This condition happens almost at the offset where pump and signal are critically coupled. Whereas, the maximum output signal happens where the signal out-coupling coefficient is relatively high, which is closer to the centre.

Additionally, such results show that it is more likely to achieve lasing at longer wavelengths if the tapered fibre offset from the centre is increased. While, due to the higher gain, and hence, lower total losses on the signal at short wavelengths (i.e. ~1030nm), lasing becomes possible with small offsets. Lasing at longer wavelengths is possible if, either for fixed dopant concentration, the intrinsic losses are lowered, or alternatively, the dopant concentration is increased. Such compensation should be considered to obtain enough inversion, and therefore, broaden the possible lasing spectra, owing to the low gain of Yb dopants at long wavelengths.

The analyses presented in this chapter, can be employed to study the characteristics of higher order lasing modes. Such study will be presented in the next chapters along with experimental analysis.

Chapter 5 Yb^{3+}-doped Microbottle Resonator Lasers

5.1 Introduction

In this chapter, the performance of MBLs excited by tapered fibres is experimentally explored. The theoretical model of Yb^{3+}-doped MBLs which was developed in Chapter 4, is employed to elucidate the characteristics of such lasers. Owing to availability of optical telecom devices at C-band, first the performance of MBL is characterised at standard 1550nm wavelengths. Our study will involve estimations of the types of excited WGMs, Q-factors, resonance frequency spacing and profile of a WGM resonator. Such analysis can be further extended to predict properties of the device at 1μm wavelength range where the availability of tunable lasers is limited. Microbottles have shown great potential in realization of selectively-excited WGM resonators. This capability would be very beneficial in employment of MBRs as laser cavities, since precise pump mode selection is essential in determining the lasing characteristics and wavelength. In this study, it is demonstrated how the lasing threshold, slope efficiency and wavelength is altered by means of only translating the tapered fibre along the MBL profile.

Moreover, MBLs normally exhibit multimode lasing due to the non-degenerate multimode nature of such resonators. This affects the performance and stability of MBLs through thermal instability and gain competition between lasing modes. Reducing the number of lasing modes propagating inside the laser cavity will be important, especially in the case when such devices are used as sensors. In this chapter, three different methods are employed in order to clean-up the spectra: 1) high index droplet, 2) excitation taper diameter alteration, and 3) FIB-milled microgroove scatterers. Such methods are shown to be promising in achieving single/few-moded lasing in such highly multimoded cavities.

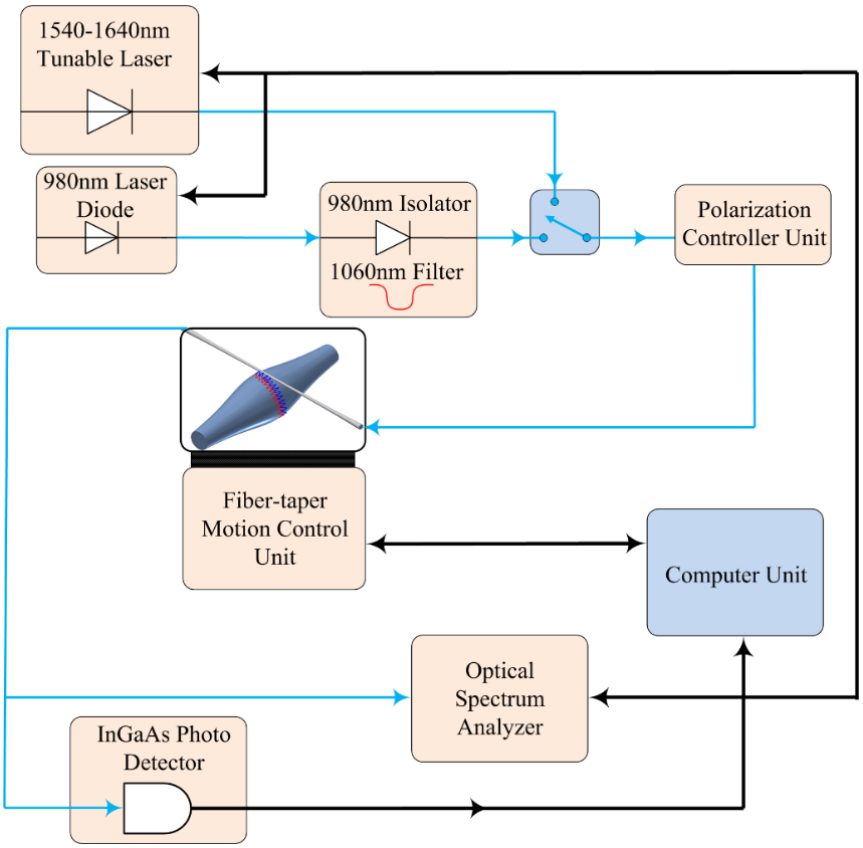

Figure 5-1 Passive and active characterisation setup used to characterize passive microbottle resonators and lasers.

5.2 Characterisation Setup and Fabrication of MBL

The schematic diagram of the experimental setup used for characterisation of active and passive microresonators is shown in Figure 5-1. A Tunable Laser Source (TLS) at 1540-1640nm wavelength range is used for passive characterisation. Alternatively, a fibre Bragg grating stabilized single mode Continuous Wave (CW) ~976nm Laser Diode (LD) is used in order to pump active devices. The output of the 976nm LD passes through a 980nm optical isolator in order to prevent coupling of any back-reflected pump light into the LD. The isolator naturally acts as an attenuator for longer wavelengths, such that at around 1060nm, a favourable-attenuation of about 15dB was measured. Then, the pump beam goes through a series of fiberized polarisation controllers, which provides a maximum of 15dB discrimination between the two orthogonal polarisations of the fibre modes. The polarisation controller unit is used in order to optimize the coupling condition of taper-microresonator system and/or perform polarisation-dependent measurements. The output of the polariser is spliced to a tapered fibre in order to evanescently couple light into the microresonator. Then, the

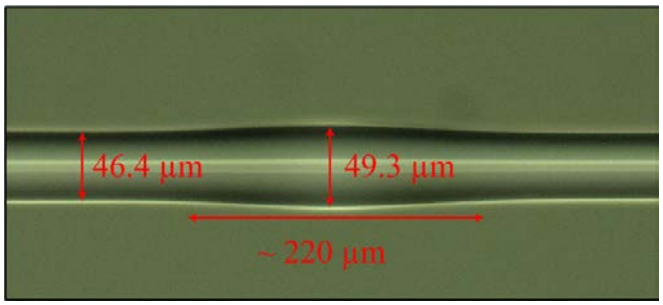

Figure 5-2 Optical image demonstrating the dimensions of the fabricated MBL.

out-coupled intra-cavity generated signal, the residual uncoupled and out-coupled pump are transmitted through the tapered fibre into an Optical Spectrum Analyser (OSA). An InGaAs Photo Detector (PD) is used to measure the transmitted power of the device at steady-state in 1550nm wavelength band by sweeping the TLS wavelength.

The tapered fibre is fabricated using a micro-heater tapering rig system [128] and is fixed on a U-shape stand on which the tapered fibre is taped from both sides. This prevents the taper from unwanted mechanical drifts. The U-shape stand is then fixed on a 3-axis translational stage providing a precise movement for the taper along the microresonator using electrical servomotors. Such system is schematically shown in Figure 5-1 as a block named "fibre-taper motion control unit".

I fabricated Microbottle resonator Lasers (MBLs) using a large core Yb^{3+}-doped silica fibre (provided by Heraeus Quarzglas GmbH). The initial outer diameter of the fibre is 240µm and the doped core has a diameter of 200µm. Using a micro-heater setup, the fibre diameter is tapered down to ~46µm resulting in an estimated active core diameter of ~39µm. This leaves the active fibre with an un-doped cladding thickness of ~3.5µm. MBLs are then fabricated using the "soften and compress" method discussed in Chapter 3. In this method, electrical arcs are applied onto the middle of a silica fibre, while the two stems are pressed towards each other. Mechanical pressure and thermal softening of the glass results in a bulge popping out in radial axis of the fibre which is called Microbottle Resonator (MBR).

Further thermal polishing of the resonator will provide smoother surface leading to higher Q-factor resonances, which may be beneficial in some applications. Figure 5-2 shows the fabricated MBL with stem fibre diameter of D_f = 46.4µm, maximum resonator diameter of D_c = 49.3µm and approximate neck-to-neck length of L = 220µm.

5.3 Passive and Active Response of MBL

First, the resonator is characterised at 1550nm wavelength range where the Yb^{3+} dopants exhibit no light absorption and emission. A tapered fibre with ~2µm waist diameter is coupled to the MBL from the top while touching the resonator surface. In order to have sufficient coupling, the resonator and tapered fibre air gap should be smaller than ~500nm owing to the fast decay of WGM evanescent field outside the resonator. This requires a complex and expensive arrangement to avoid any mechanical fluctuations. For instance, the tapered fibre can easily move around due to the air flowing in a lab environment. Any change in the air gap can significantly alter the coupling condition. A direct contact between the resonator and the tapered fibre can provide better mechanical stability and guarantee a fixed zero air gap. Having precise control on the resonator-taper air gap is extremely important in single (few)-moded resonators such as microtoroid and microring resonators in order to efficiently phase-match and couple to a specific mode. On the other hand, MBRs, due to their curved profile and extended geometry along the axial direction, have shown better flexibility

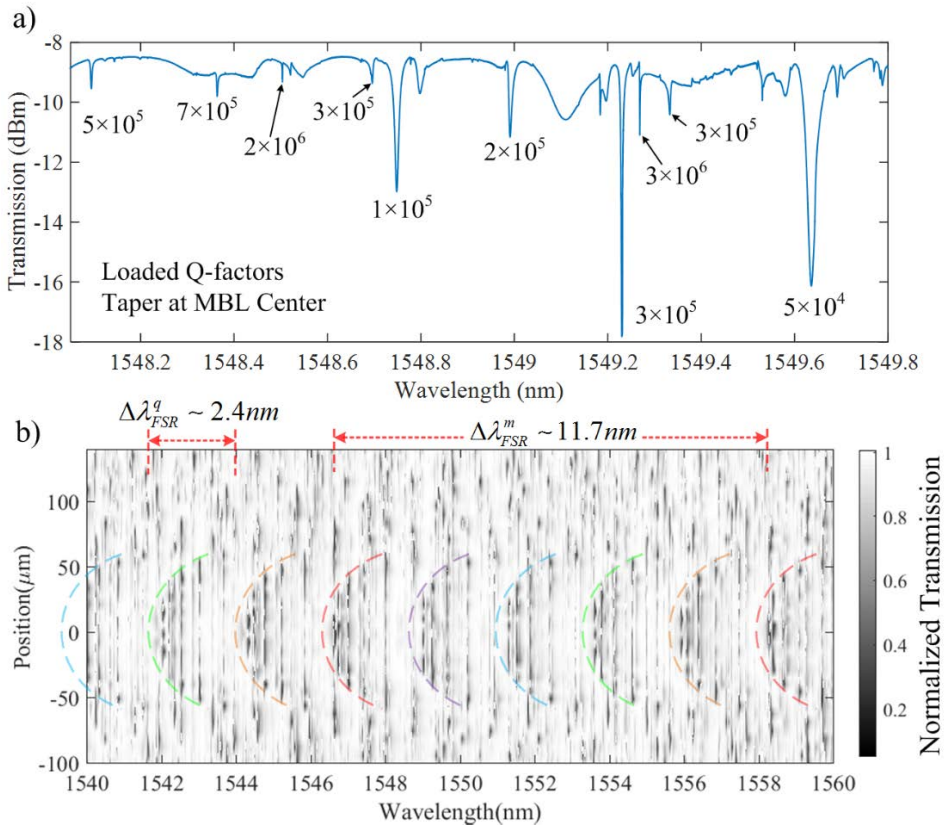

Figure 5-3 a) Close spectrum of fabricated MBR excited by 2µm-diameter taper from the centre showing various resonances with distinct total Q-factors, and b) spectra of MBR as function of taper position along the resonator axial axis exhibiting periodic excited groups of modes corresponding to azimuthal and axial FSRs.

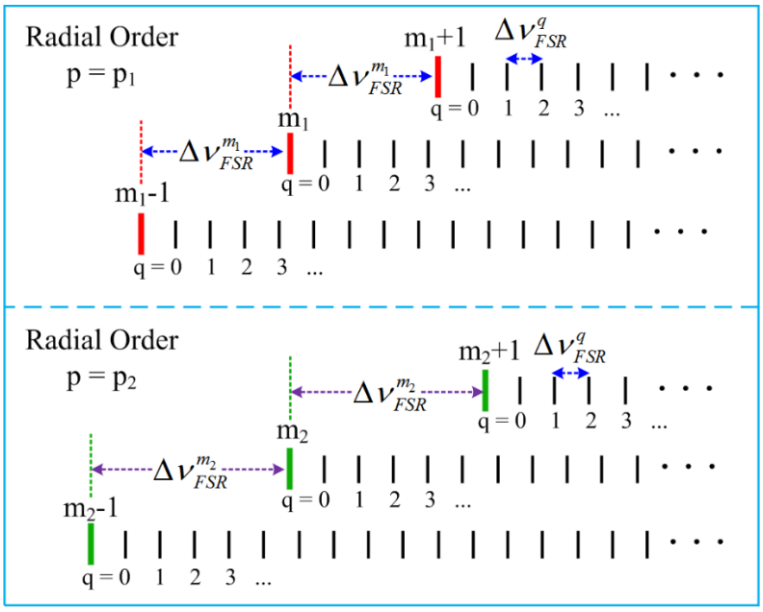

Figure 5-4 Schematic demonstration of typical MBR resonance spectrum showing the definition of axial and azimuthal FSRs for two different radial orders $p = p_1, p_2$ consisting of three arbitrary consecutive azimuthal orders.

in selective-excitation and collection of WGMs by only translating the tapered fibre along the resonator profile [117].

Figure 5-3 (a) plots a typical transmission spectrum of the fabricated MBR close to 1550nm band when the tapered fibre is placed on the centre of the resonator. The input signal power is set to -5dBm in order to lower the thermal effects due to the heat generated by the intra-cavity power build-up. WGMs with various total Q-factors are observed to be excited. Such spectrum shows that depending on the coupling condition, various resonances with desired Q can be excited. In this measurement, Q's between 5×10^4 and 3×10^6 are observed.

Furthermore, similar to [129, 130], in order to determine the order of the excited modes, transmission spectra of the resonator is measured along its profile. Figure 5-3 (b) shows the spectra of the resonator between 1540-1560nm wavelengths when the taper position is varied along the resonator profile. In order to understand such map it is important to distinguish between groups of eigenmodes supported by an MBR. Eigenfrequencies of an MBR are determined through three different quantum numbers indicated by m, p and q corresponding to azimuthal, radial and axial spatial directions of the MBR, respectively. The axial and azimuthal Free Spectral Ranges (FSRs) can be defined as $\Delta\nu^q_{FSR} = \nu_{m,p,q} - \nu_{m,p,q+1}$ and $\Delta\nu^m_{FSR} = \nu_{m,p,q} - \nu_{m+1,p,q}$. It is well-known that the eigenfrequencies along the axis exhibit the same frequency spacing, and $\Delta\nu^q_{FSR}$ is linearly dependent to the profile of the MBR ($\Delta\nu^q_{FSR} \propto \Delta k$). Δk determines the quasi-harmonic profile of the

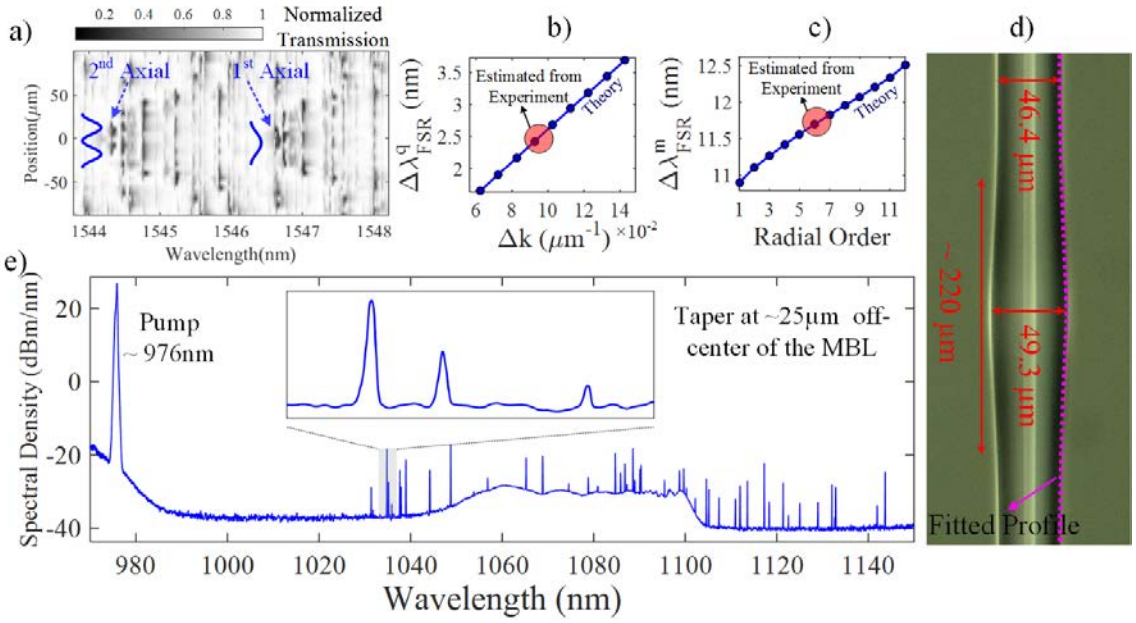

Figure 5-5 a) Detailed spectra of the fabricated MBR as function of taper position along the resonator profile showing excitation of various axial modes, b) calculated axial FSR of the MBR as function of curvature coefficient of the MBR profile, c) calculated azimuthal FSR as function of WGM radial order for $\Delta k = 0.0103\mu m^{-1}$, d) optical micrograph of the fabricated MBR and corresponding fitted harmonic profile (dotted line), and e) typical spectral density obtained by exciting MBL coupled to a tapered fibre at offset of ~25μm from the resonator centre (inset shows typical lasing peaks with various linewidths).

MBR radius such that $R(z) = R_c / \sqrt{1+(\Delta k z)^2}$ where R_c is the centre radius of the MBR and z determines the axial distance from MBR centre [13]. On the other hand, the azimuthal FSR ($\Delta\nu^m_{FSR}$) varies for different groups of radial order modes. Higher order radial modes show longer $\Delta\nu^m_{FSR}$ since they have smaller effective refractive index (n_{eff}) or equivalently smaller effective radius.

Figure 5-4 schematically illustrates the distribution of resonance modes of a typical MBR for two different radial orders of p_1 and p_2, for which three consecutive azimuthal orders are shown. Each group of modes with identical azimuthal order (m), is consisted of axial modes with same n_{eff} spaced with $\Delta\nu^q_{FSR}$ in frequency. The next group of modes with smaller azimuthal order ($m-1$) exhibit slightly smaller n_{eff}, and all are shifted by $\Delta\nu^m_{FSR}$.

The spectral map given in Figure 5-3 (b) exhibits these two different FSRs such that $\Delta\lambda^m_{FSR}$ = 11.7nm and $\Delta\lambda^q_{FSR}$ = 2.4nm, where $\Delta\lambda_{FSR}$ denotes the FSR in wavelength. The overlap between fibre mode and WGMs varies as the taper position moves along the resonator profile. The strength of the overlap follows the WGM intensity profile at the MBR-air boundary. Such characteristics can be used to visualize the axial order of the excited modes. Figure 5-5 (a) shows a close view of the spectra displaying the first and

second order axial excited modes. The higher order modes, which are spaced relatively close to these modes, correspond to higher order axial ones having smaller azimuthal order.

Furthermore, the axial and azimuthal FSRs can be used to accurately determine the radial order of the excited WGMs, as well as the profile of the MBR. An analytical solution to determine the resonance wavelengths of MBRs is given in [13]. Figure 5-5 (b) plots the calculated $\Delta\lambda_{FSR}^{q}$ as function of Δk for an MBR with $R_c = D_c/2 = 24.65\mu m$. The measured $\Delta\lambda_{FSR}^{q}$ from Figure 5-3 (b) is in good agreement with the calculated one from the analytical solution. Δk is estimated to be $\sim 0.010 \pm 0.002 \mu m^{-1}$ by fitting a harmonic curve to the MBR shown in the optical image in Figure 5-5 (d) (the inaccuracy in measurement is calculated from the diffraction limit of the microscope objective with NA = 0.25, and resolution of the captured image). There is slight deviation between the calculated and experimentally-measured $\Delta\lambda_{FSR}^{q}$ which is due to the difference between the considered refractive index of glass (n = 1.45) in calculations and the real value (which is not measured here due to experimental difficulties).

Moreover, Figure 5-5 (c) plots the calculated azimuthal FSR, $\Delta\lambda_{FSR}^{m}$, as a function of radial order of WGMs. The measured $\Delta\lambda_{FSR}^{m}$ indicates that radial order of the excited modes should mainly lay within the range of 5-7. This is preferred when the MBR is used as a laser cavity, since the Yb^{3+} dopants are distributed deeper inside the core of the active fibre of which the MBR is initially made.

Given the high Q-factor and small mode volume of such MBRs, they are favoured to realize narrow linewidth and low threshold microlasers. In order to characterize the MBR as a cavity laser, a CW 976nm pump LD with ~300mW power and ~300pm linewidth is launched through the tapered fibre. Figure 5-5 (e) shows the spectral density of the collected output light through the other side of the tapered fibre after coupling to the MBL at offset of ~25μm from the centre of the resonator. Pump mode guided by the fibre is evanescently coupled into WGM of the resonator, and excites the active dopants. Then the resulting spontaneously-emitted light from the active medium couples in WGM of the resonator, and is amplified through stimulated emission. Lasing lines corresponding to generated WGMs are observed in the emission range of Yb^{3+} between 1030-1150nm wavelengths. Any specific WGM within the dopants emission band can be excited depending on the total induced loss and/or gain for that specific mode. In the next sections, the required conditions and probability of lasing of WGMs in an Yb^{3+}-doped MBL is investigated.

5.4 MBL Characteristics

For the sake of experimental convenience, the axial centre of MBL is used as a reference point indicated by the maximum radius along the MBL. The fabricated MBL is first characterised by a 2μm-diameter tapered fibre placed close to the centre of the MBL. Figure 5-6 (a) shows the measured spectral density as function of launched pump power. The spectra shows several lasing WGM signals collected through the tapered fibre depending on the coupling condition. The power characteristics of the MBL as a function of the pump power through the taper fibre is plotted in Figure 5-6 (b). It should be noted that, for the sake of consistency through all experiments in this chapter, the pump power is the measured pump power at the output of the tapered fibre when uncoupled from the resonator. Output pump power of the taper is not nescessarilly equal to its input power since the taper is not adiabatic for the possible excited higher order modes. This value is always measured during each experiment. The output signal power is obtained by adding up the integrated power spectral density of all lasing peaks. The threshold launched pump power is ~4 mW as shown in Figure 5-6 (c). It should be noted that the lasing takes place in both forward and backward azimuthal directions,

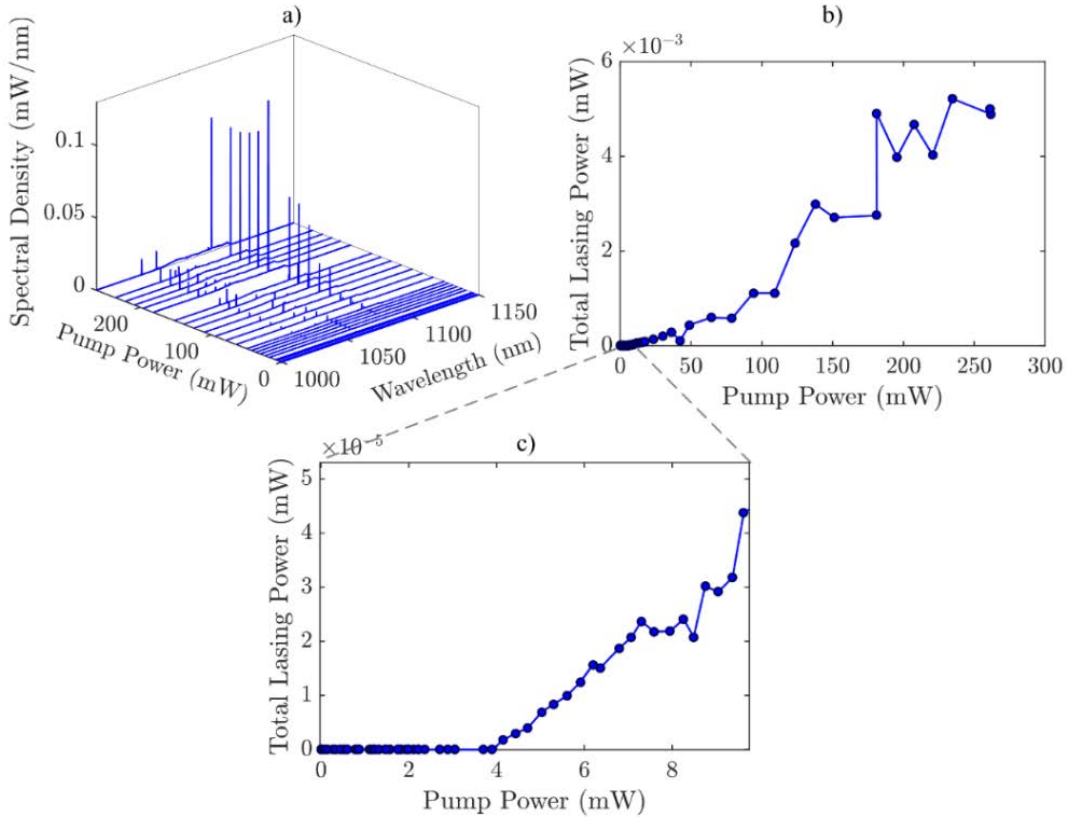

Figure 5-6 a) Spectral density, b) total lasing power characteristics, and c) close-to-threshold characteristics of MBL as function of the launched pump power measured at the tapered fibre output.

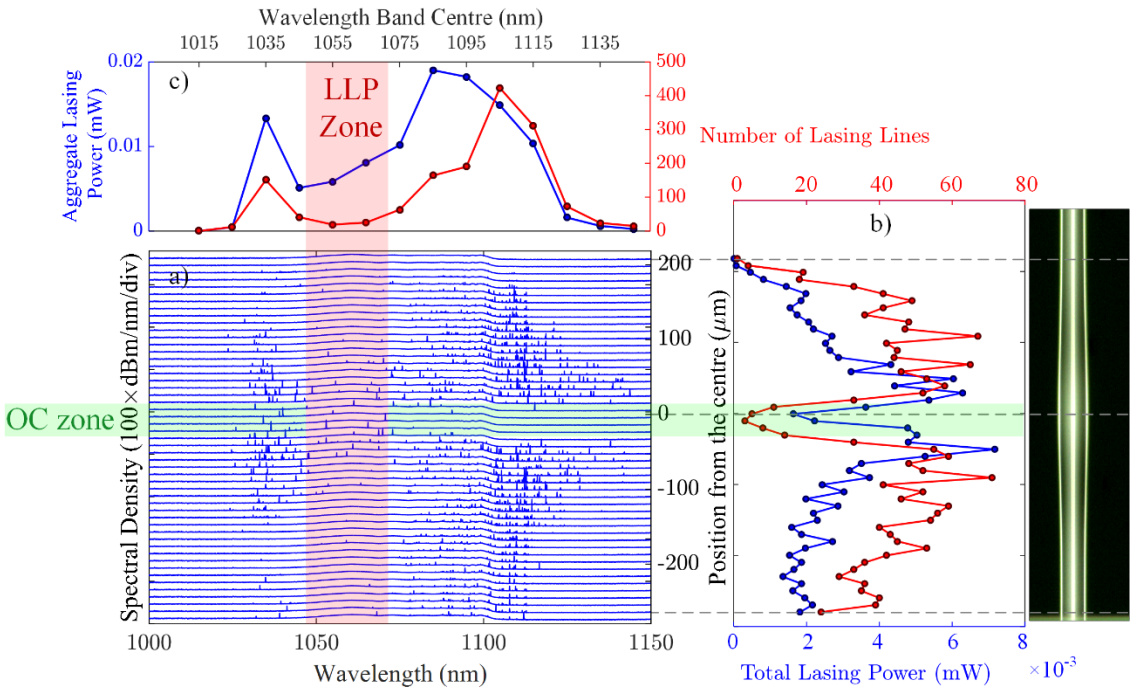

Figure 5-7 a) Spectral density of the collected light, b) total lasing power and number of lasing lines as function of excitation/collection taper position along the MBL profile, and c) aggregated lasing power and number of lasing lines across the spectrum for all positions integrated with steps of 10nm (The launched pump power is set on ~300mW).

and the spectra and total lasing power shown here correspond only to the forward direction.

As it was shown in Section 5.3 and demonstrated in [117], for passive MBRs, it is possible to selectively-couple to distinct WGMs by only translating the tapered fibre along the microresonator profile. Here, the same method is applied for the case of active MBR. Figure 5-7 (a) shows the spectral density evolution of the collected light obtained by varying the taper position along the MBL profile for a fixed launched pump power of ~300mW. Subsequently, the total lasing power and number of lasing lines are plotted in Figure 5-7 (b) as function of taper position from the centre of the MBL. Results show that the maximum signal power is collected when the excitation fibre is placed slightly off the centre and close to the edges of the bottle at ~±15μm, where the maximum number of modes is excited. At the vicinity of the MBL centre, few WGMs are excited/collected, and the total lasing power drops dramatically. I denote such region as the "Over-coupled (OC) zone", since due to the relatively-strong overlap between the fibre and resonator (pump and signal) modes (depending on the order of the mode), there is excessive loading loss on WGMs. This effect increases the lasing threshold, and lowers the intra-cavity pump and signal power of the WGMs. Moreover, as the taper fibre offset from the centre is further increased, the total lasing power drops gradually, while the number of the collected lasing lines fluctuates along the resonator profile for

a range of about 100μm away from the centre. At sufficiently large offsets from the centre, both the total lasing power and the number of lasing peaks vanish. The asymmetric response of the MBL with respect to the centre plotted in Figure 5-7 (b), stems from the imperfect and asymmetric profile of the fabricated MBL.

Furthermore, in order to quantify the lasing probability of the WGMs across the lasing spectra, lasing power and number of collected lasing lines are summed-up (integrated) over 10nm wavelength steps. Then, all the values are aggregated for all the various taper positions. Results are plotted in Figure 5-7 (c), where two peaks are observed for both aggregate lasing power and number of lasing lines at around 1030nm and 1100nm. This indicates that the Yb-lasing takes place mainly in the 1030nm or 1100nm wavelength bands. It is observed that 1040-1080nm band contains the lowest aggregate lasing power and number of lines. Such region is denoted as the "Low Lasing Probability (LLP) zone".

These two spectral and spatial lasing characteristics, corresponding to LLP and OC zones, are explored in more detail in the next two sub-sections.

Lasing probability spectra in Yb^{3+}-doped MBLs

I start with the gain spectra of Yb^{3+}-doped silica material in terms of the dopant population inversion percentage calculated from the absorption and emission cross-sections of Yb^{3+}. The gain/loss per meter for a total dopant concentration of $1.16\times10^{26}m^{-3}$ is plotted in Figure 5-8 (a) in which the gain spectra are plotted for inversion levels up to 100%. As shown in Figure 5-8 (b), the maximum achievable inversion percentage depends on the pumping wavelength, and pumping at 976nm can provide maximum 50% population inversion. On the other hand, the inversion level determines the lasing possibility across the spectrum. The wavelength where the peak of the gain happens as a function of inversion percentage is plotted in Figure 5-8 (c). There are three distinct wavelength bands where lasing is more likely: 1) 976nm band which requires inversions more than ~60%, 2) 1030nm lasing band corresponding to inversions between ~8%-60%, and 3) 1100nm lasing band which occurs at lower inversions than ~8%.

Although WGMs are forced to happen at discrete wavelengths due to the nature of MBRs, the cavity itself is not spectrally constrained. This is due to the relatively large dimensions, and hence complex and dense modal spectra of such cavities. In case of a standard MBL then, the operating wavelength is set by the amount of inversion inside the cavity. As the experimental results in Figure 5-7 show, the two lasing bands of

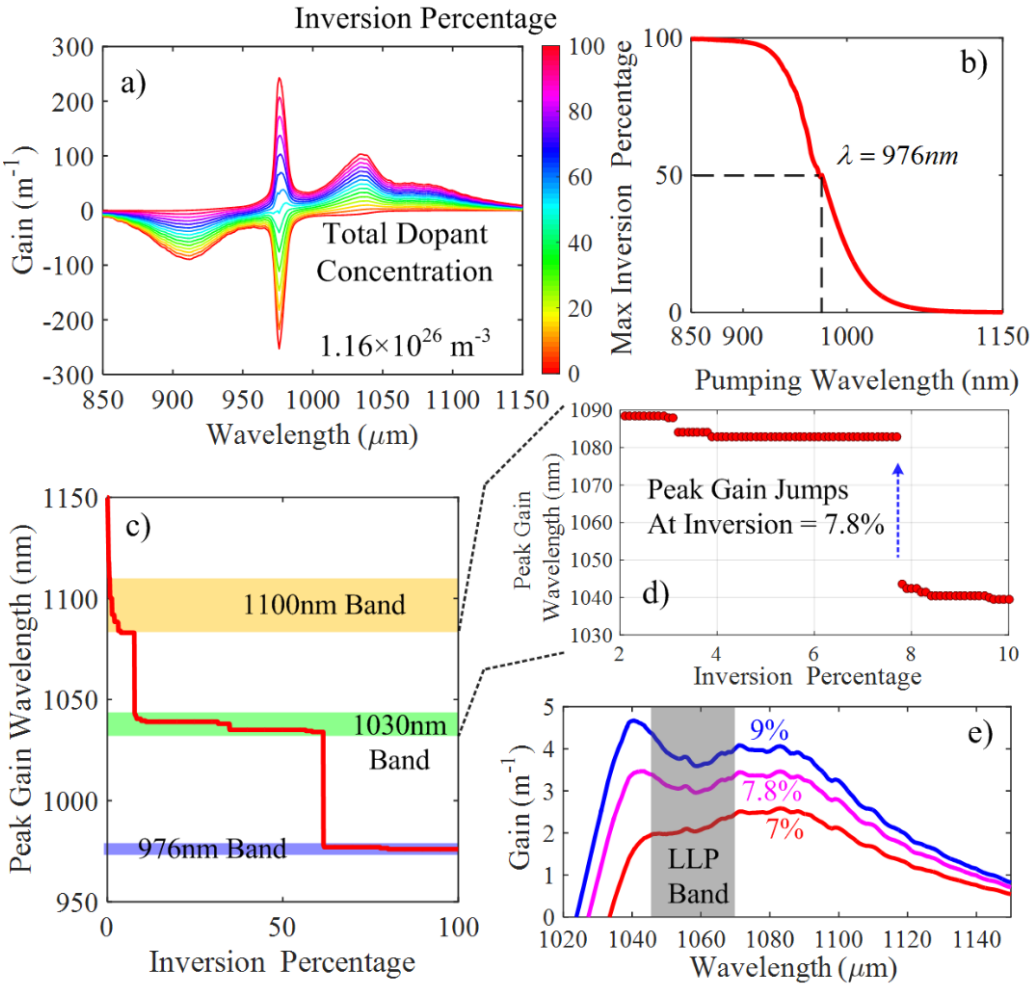

Figure 5-8 a) Gain per meter spectra of Silica:Yb^{3+} as function of inversion percentage for the experimentally-measured total dopant concentration, b) percentage of the maximum obtainable population inversion as function of pumping wavelength, c) wavelength of the peak gain as function of inversion percentage, d) sharp transition of peak gain wavelength between 1030nm and 1100nm lasing bands, and e) gain spectra at inversion values close to the critical value of 7.8 % showing the peak gain jumping from ~1090nm to 1040nm, and LLP zone at ~1050-1070 range induced by a trough in the gain spectra.

1030nm and 1100nm correspond to high and low inversion levels of Yb^{3+}, respectively. Figure 5-8 (d) shows the abrupt transition of the peak gain wavelength between such two lasing bands, which happens at inversions around 7.8%. The evolution of the gain spectra is plotted in Figure 5-8 (e) for three different inversions of lower (7%), very close (7.8%) and higher (9%) than the critical point. It is clear that the maximum gain jumps to shorter wavelength as the inversion increases. It should be noted that the LLP zone between 1040-1080nm wavelengths, where very small number of modes lase, corresponds to the displayed gain trough in Figure 5-8 (d).

Distribution and coupling of pump WGM

It is important to know the intra-cavity intensity of the pump mode. The pump intensity determines the population inversion level, and hence, sets the amount of the gain for a signal mode. It should be noted that several pump WGMs can be excited simultaneously in an MBL. This is due to the relatively wide bandwidth of the 976nm LD pumps (>300pm), and closely-spaced WGMs of an MBR.

Figure 5-9 (a) compares the number of the supported WGMs and the pump spectrum. For the sake of clarity, only the first four radial orders are considered. The experiments conducted in section 5.3 showed that higher order radial modes up to seventh (at 1550nm) are possible to be excited depending on the taper coupling condition. Figure 5-9 (a) demonstrates the large number of possible WGMs within the pump bandwidth. The internal built-up pump power will be a weighted combination of such modes based on their individual coupling coefficients. The measured coupled pump power from the tapered fibre into the resonator as a function of the taper offset from the centre of the resonator is plotted in Figure 5-9 (b). The coupled pump power is measured by taking the difference of the pump power through the taper when uncoupled and coupled to the resonator. It should be noted that the coupled pump power manifests both the on-

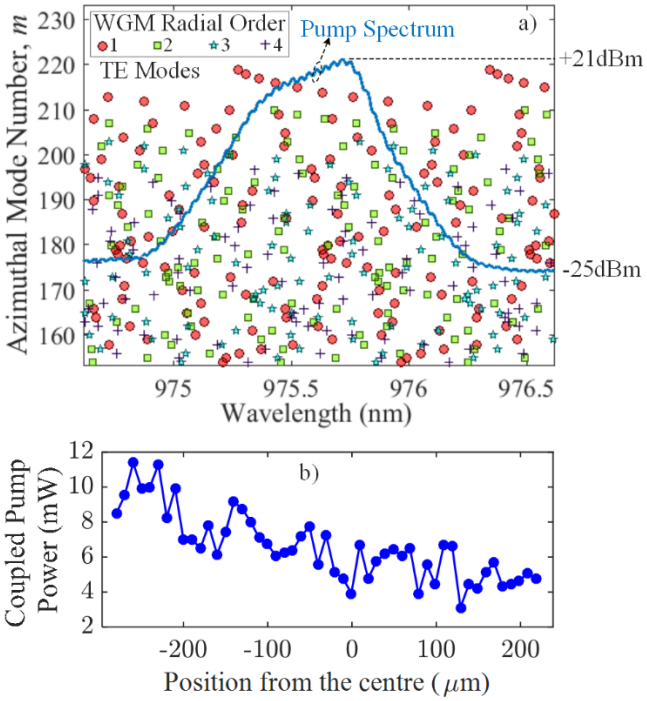

Figure 5-9 a) Comparison between the experimental pump spectra and the calculated WGM resonances (in terms of azimuthal mode number) within the spectral bandwidth of the pump, and b) calculated coupled (absorbed) pump power as a function of the tapered fibre offset from the resonator centre.

resonant and off-resonant power coupling to the MBL. The observed coupled (total resonator material + taper losses) pump power lies within 3-12mW range and generally fluctuates with ±1mW deviation along the resonator profile. Such non-uniform pattern of the absorbed pump power shows coupling to various pump WGMs due to the large bandwidth of the input pump mode(s).

Figure 5-9 (a) shows the calculated internal power of the individual WGMs as function the taper position along the resonator profile (the calculation method is given in previous chapter). Here, without loss of generality, the first 30 axial orders of the first radial mode around 976nm wavelength are considered to be excited, and the intrinsic Q-factor ($Q_{(0)p}$) for all modes is fixed at 10^6. The input pump power for each WGM is 1mW and simulations are done independently for each single WGM. As the results show, modal powers vary depending on the spatial distribution of each WGM. Coupling coefficient and phase-matching between fibre and resonator modes depend on the taper fibre position along the resonator profile. Thus, by translating the taper fibre along the MBR, a specific WGM can operate in one of the 1) under-coupling ($Q_0 < Q_{ext}$), 2) critical-coupling ($Q_0 = Q_{ext}$) or 3) over-coupling ($Q_{ext} < Q_0$) regimes. Here, $Q_{ext} = m\pi / |\kappa_{fc}|^2$ where κ_{fc} is the cavity out-coupling coefficient to the fibre mode, and is related to both modal

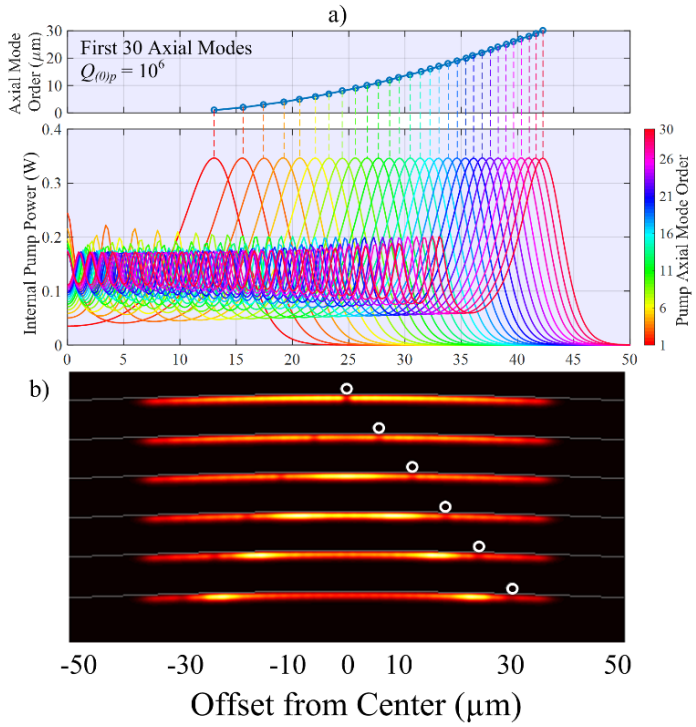

Figure 5-10 a) Bottom: calculated WGM pump power as a function of taper offset from the centre for passive MBR considering the first 30 axial modes around 976nm wavelength for input pump power of 1mW to each WGM, and top: relation between the position of the taper and the WGM order which is critically coupled, and b) normalized total pump WGM intensity calculated by summing-up weighted intensities of modes for various taper positions along the MBR profile.

overlap integral and phase mismatching ($\beta_f - \beta_{wgm}$). Here, the critical coupling for all the modes is satisfied beyond the turning point where the WGM field has maximum intensity. The maximum internal power along the resonator profile corresponds to the critical coupling condition. Beyond this point, the mode is under-coupled as the coupling coefficient is very small due to small modal overlap. Close to the centre of the resonator, the WGMs are generally over-coupled owing to the excessive power leakage into the fibre mode (greater out-coupling coefficient).

Figure 5-9 (b) illustrates the calculated total intensity distribution of the excited pump modes for various taper fibre positions along the MBR. The results are obtained by summing up the individual WGM intensities weighted by the mode power calculated at each taper position. It should be noted that, at small offsets from the MBR centre, the intensity at the centre is high. This is due to the coupling to lower order modes which have smaller mode areas (and volume). This configuration is preferred for lasing at shorter wavelengths (i.e. 1030nm) due to higher pump intensities and larger inversions. Moreover, as the taper position is further translated to longer offsets, critical-coupling to higher order modes takes place. At the same time, lower order modes are highly under-coupled. Consequently, at large offsets only higher order pump modes are excited which maintain a lower total internal intensity, and hence, provide lower inversions. This is preferred for lasing at longer wavelengths (i.e. 1100nm).

Let us reconsider the measured spectral density shown previously in Figure 5-7 (a). In order to clearly visualize the lasing lines along the spectra, the peak power intensity of each lasing line in terms of the line wavelength and position of the excitation-tapered

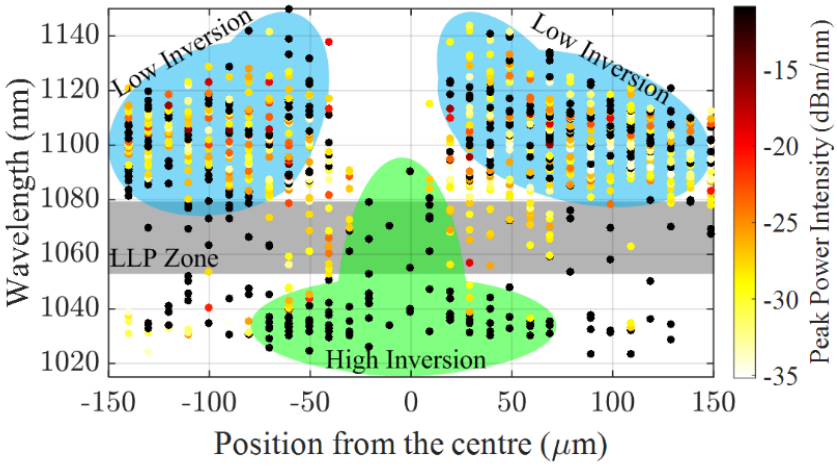

Figure 5-11 Measured power intensity of each lasing line as function of lasing wavelength and the taper position from the centre showing various selectively-accessible signal wavelengths by setting the inversion level defined by the pumping WGM.

fibre from the centre of the MBL, is plotted in Figure 5-10. It is clearly observed that, at relatively small offsets from the MBL centre, only the 1030nm lasing band is accessible due to the high population inversion level provided by excitation of lower order pump modes. While, at larger offsets most of the lasing lines take place about 1100nm band due to lower pump intensity (greater mode volume), and thus, retaining lower population inversions.

Internal generation and output collection of signal in Yb^{3+}-doped MBLs

Thus far, in this section, effects primarily due to excitation and spatial extend of the pump WGMs are investigated. The required upper-state population inversion in order to provide enough gain for different orders of signal WGMs varies depending on total passive losses. Recalling from Chapter 4, the required normalized upper-state population inversion, at and above threshold, is given by $\bar{N}_2 = (\alpha_s + 2\pi n_s(1/Q_{0(s)} + 1/Q_{ext(s)})/\lambda_s)/(\alpha_s + g_s^*)$, where α_S and g_S^* are the Giles parameters, respectively, indicating the total absorption and emission of the signal light. n_s and λ_s indicate the refractive index and wavelength of the signal, respectively. Then, gain of the signal is related to inversion such that $g_s = \bar{N}_2(\alpha_s + g_s^*) - \alpha_s$, and the Yb^{3+}-induced loss on the pump can be evaluated by $l_p = \alpha_p - \bar{N}_2(\alpha_p + g_p^*)$. Consequently, given the intrinsic Q of the pump mode ($Q_{0(p)}$), and the coupling conditions, given by the external Q's, the total internal pump power can be evaluated from the coupling relations of the fibre-resonator system. Then, the intra-cavity signal power is determined by the rate equation, at steady state, which relates the pump and the signal powers.

Figure 5-11 (a) demonstrates the calculated intensity profile for the pump axial order of q_p = 7 and signal axial orders of q_s = 1-8. Since the intensity of a WGM is highest at the turning points and decays very fast beyond such point, it is reasonable to assume that only those signals which are spatially well-contained within the excited pump WGM volume will be generated. As mentioned previously, the pump axial mode is set by the coupling condition determined by the offset of the tapered fibre from the centre of the resonator. Thus, the pump WGM order defines the spatial distribution of the inverted medium. The internal and output signal powers for the first 30 axial orders of the signal WGMs at a wavelength band around 1030nm, as a function of the taper offset, are plotted in Figure 5-11 (b) and (c), respectively. The input pump power for each WGM is 1mW, and both pump and signal intrinsic Q's are fixed at 10^6. Calculations are performed for fixed pump axial orders of 1, 6, 11, 16, 21, 26, and 30. It should be noted that, for a specific pump only signals with axial orders smaller or equal

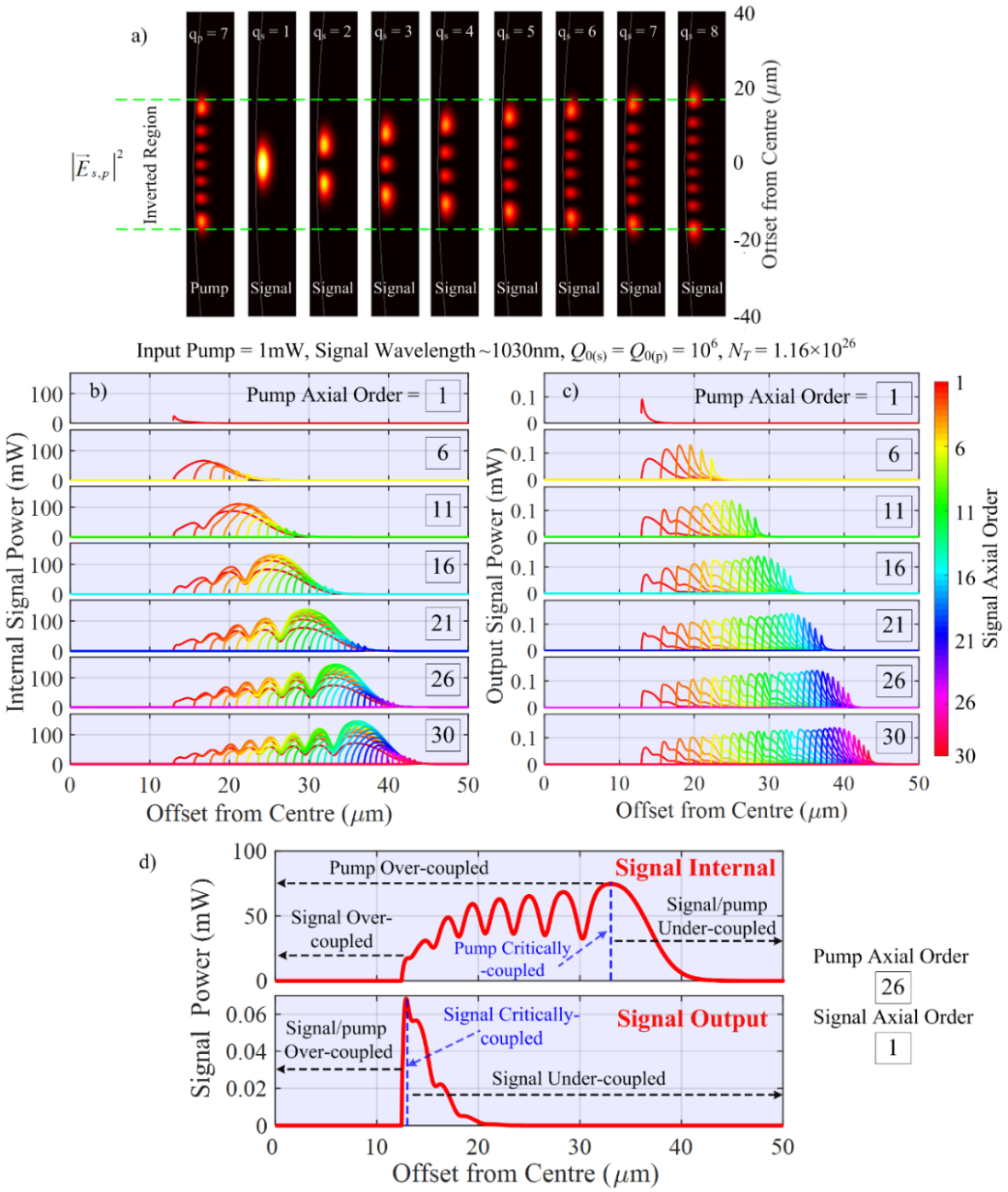

Figure 5-12 a) Intensity profile of excited pump WGM as an example showing the corresponding possible generated signals with various axial orders, b) internal, and c) output powers of all considered signal WGMs as function of tapered fibre offset from the resonator centre when various fixed pump modes are excited, and d) the internal and output signal powers in terms of taper offset for excited pump and signal axial orders of $q_p = 26$ and $q_s = 1$, respectively, as an example showing the existence of unobserved internal WGMs.

to the pump order are considered. For the sake of simplicity, it is assumed that always one pump mode and one signal mode are operating, and each signal mode power is calculated independently from the other ones. Therefore, signal modal overlap and modal competition are ignored.

No lasing is possible for offsets smaller than ~12μm for the considered WGMs, since both signal and pump modes are highly over-coupled and the total Q factors are

excessively low. On the other hand, as the tapered fibre is translated to larger offsets, internal and out-coupled powers of a specific signal do not follow the same trends. The output signal power is always maximum where the critical-coupling condition is satisfied (at least for the first radial order WGMs considered in this modelling). The internal signal power, on the other hand, varies depending on both the offset-dependent coupling efficiency and pump power. The signal modes can build-up a significant amount of intra-cavity power suitable for light generation through Raman and Four Wave Mixing (FWM) processes. Figure 5-11 (d) plots an example in which the 26^{th} order of pump excited and the fundamental signal mode is considered to be generated. Results reveal that at large taper offsets although zero output power is observed, there is strong internal signal power, for the lower axial order modes. Such modes do not contribute to the total output power and affect the laser performance through Spatial Hole Burning (SBH) and modal competition.

Due to multimode lasing in MBLs, depending on the Q factor of the resonator, and internal powers, SHB can practically occur. The spatially-distributed saturated population inversion along the resonator profile, changes the net gain seen by each signal WGM. The effect of gain saturation and SHB is more for lower axial order WGMs due to smaller mode volume, and hence, higher intensity, which can limit the efficiency of lasing modes. On the other hand, spatially-modulated gain imposed by higher order pump WGMs, induces a partially-unpumped medium, and thus, reabsorption of specific signal WGMs. This effect can be beneficial in reduction of lasing lines [131, 132]. The nonlinear effect of SBH in MBLs can be reduced by either increasing the dopant concentration [132], or placing the coupled taper at larger offsets from the resonator centre (inducing coupling to higher order and less intense WGMs) with the expense of increasing the number of lasing lines and hence a more instable laser. It should be noted that SHB happens in both axial and azimuthal directions due to standing wave nature of WGMs. Such effects are neglected in my theoretical analyses in order to clearly model the effects of passive losses, dopant concentration, lasing wavelength, etc on the MBL characteristics. However, incorporation of spatially-distributed population inversion and SHB can be an interesting subject for future studies in WGM lasers.

Analysis of multimode laser cavities is a complex task. However, by averaging the power of all possible combinations of excited pump and signal WGMs, a useful and simple understanding of the multimode lasing behaviour in an MBL can be provided. Figure 5-12 (a) shows the averaged output signal power of all the possible signal-pump mode pairs as function of taper offset from the centre. The total output power is calculated for four different lasing wavelength bands at constant dopant concentration

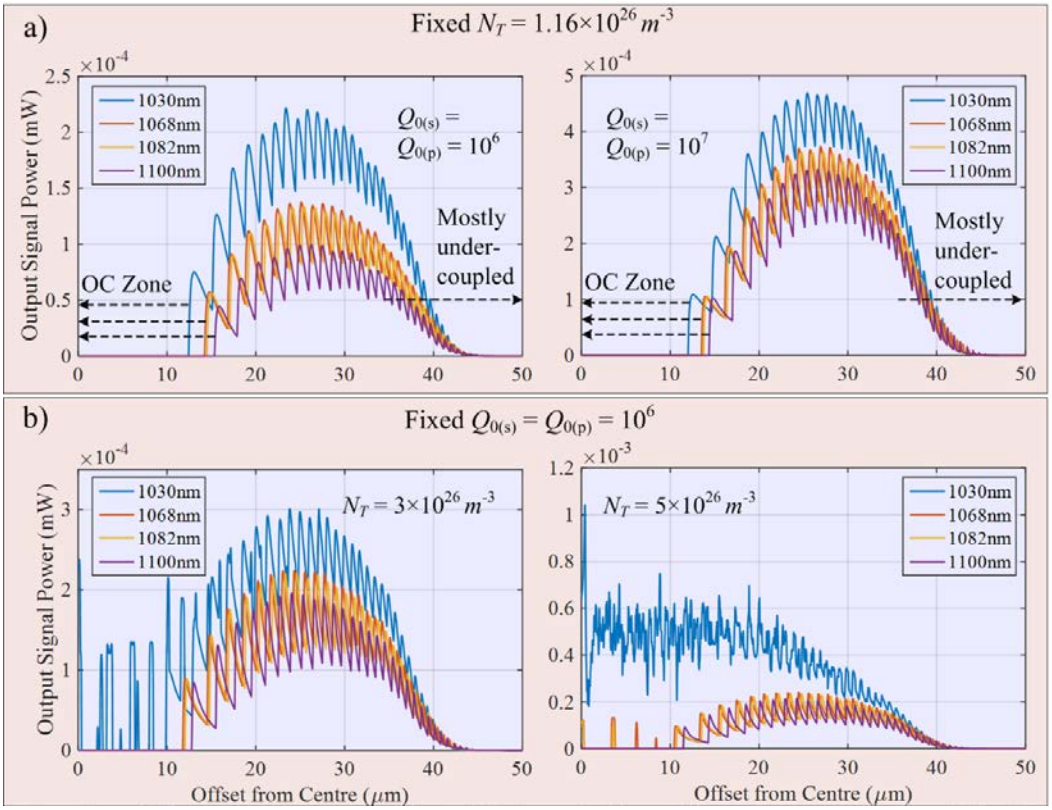

Figure 5-13 Averaged output signal power of all possible signal-pump mode pairs at various signal wavelength bands as function of taper offset from the centre a) at fixed dopant concentration of $1.16\times10^{26}m^{-3}$ for intrinsic Q's of 10^6 and 10^7, and b) at fixed intrinsic Q's of 10^6 for dopant concentration of $3\times10^{26}m^{-3}$ and $5\times10^{26}m^{-3}$.

of $1.16\times10^{26}m^{-3}$. The results show a serrated total power (observed in experiments as well – see Figure 5-7 (b)) varying as the taper offsets from the centre, due to out-coupling of various axial modes of different axial order. Moreover, as the lasing wavelength increases the over-coupled (OC) zone enlarges and the total power drops, due to Yb^{3+}-gain reduction.

On the other hand, as shown in Figure 5-12 (a), the OC zone can be slightly narrowed by increasing the intrinsic pump and signal Q's. Further improving the cavity quality factors, increases the total power, as well. The total output signal power drops at large offsets. Additionally, the OC zone can be further narrowed by increasing the dopant concentration. Figure 5-12 (b) shows the averaged signal power as function of taper offset for various lasing wavelength bands at fixed pump and signal intrinsic Q's of 10^6 for $N_T = 3\times10^{26}m^{-3}$ and $5\times10^{26}m^{-3}$. Results show that, generally, increasing the dopant concentration increases the gain, and hence, the total loss for a specific signal lowers allowing close-to-critical-coupling operation. 1030nm shows to be the most affected band due to large gain of Yb^{3+} at this wavelength comparing to longer wavelengths (i.e. 1100nm).

Threshold and efficiency

The experimental output power characteristics of the MBL as a function of launched pump power through the tapered fibre coupled to the resonator for various taper offsets from the resonator centre, is plotted in Figure 5-13 (a). The total lasing power is obtained by adding up the integrated power from spectral density for all lasing peaks. The corresponding threshold pump power and slope efficiency are shown in Figure 5-13 (b). These results reveal that, at offsets close to the centre of MBL (<25μm), the threshold pump power is high (~19.6mW). This is due to the excessive loss on both pump and signal WGMs which is induced by the over-coupling condition. Further, the threshold stays around its minimum value of ~1.7-3mW for offsets between ~25μm-130μm. The slope efficiency does not fluctuate significantly when the taper offset is below 130μm. Figure 5-13 (c) plots the spectral density of the collected light for four different taper offsets: 1) very close to centre (~1μm), 2) just off-centre (~26μm), 3) close to neck-point (74μm), and 4) large offsets (197μm). The spectra are plotted for pump powers close to threshold (P_{th}) and increased by steps of 4mW. At offsets very close to centre, only few relatively-high peak power lasing modes are observed. As the tapered fibre is positioned at 26μm and 74μm, the number of excited modes is clearly increased, while the peak power of lasing lines is dropped.

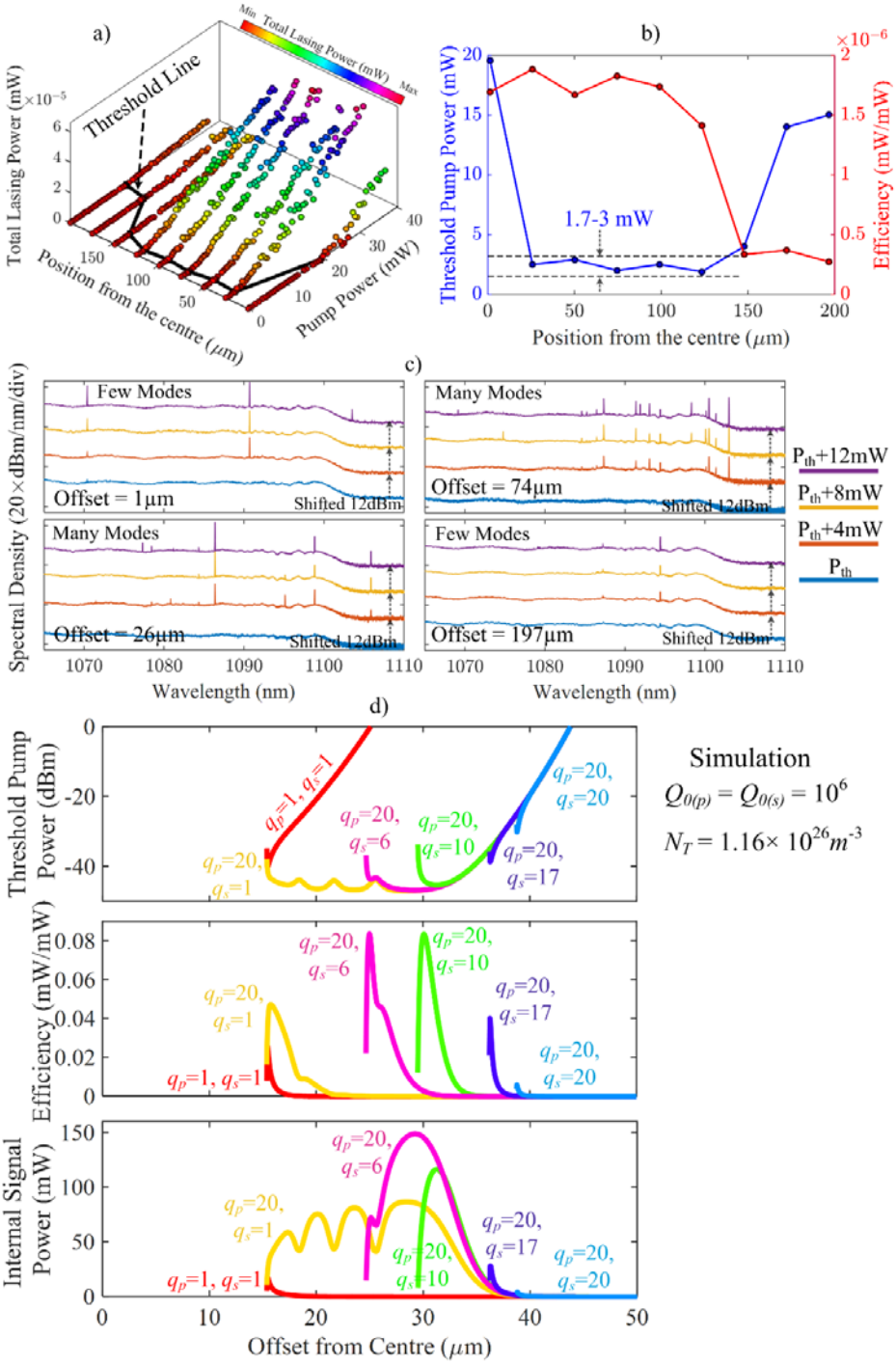

Figure 5-14 a) Experimental light-light curve of MBL as function of taper offset from the resonator centre, b) threshold pump power and slope efficiency as function of taper offset obtained from the light-light characteristics of the MBL, and c) spectral density of MBL for taper positioned at various offsets for pump powers corresponding to threshold value and linearly increased ones, showing position-dependent threshold and efficiency of lasing WGMs.

In order to elucidate this behaviour, the threshold pump power, slope efficiency and internal signal power for few representative WGMs are theoretically calculated. Results are plotted in Figure 5-13 (d) as a function of taper offset for the first radial-order pump-signal pairs of axial orders of

(q_p , q_s) = (1,1), (20,1), (20,6), (20,10), (20,17), (20,20). As previously discussed, no lasing takes place at offsets below ~15μm due to mode over-coupling. Considering the fundamental pump and signal modes (q_p = q_s = 1), at the critical-coupling point, the threshold and efficiency become significantly low and high, respectively. Next, for instance, a pump mode with q_p = 20 is assumed to be excited. Such relatively high-order pump mode can be excited with different strengths by positioning the taper fibre at both small and large offsets. As calculations show in Figure 5-13 (d), the threshold pump power at small offsets (over the OC zone) is very low for small signal orders (i.e. q_s = 1). This is due to the negligible external loading and large signal power built-up inside the resonator (see internal signal power in Figure 5-13 (d)), and/or small mode volume of such WGMs. In addition, the efficiency is always maximum at the critical-coupling point of the signal modes. As the signal order increases, the over-coupling zone increases, and lasing starts at slightly below the critical-coupling offset. The threshold suddenly drops, as the offset increases to values below the critical coupling. On the other hand, the threshold increases and efficiency decreases gradually for very large offsets, due to highly under-coupled signal and pump modes.

From the experimental point of view, the likelihood of critically-coupling to one or more WGMs increases as the tapered fibre moves to larger offsets. Therefore, the lasing threshold is always low and the cumulative signal power high at off-centre taper positions. Although the collected signal peak powers at large offsets are lower compared to small offsets, the overall slope efficiency is maintained high, due to the increased number of lasing lines.

5.5 Spectral Cleaning of MBL

MBRs support highly nondegenerate modes, which results in extremely dense spectra. Although such dense spectrum is preferred in CQED studies [133] where a cavity-resonance is required to coincide with a specific frequency, it can be a disadvantage in sensors where a well-defined resonance with large tunability range is preferred. In lasers, given adequate pump-signal modal overlap, several signal modes can be simultaneously generated. The multimode lasing in general results in modal competition and lasing instability and deteriorates the performance of the laser. MBLs are intrinsically multimode due to of the large number of spectrally and spatially separated WGMs, which originated from the highly prolate shape of the resonator. Different axial order WGMs in MBRs are distributed spatially across the resonator profile. Such characteristics can be exploited to filter out modes with different axial

mode number. Few methods have been employed to clean-up the spectra of passive resonators including micro-droplets [12], high index prisms [134] and micro-milling [121]. High index micro-droplets are in liquid form and can drift along the resonator surface with time. I have also seen considerable evaporation of liquid after few hours of operation. High index prisms suffer from sensitivity to mechanical vibrations and other instabilities and are difficult to utilize in practical systems. To date, Focussed Ion Beam (FIB) milling of microgrooves on the surface of an MBR is the most promising method to select WGMs in microresonators [121]. Such approach shows improvement in controllability, efficiency and reproducibility of mode reduction in microresonators. In this section, I employ an improved variation of the high index micro-droplet method, as well as fabrication of FIB-milled micro-scatterers on MBLs. Furthermore, effects of the microtaper diameter on excitation/collection of lasing WGMs are also studied.

Mode Reduction Using High Index Scatterer

The high index liquid droplet employed in [135] is chosen from a liquid polymer material. As previously discussed, such materials are mechanically and thermally unstable. Here, I use a positive UV-cure photoresist (MICROPOSIT S1813) with refractive index of ~1.6. A droplet of the high index photoresist is placed on the edge of the MBL and is dragged towards the centre using the tip of another tapered fibre with ~15μm diameter. Afterwards, the droplet is exposed to UV light.

Figure 5-14 (a) shows the photoresist on top of the device which leaves an uncovered length of ~50μm from the centre of the resonator. A tapered fibre with 2μm diameter is placed close to the centre at an offset of ~12μm. The spectra of the collected light as function of launched pump power is plotted in Figure 5-14 (b). A single lasing mode is observed at wavelength of ~1028.3nm. The integrated signal power increases almost linearly as the pump power increases. Figure 5-14 (c) shows the input-output characteristics of the MBL. A more detailed view of the MBL characteristics is plotted in Figure 5-14 (d) showing an observed threshold pump power of ~21mW. Due to significant decrease in generated lasing modes, the total lasing power shows significant improvement in the MBL performance in terms of output power fluctuation.

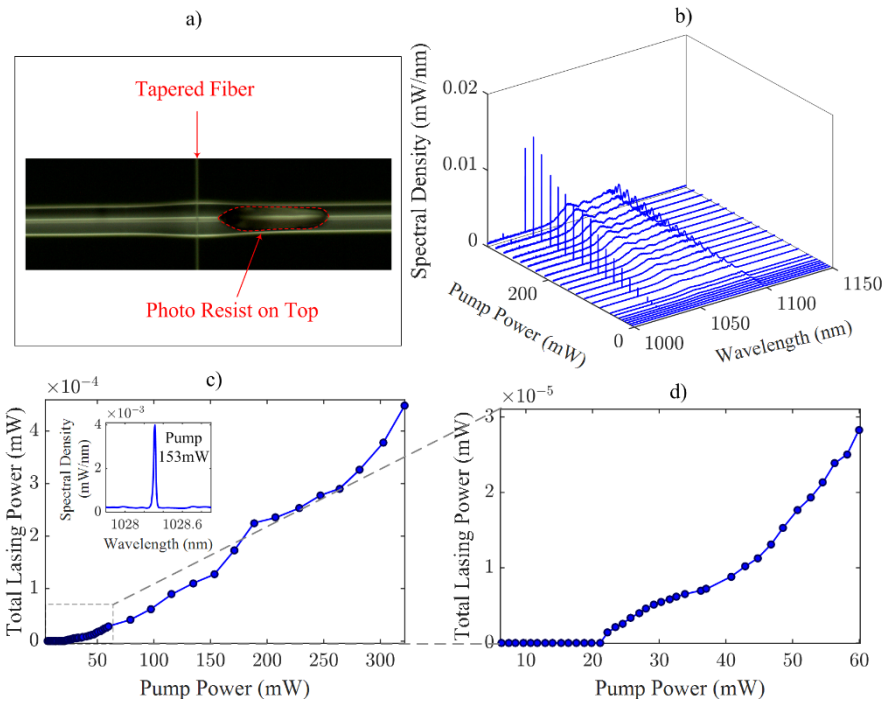

Figure 5-15 a) Optical micrograph of cleaned-up MBL with photoresist on top, b) spectra, c) characteristics curve of MBL coupled to tapered fibre at ~12µm offset as function of pump power (inset shows the lasing signal spectrum at 153mW input pump power), and d) close view of the MBL characteristics showing threshold pump power of ~21µm.

Furthermore, Figure 5-15 (a) plots the spectral density map of the cleaned-up MBL as function of the tapered fibre position along the resonator. The corresponding total lasing power and number of lasing lines are displayed in Figure 5-15 (b). Similar to normal MBL on which there is no induced external loss mechanism, MBL with photoresist on top shows an OC zone within ~±12µm offset range around the centre. The spectra of the MBL, shows a clear symmetric response around the centre of the resonator. Since the higher axial-order modes spatially expand to large offsets, they have significant overlap with the high index photoresist. Hence, such modes exhibit very small Q factors due to large scattering by the large index difference between silica and photoresist. Therefore at very large offsets (>50µm) no lasing WGM is observed. It should be noted that due to low Q of the pump mode when the taper is placed at large offsets, the inversion level is very low. Hence, the signal WGMs, not only retain a very small intrinsic Q, but also, experience a low gain.

Furthermore, the aggregate lasing power and total number of lasing lines for spectra corresponding to all various taper offsets, is plotted in Figure 5-15 (c). Since the cleaned-up MBL is limited to lase only at offsets close to the centre (~±50µm), the excited pump WGMs sustain small axial mode orders. Thus, the upper-state population inversion level is high owing to small mode volume of the pump WGMs. As earlier demonstrated

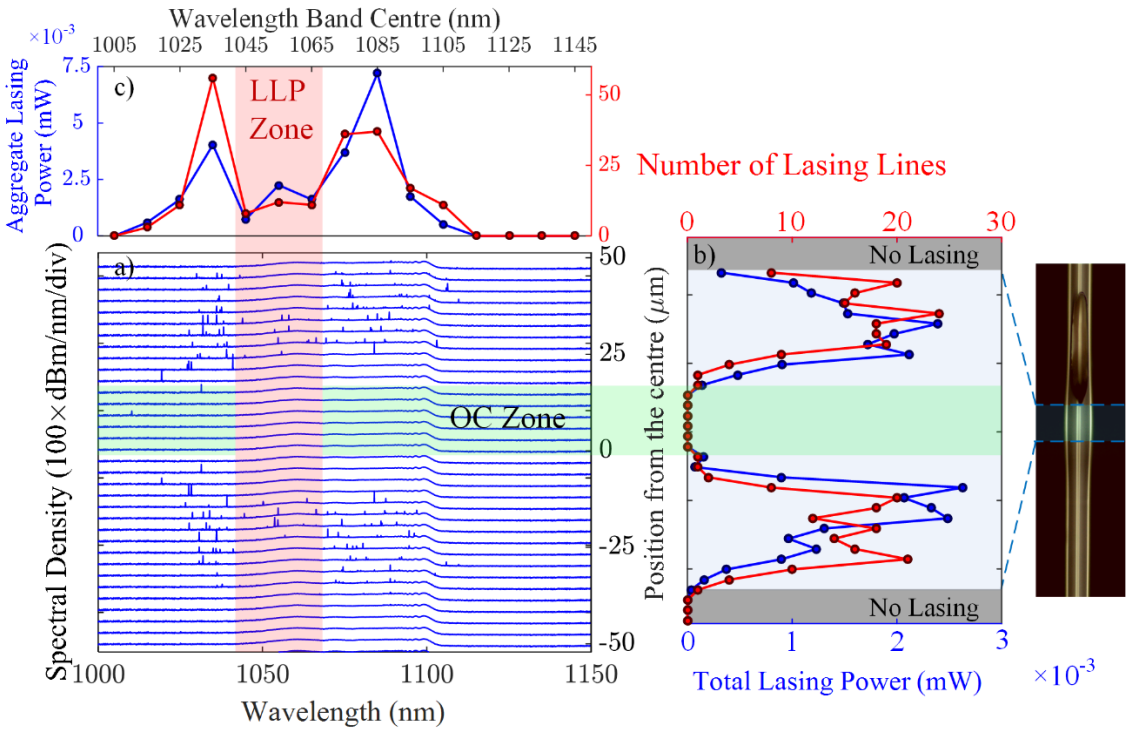

Figure 5-16 a) Spectral density of the collected light, b) total lasing power and number of lasing lines as function of excitation/collection taper position along the MBL with high-index photoresist on top, and c) corresponding aggregated lasing power and number of lasing lines across the spectrum for all positions integrated with steps of 10nm (The launched pump power is set on ~300mW).

in Figure 5-8 (c), the peak gain wavelength of Yb^{3+} at high inversion levels appears at 1030nm wavelength band. As demonstrated in Figure 5-15 (a), lasing starts at wavelengths ~1030nm as the taper offset increases from zero offsets. This is due to critically-coupling of pump WGMs with very small axial orders providing high inversions. Further increasing the taper offset, increases the probability of coupling to larger order axial pump modes with lower intensities. Hence the inversion level decreases and lasing is also enabled for wavelengths about 1090nm at very large taper offsets within the ~±30-50μm range. The low lasing probability (LLP) zone corresponds to the sharp jump in the peak gain wavelength from 1030nm to 1080nm as the inversion drops to values lower than 7.8% of its maximum.

It is worth mentioning that no WGM is observed to lase for taper offsets below ~12μm in the cleaned-up MBL, while in a normal MBL, few lasing lines are excited/collected in the centre. Both the total lasing power and number of lasing lines for normal and cleaned-up MBLs, are plotted in Figure 5-16 (a). The limited number of lasing modes at the centre of a normal MBL likely correspond to higher order radial modes which exhibit higher loaded Q-factors due to small resonator-fibre modal overlap. Figure 5-16 (b) shows a comparison between few of the measured spectra corresponding to taper offsets for both normal and cleaned-up MBLs.

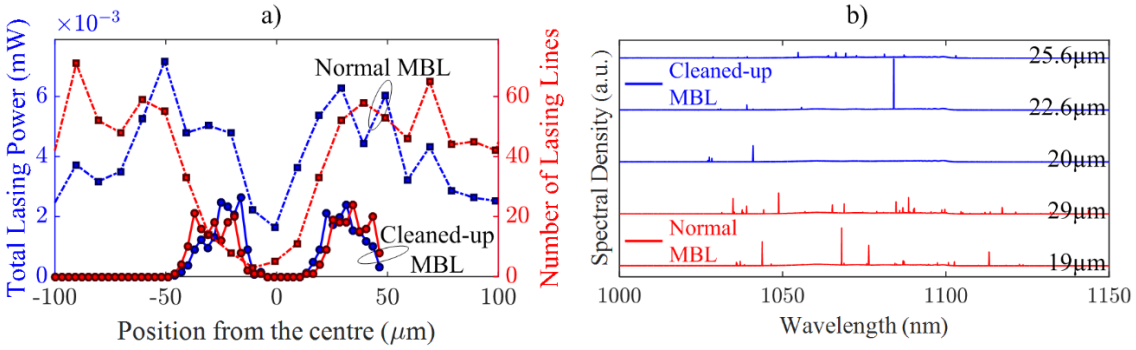

Figure 5-17 a) Comparison of normal and cleaned-up MBL in terms of the total lasing power and the number of observed lasing lines, and b) examples of spectra of normal and cleaned up MBL with excitation taper at offsets close to the centre.

Such well-defined lasing lines strongly demonstrate the high potential of cleaned-up MBL when compared to the normal one, in selective excitation/collection of lasing lines by only varying the taper offset.

Finally, the lasing characteristics of the cleaned-up MBL at various taper offsets are plotted in Figure 5-17 (a). The corresponding threshold launched pump power and efficiency as function of taper position are shown in Figure 5-17 (b). The results show that, for central excitation the efficiency is zero since no signal WGM is observed at the output. This is due to the extremely high threshold pump power at the centre, owing to the low total Q of pump and signal modes. The over-coupling can be overcome by either coupling to WGMs with very high axial orders, or offsetting the tapered fibre from the centre. The first condition cannot be satisfied, since such modes exhibit very low Q in presence of the high index droplet. Hence, these modes produce very low internal powers. Offsetting the tapered fibre towards the resonator sides provides critical

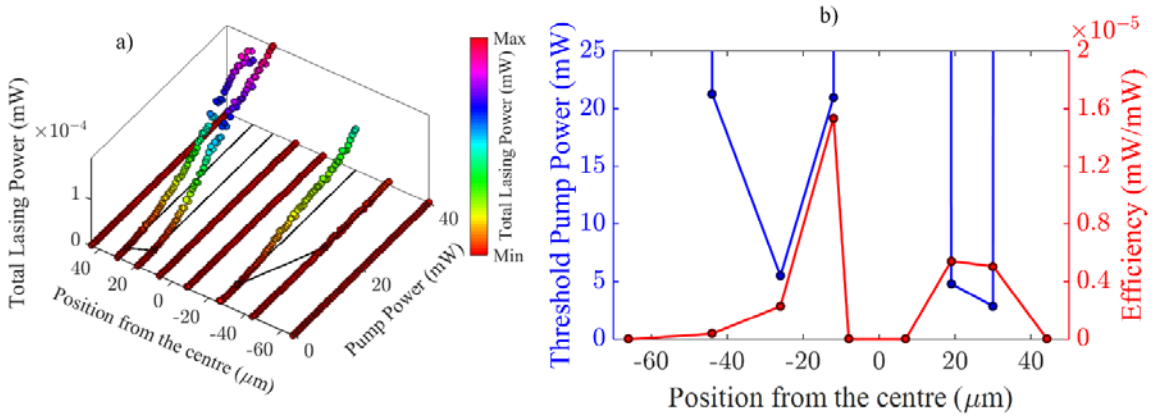

Figure 5-18 a) Experimental light-light curve of cleaned-up MBL with photoresist on top with as function of taper offset from the resonator centre, and corresponding b) threshold pump power and slope efficiency as function of taper offset .

coupling to low order modes, by reducing the modal overlap. In a normal MBL efficiency at offsets close to centre is not zero due to excitation of few high Q modes, while a zero efficiency is observed for the cleaned-up MBL.

Effects of altering the coupled tapered fibre size

As it is demonstrated in [91] for passive MBRs, increasing the tapered fibre diameter potentially provides cleaner and simpler transmission spectra. This happens due to variations in phase-matching and modal overlap between the fibre and resonator modes. Increasing the taper diameter decreases the modal overlap between the fundamental fibre mode and the WGMs. Therefore, generally speaking, the external Q factor increases. On the other hand, depending on the radial order of the WGMs, the phase matching condition is affected by changing the taper diameter. Normally, increasing the taper diameter increases the phase-mismatch between the fundamental mode of the taper and higher order radial WGMs.

Furthermore, for the sake of maintaining consistency in experiments, the same tapered fibre is always kept to couple light into the resonator during all experiments. With this approach, variations due to change in insertion loss and polarisation, caused by replacing various tapered fibres, are avoided. For this reason, the MBL is translated along the tapered fibre, in order to study the effects of variations of the tapered fibre diameter at the coupling point on MBL performance. Figure 5-18 demonstrates a schematic view of how different diameters of the taper fibre is accessed through moving the MBL along the tapered fibre.

Figure 5-19 (a) shows the obtained spectra as a function of taper offset from the centre of the MBL for four different taper diameters. Taper 1 corresponds to coupling at the waist of the taper where the diameter is ~2μm. Tapers 2, 3 and 4 are the spectra obtained by translating the MBL along the tapered fibre with steps of ~1mm. Taper

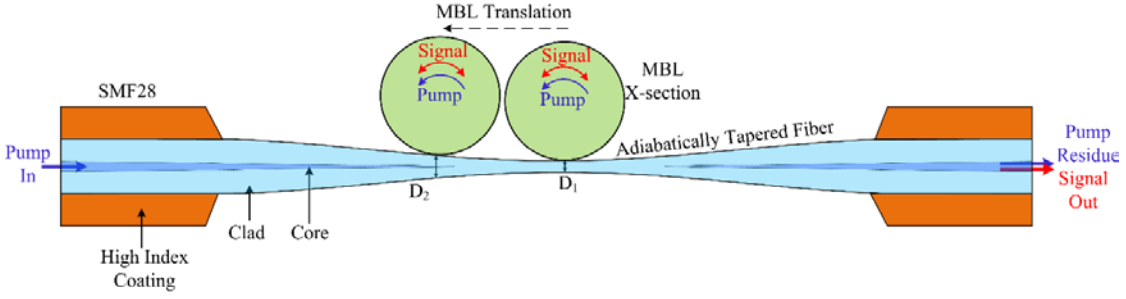

Figure 5-19 Schematic view of coupling MBL to tapered fibre at various diameters by translating the resonator along the taper.

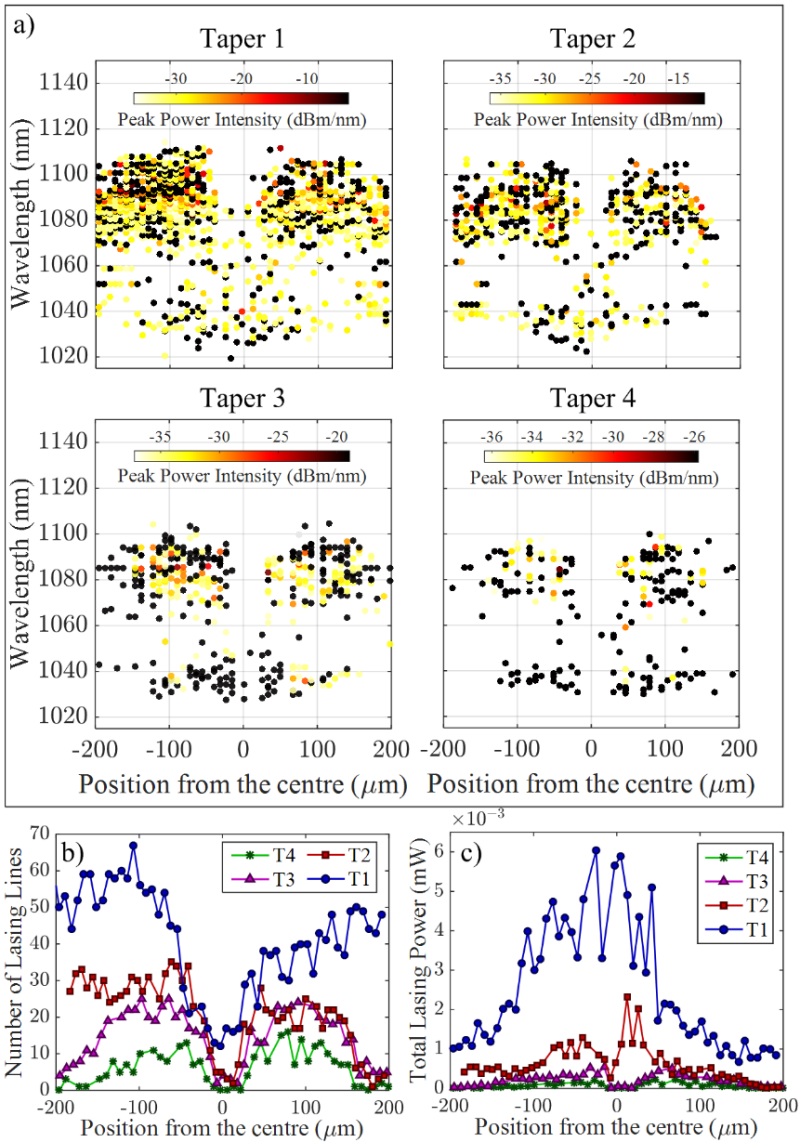

Figure 5-20 a) Spectral density peaks, b) number of lasing lines, and c) total lasing power of MBL as function of taper offset for various taper diameters indicated by T_1, T_2, T_3 and T_4.

diameters ($D_1 < D_2 < D_3 < D_4$) are roughly estimated to be 2µm, 3µm, 4µm and 5µm, from the obtained optical micrographs. For the sake of clarity, peaks of the spectral densities are plotted in Figure 5-19 (a). Results show a significant reduction in the number of the excited/collected lasing lines as the taper diameter increases. As shown in Figure 5-19 (b), the number of lasing lines at offset of ~100µm drops from ~60 for T_1 to ~10 for T_4. As discussed in previous sections, at the centre, due to over-coupling of pump and signal modes, few number of lasing lines survive. Such modes are presumably higher order radial ones, which are phase-matched to the fibre-modes when the taper diameter is small. Moreover, as the taper diameter increases, and therefore, n_{eff} of the fibre mode increases, the possibility of phase matching to low order radial WGMs increases. Therefore, in case of large taper diameter the excited/collected lines are limited to low order radial ones.

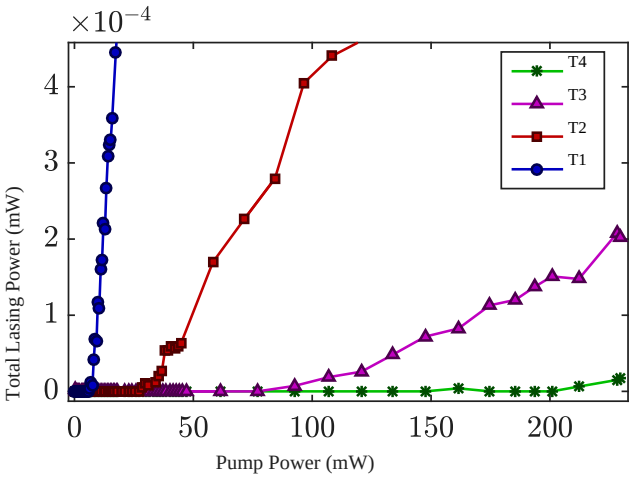

Figure 5-21 Light-light characteristics curve of MBL at different diameters along the coupled to tapered fibre.

At the same time, the number of supported modes by the tapered fibre increases at larger diameters. The tapered fibre is drawn from commercial SMF28, which is multimoded below 1260nm wavelength. Hence, pump and signal modes could out-couple into higher order modes of the tapered fibre [91]. Such higher order modes couple into the cladding of the fibre in the up-taper section and finally are absorbed by the high index polymer coating. Therefore, they contribute to an apparent decrease of the overall lasing efficiency. Moreover, lasing characteristics of the MBL coupled to the taper at different diameters are plotted in Figure 5-20. The taper is placed at the centre of the MBL, hence, smaller number of modes are excited comparing to off-centre excitation. The corresponding spectra as a function of pump power are given in Figure 5-22 in Appendix 1. These results reveal that as the taper diameter increases the threshold pump power increases, and corresponding slope efficiency decreases. This is due to, firstly, significant decrease in the number of lasing lines, and secondly, excitation of higher order pump and signal fibre modes during the out-coupling process. The latter causes the power drop along the transition length of the taper, as a result of non-adiabacity of the taper for higher order modes.

Mode reduction using microgrooved scatterers

A normal MBL with a maximum diameter of ~108μm and neck-to-neck length of ~240μm is fabricated. Such dimensions should significantly increase the number of supported WGMs. Figure 5-21 (a) shows an optical image of the fabricated MBL coupled to a tapered fibre at the centre. The spectrum of the resonator shows dense number of excited/collected number of modes. Observed lasing lines span a wide wavelength range

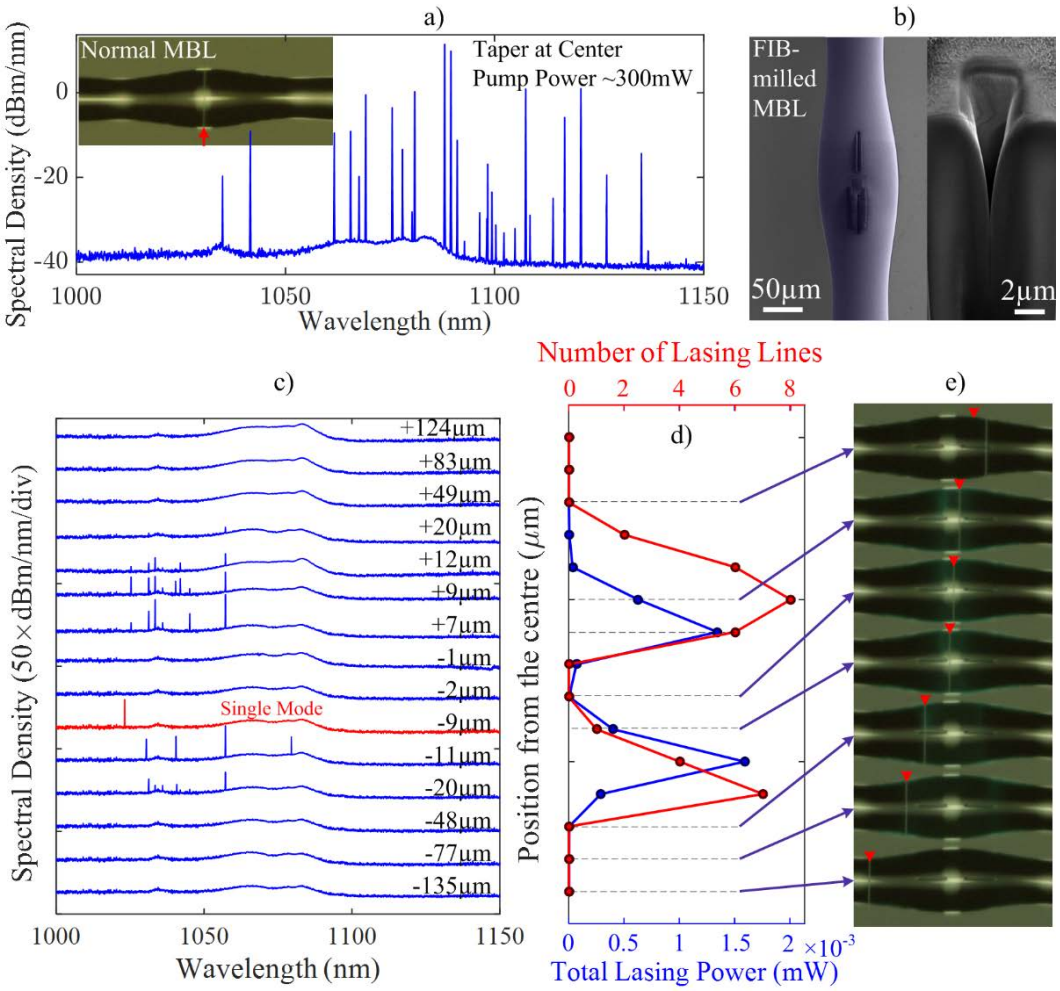

Figure 5-22 a) Spectral density of the fabricated MBL before cleaning-up for taper placed at the centre of the resonator as shown in the inset, b) FIB-milled microgrooves on MBL positioned symmetrically at 15µm offset from the centre, and the corresponding cross-section cut showing depth and structure of the microgrooves, c) spectral density of FIB-milled MBL, d) and corresponding total signal power and nmber of lasing lines as function of taper offset from the resonator surface, and e) optical micrographs of FIB-milled MBL under operation coupled to tapered fibres at various offsets from the resonator centre.

from 1030nm to 1140nm. It should be noted that, as previously discussed, the number of excited/collected lines at slightly off-centre excitation, should be more compared to central excitation.

Furthermore, rectangular micro-grooves with dimensions of 50×3µm^2 are precisely fabricated on the surface of MBL using Focused Ion Beam (FIB) milling. The microgrooves are milled on the MBL surface, following coating the device with a 30nm-thick gold layer using thermal evaporation. Acceleration voltage and current of the FIB are set to 30kV and 2.7nA, respectively. SEM of the FIB-milled MBL and cross-section view of one fabricated groove are depicted in Figure 5-21 (b). The grooves have a V shape, which stems from the conical shape of the ion beam, such that as the milling depth increases the amount of ions reaching the material decreases. This can be slightly

improved by widening the width of the grooves. The effective depth of each groove is about 5μm and are both positioned on the MBL surface with 15μm offset from the centre. As shown in [121], loss introduced by the micro-grooves attenuates the intra-cavity power of most of the high order axial modes which overlap with the micro grooves. This is due to light scattering and Q factor reduction.

Collected spectral density of the MBL as a function of the taper offset from the resonator centre is plotted in Figure 5-21 (c). The generated lasing lines mostly lie in the 1020-1060nm wavelength range. This is due to the small mode volume of the excited pump WGMs, providing high intensities. Such high intensity of the modes yields higher population inversion levels, and hence, the peak gain wavelength shifts to shorter wavelengths. The total lasing power and number of observed lasing lines as function of taper offset are plotted in Figure 5-21 (d). The corresponding optical micrographs of the taper position on the MBL are depicted in Figure 5-21 (e). Results show that beyond the microgrooves no lasing peak is collected. By placing the taper fibre at the centre, significant reduction in the excited/collected lasing lines takes place such that no lasing is observed close to this point. Varying the tapered fibre around the centre, increases the chance of reducing the mode over-coupling. Few (less than 9) lasing lines appear when the taper fibre is offset farther than about ±8μm from centre. As shown in Figure 5-21 (c), single mode lasing is achieved with tapered fibre at ~9μm offset. Interestingly, such single mode lasing line appears at 1023.2nm wavelength, which indicates that the inversion level is around 50% reached by coupling to (presumably) the fundamental pump mode, and unaffected high Q of the resonator mode during FIB-milling.

5.6 Summary and Conclusion

MBRs coupled to tapered fibres are promising devices for providing a wide range of WGMs with different spectral and spatial properties, which could be selectively utilized for a range of applications. In this chapter, MBLs are experimentally studied, and the obtained results are accompanied by theoretical calculations. The azimuthal and axial FSRs, at 1550nm wavelength band, are employed to estimate the radial and axial orders of the excited modes, as well as, the accurate profile of the resonator. The lasing characteristics of an MBL depends on the offset of the coupled tapered fibre from the centre of the resonator. At positions very close to the centre a significant reduction in the power and number of lasing modes is observed. This is due to the over-coupling conditions prevailing at the centre, which considerably lower the Q factor of both pump and signal WGMs. Further increasing the tapered fibre offset, provides critical coupling

to higher order modes. A significant increase in obtained total power and number of lasing lines is observed at slightly off-centre tapered fibre positions. Furthermore, the over-coupling zone can be narrowed by either increasing the signal and pump Q factors, and/or increasing the dopant concentration.

Moreover, as the taper offset increases, the lasing wavelength jumps from 1030nm band to 1100nm band. These two lasing bands correspond to high and low population inversion levels, defined by the order of the excited pump mode as the taper is progressively more offset. Theoretical simulations predict that, lower and higher order axial WGMs can be simultaneously excited by placing the taper fibre at slightly off-centre positions. This provides both low (at large offsets) and high (at small offsets) inversion levels, which satisfy lasing at long and short wavelengths, respectively.

Threshold pump power and slope efficiency of collected lasing lines depend on the offset of the tapered fibre from the centre. The threshold is observed to be high due to over-coupling at centre positions, while the slope efficiency is maintained relatively high at this point. Theoretical simulations show that although the threshold for some specific signal WGM may be relatively higher compared to other modes, the maximum efficiency generally happens at the critical-coupling point of that mode. For a large portion of the resonator length at off-centre excitations, the threshold stays minimum. On the other hand, the slope efficiency drops at very large offsets due to excitation of highly under-coupled pump and signal WGMs.

However, due to complex spectra and multiple WGM competition, standard MBL suffers from spectrally unstable and fluctuating output, which make it cumbersome to operate as sensor or other applications. By applying three different spectrum-cleaning techniques: 1) high index droplet scatterer, 2) altering the excitation taper diameter, and 3) FIB-milled microgroove scatterers, fewer mode, and considerably more robust and stable MBLs are demonstrated. The high index droplet mode stripping method grantees a low-cost and fast approach to obtain fewer laser lines. However, accurately placing the droplet on the resonator and close to the centre, can be a complex task. Alternatively, placing the MBL at larger diameters along the taper decreases the number of collected lasing modes. However, this method suffers from degrading the threshold and efficiency of the laser system. Alternatively, the FIB-milling method is demonstrated to be the most promising and accurate method in spectral cleaning of MBLs. Despite being experimentally expensive, FIB-milling method provides a precise and selective mode stripping tool, without significant degradation of the laser

performance. It should be stressed that single mode lasing is achieved by all these three approaches.

5.7 Appendix 1

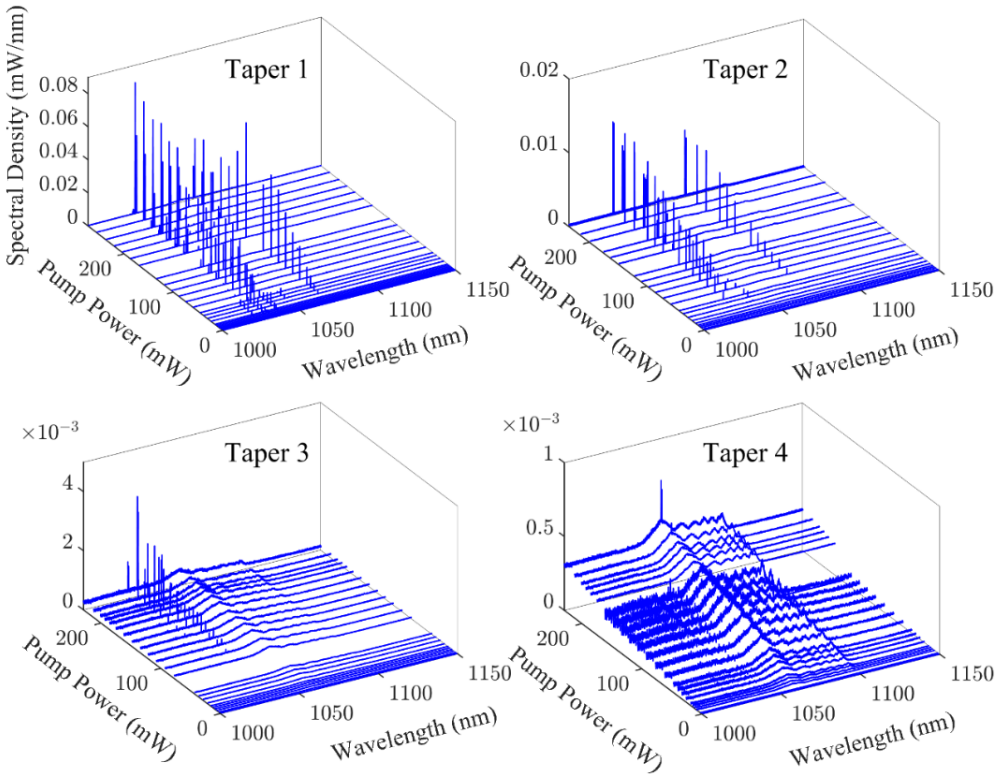

Figure 5-23 Spectra of MBL as function of pump power for different taper diameters corresponding to T1-T4 tapers for tapers placed at the centre of the resonator.

Chapter 6 Side-pumped Optical Microstub Resonator Lasers

6.1 Introduction

Over the years, a number of different WGM microresonator cavities have been proposed and studied extensively. Microbottle Resonators (MBRs) [12, 13, 115, 121] are a newly developing class of WGM cavities fabricated by deforming locally available commercial optical fibres. Their quasi-harmonic oscillator profile gives rise to multiple three-dimensional overlapping cavity modes and complex spectra. MBRs are promising structures for future cavity Quantum Electrodynamics (QED) studies [115], strain [47] and optofluidic sensors [44], as well as, add-drop multiplexers [119]. Their transmission spectra depend strongly on the excitation conditions [12, 91, 117], which can potentially compromise their repeatability and effectiveness as a sensor. Furthermore, in case of active medium, lasing actions have been observed in a variety of microresonators [21-23]. Among the various geometries and in contrast with MBRs, microcylindrical cavity lasers exhibit azimuthal resonances around the microcylinder perimeter without any significant light confinement in axial direction. As previously discussed, WGM cavities usually provide very high quality factors (Qs) as well as high intra-cavity energy densities which make them optimal microcavities for low threshold and narrow line-width lasing.

Robust excitation and light collection in such resonators without degrading the coupling efficiency and cavity performance is a serious challenge. Optical characterisation, launching or collecting light is normally achieved by methods such as monitoring scattered light, evanescently coupled prisms [22, 88], fibre microtapers [20, 21] and integrated-optic waveguides [23]. To date, microtaper coupling is proven to be the most widely-used and efficient method. MBRs are naturally formed in between two fibre stems, which facilitate handling and easy incorporation into optical systems, as well as, integration with on-chip waveguides [23, 136]. It has been shown that WGMs of bottle [119] and cylindrical [137] resonators can be collected through residual leakage of such modes into the stem fibres. In case of active MBRs, pumping and signal collection can be achieved through the fibre stems between which the resonator is formed.

In this chapter, in order to retain and utilise some of the aforementioned optical and mechanical features of MBRs, the optical performance of a new passive and active

optical resonator, namely the microstub resonator (MSR) is investigated. MSRs are short rectangular high-Q microcavities with cylindrical symmetry supporting three-dimensional WGM confinement. The fabrication technique is straightforward and yields high quality microresonators. Passive cavities with Qs of 10^6 with transmission dips below 15dB is achieved. In case of active MSR, the device is demonstrated to work as a stand-alone WGM laser cavity where, to the best of my knowledge, for the first time the pumping and collection of generated light are realized through the stem fibres. In contrast with conventional complex and cumbersome resonator-microtaper system, this device can be important in developing new, functional, fully-integrated and low-threshold microlasers.

6.2 Passive MSR

MSRs are fabricated by employing two different optical fibres with non-identical diameters, as shown in Figure 6-1. Fibre A with outer diameter D_1 is spliced to fibre B with outer diameter D_2 using a conventional fusion splicer. Fibre B is then accurately cleaved at the desired stub length and spliced to another fibre A with diameter D_1. This results primarily in a cylindrical cavity (here called "stub") of length L_2 and diameter D_2 which is constant over the majority of length L_2. The edges of the fabricated stubs are rounded due to the generated heat during the glass fusion, improving the optical performance of the stub as a WGM resonator. The shape of the edges are controllable by varying the splicing parameters such as current and duration of the electrical arc pulses. Fabricated passive MSRs have parameters of D_1 = 125µm, D_2 = 200µm and L_2 in the range of 200-400µm. This microcavity fabrication approach provides the flexibility

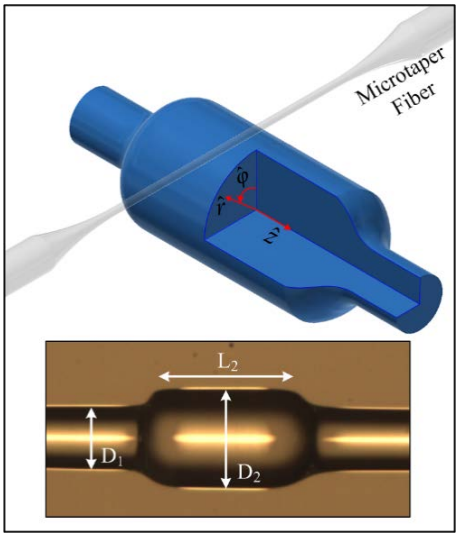

Figure 6-1 Schematic view of microtaper coupled MSR and optical image of a fabricated device.

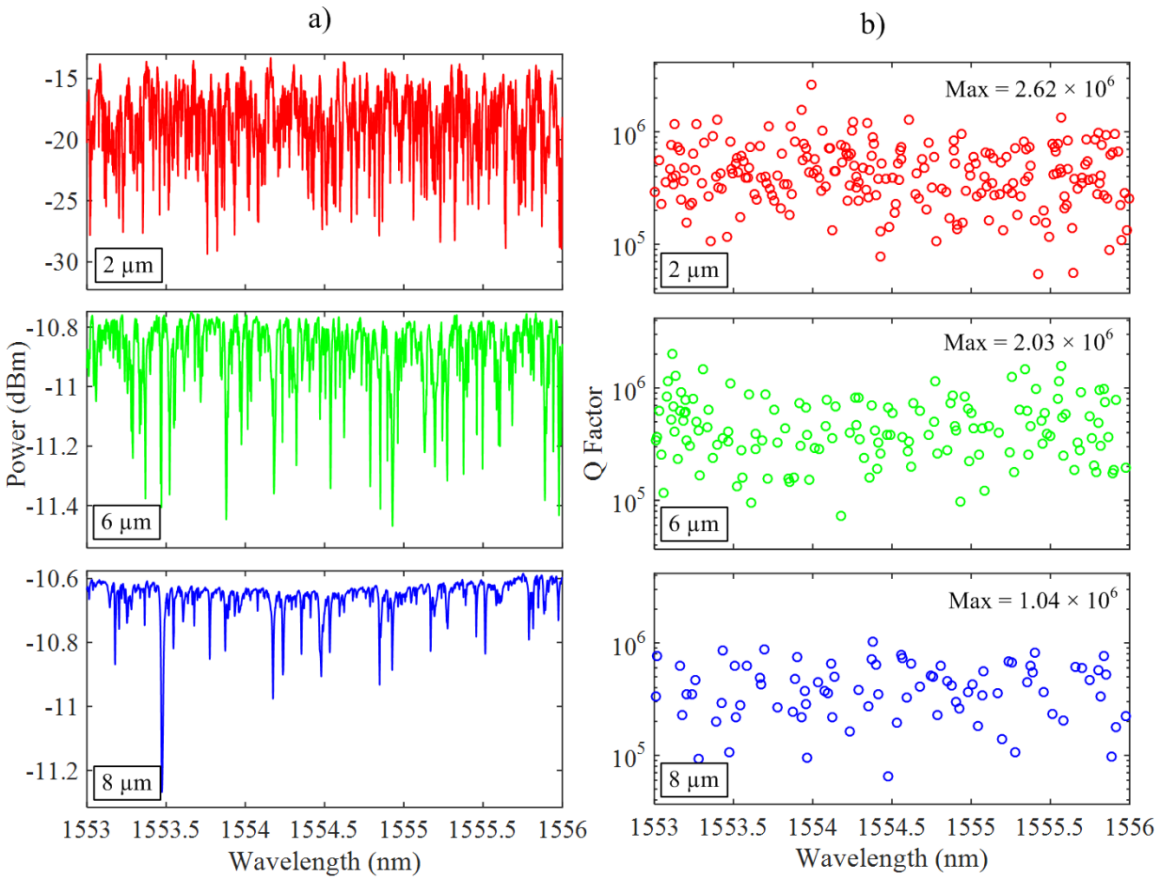

Figure 6-2 a) Transmission and b) corresponding Q-factor spectra of MSR with 2µm, 6µm and 8µm microtapers excitation (D_1 = 125µm, D_2 = 200µm and L_2 = 200µm).

of combining a wide range of existing passive and active fibres to form passive or active MSRs.

Passive MSRs are characterised by evanescently coupling microtapers of different diameters. A tunable narrow-linewidth light source with -10dBm power is swept over 1550nm wavelength range, and the transmitted power is monitored using an InGaAs photodetector. Figure 6-2 shows typical transmission and corresponding Q-factor spectra of a MSR with L_2 = 200µm excited using tapered fibres with diameters of 2µm, 6µm and 8µm, respectively. The tapered fibre is positioned on the centre of MSR with a zero air gap. It is shown that, in the case of 2µm microtaper excitation, the transmission spectrum is very dense, compared to the excitation with larger diameter tapered fibres. Transmission dips in excess of 15dB, corresponding to near-critical-coupling, are observed. The maximum transmission level appears to be dropped to ~-15dBm. This apparent transmission (insertion) loss is primarily due to the dense resonance spectrum and the large number of overlapping resonances. As the microtaper diameter increases, the number of excited/collected modes decreases and the transmission dips become shallower. In addition the maximum transmission recovers closely to the initial -10dBm level. Figure 6-2 (b) illustrates that the Q factors of WGM

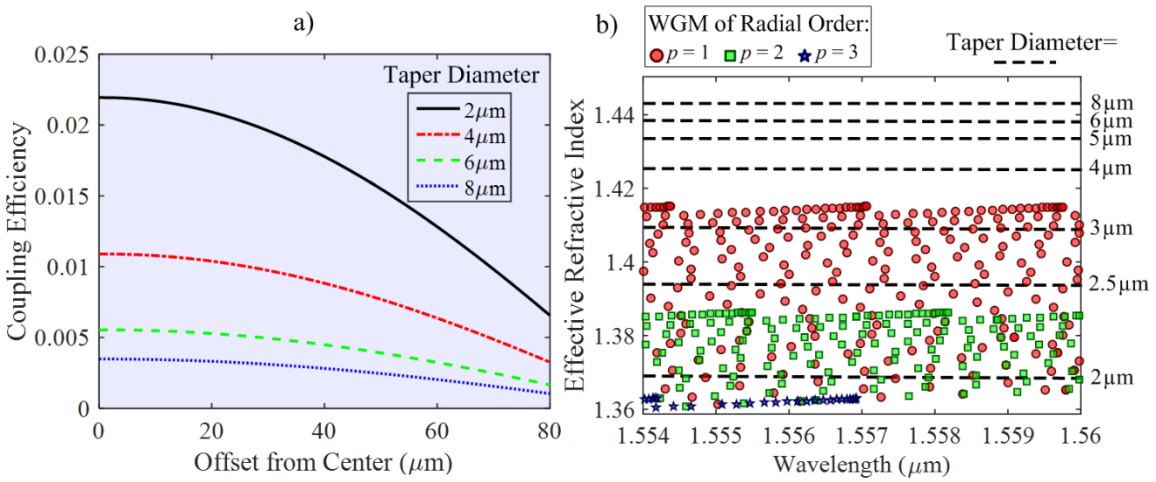

Figure 6-3 a) Calculated coupling coefficient (as defined in [85]) of the LP_{01} fibre mode for various microtaper diameters, to the fundamental WGM as a function of microtaper position along the MSR, and b) calculated effective refractive index of the MSR WGMs and LP_{01} fibre mode with various diameters.

resonances obtained from the experiment after fitting a Lorentzian curve to each resonance for different microtaper diameters, are all in the same range, between 10^5 and 10^6 with an average value of ~0.5×10^6.

Figure 6-3 (a) plots the coupling coefficient of the first order linearly polarized mode (LP_{01}) of the microtaper to the fundamental WGM of the MSR (D_1 = 180μm, D_2 = 200μm and L_2 = 200μm, $p = q = 1$) along the axial length of the resonator. p and q denote the radial and axial mode numbers, respectively. The coupling coefficients are numerically calculated from the overlap integral and approximation given in [85], and indicate the amount of power coupling between the fibre and WGMs. Results show that as the diameter of the microtaper increases, the overlap of the fibre mode and the fundamental WGM decreases which results in smaller coupling efficiency. Hence, smaller taper diameters generally induce stronger coupling and deeper transmission dips.

Additionally, Figure 6-3 (b) shows the calculated effective indices (n_{eff}) of the first three radial orders (p = 1-3) of microstub WGMs with dimensions D_1 = 180μm, D_2 = 200μm and L_2 = 200μm, and tapered fibre with various diameters. The propagation constant of WGMs is proportional to the azimuthal mode number, m, expressed as $\beta = m / R$, where R is the radius of the resonator. Larger radial WGM numbers have smaller m, hence smaller n_{eff}. Smaller diameter microtapers, on the other hand, result in smaller n_{eff}'s of propagating fibre modes, which can result in phase matching to a larger number of overlapping WGM families [138] (see Figure 6-3 (b)). Therefore, in the case of small microfibre diameter, large radial (and/or axial) order WGM numbers are more likely to be excited/collected, compared to larger fibre diameters. Increasing the microtaper diameter (e.g. to 8μm) results in large phase mismatching with the MBR supported

WGMs and, therefore, a smaller number of weaker resonances is expected, in good qualitative agreement with the experimental results in Figure 6-2 (a). This dependence is similar to the one observed in MBRs [117] and microdiscus resonators [139]. Thicker excitation microtapers are also much more robust and environmentally stable and can potentially be more suitable for practical applications, such as sensors, where small but well separated and discernible resonances are advantageous.

The fabricated MSRs were also characterised as the excitation microtaper is translated along the resonator length. Figure 6-4 illustrates the transmission spectra of the MSR coupled to a 2μm-diameter microtaper at various offsets along the resonator. The optical micrographs show the scattered light from the surface of the resonator at 1550nm wavelength. The density of the excited/collected WGMs remains substantially unchanged along the MSR. This can be understood by calculating the coupling coefficient between the microtaper and the MSR modes. Figure 6-5 shows the calculated coupling coefficient between the tapered fibre LP_{01} and the fundamental WGMs of stub and bottle microresonators for comparison. The dimensions of the microstub are identical to the fabricated one and the microbottle has a maximum radius of 100μm and

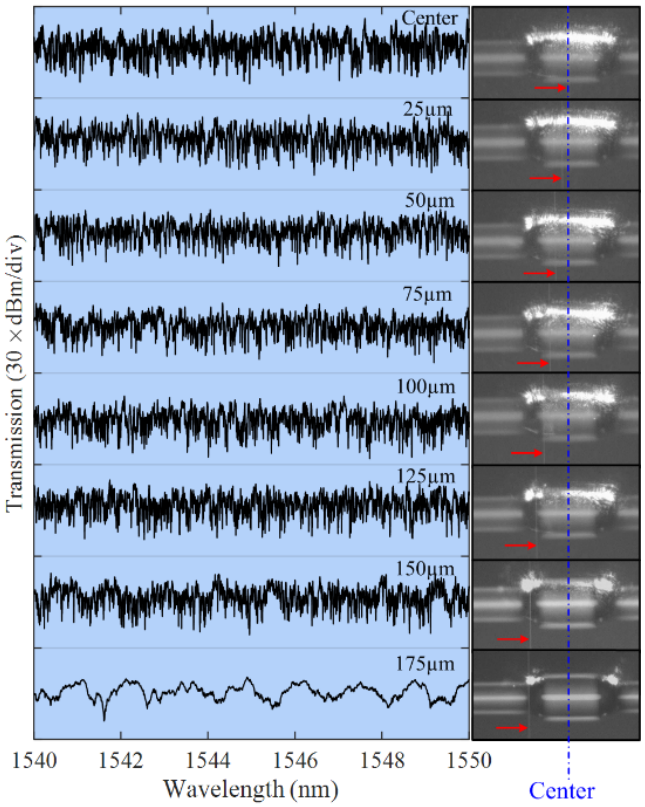

Figure 6-4 Transmission spectra and corresponding scattered light at 1550nm wavelength of MSR with 2μm microtaper excitation at various positions along the resonator. (Solid red arrows show the position of microtaper)

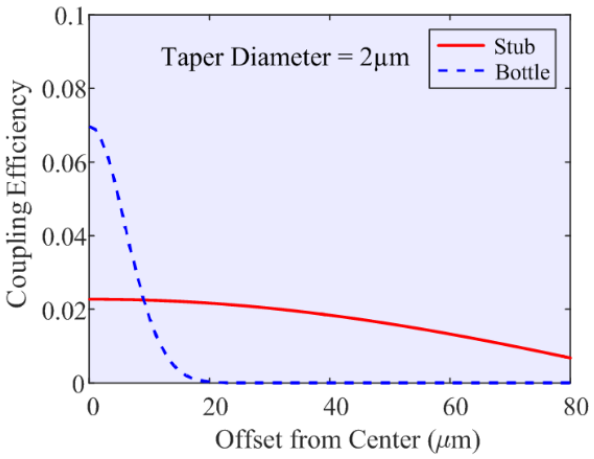

Figure 6-5 Calculated coupling coefficient (as defined in [85]) of a 2µm-diameter microtaper to the fundamental mode of MSR and MBR resonator as a function of microtaper position along the resonator.

curvature constant (as defined in [13]) of $\Delta k = 0.2\mu m^{-1}$. This keeps the stub and bottle resonators dimensions comparable in terms of diameter and effective resonator length. Results show that as the microtaper position is translated along the MSR, the coupling constant does not exhibit dramatic changes. Whereas, in the case of bottle resonator the coupling efficiency drops rapidly away from the centre of the resonator.

Using transfer matrix method developed in [127], the mode profile of stub, bottle and sphere micresonators are calculated. In this technique, the profile of the resonator is approximated by small cylindrical sections with adequately small thicknesses. Wave equation in cylindrical coordinates is then solved for each section. Accordingly, by applying the well-established transfer matrix method for optical fibres between consecutive sections, and setting the boundary conditions, propagation of such modes along the resonator is evaluated. Figure 6-6 (a-c) depict the electric field (E_φ) intensity distribution of the resonators for the first, third and 29th axial mode order (q) of the first radial WGM ($p = 1$). The dimensions of the stub and bottle are as the same aforementioned, and the sphere radius is 100µm identical to maximum radii of stub and bottle resonators. The mode intensity distributions of such resonators show that for MSRs the mode turning point along the resonator is almost independent from the axial mode number and it is very close to the resonator edges. While, for microbottles, the turning point is almost proportional to the square root of q [117]. This forces the coupling efficiency for microbottle to drop fast as the taper moves off-centre. Moreover, the mode intensity of MSR is almost uniformly distributed along the resonator length, while in the case of microbottle and microsphere resonators the field intensity increases (on average) along the axial dimension. The field intensity along the axis of bottle and

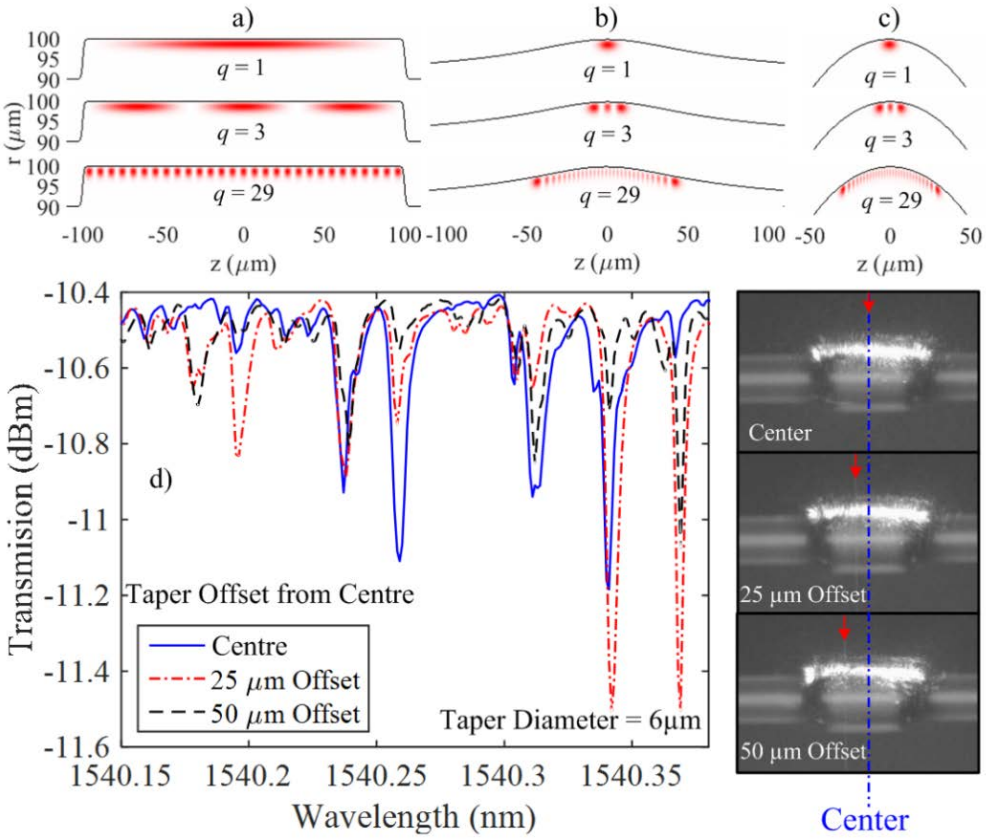

Figure 6-6 a) Calculated first order radial mode profile of (a) MSR, (b) MBR, and (c) microsphere resonator for q = 1, 3 and 29, and d) detailed transmission spectra of MSR with tapered fibre at 0, 25μm and 50μm offset from the centre, and corresponding optical micrograph at 1550nm wavelength showing the relative position of the tapered fibre and the resonator centre (red arrows show the fibre taper position).

sphere resonators can be analytically expressed in terms of Hermite polynomials of order q [12], which well describes the origin of maximum field intensities close to the mode turning points.

Experiments on MSRs show that, almost the same resonance spectra is obtained at few tens of microns offsets around the centre regardless of the microtaper position. Detailed spectra of the MSR excited by a tapered fibre with 6μm diameter at zero, ~25μm and ~50μm offsets is plotted in Figure 6-6 (d). Only the relative strength of the resonance excitation is affected, depending on the individual modal overlaps at various excitation positions. These results also demonstrate that the MSR excitation is less sensitive to the exact position of the excitation microtaper when compared to bottle and sphere resonators. Similar scattered patterns of light were obtained for all microtaper positions. This is markedly different to MBRs of which both scattering patterns and spectrum change substantially with the excitation position, [12, 117].

Next, I compare the resonance spectra of MSR with respect to the well-known bottle and sphere resonators in order to elucidate the spectral response of MSRs. Figure 6-7 compares the calculated resonance wavelengths of the aforementioned stub, bottle and sphere microresonators for the first three radial order WGMs (p = 1-3). The structure of the resonators are plotted in Figure 6-7 (a) showing a maximum radius of 100μm for all resonators. The MSR resonator, as shown in Figure 6-7 (b) and (c), exhibit an azimuthal FSR ($\Delta\nu_{FSR}^{m}$) in frequency determined by the diameter of the resonator. The same $\Delta\nu_{FSR}^{m}$ is observed for microbottle and sphere resonators as shown in Figure 6-7 (d) and (e). On the other hand, the microbottle shows axial FSR of $\Delta\nu_{FSR}^{q}$ which is proportional to its curvature constant ($\Delta\nu_{FSR}^{q} \propto \Delta k$). On the other hand, an ideal microsphere exhibits frequency-degenerate angular WGMs. Therefore, the spectra of microbottles and microspeheres always show groups of modes [12, 47, 117, 140] containing various axial WGMs. In case of MSRs, no periodicity in the frequency of the axial modes is observed. WGMs with identical (m, p) pairs show increasing frequency spacing as the resonance wavelength decreases. Hence, no group of modes with particular periodicity is observed in the transmission of MSR shown in Figure 6-4. This

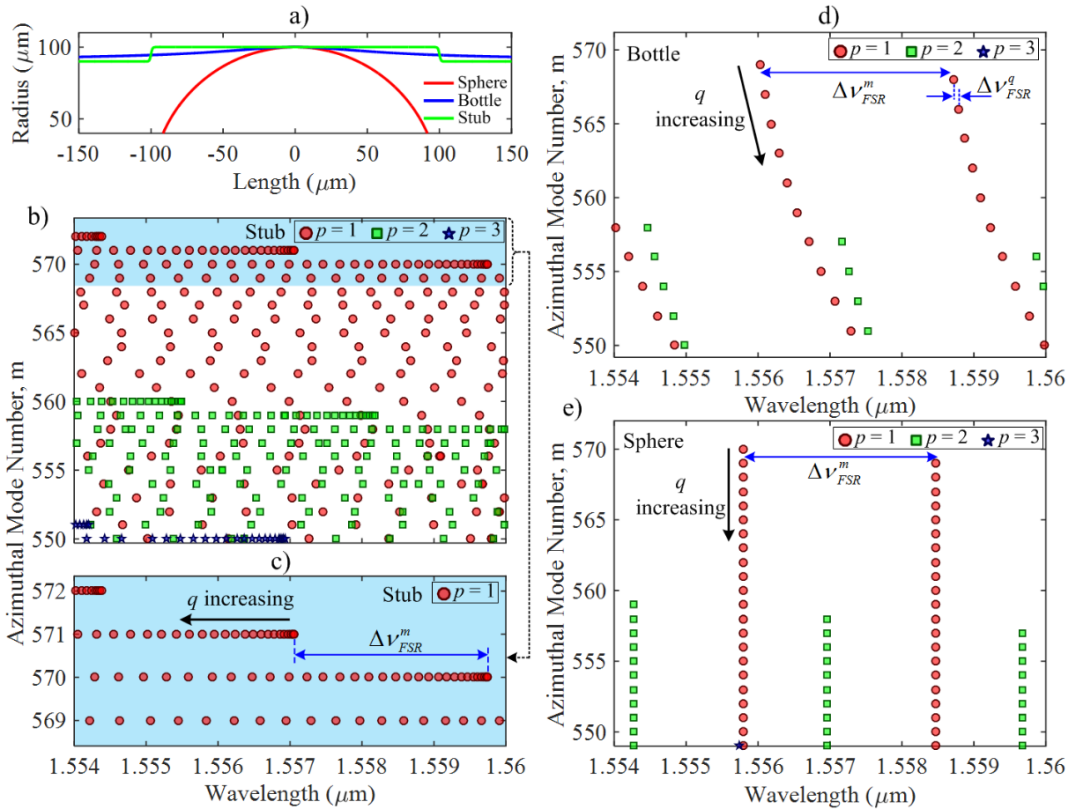

Figure 6-7 a) Profile of simulated MSR, MBR and microsphere resonators, b) calculated resonance wavelength of MSR, c) detailed spectra of MSR for m = 569-572, and calculated resonance wavelength of d) MBR and e) microsphere resonator. (The arrows show the direction of increase in q for a constant p number)

property of MSRs is beneficial for applications (such as CQED) where there is a stringent condition on the required frequency, as it provides a quasi-continuum of resonances.

6.3 Active MSRs

A special Yb^{3+}-doped fibre, provided by Heraeus Quarzglas GmbH, is used as the active medium and by employing the aforementioned fabrication technique, active MSRs with stem diameter $D_1 = 125\mu m$, stub outer diameter $D_2 = 240\mu m$ and stub length $L_2 = 50\text{-}500\mu m$ are fabricated. The MSR has a uniformly Yb^{3+}-doped core with diameter of $D_c = 200\mu m$ and fluorinated cladding resulting in core/cladding refractive index difference of $\Delta n = 22.3\times10^{-3}$. The active MSRs can be simply pumped by launching pump power through the multimode stem fibre. With this approach, there is no need of additional optics and other complicated setups such as free space, prism or microtaper coupling. In the present implementation, since the doped core diameter is larger than the stem diameter, only the central part of the active core is expected to be highly inverted. As schematically demonstrated in Figure 6-8, the edges of the doped core remain largely un-pumped which affects the laser characteristics such as threshold, efficiency and stability. It was previously observed that excitation of WGMs in MBRs will result in axial leakage of modes power through the fibre stem [119]. This is advantageous when compared to microtaper-resonator system, since collection of WGMs through the leakage does not require phase matching. In the case of active resonator, the leaky WGMs contribute to the microlaser output. Due to symmetry, the generated WGM signals are emitted in both axial directions into the stems, where it

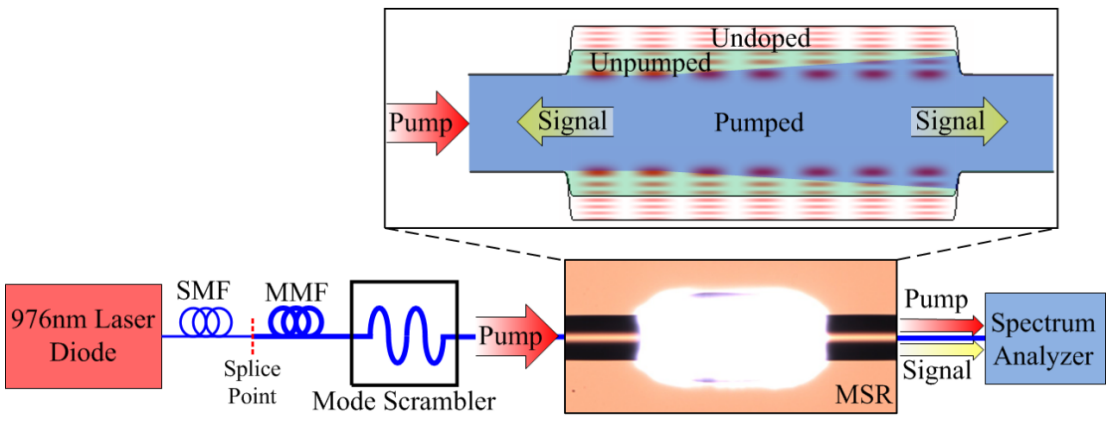

Figure 6-8 Schematic image of active MSR, and mechanism of side pumping and signal collection. The inset shows the inefficient and partial pumping of the active medium, and distribution of a typical higher order signal WGM. SMF: single mode fibre, MMF: multimode fibre.

can be monitored. A laser diode pump at 976nm wavelength and ~300pm linewidth is launched into one of the stem fibres. The residual pump and the generated signal are collected through the multimode fibre stem from the other side of the resonator, and coupled into an optical spectrum analyzer. Lasing peaks in the 1060nm wavelength range are observed. No surface roughness-induced, transversely scattered signal/pump light is detected. This indicates that the WGMs are formed at the inner doped core/cladding interface (or retain high radial orders with maximum intensity lying well inside the MSR core). The number of excited/collected lasing lines is increased by bending the input fibre stem, which scrambles the pump modes through the multimode fibre launch and increases the numerical aperture of the pump. Such mode mixing can significantly increase the pump absorption close to the active-passive glass boundaries where the signal WGMs lie. This results in efficiently pumping a larger portion of the doped core and improving the lasing action. It should be mentioned that this is similar to effects observed in high power, cladding-pumped fibre lasers [141, 142].

Figure 6-9 (a) plots the spectral density of the collected signal at various pump power values. The spectra show three sections in wavelength, demarcated P_I (1000-1050nm),

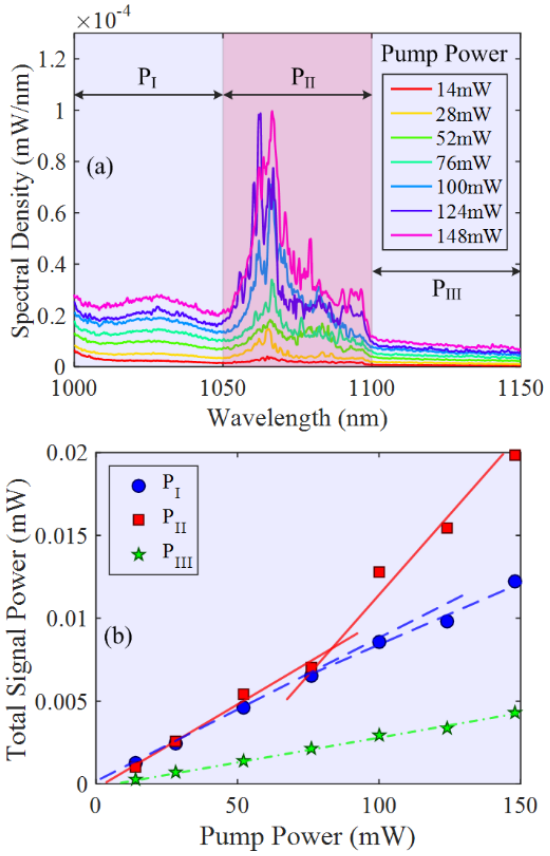

Figure 6-9 a) Measured output power spectral density of the active MSR as a function of pump power and, b) signal power related to three regions of the signal spectra shown in part (a) as a function of pump power.

P_{II} (1050-1100nm), and P_{III} (1100-1150nm), which follow different evolutions with pump power. The total signal power calculated by integrating the power spectral densities for each region as a function of pump power is plotted in Figure 6-9 (b). The main activity is observed in region P_{II} where for launched pump powers greater than 75mW, a change in the slope is observed indicating the presence of a threshold and lasing action. Sharp lasing peaks are observed to be particularly around 1080nm wavelength. These lasing lines are observed to be unstable showing strong modal competition. This is expected since all WGMs in MSRs occupy the entire cavity length and strongly overlap. On the other hand, P_I and P_{III} regions show almost linear characteristics as the launched pump power varies, implying simply Amplified Spontaneous Emission (ASE) nature. In fact, the P_I integrated power shows a slighter smaller slope above 75mW, which is a sign of partial inversion clamping and/or spectral hole-burning [132, 143, 144].

As the pump power exceeds 100mW, the collected signal power is observed to be fluctuating. This is likely due to the un-pumped portion of the active resonator which provides loss as a saturable absorber (see Fibre 6-8). Similar instabilities have been previously observed in other type of lasers [145, 146], as well as been predicted in microcylinder-based lasers [147]. These sort of instabilities can be mitigated by modifying the MSR structure and achieving more uniform inversion, particularly by controlling the size of the undoped cladding and/or redesigning the cavity edges where the WGMs reside.

6.4 Summary and Conclusion

I have presented the fabrication and optical performance of a new optical microstub resonator. The fabrication technique is versatile and involves splicing of a small fibre segment ("stub") with few tens to hundreds of micron length between two fibre stems of smaller diameter. The optical resonator remains cylindrical (constant diameter) almost over its entire length. In contrast to bottle and microsphere resonators, the excitation spectra of MSRs do not exhibit distinguishable azimuthal FSR. The resonance spectra remains dense as the tapered fibre is translated along the stub length which is favoured for CQED applications. The measured maximum fully loaded Qs were about 10^6, and close-to-critical coupling was achieved with 2μm diameter fibre microtapers. Increasing the diameter of the excitation microtaper decreases the coupling coeficient and simplifies the transmission spectra. The central part of the resonator (the "stub") can be different to the adjacent fibre stems to achieve additional functionalities. For example, efficient microlasers can be fabricated by splicing active

large-mode-area fibre stubs. Also, highly nonlinear resonators can be achieved by using chalcogenide or tellurite glass fibre stubs.

Using a special Ytterbium doped fibre with 200μm doped-core diameter and 240μm cladding diameter, we (with the help of ORC Advanced Laser Lab staff) formed active MSRs with 200-400μm lengths and 125μm stem diameters. The active MSRs were, for the first time, side-pumped by 976nm single-mode diodes through their stems. Residual pump and generated signal were monitored at the opposite fibre stem end. Lasing peaks in the 1060-1100nm wavelength range were observed. This is the first demonstration of a robust, fully integrated, stand-alone microlaser without the need of additional launching and collecting optics. These composite structures are expected to result in a number of novel, high performance devices. A subject of our future work is optimizing the dopant distribution and pump configuration in order to increase the lasing efficiency and mode collection/excitation and stability.

Chapter 7 Microrod Resonator Lasers

7.1 Introduction

The most common coupling set-ups used for excitation and signal collection of WGM microresonators are based on tapered fibre coupling owing to their high coupling efficiency [14, 20, 148-150]. Other methods rely on integrated waveguides [23], prisms [22] and/or collecting the scattered light [121]. As the spectrum and coupling efficiency highly depend on the excitation position, most of these coupling systems require precise alignment and complex packaging. Hence, providing a platform where the excitation and collection of light along with the WGM laser cavity are all integrated as a stand-alone device would be important in developing new, fully-functional and low-threshold lasers. Here, I demonstrate a completely new microrod resonator laser based on WGM resonators micro-machined directly in an Yb^{3+}-doped optical fibre, where the pump excitation and/or signal collection can be achieved through the same fibre stem on either side of the microrod cavity, thus eliminating the conventional complex coupling systems. I use a pulsed CO_2 laser in order to micro-machine, through controlled ablation of the fibre surface, and form a WGM microcavity directly on the rare earth doped fibres in a very short time. This topology is reminiscent of the previously demonstrated microstub resonators [112], but without the need of extra laborious splicing steps.

7.2 Evanescently-excited WGM Microrod Lasers (Passive and Active)

As demonstrate in Chapter 3, a new method is introduced to fabricate WGM microrod resonator lasers directly on rare-earth doped silica fibres based on pulsed CO_2 laser ablation of materials. An Yb^{3+}-doped fibre, provided by Heraeus Quarzglas GmbH, with 200μm-diameter active core and 240μm cladding diameter, is used. Sequence of pulses generated by a pulsed CO_2 laser is focused on the doped fibre tilted by an angle of ~18° from its vertical axis, resulting in a maximum ablation depth of 20μm. Afterwards, the resonator is fire-polished using a conventional fusion splicer to smoothen the side-wall roughnesses and other fabrication irregularities.

A 2μm-diameter tapered silica fibre is evanescently coupled to the fabricated microrod resonator by direct contact, to ensure the fibre position is mechanically stable. Figure 7-1 (a) shows the fabricated microrod resonator when the coupling position of the tapered fibre is varied along the resonator at few points including centre and the side

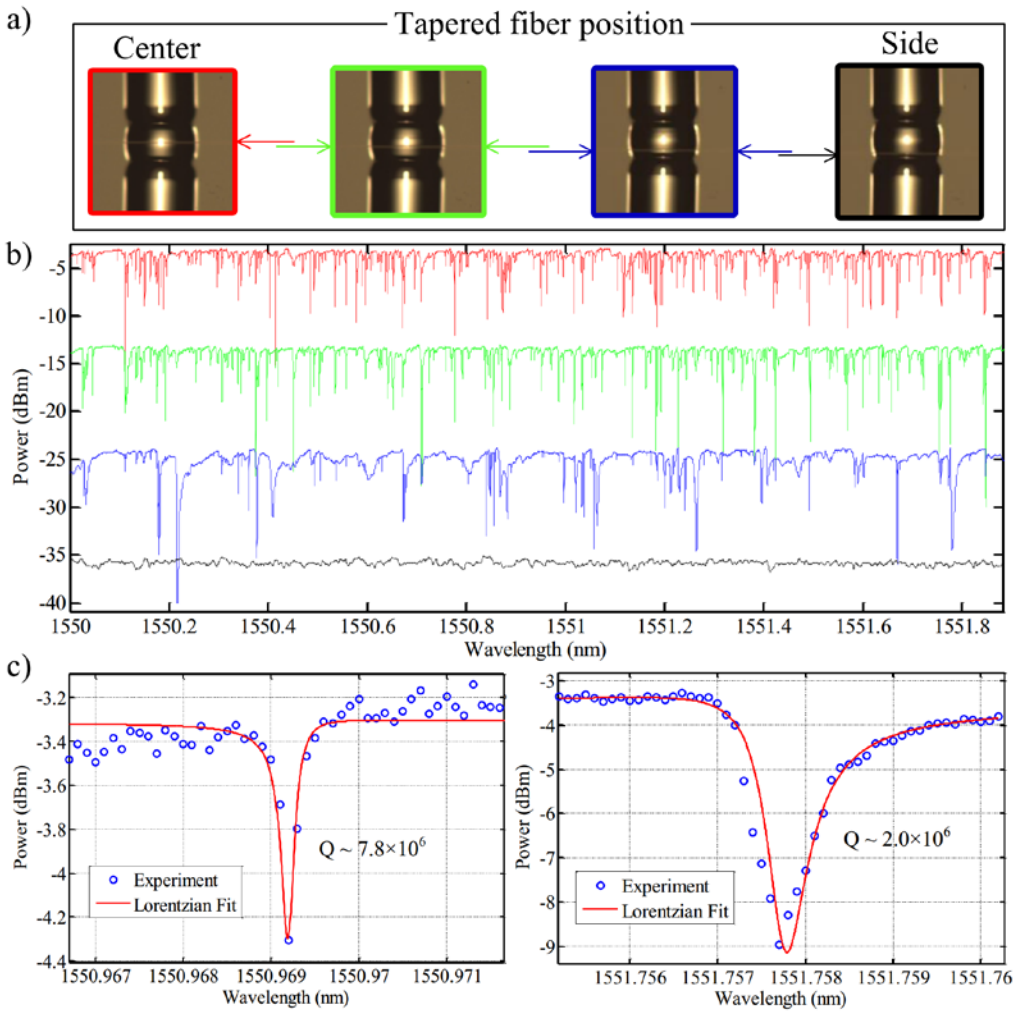

Figure 7-1 a) Microrod resonator coupled to tapered fibre at few positions along the resonator (the arrows show the position of the tapered fibre), b) spectra of the resonator when the tapered fibre position is shifted from centre to the sides, (each spectra is shifted 10dBm down, and colours correspond to the image with the same frame colour in (a), and c) spectra of two resonances around 1551nm fitted to a Lorentzian curve.

edge of the resonator. As illustrated in Figure 7-1 (b), the spectra become denser at the centre of the resonator, and the number of excited modes decreases when the position of the taper shifts to the edge. This is due to the higher surface roughness of the resonator at close to the edges, which is induced by the pulsed CO_2 laser ablation. Note that, owing to the cylindrical structure of the microrod resonator, by altering the fibre position, phase matching condition for particular modes along the resonator is satisfied that allows excitation of different modes. This is useful when selective excitation of a particular group of modes is required. Figure 7-1 (c) shows two different resonant WGMs at around 1551nm wavelength. Fitted Lorentzian curves show measured Q factors up to 7.8×10^6.

In order to characterise the lasing characteristics of the microrod laser, a laser diode pump with centre wavelength at 976nm and ~300pm linewidth is launched into the

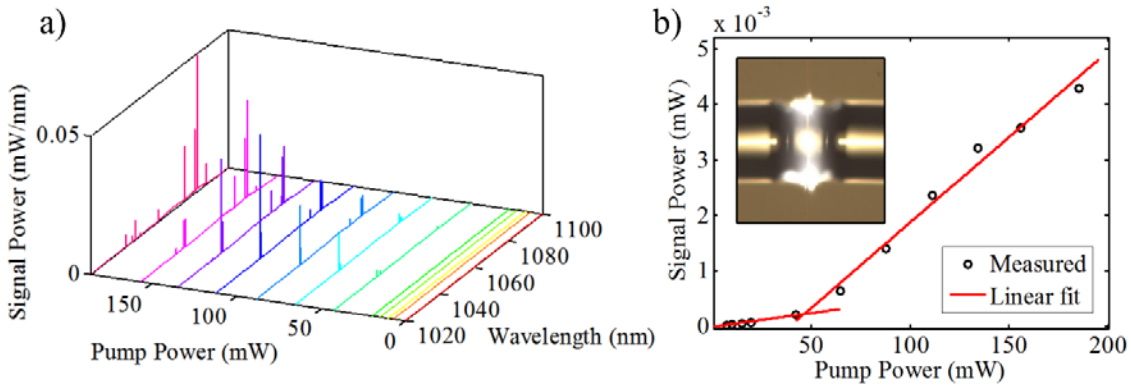

Figure 7-2 a) Spectra of signal as a function of launched pump power, and b) total measured signal as a function of launched pump power (inset shows the light observed at 70mW launched pump power).

tapered fibre and evanescently excites pump WGMs. The generated signal is collected through the same tapered fibre and monitored by an optical spectrum analyser. Lasing peaks corresponding to WGM resonances, located in the 1030-1100nm wavelength range, are observed. Figure 7-2 (a) shows the measured signal spectra as the launched pump power through the tapered fibre increases. The total signal power, calculated by summing up all individual lasing peaks, is plotted in Figure 7-2 (b). The total lasing power is almost linearly dependent to the launched pump power for the powers above a threshold of ~40mW (corresponding to measured absorption of ~1mW). Since lasing action happens along both forward and backward directions, measured values are about half the actual lasing power. The optical-to-optical efficiency with respect to absorbed pump power was ~0.1% (by taking into account both forward and backward propagations). The threshold and efficiency can be further improved by fibre design and optimizing the overlaps between the doped area and pump, and the radial order of the excited signals.

The laser threshold power, optical spectra and efficiency of the milled microrod resonators depend on the resonator length. Figure 7-3 plots the spectra of microrod laser fabricated with lengths of roughly 85µm, 100µm, 150µm and 200µm. The resonators are pumped through the tapered fibre placed at the centre of the resonator with a fixed pump power. For microrod with length of 85µm no WGM lasing is observed. Since the milled side trenches constitute a large portion of the cavity surface, the Q factors of the supported resonant WGMs are low and no lasing is possible. It should be mentioned that the observed broadband (~1050-1090nm) fluorescence is originating from the pump diode. Further increasing the length of the resonator (i.e. $L \geq 100\mu m$), reduces the surface induced scattering losses on the WGMs, and enables lasing. It should be noted that the lasing wavelength depends on the length of the resonator. For L = 100µm the lasing lines mostly lie in the 1030nm wavelength region. This is due to

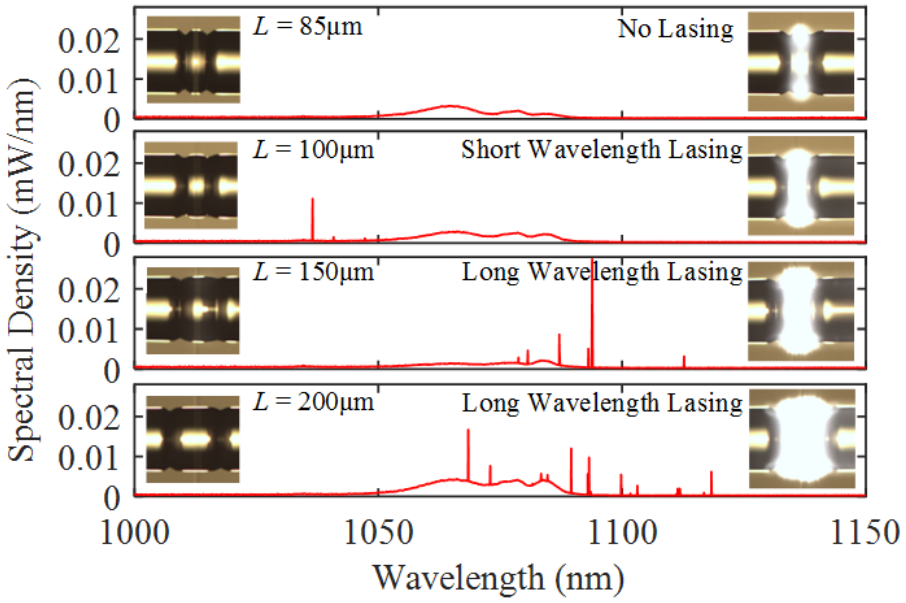

Figure 7-3: Spectral density of microrod laser with lengths of L = ~85µm, ~100µm, ~150µm and ~200µm, excited by a tapered fibre of 2µm diameter coupled to the centre of the resonators, showing different accessible lasing wavelengths as a function of the resonator length. Insets show optical images captured when the cavities are pumped (right side) and not pumped (left side).

the fact that the supported WGM Q factors are still low and therefore a high population inversion is required to achieve lasing, and as explained in Chapter 5, high population inversions favour lasing at wavelengths in the 1030nm region. On the other hand, as discussed previously, increasing the length of the cavity decreases the WGM overlap with the milled side trenches and increases the WGM Q factor. This lowers the required population inversion for lasing, and again from the Chapter 4 analysis, the lasing spectrum is expected to shift to longer wavelengths. Figure 7-3 shows lasing peaks at 1100nm wavelength observed for a microrod fabricated with an increased length of L = 150µm. Further increasing the length of the resonator (i.e L = 200µm), will increase the number of supported WGMs by the microrod resonator and results in a larger number of lasing lines in the spectra.

It should be noted that, as shown in [112] for passive bottle resonators, it is possible to selectively pick different lasing peaks by placing the tapered fibre at different positions along the resonator axis. I have used such property in Chapter 5 and have demonstrated selective excitation of WGM lasing lines in a microbottle resonator across the emission spectrum of Yb ions. In contrast, microrods do not exhibit such characteristic since the modal excitation is not significantly dependent on the taper position along the resonator. I observed that changing the taper position along the microrod laser does not affect the lasing wavelength band. However, due to different

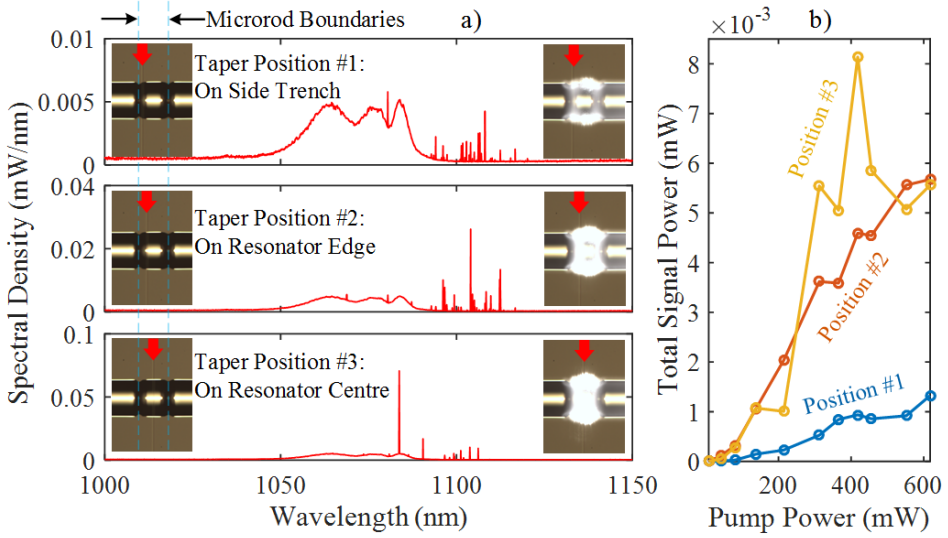

Figure 7-4 a) Spectral density of microrod laser with length of ~200µm, excited by a tapered fibre of 2µm diameter placed on the side trench, edge and centre of the resonator. Insets show optical images captured when the cavity is pumped (right side) and not pumped (left side), and red arrows show the position of the input tapered fibre. b) Lasing characteristics of the microrod laser for taper positions of #1, #2 and #3.

amount of cavity loading and coupling of tapered fibre to various WGMs at different positions, the threshold, output power and slope efficiency are significantly affected.

Figure 7-4 (a) shows the spectra of the microrod laser excited by tapered fibre placed on three distinct positions along the resonator profile. First, the lasing lines appear at longer wavelengths (i.e. 1100nm band) independent from the taper position, due to relatively high WGM Q factors ensured by the long resonator length (L = 200µm) and the low inversion levels required. The scattered light from the resonator shown in the insets of Figure 7-4 (a) appears considerably lower when the taper is placed towards the resonator edges (position #1). Second, as shown in Figure 7-4 (b), position #1 gives also the lowest optical efficiency, due to the relatively lower Q of the WGMs in this case. The highest optical efficiency is observed with the tapered fibre in the resonator centre (position #3). However, in this case, the output power showed large fluctuations, due to stronger internal WGM powers, and modal spatial and spectral competition.

7.3 Side-collection and -pumping of WGMs in Microrod Lasers

In the previous section, I used the conventional tapered-fibre excitation/collection approach in order to benchmark the microrod laser performance. In this next section, I first demonstrate the possibility of side-leakage in microrod resonator lasers when evanescently excited with a tapered fibre, and then show lasing in such resonators without the use of evanescent fibre taper excitation.

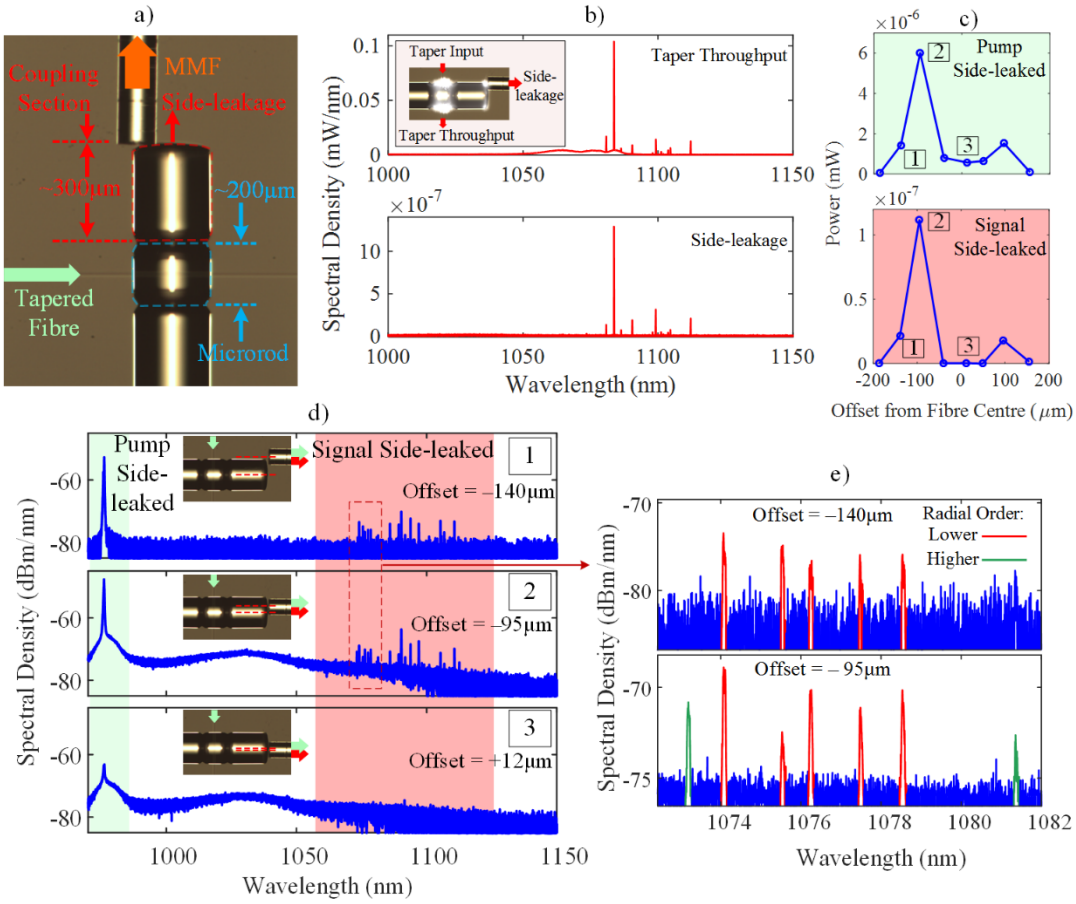

Figure 7-5: a) Optical micrograph of mircrorod laser coupled to tapered fibre including a coupling section butt-coupled to a multimode fibre in order to collect the side-leaked power, b) spectral density of the taper throughput and side-leakage through MMF at ~95µm centre-to-centre offset with the coupling section as shown in the inset, c) side-leaked pump and signal total powers collected by the MMF as function of its centre-to-centre offset with the coupling section, d) side-leaked pump and signal spectra corresponding to MMF offsets of -140µm, -95µm and +12µm, and e) detailed spectra of collected signal by the MMF showing various radial order WGMs accessible by offsetting the collection fibre along the coupling section.

Figure 7-5 (a) shows the microrod resonator with length of L = 200µm coupled to a tapered fibre at the centre. One side of the stem fibre is cleaved at an offset of ~300µm from the resonator side trench using pulsed CO_2 laser cleaving. A multimode fibre (MMF) with core and cladding diameter of respectively 50µm and 125µm is butt-coupled to the cleaved end of the structure, as illustrated in Figure 7-5 (a). Pump power at 976nm is evanescently coupled to the resonator using the tapered fibre at the microrod centre, and the output powers of the taper and the MMF are monitored simultaneously using two OSA's. Figure 7-5 (b) plots the taper throughput and the MMF spectral density with a centre-to-centre transverse offset (in the plane of the page) of ~95µm between the MMF collection and the coupling section as shown in the inset of the figure. Each WGM line collected at the taper throughput shows a corresponding

lasing line leaked out through the stem coupling section. Due to the 20μm-deep undoped cladding, the higher radial order pump WGMs should be excited in order to have significant overlap with the active core, and hence, achieve adequate population inversion. This, in turn, enables excitation of high radial-order modes for the lasing signal. On the other hand, due to the limited depth of the macro-machined grooves forming the microrod cavity, these modes can leak out into the adjacent fibre stems. This is similar to the leakage observed in passive micro-bottle resonators [119].

Figure 7-5 (c) plots the integrated power of both signal and pump side-leaked from the resonator and collected by the MMF as a function of the centre-to-centre offset between the cleaved fibre cross-section and the MMF. Pump and signal powers are maximum at offsets close to the edges of the active fibre, which indicates that both pump and signal are in WGMs. The collected signal and pump spectra for MMF offsets very close to the edge of the coupling section (i.e. -140μm and -95μm) and close to the centre are plotted in Figure 7-5 (d). No WGMs were observed close to the centre of the coupling section cross-section. While, as shown in detail in Figure 7-5 (e), different radial order modes can be accessed by offsetting the MMF collection from the edges of the coupling section. Higher order radial WGMs exhibit a maximum field intensity at smaller radii from the centre.

Figure 7-6 (a) shows a fabricated microrod resonator with length of ~200μm and a coupling section of ~450μm long. The depth of the side trenches is reduced to ~10μm in order to increase the efficiency of the WGM out-coupling. A 976nm LD pump using a single mode fibre is now butt-coupled to the device. The pump power is launched into the microrod resonator after propagating through the coupling section. In this predominantly single-pass pumping scheme, the bulk of the active medium inside the microrod is pumped and inverted and no strong pump WGMs are expected to be excited. A tapered fibre is used in this case, primarily, as an out-coupling port to pick up the generated signal WGMs. Figure 7-6 (b) shows the spectra obtained when the tapered fibre is placed on the stem (outside of the resonator) and on the centre of the microrod resonator. Lasing lines between 1060-1100nm indicate the generation of signal WGMs. As the tapered fibre is placed on the resonator, a significant reduction in the number of lasing peaks is observed. This is because of the decrease in the total Q of the signal modes due to excessive out-coupling into the tapered fibre, which increases the lasing threshold for a number of signal WGMs. It is worth mentioning that, lasing is obtained only when the input pump fibre is coupled close to the edge of the coupling section. This indicates that given that the generated signal WGMs are generally located close to the

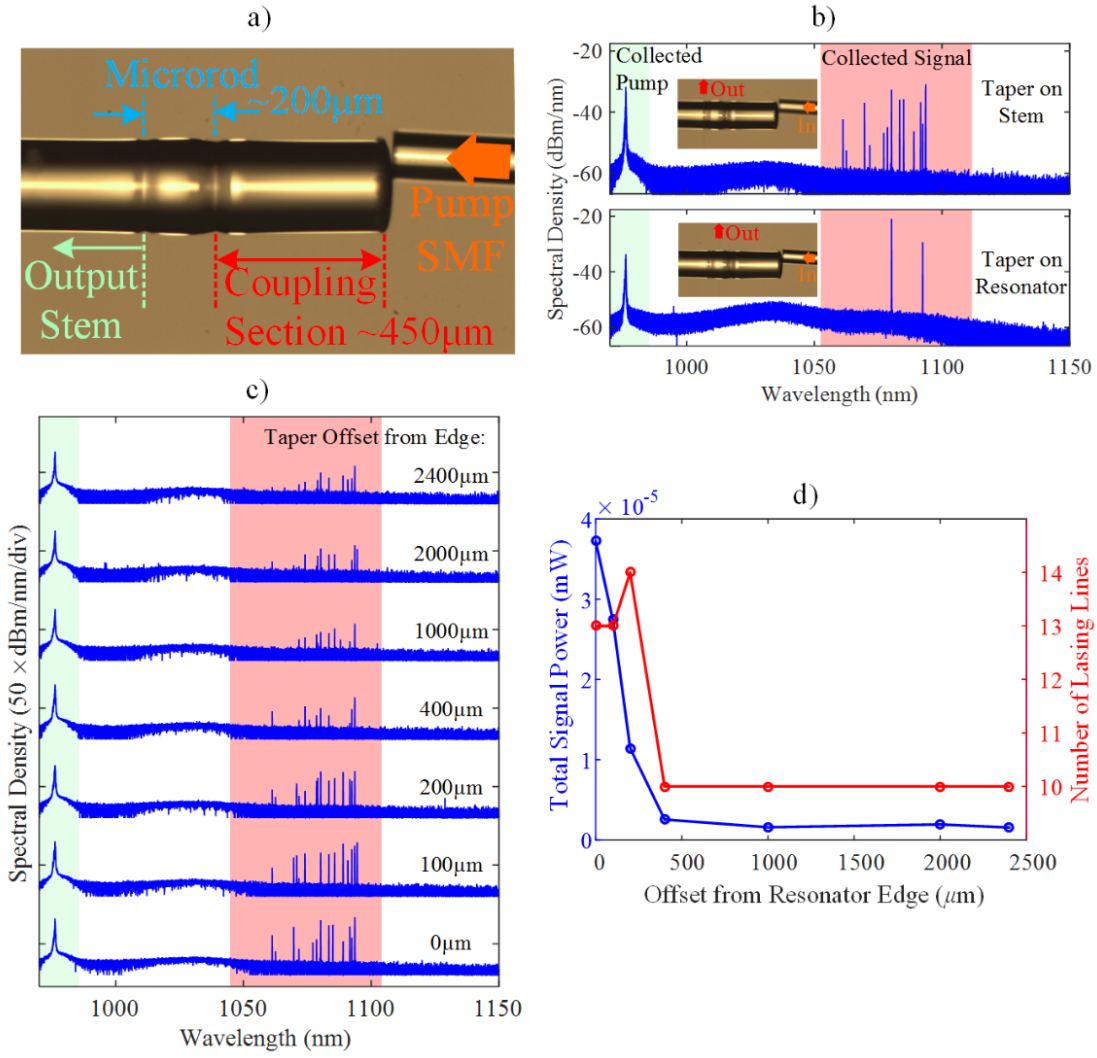

Figure 7-6 a) Optical micrograph of mircrorod laser consisting of coupling section side-pumped using a SMF, b) spectra of collected light by a tapered fibre evanescently-coupled to the stem and centre of the resonator while side-pumped, c) collected spectra leaked out into the output stem as a function of the tapered fibre offset from the edge of the resonator, and d) corresponding total integrated signal power and number of lasing lines.

edges of the resonator, we only need to predominantly invert the portion of the active medium close to the boundary of the resonator with the surrounding air.

The spectra of the collected light through the tapered fibre at various positions along the output stem are plotted in Figure 7-6 (c). Accordingly, the corresponding integrated signal power and number of observed lasing lines as a function of the taper offset from the resonator edge are shown in Figure 7-6 (d). Results show that, the signal power is attenuated more than 10dB within the first 400µm propagation length, and, then remains constant up to offset of 2.4mm (maximum offset set by our translational stage). At the same time, the number of survived modes reduces from 14 to 10 and clamps to that number for offsets above 400µm. The number and type of signal WGM that survive

after propagation in the output stem depends on the relative overlap with the residual pump and, therefore, inverted medium in this section. Since the pump is primarily launched close to the outer core/cladding interface of the active fibre, the surviving signal WGMs are expected to be of lower radial order. No signal WGM is observed at the end facet of the output stem fibre having a length of ~7cm.

By modifying the coupling section and the resonator side-trenches, pumping and WGM out-coupling of the microrod can be further enhanced, leading to elimination of the tapered fibre out-coupling mechanism. Figure 7-7 (a) shows a milled-180µm-long microrod with ~140µm long coupling section side-pumped non-evanescently using a single mode 976nm LD pump. The scattered light and output stem, through which the residual pump and generated signal WGMs are monitored, are also shown in Figure 7-7 (a). The coupling section controls the shape and modality of the pump light before entering the resonator section. Subsequently, the generated signal WGMs and residual pump leak out through the collection fibre stem. Figure 7-7 (b) plots the obtained spectra at the output of the stem fibre, with a length of ~4cm, as the launched pump power increases. Signal WGMs with various thresholds are collected at the output of the device. The WGM signal leakage serves as an effective "output coupler" [119], and, along with the WGM selection and overall laser efficiency, can be controlled by the micro-groove shapes and the pumping configuration. A closer look at the output signal spectra shows red-shifting of the excited signal WGMs as the pump power increases

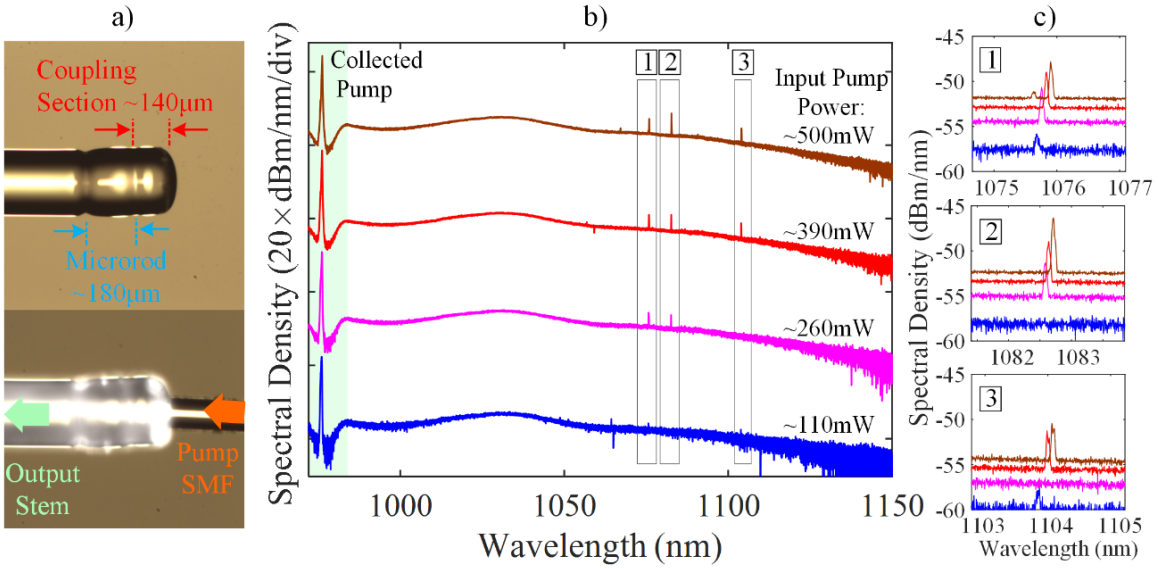

Figure 7-7 a) Optical micrograph of modified mircrorod laser (top) and scattered light when side-pumped using a SMF (bottom), b) spectra of the collected signal from the output stem fibre at various pump powers, and c) detailed spectra of the three distinct WGMs generated at signal wavelengths.

(see Figure 7-7 (c)). This is due to the temperature increase caused by the intense pump beam in the microrod cavity.

7.4 Conclusion and summary

In this chapter, microrod resonator lasers are fabricated directly from rare-earth doped fibres. Micro-milling is done using controlled pulsed CO_2 lasers on the fibre surface. Such method significantly shortens the fabrication time, offers much more control over the microcavity design, and potentially enables large number of identical microresonators in one-fabrication-step process. High passive loaded Q factors at 1551nm wavelength close to 10^7 were measured.

Lasing in an Yb^{3+}-doped microrod resonator coupled to a tapered fibre is first demonstrated. It is found that the lasing wavelength band depend on the microrod length. For very short ones (i.e. L~85μm) no lasing was observed due to high losses induced by surface roughness at the side trenches. Short microrods (i.e. L~100μm) exhibit lasing at short wavelengths (at 1030nm band) due to lower signal WGM Qs and higher level of required population inversion. Longer microrods ($L \geq 150$μm) result in lasing at longer wavelengths (at 1100nm band), which corresponds to the peak gain wavelength at low inversion levels. In contrast with microbottle lasers for which the lasing wavelength band was found to be dependent on the taper offset from the resonator centre, microrod lasers show no significant shifts between 1030nm and 1100nm band as the taper is translated along the resonator profile.

Furthermore, it is demonstrated that the WGMs in a microrod can leak-out into the stem fibre. The fibre stem is terminated at one side of the resonator forming a coupling section through which the leaked-out WGMs are collected using a MMF. It is shown that different radial order WGMs can be collect by offsetting the collection MMF along the cross-section of the out-coupling fibre stem, when a tapered fibre evanescently excites the microrod. On the other hand, pumping can be achieved without using tapered fibres, by simply butt-coupling the pump out of a SMF into the coupling section. I observed excitation of WGM signals and leakage of these modes into the output stem fibre using tapered fibre probing. Finally, I showed that by modifying the resonator structure, such as reducing the coupling section and the depth of the side trenches, it is possible to remove the need for a tapered fibre out-coupling system, and the signal power can be collected at the end of the stem fibre. Modifying the pump power distribution and optimizing the distribution of the dopants can further improve the performance of the device.

This work is a significant step towards development of stand-alone, robust and fully fiberised WGM microresonator lasers, where the pump launching and signal collection are achieved through the fibre stems in order to eliminate the need of conventional additional coupling and launching optics in WGM microresonators. Such microresonator structures, with two fibre stems attached naturally to the resonator ends, will enable a variety of future robust sensing and other applications.

Chapter 8 Wide-band Cooperative Raman Lasing in Yb^{3+}-doped Microresonators

8.1 Introduction

Nonlinear optical processes such as Raman amplification and Four-wave Mixing (FWM) can be stimulated with high optical intensities in silica. The main application of these processes is to generate light at other wavelengths, which are not accessible by rare-earth transitions. On the other hand, additional costs and fabrication difficulties in making rare-earth doped glasses, can be lowered by using such nonlinear optical phenomena. WGM resonators, due to their high Quality (Q) factor and low mode volume (V), are great platforms for realization of such nonlinear optical processes, which require relatively high intensities inside the medium. Low threshold Raman lasing in undoped WGM silica, silicon and CaF_2 microresonators have been demonstrated so far [151-157].

In order to increase the intensity of WGMs, the intrinsic losses of the resonator should be lowered. One way is to improve the surface roughness of the resonator by thermally melting and reflowing the resonator surface. In this study, I achieved cascaded Raman lasing up to fifth order over 160nm wavelength range in un-doped (passive) Microstub Resonators (MSRs). Combining Raman and rare-earth lasing will enable extending the lasing wavelength beyond the normal emission range of the rare-earth ions. More importantly, by enhancing the Q of Yb-doped (active) MBRs and microspheres, aforementioned nonlinear optical processes arise, and can cooperatively extend the lasing action to more than 350nm wavelength shift by pumping at 976nm. This is a promising advancement in generation of narrow linewidth optical signals close and/or within O-band telecom wavelength band. On the other hand, microbottle resonators are fabricated as integrated part in the middle of optical fibres capable to be mechanically tuned by pulling or pushing from the side fibre stems.

8.2 Cascaded Stimulated Raman Scattering in Passive Microstub and Microbottle Resonators

Figure 5-1 (a) demonstrates a fabricated microstub (MSR) with length of ~390μm and diameter of 150μm. The MSR is fabricated from normal silica SMF28 (diameter of 125μm), and to increase the Q of the supported WGMs, the edges of the resonator are

significantly smoothed comparing to the device fabricated in Chapter 6. Supported resonances are predicted to exhibit Q factors in excess of 3×10^7, which is the maximum measurable Q by our experimental setup.

In a medium with an intensity-dependent gain (such as Raman gain), the threshold launched pump power (P_{th}) in terms of pump effective mode volume (V_{eff}), and pump and Raman signal wavelengths (λ_p, λ_R) is given by [152]

$$P_{th} = \frac{\pi^2 n^2}{\lambda_p \lambda_R} \frac{V_{eff}}{\Gamma B g} Q_{ext(p)} \left(\frac{1}{Q_p^T} \right)^2 \frac{1}{Q_R^T} \qquad 8\text{-}1$$

where n is the refractive index, Γ ($0 \le \Gamma \le 1$) is the spatial overlap factor between the pump and Raman WGMs, g is the nonlinear bulk Raman gain coefficient, and B is the

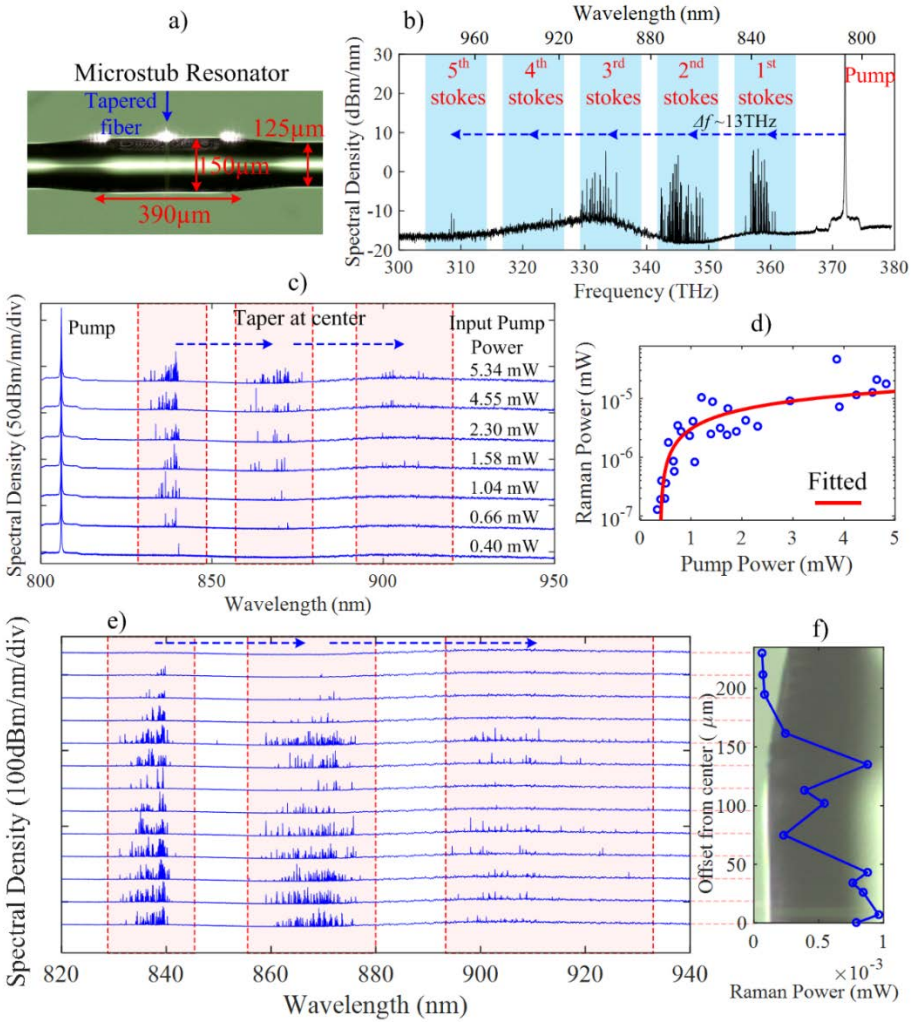

Figure 8-1 a) Fabricated MSR coupled to tapered fibre at centre, b) cascaded SRS up to fifth order obtained by pump MSR at ~806nm, c) Raman spectra of MSR as function of launched pump power, d) integrated Raman power as function of the input pump power and corresponding fitted theoretical curve, e) spectra of the MSR as a function of tapered fibre coupled at various offsets from the resonator centre, and, f) total obtained Raman power as a function of the taper offset from the resonator centre.

circulating intra-cavity power correction factor when the backscattered WGM is also taken into account ($0.5 \le B \le 1$). $Q_{ext(p)}$ denotes the external Q of pump, and Q_p^T and Q_R^T are the total Q of pump and Raman modes, respectively. The total Q's are determined from the intrinsic Q such that $1/Q_{WGM}^T = 1/Q_{ext(WGM)} + 1/Q_{0(WGM)}$ where $Q_{0(WGM)}$ indicates the intrinsic Q of WGM. Generally speaking, the threshold pump power is proportionally related to V_{eff}/Q^2. This means that the Q factor of the resonator is a substantial factor in determining the Raman lasing characteristics. With previous resonators studied so far in this study, no Raman lasing was observed due to relatively low Q (~10^6). With further fire-polishing and precise care during fabrication of microresonators, the intrinsic Q factor can be increased beyond 10^8.

With MSRs, in addition to surface roughness, the light scattering due to sharp edges of the stub should be mitigated. Therefore, the angle of stub edges is further increased providing a smooth transition from the rectangular region to the stem fibres, resulting in almost two orders of magnitude better Q factors. Pump light at ~806nm wavelength from a Ti:Sapphire laser, is launched into a tapered fibre with ~2μm waist diameter. The tapered fibre is evanescently coupled to the MSR from the top by touching the resonator surface at the centre. Figure 5-1 (b) plots the obtained spectra, for a pump power far beyond the threshold value, showing cascaded Raman lasing up to the fifth order between ~830-970nm. Groups of Raman lines are shifted in frequency by ~13THz on average along the spectra corresponding to the shift of Raman peak gain in Silica.

In order to investigate the threshold pump power, the incident pump power is gradually increased. The spectra are plotted in Figure 5-1 (c) for various input pump powers where cascaded Raman stokes rise consecutively. The total integrated power of Raman lasing lines as a function of the input pump power is plotted in Figure 5-1 (d). The obtained threshold input pump power is ~400μW. It should be noted that, the Raman power does not change linearly with the input pump power. If we assume identical Q factors for both pump and signal WGMs, the Raman power (P_R) is related to the input pump power (P_p) such that [36]

$$P_R = \frac{\lambda_p}{\lambda_R}\left(\frac{1}{Q_{ext}}\right)^2\left(\frac{1}{2Q_0}+\frac{1}{2Q_{ext}}\right)^{-2}\cdot P_{th}\left(\sqrt{\frac{P_p}{P_{th}}}-1\right). \qquad 8\text{-}2$$

The nonlinear dependence of the output Raman power to the input pump power stems from the fact that, for a given coupling condition, the intra-cavity pump field is fixed to its value at threshold. The red solid line in Figure 8-1 (d), which is obtained by fitting Eq. 8-2 to the measured Raman power, illustrates such nonlinear relation.

Moreover, spectra of the MSR when the tapered fibre is coupled at various positions along the resonator is plotted in Figure 5-1 (e). The corresponding total Raman power

as a function of taper offset from the MSR centre is shown in Figure 5-1 (f). As we have previously observed, the density of the excited modes in transmission spectra of passive MSRs does not change dramatically by shifting the tapered fibre offset along the resonator length. This originates from the uniform spatial distribution of the WGM fields along the resonator profile. Unlike MBRs (which will be discussed later), the Raman lasing takes place at almost every point along the MSR. The dip in the Raman power at ~75μm offset from the resonator centre is due to low Q of the resonator, which is induced by imperfections (change in mechanical stress) at the splice point between the large and small diameter fibres.

In Section 8.2 of this chapter, SRS is employed to further improve the performance of Yb^{3+}-doped MBRs. Thus, it is worth, first, investigating the characteristics of Raman lasing in passive MBRs. An optical image of a fabricated MBR from a normal silica SMF28 with a maximum diameter and length of respectively ~142μm and ~294μm, is displayed in Figure 8-2 (a). The resonator is further fire-polished in order to improve the surface quality, and thus, lower the lasing threshold. No SRS lasing is observed when the excitation tapered fibre is placed on the centre of the resonator. Therefore, the tapered fibre is coupled to the resonator at an offset of ~100μm from the centre where the maximum number of lasing lines are obtained. Spectral densities of the cascaded SRS lasing for various pump powers at ~806nm wavelength are plotted in Figure 8-2 (b). The corresponding integrated Raman power as function of the incident pump power is plotted in Figure 8-2 (c). Fitted curve shows the square root relationship of the Raman power to the input pump power. The threshold launched pump power, at this taper offset, is measured to be ~5mW.

Moreover, the spectra corresponding to excitation tapered fibre at offsets along the MBR is shown in Figure 8-2 (d). The highest observed order of cascaded SRS stokes with MBRs was three. As demonstrated in Figure 8-2 (e), the Raman power is zero at central excitation due to over-coupling of excited WGMs to the fibre mode. On the other hand, at slightly off-centre excitations, there is an increase in the Raman power corresponding to critical coupling to low axial WGMs.

Higher threshold pump power, and lower number of cascaded stokes in MBR comparing to MSR, is due to the lower total Q of the MBR. It should be noted that all parameters in fabrication of both MBR and MSR are kept fixed. The critical point in determining the intrinsic Q is the splicing point where arching is more intense and there is excessive scattering due to surface roughness (due to metallic tip residues) and change in the glass index owing to induced mechanical stresses. For a MSR the splice points are far from the centre of the resonator, hence, exhibits higher Q's. While, in a MBR, the splicing point is at the centre of the resonator, which significantly degrades the Q factor

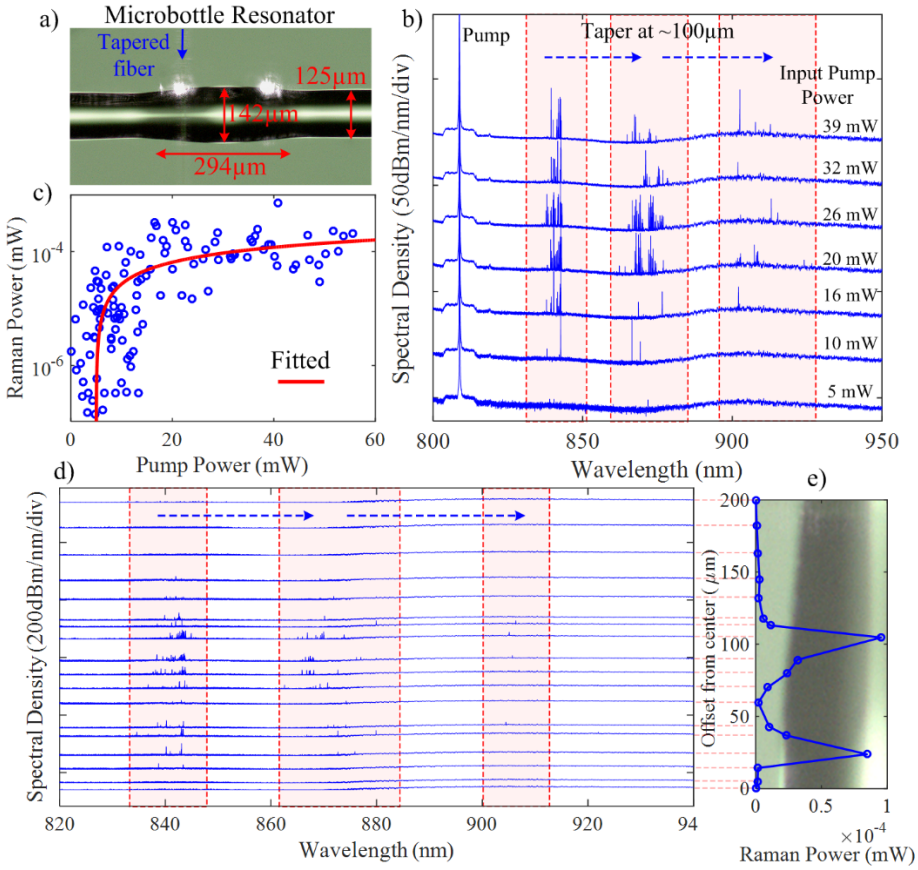

Figure 8-2 a) Fabricated MBR coupled to tapered fibre at ~100µm offset from the resonator centre, b) Raman spectra of MBR as function of launched pump power, c) integrated Raman power as function of the input pump power and corresponding fitted theoretical curve, d) spectra of the MBR as a function of tapered fibre coupled at various offsets from the resonator centre, and, e) total obtained Raman power as a function of the taper offset from the resonator centre.

of the WGMs. Hence, the threshold pump power is higher in a MBR comparing to MSR. On the other hand, lower Q produces lower internal SRS power, resulting in lower number of cascades.

It should be noted that this is an indication of importance of Q factor in lowering the Raman threshold. Although MSRs exhibit greater mode volumes comparing to MBRs, they show lower threshold pump powers and greater number of SRS cascades.

8.3 Cooperative Yb^{3+}-Raman Lasing in Active Microbottle Resonators

As investigated in Chapter 5, MBRs are promising candidates for the realization of selectively-excited low threshold microcavity lasers. On the other hand, further improving the fabrication process and optical quality of such devices gives rise to a large number of optical nonlinear phenomena. Such processes are extremely important in

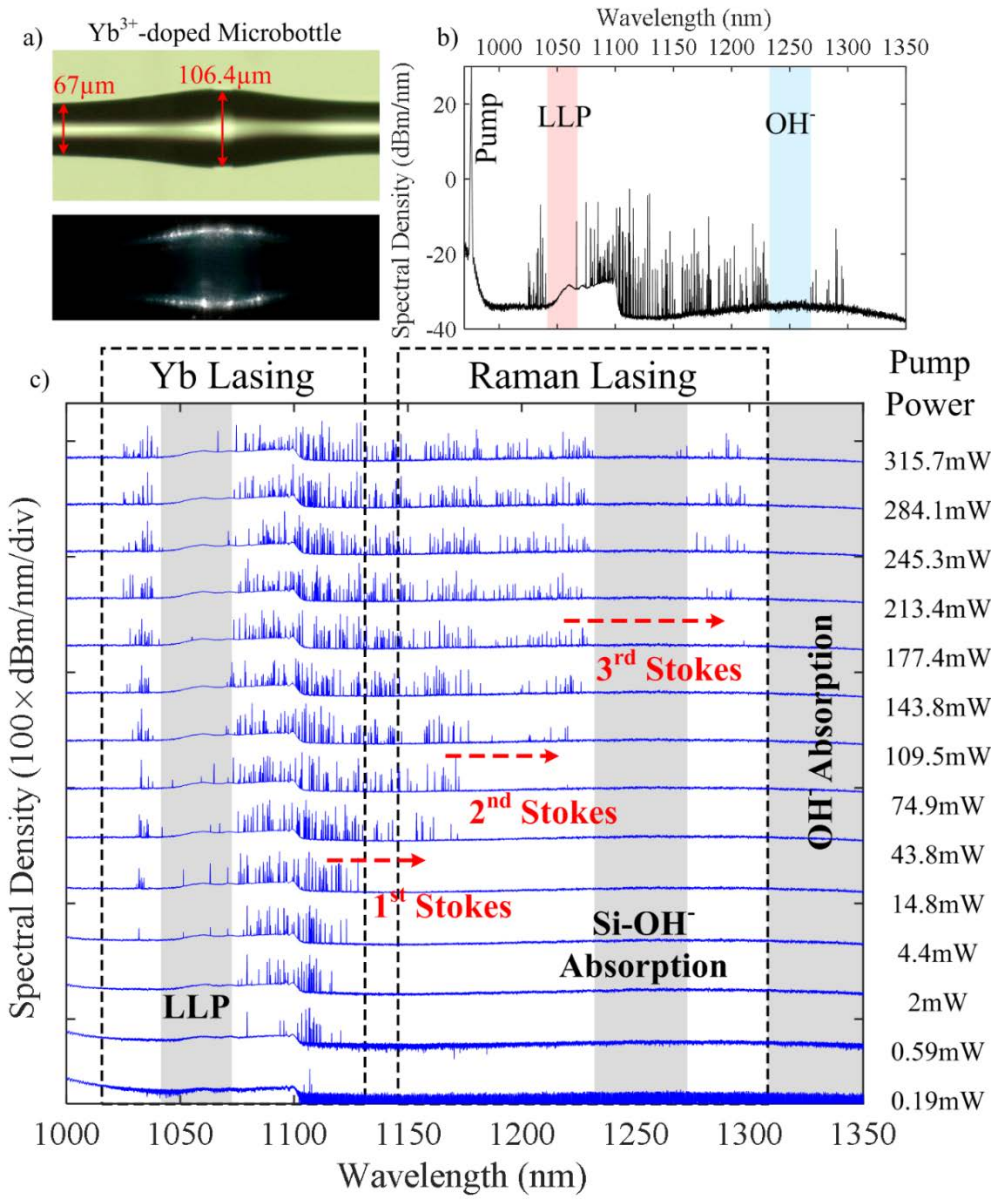

Figure 8-3 a) Super-polished Yb^{3+}-doped MBL coupled to a tapered fibre at off-centre (~19µm) showing blue and green lights scattering from the surface of the resonator, corresponding to Yb-Yb cooperative up-conversion and signal florescence, the shown LLP and OH^- gaps correspond to low lasing probability zone and loss due to OH ions absorptions, respectively b) obtained cooperative Yb–SRS lasing spectra of MBL at pump power far beyond the threshold value, and c) spectra of the MBL as function of pump power showing Yb-lasing and cascaded SRS rising at different pump powers.

light generation beyond the emission band of rare-earth ions, metrology and sensing applications.

Figure 8-3 (a) displays a fabricated MBL from a commercial large core Yb^{3+}-doped fibre using fabrication method discussed in Chapter 3. The microresonator is further fire-polished in order to improve the surface quality of the resonator resulting in total Q factors beyond 3×10^7. The fabricated MBL has a maximum diameter of ~106.4µm and stem diameter of ~67µm. A tapered fibre is coupled to the resonator at ~19µm offset where the most number of lasing lines are observed. The blue and green light

discernible in Figure 8-3 (a), are related to Yb^{3+} cooperative up-conversion corresponding to pump wavelength and signal fluorescence, respectively, which are scattered out due to surface roughness. Figure 8-3 (b) plots the obtained spectral density when the MBL is pumped by a 976nm wavelength LD at ~315mW power. The spectra shows a significant increase in the observed lasing lines when compared to the MBL presented in Chapter 5 with relatively lower Q factors of about 10^6. On the other hand, lasing spectra is extended far beyond the emission band of Yb ions up to 1300nm due to cascaded SRS. Two gaps in the spectra indicated by LLP and OH^- respectively correspond to the Low Lasing Probability zones and optical loss due to the OH ions absorption in silica.

Furthermore, the spectra of the MBL as a function of input pump power are plotted in Figure 8-3 (c). Yb^{3+}-lasing commences first at a threshold pump power as low as ~190µW, due to high intrinsic Q factor of the resonator (compared to the lowest threshold of ~1.3mW obtained with resonator having loaded Q of ~10^6). It should be noted that, lasing starts first at 1100nm lasing band, owing to the low population inversion induced by low pump power. As the input pump power is further increased,

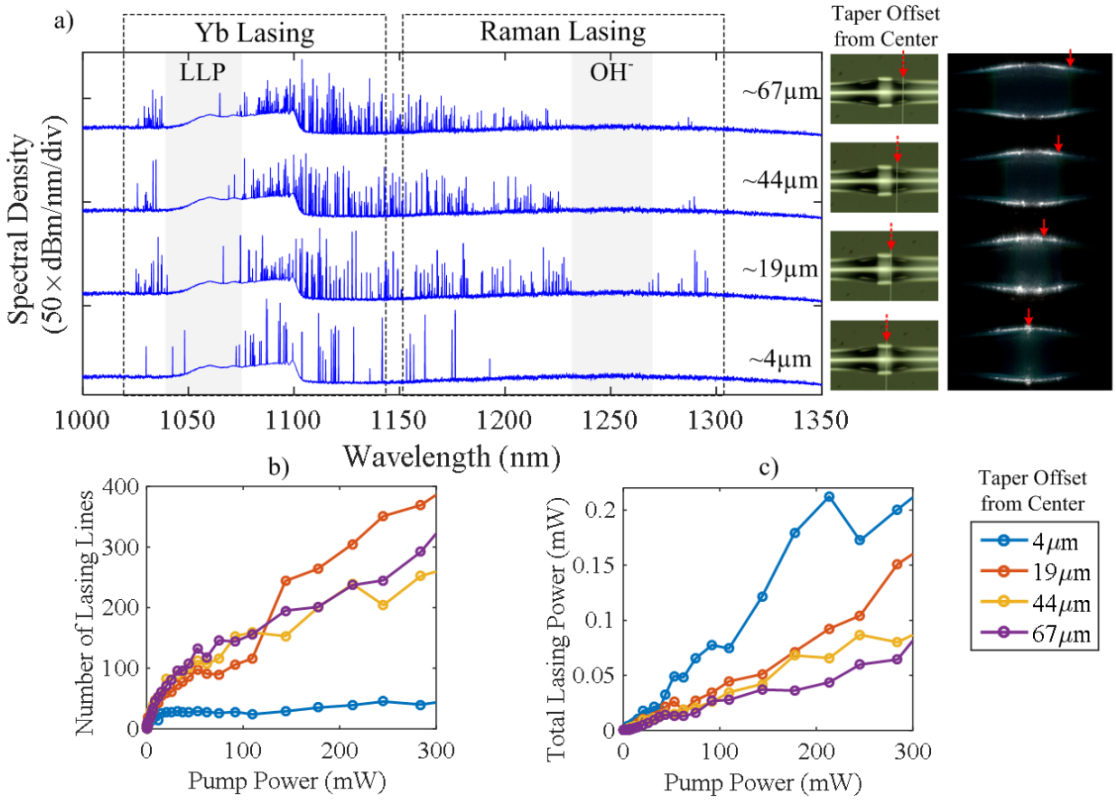

Figure 8-4 a) Spectra of MBL pumped at a power of ~315mW with tapered fibre at various offsets from the centre for which the corresponding optical images showing the position of the taper and emitted visible light from the MBL under operation (the red arrows show the position of coupling), b) Number of lasing lines, and c) total lasing power as function of pump power for taper offset of ~4, 19, 44, 67µm from centre of the MBL.

the intra-cavity pump intensity increases, resulting in higher inversions, resulting in lasing at the 1030nm band. On the other hand, the OH^- loss increases at wavelengths beyond 1300nm resulting in significant reduction in the intra-cavity powers.

Next, the tapered fibre is shifted along the resonator axial length at four different offsets from the MBL centre. Figure 8-4 (a) plots the obtained spectra, at a fixed pump power (well-above the threshold of the third order cascaded SRS lasing) at taper offsets of ~4, 19, 44, 67μm from the centre. The optical images showing the tapered fibre coupled to MBL for each taper offset, and corresponding scattered light from the resonator, are also shown. Results show that the broadest spectrum happens at offset of ~19μm where the fibre mode is critically-coupled to the low order axial WGMs. There are fewer number of WGMs excited/collected at the centre, owing to over-coupling to low order axial modes. As the tapered fibre translates towards the large offsets, the spectra stay relatively broad. However, the output power at longer wavelengths, where the third order SRS Stokes are located, diminishes due to under-coupling. The number of lasing lines and total integrated lasing power as function of input pump power, are plotted in Figure 8-4 (b) and (c), respectively. The number of lasing lines stays almost unchanged, for taper placed close to centre and pump powers well above the threshold. While, the total lasing power increases with respect to the input pump power. These lines mainly correspond to Yb^{3+}-lasing. As the taper fibre shifts to larger offsets, the number of lasing lines grows as the pump power increases which indicates that Raman lines appear in the spectra. On the other hand, the obtained total power is highest when the tapered fibre is placed very close to the centre. This is due to the higher intrinsic Q of the resonator, combined with high order (axial and/or radial) WGMs resulting in large internal powers. When compared to the MBL with relatively lower Q factor (studied in Chapter 5), most of the modes were highly suppressed when the tapered fibre was place at the centre.

8.4 Cooperative Yb^{3+}-Raman Lasing in Active Microsphere Resonators

Although MBLs provide the unique capability to selectively couple to distinct axial modes by changing the taper position along the resonator profile, to some extent, they lack the capability of independent large Q improvements. This is because, additional fire-polishing, required for the Q improvement, increases the possibility of uncontrolled deformation of the profile of the microbottle. It has been experimentally observed that precise control of the microbottle parameters during the fabrication process is a complex

task. However, the Q factor of microspheres fabricated at the tip of optical fibres can be improved enormously by fire-polishing without significantly affecting the spherical shape of the resonator. On the other hand, initial fibre diameter and the number of applied electrical arcs determines the final diameter of a microsphere. Several microspheres, with various diameters, are fabricated for this study. The number of applied electrical arcs is fixed for all the fabricated spheres, while the initial fibre diameter is altered in order to obtain various sphere diameters. The same Yb^{3+}-doped active fibre is tapered down to smaller diameters. Figure 8-5 includes optical images of the fabricated super-polished microspheres with radii between ~45-140μm. The measured eccentricity of the fabricated devices (defined as $1–R_{minor}/R_{major}$) from the optical images, is calculated to be less than 0.015.

The measured spectra of the microspheres pumped at 976nm wavelength is shown in Figure 8-5. The launched pump power is ~300mW, and the excitation-tapered fibre is positioned on the resonator where the maximum number of modes is observed. The obtained spectra show Yb-lasing and the following cascaded SRS lines up to the third order. OH^- absorption is again responsible for the gap at around 1250nm wavelength and the abrupt power drop beyond 1330nm wavelength. It should be noted that, as the resonator radius decreases from 140μm to 45μm, the lasing wavelength range expands towards both shorter and longer wavelengths. An analytical estimation of the effective mode volume in spherical resonators is given in [158] as

$$V = 3.4\pi^{3/2}\left(\frac{\lambda}{2\pi n}\right)^3 l^{11/6}\sqrt{l-m+1} \qquad 8\text{-}3$$

where ℓ and m denote the azimuthal and angular mode numbers. Former relation implies that, a microsphere with radius of 140μm exhibit a fundamental mode volume (for which $\ell = m$) of ~8 times larger than one with radius of 45μm. Hence, larger microspheres generally support lower intensity WGMs, resulting in lasing at longer wavelengths (i.e. above 1100nm) due to lower level of population inversion. On the other hand, due to relatively lower gain of Yb^{3+} at long wavelengths, and low mode volume of large spheres, the internal WGM power is lower when compared to small ones. Therefore, large spheres show also limited spectral broadening due to SRS. As a result, lasing lines between 1040nm and 1350nm are obtained with a microsphere of 45μm radius. It should be noted that larger spheres naturally show greater number of modes.

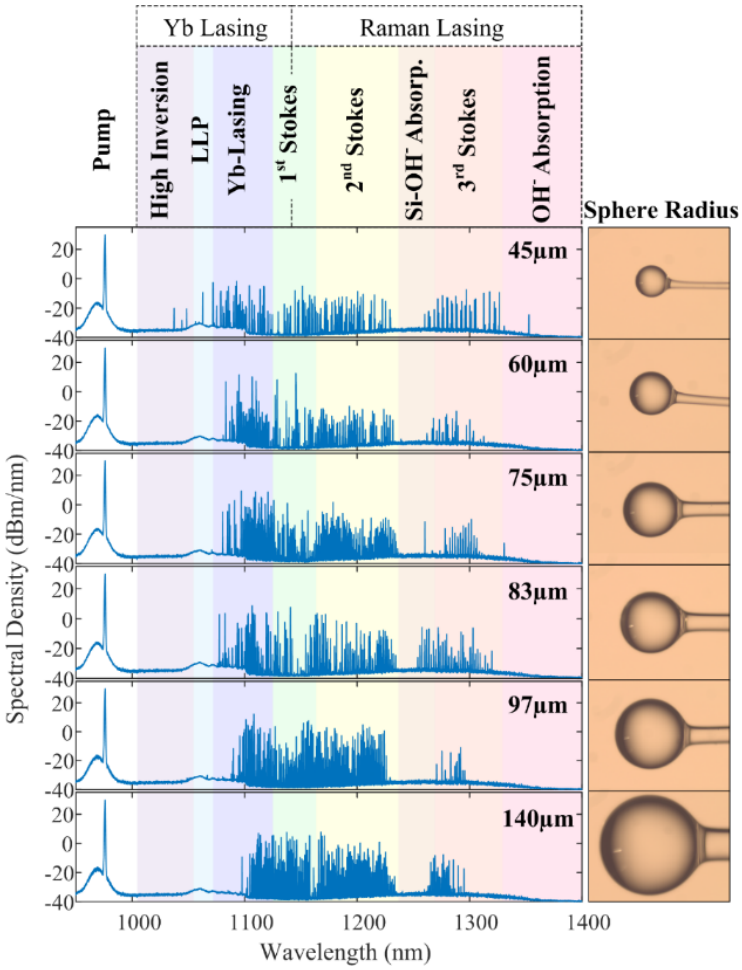

Figure 8-5 Spectral densities of cooperative Yb-Raman lasing for super-polished Yb^{3+}-doped microspheres with various diameters between 45-140µm showing lasing spectrum broadening as microsphere diameter decreases. Input pump power of ~300mW launched into a tapered fibre is coupled to the resonator where the maximum number of lasing lines is obtained.

Furthermore, due to unavoidable small eccentricity of the fabricated microspheres, the angular modes (with same azimuthal and same radial orders) are no longer frequency degenerate. On the other hand, the stem fibre on which the microsphere is formed, breaks the spherical symmetry of the resonator, as well as producing a nonhomogeneous stress distribution along the resonator. These effects result in a small dependency of the resonator spectra on the position of the coupled taper. It should be noted that ideally the spectra of a perfect microsphere do not depend on the relative tapered fibre position, and WGMs always circulate along the circumference. Figure 8-6 shows the obtained spectra for a fixed pump power as function of taper offset from the centre of microspheres with radii of 45µm, 83µm and 97µm. For 45µm-radius microsphere, the spectrum is significantly dependent on the taper position. At –20±5µm offsets, a significant reduction in the number of lasing lines, is observed due to over-coupling to WGMs. At slightly off-centre excitation, critical-coupling to low order

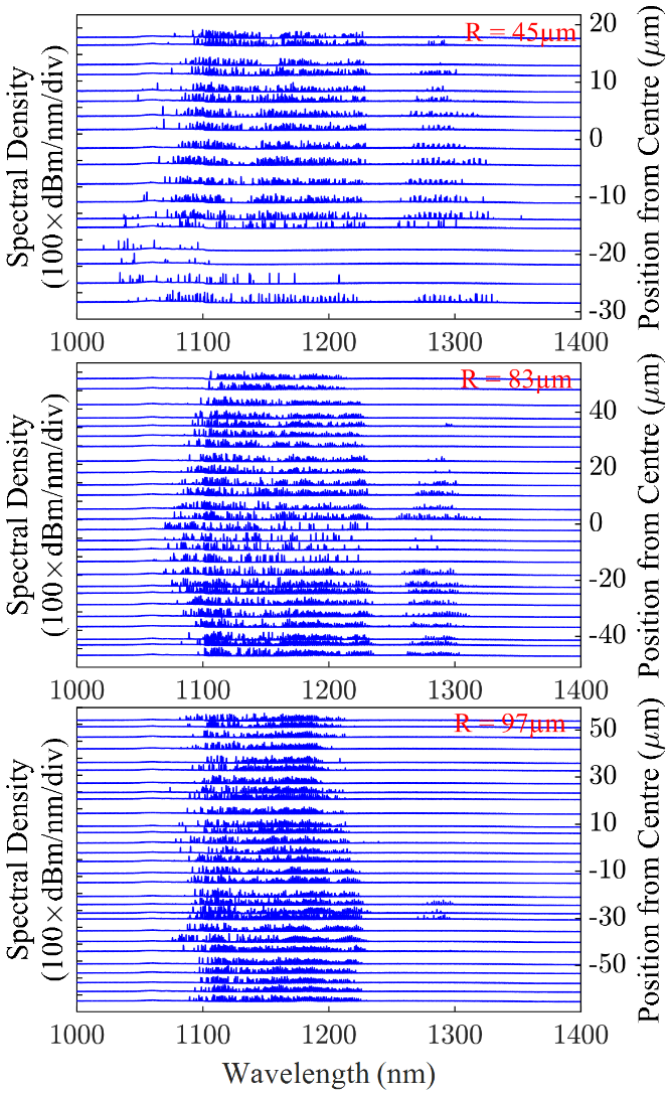

Figure 8-6 Spectral density as a function of taper offset from the centre of microspheres with radius of 45μm, 83μm and 97μm. Launched pump power is set to ~300mW.

angular modes is satisfied, and hence the number of lasing lines is dramatically increased. As the microsphere size increases the dependency of the spectra to the taper position decreases. First, owing to the large size of the resonator the effects of the stem fibre on the resonator modes decreases. Second, larger spheres exhibit smaller frequency spacing between angular WGMs for a certain eccentricity when compared to small spheres. This makes larger microspheres less sensitive to variations of the coupling position of the tapered fibre.

Lasing characteristics of microspheres with various radii is plotted in Figure 8-7 (a). The tapered fibre is placed at the centre of the microspheres. The lowest obtained output powers refer to the microspheres with 45μm and 60μm radii. Larger microspheres exhibit output powers roughly in the same range. It should be noted that the obtained output powers are in mW levels (~4mW for an input pump power of 300mW), and to the best of our knowledge, this is the highest output power ever

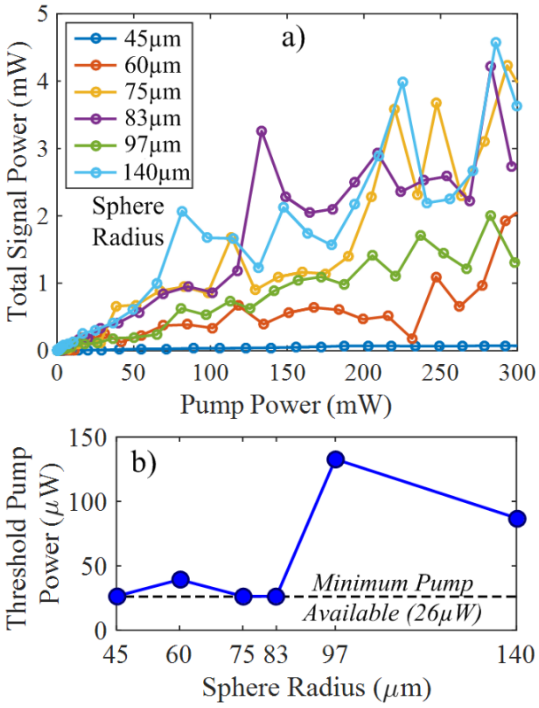

Figure 8-7 a) Total signal power as a function of input launched pump power (light-light curve) for various sphere diameters when the taper fibre is placed at the centre of the resonator, and b) threshold pump power as a function of sphere diameter. The minimum available pump power for us is 26µm.

reported for a WGM laser. Furthermore, the threshold (launched) pump power as a function of sphere radius is plotted in Figure 8-7 (b). I generally observed thresholds lower than 140µW, corresponding to Yb-lasing appearing at 1100nm wavelength band, due to high Q of these resonators. For radii smaller than 83µm, the threshold drops to values lower than 50µW (Our lowest available pump power was ~26µW). The relatively lower threshold at small radii is due to smaller WGM volume. It should be noted that, the first Raman Stokes come up for input pump power of ~700µW.

Now, the question is, given such wide spectrum of resonances, which wavelength band is the most advantageous for a desired application? For this purpose, I compare the performance of two studied MBL and microsphere resonators. Figure 8-8 plots the spectra of a microsphere (top), with diameter of 194µm, and a microbottle (bottom), with maximum diameter of 108µm, for various taper positions along the microresonators axial axis. The spectra are shown for wavelength bands corresponding to Yb-lasing and the second order SRS. First, for both microsphere and microbottle, the lasing spectra is significantly dependent on the taper position. This is because of the dependency of the Yb gain to the population inversion. Inversion level is spatially determined by the pump mode set by the coupling conditions. On the other hand, although the SRS lines here are generated from the Yb lines acting as pump, due to multi-mode lasing of Yb lines, an almost uniform distribution of internal light intensity is provided. Hence, in a microsphere, Raman lines show less sudden changes as the tapered fibre moves along

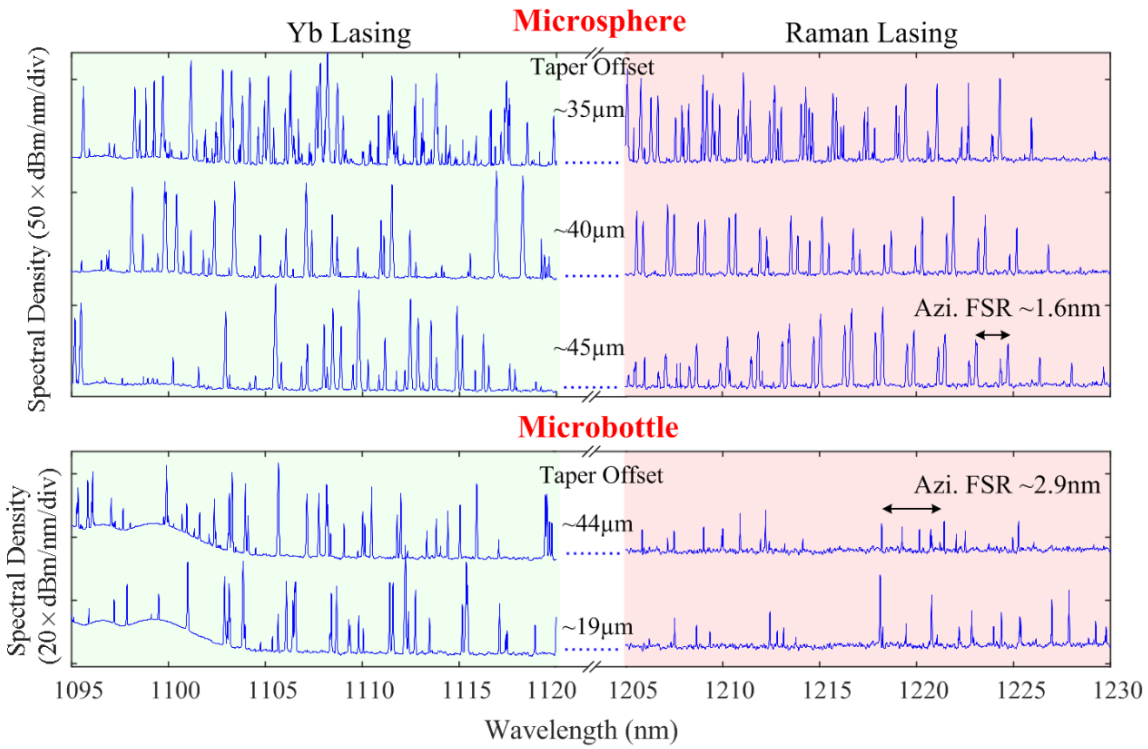

Figure 8-8 Comparing Yb and Raman lasing as function of taper offset from the centre of the active resonator for a microsphere (top) with diameter of 194µm and an MBL (bottom) with maximum diameter of 108µm.

the resonator. In a microbottle (which can be considered as an extremely deformed microsphere), the coupling is much more dependent on the position of the coupled tapered fibre. From Figure 8-8, it is apparent that the corresponding microbottle spectra show strong irregularities and more sensitivity to the taper offset.

Such well-defined WGMs and cleaner spectra at SRS band comparing to Yb-lasing band, can be beneficial when the devices are used as sensors, such that changes in the FSR of the lasing modes can be precisely tracked with perturbations caused on the resonator. Moreover, the Yb-lasing lines exhibit higher output powers, and show lower sensitivity to Q of the resonator, when compared to Raman lines for which the threshold is related to $(1/Q)^2$. Therefore, one can utilise the Yb-lasing lines when Raman lasing is not possible, for instance in an aqueous environment where the losses may increase due to absorptions.

8.5 Summary and Conclusion

In this chapter, first, cascaded SRS lasing in passive MSR and MBR is investigated. Such MSR and MBR are fabricated with same fabrication parameters in order to avoid any additional variations. MSRs exhibit significantly lower threshold pump power compared to MBRs. This is due to the higher Q of a MSR compared to a MBR,

originating from the lower amount of scattering of WGMs, predominantly at the fibre splicing points. On the other hand, MBRs show no Raman lasing at centre of the resonator due to over-coupling condition, while SRS is observed at all points along the MSR including the centre. This stems from the uniform distribution of WGM intensity of MSRs along the resonator profile. Furthermore, the Raman power is shown to be proportional to the square root of the input pump power.

Raman lasing in Yb^{3+}-doped MBLs and microspheres is also investigated. Since, Raman lasing threshold is proportionally related to V/Q^2, enhancing the Q factor significantly lowers the SRS lasing threshold. Super-polished active MBL and microsphers exhibiting Q's in excess of 3×10^7 are demonstrated to extend the lasing possibility beyond 1300nm wavelength by pumping at 976nm. For such laser structures, Yb^{3+}-lasing starts at 1100nm corresponding to low inversion levels and high Q resonances. Then 1030nm lasing takes place as the inversion increases by increasing the pump power, due to lower Q resonances that require higher inversions. For large diameter microspheres, no 1030nm lasing was observed, due to larger mode volume and associated high Q resonances. The lasing wavelength is further extended to longer ones through cascaded SRS lasing. The spectra are shown to be denser and broader (favoured for CQED applications) compared to low-Q-MBLs.

On the other hand, lasing spectra in Yb-doped super polished microspheres showed to be significantly related to the size of the device. Generally, smaller spheres exhibit wider spectra. This is due to their small mode volume and high population inversions which shift the lasing to shorter wavelengths, and simultaneously decreases the Raman threshold to longer ones. With small spheres threshold pump power as low as 26μW is demonstrated.

I showed that, either Yb-lasing lines and/or the Raman ones can be exploited, depending on the desired application. SRS lasing exhibit well-defined and less dense spectra, but are very sensitive to cavity Q variations. Whereas, Yb-lasing generally shows higher output powers, when compared to Raman lines, and can be achieved in cavities with relatively small Q's. Moreover, such devices show potential in development of lasers in important O-band telecom wavelengths.

Chapter 9 Conclusion and Future Work

9.1 Conclusions

In this thesis, theoretical and experimental aspects of new type of active and passive WGM microresonators manufactured from normal silica fibres are investigated.

In Chapter 2, an analytical model is developed to elucidate the coupling mechanism to the spherical WGMs using tapered fibres. General coupled mode theory is employed in order to model multimode propagation of degenerate WGMs in the ideal spherical resonator. The total transmission of the device is given as a function of the intrinsic and external Q factors. Depending on the taper diameter, a WGM can be forced to operate in either under-, over- or critical-coupling regimes. Both analytical and FDTD analysis show that in the presence of the tapered fibre, degenerate WGMs are actually cross-coupled through the tapered fibre coupling mechanism. This effect is considered for the first time and is shown to change the coupling of simultaneously excited degenerate WGMs and affects the overall transmission characteristics. This analysis can be utilized to determine the intra-cavity intensity distribution of microresonators, which is important in laser and nonlinear applications.

In Chapter 3, I developed a method based on high power pulsed CO_2 laser to fabricate high Q factor WGM microrod resonators. The method is very fast, and the pulsed CO_2 laser-milling enables controllable ablation of glass without melting, in contrast with CW CO_2 lasers. Q factors of the order of 10^5 were obtained, which were subsequently improved by more than one order of magnitude with fire-polishing. Effects of fire-polishing on fabricated triangular-cross-section microrod resonators are studied, and the Q factor was shown to increase by a factor of about ~4.

In order to operate such structures as laser cavities, in Chapter 4, a theoretical study on performance of rare-earth doped WGM resonator lasers was given. Such analysis provided an estimation of the resonator design parameters in terms of the threshold pump power, efficiency and lasing wavelength. It was demonstrated that tapered fibre coupling condition, cavity losses and dopant concentrations are critical parameters in achieving lasing in a particular WGM. Such parameters can be precisely controlled during fabrication and experiment.

Furthermore, the performance of MBL coupled to a tapered fibre was experimentally investigated in Chapter 5. The obtained results demonstrated the capability of such

devices to realise selective lasing of WGMs. It was also demonstrated that the threshold, efficiency and lasing wavelength spectrum can be controlled by translating the tapered fibre along the quasi-harmonic profile of the MBL. It was theoretically shown that a number of internal lasing WGMs can exist, which are observed at the output and can contribute in modal competition and output power fluctuations. The output power stability was shown to improve considerably by reducing the number of supported WGMs. Three distinct methods were applied to reduce the number of lasing lines in a MBL including: 1) introduction of a high index droplet scatterer on the resonator surface, 2) altering the excitation taper diameter, and 3) FIB-milled microgroove scatterers on the surface. Among these approaches the FIB-milling method proved to be the most accurate, efficient and robust way of cleaning-up the lasing spectra. Using these methods, MBLs with single lasing line was demonstrated for the first time in Chapter 5.

Fiberized side-pumped Yb^{3+}-doped microlasers, where the pump launching and signal collection were achieved through the fibre stems were demonstrated in 0Chapter 7. Microstub and microrod resonators were fabricated using splicing dissimilar fibres and pulsed laser-milling methods, respectively. Such devices avoid the cumbersome and sensitive fibre taper coupling mechanism which was previously used to excite WGMs. They act as robust and compact WGM resonators and promise to become a new type of all-in-fibre WGM microlasers, which can be easily incorporated into optical systems.

Finally in Chapter 8, it was observed that by further improving the Q factor of the resonators, the lasing threshold of stimulated Raman scattering can be significantly lowered. Cascaded Raman scattering up to the fifth order in super-polished un-doped MSRs and third-order in MBRs were observed. MSRs show better SRS efficiency and lower threshold pump power, compared to MBRs. Moreover, it is demonstrated that lasing in Yb^{3+}-MBRs and microspheres can be further extended beyond the emission band of Yb ions. Such high Q active resonators can achieve lasing up to and beyond 1300nm wavelength through cooperative Yb and cascaded SRS lasing, opening a wide window of opportunities for sensing and telecom applications.

9.2 Future Work

The work presented in this thesis can open up a variety of further theoretical and experimental studies in both passive and rare-earth doped WGM lasers. The given theory on multiple degenerate WGM excitation in 0 and modal cross-coupling induced by the taper fibre can be further experimentally explored. Combination of such

formulation with the given laser theory for microbottles in Chapter 4 could be used in order to explore the multimode lasing and output power instability in these microlasers. It is important to further understand and investigate in more depth the modal competition and power instabilities in these microlasers, if they are to be incorporated in practical and high performance future optical systems.

An important practical challenge with the deployment of WGM microresonators is the light in- and out-coupling using tapered fibres. Almost no practical robust device is realized out of fibre taper-coupled WGM resonators, not only for industrial applications but also at the laboratory conditions. Few works have been done on packaging such fibre taper-resonator system using UV-curable glues [159], polymer coating [160, 161] or an enclosure box [162-164]. Most of them result in degrading the quality factor of the resonator, as well as, the coupling conditions, which hinders their use in mechanical or microfluidic sensing applications. The novel technique using stand-alone side-pumped microrod and microstub resonator lasers can be further investigated in order to improve the remote pumping and increase the lasing efficiency. Such "all-fibre" stand-alone remotely-pumped and remotely interrogated devices will facilitate the practical use of microcavity WGM lasers in advanced future sensing applications.

Microfluidics play an increasingly important role in small-volume biosensors and refractometers. The sensor sensitivity is increased dramatically if the microfluidic measurements involve an optical microcavity. WGMs provide an excellent platform for single molecule detection due to the high sensitivity of such modes to environmental perturbations. They provide label-free detection of molecules without modifying the molecule analyte. In principle, binding molecules to the resonator surface will change the resonance frequency.

WGMs naturally propagate very close to the resonator-ambient interface and a number of passive hollow-core cylindrical or microbottle resonator microfluidic sensors have been demonstrated.

The ideas of solid core, "all-fibre" remotely pumped, remotely interrogated microresonator lasers explored in this thesis can be extended to hollow core geometries, which can be used for laser-based microfluidic applications. Figure 9-1 shows a schematic of such hollow-core remotely pumped and interrogated MBL. A layer of active medium with higher refractive index is sandwiched between two (inner and outer) passive layers. WGMs will generally be generated and propagate close to the higher index active layer and outer cladding layer interface. These modes can leak out

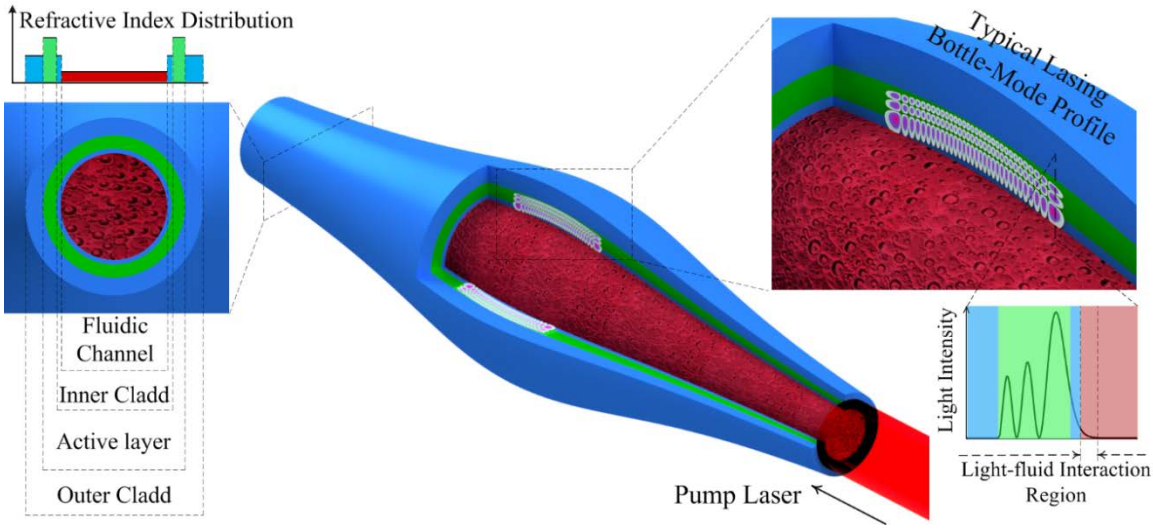

Figure 9-1 Demonstration of side pumping and structure of the hollow active microbottle resonator laser. Left: cross-section of the hollow active fibre showing the deposited layers and refractive index distribution, middle: proposed device as a microfluidic channel sensing device where condition of side-pumping is illustrated, right: generated WGM propagating in the active layer and overlapping with the sensing fluid.

into the fibre stems and be monitored. The active layer will be deposited inside a silica tube using standard Modified Chemical Vapour Deposition (MCVD) techniques and solution doping. An additional "sealing" inner silica layer can also be deposited to optimise the WGM overlap with the active layer. Different active dopants can be used for operation at different spectral regions to match/optimise the properties of biomaterial.

In addition, the proposed novel geometry eliminates the requirement of fragile and complex fibre taper-coupling systems to such resonators, and enables easy and flexible handling of such devices. As demonstrated in Figure 9-1, the hollow nature of the device enables highly sensitive real-time detection of biomolecules and full characterisation of physical phenomena. Besides, such hollow MBR laser configuration is an integral part of an optical fibre arrangement, making it suitable for highly sensitive mechanical sensing applications (such as strain sensor).

List of publications

1. **S. Bakhtiari Gorajoobi**, M. N. Zervas, *"Ytterbium and Raman microbottle lasers (Invited)"*, **invited,** IEEE Photonics Conference (IPC), Orlando, USA, 2017
2. **S. Bakhtiari Gorajoobi**, G. S. Murugan, M. N. Zervas *"Mode-selective spectrally-cleaned-up microbottle resonator laser"*, 29th Annual Conference of the IEEE Photonics Society, US, 2016
3. **S. Bakhtiari Gorajoobi**, G. S. Murugan, M. N. Zervas *"Fiber taper-coupled micro bottle lasers"*, Conference on Lasers and Electro-Optics (CLEO 2016), San Jose, 2016
4. M. N. Mohd Nasir, **S. Bakhtiari Gorajoobi**, G. S. Murugan, A. Langner and M. N. Zervas, *"Polarisation effects in optical microresonators"*, IEEE Photonics Conference (IPC), Reston, Virginia, 2015
5. **S. Bakhtiari Gorajoobi**, G. S. Murugan, A. Langner and M. N. Zervas, *"Microrod resonator laser with versatile pumping configurations"*, IEEE Photonics Conference (IPC), Reston, Virginia, 2015
6. **S. Bakhtiari Gorajoobi**, G. S. Murugan and M. N. Zervas, *"Side-pumped WGM milled microstub resonator laser"*, CLEO/Europe, Munich, Germany, 2015
7. **S. Bakhtiari Gorajoobi**, G. S. Murugan and M. N. Zervas, *"Yb^{3+}-doped Silica WGM Milled Microrod laser"*, SF1H.7, CLEO2015, San Jose, CA, 2015
8. **S. Bakhtiari Gorajoobi**, G. S. Murugan and M. N. Zervas, *"WGM microrod laser fabricated by pulsed CO_2 laser micromilling"*, International Workshop on Optical Wave & Waveguide Theory and Numerical Modelling" (OWTNM2015), City University London, 2105
9. G. S. Murugan, **S. Bakhtiari-Gorajoobi**, C. A. Codemard, M. N. Mohd Nasir, G. Y. Chen, A. Langner, M. N. Zervas, *"Optical microstub resonator lasers"*, In Proceeding of SPIE, 2014

Bibliography

1. Gérard, J., et al., *Enhanced spontaneous emission by quantum boxes in a monolithic optical microcavity.* Physical review letters, 1998. **81**(5): p. 1110.
2. Chern, G.D., et al., *Unidirectional lasing from InGaN multiple-quantum-well spiral-shaped micropillars.* Applied Physics Letters, 2003. **83**(9): p. 1710-1712.
3. Birks, T., J. Knight, and T. Dimmick, *High-resolution measurement of the fiber diameter variations using whispering gallery modes and no optical alignment.* IEEE Photonics Technology Letters, 2000. **12**(2): p. 182-183.
4. Moon, H.-J., et al., *Cavity-Q-driven spectral shift in a cylindrical whispering-gallery-mode microcavity laser.* Applied Physics Letters, 2000. **76**(25): p. 3679-3681.
5. Rabus, D.G., *Integrated ring resonators*. 2007: Springer.
6. Little, B.E., et al., *Microring resonator channel dropping filters.* Journal of lightwave technology, 1997. **15**(6): p. 998-1005.
7. McCall, S., et al., *Whispering-gallery mode microdisk lasers.* Applied physics letters, 1992. **60**(3): p. 289-291.

8. Djordjev, K., et al., *Microdisk tunable resonant filters and switches.* IEEE Photonics Technology Letters, 2002. **14**(6): p. 828-830.

9. Borselli, M., et al., *Rayleigh scattering, mode coupling, and optical loss in silicon microdisks.* Applied Physics Letters, 2004. **85**(17): p. 3693-3695.

10. Armani, D., et al., *Ultra-high-Q toroid microcavity on a chip.* Nature, 2003. **421**(6926): p. 925-928.

11. Garrett, C., W. Kaiser, and W. Bond, *Stimulated emission into optical whispering modes of spheres.* Physical Review, 1961. **124**(6): p. 1807.

12. Murugan, G.S., et al., *Hollow-bottle optical microresonators.* Optics express, 2011. **19**(21): p. 20773-20784.

13. Sumetsky, M., *Whispering-gallery-bottle microcavities: the three-dimensional etalon.* Optics letters, 2004. **29**(1): p. 8-10.

14. O'Shea, D., et al., *Fiber-optical switch controlled by a single atom.* Phys Rev Lett, 2013. **111**(19): p. 193601.

15. Vahala, K.J., *Optical microcavities.* Nature, 2003. **424**(6950): p. 839-846.

16. Peng, X., et al., *Fiber-taper-coupled L-band Er^{3+}-doped tellurite glass microsphere laser.* Applied physics letters, 2003. **82**(10): p. 1497-1499.

17. Miura, K., K. Tanaka, and K. Hirao, *CW laser oscillation on both the $^4F_{3/2}$–$^4I_{11/2}$ and $^4F_{3/2}$–$^4I_{13/2}$ transitions of Nd^{3+} ions using a fluoride glass microsphere.* Journal of non-crystalline solids, 1997. **213**: p. 276-280.

18. Conti, G.N., et al., *Spectroscopic and lasing properties of Er^{3+}-doped glass microspheres.* Journal of non-crystalline solids, 2006. **352**(23): p. 2360-2363.

19. Yang, L. and K. Vahala, *Gain functionalization of silica microresonators.* Optics letters, 2003. **28**(8): p. 592-594.

20. Knight, J.C., et al., *Phase-matched excitation of whispering-gallery-mode resonances by a fiber taper.* Optics letters, 1997. **22**(15): p. 1129-1131.

21. Cai, M., et al., *Fiber-coupled microsphere laser.* Optics letters, 2000. **25**(19): p. 1430-1432.

22. Sandoghdar, V., et al., *Very low threshold whispering-gallery-mode microsphere laser.* Physical Review A, 1996. **54**(3): p. R1777.

23. Murugan, G.S., et al., *Integrated Nd-doped borosilicate glass microsphere laser.* Optics letters, 2011. **36**(1): p. 73-75.

24. Gaber, N., et al., *On the free-space Gaussian beam coupling to droplet optical resonators.* Lab Chip, 2013. **13**(5): p. 826-33.

25. Park, Y.-S. and H. Wang, *Radiation pressure driven mechanical oscillation in deformed silica microspheres via free-space evanescent excitation.* Optics Express, 2007. **15**(25): p. 16471-16477.

26. Ilchenko, V.S., X.S. Yao, and L. Maleki, *Pigtailing the high-Q microsphere cavity: a simple fiber coupler for optical whispering-gallery modes.* Optics Letters, 1999. **24**(11): p. 723-725.

27. Savchenkov, A.A., et al., *Kilohertz optical resonances in dielectric crystal cavities.* Physical Review A, 2004. **70**(5): p. 051804.

28. Gorodetsky, M.L., A.A. Savchenkov, and V.S. Ilchenko, *Ultimate Q of optical microsphere resonators.* Optics Letters, 1996. **21**(7): p. 453-455.

29. Kippenberg, T.J., R. Holzwarth, and S. Diddams, *Microresonator-based optical frequency combs.* Science, 2011. **332**(6029): p. 555-559.

30. Wang, C.Y., et al., *Mid-infrared optical frequency combs at 2.5 μm based on crystalline microresonators.* Nature Communications, 2013. **4**: p. 1345.

31. Del'Haye, P., et al., *Optical frequency comb generation from a monolithic microresonator.* Nature, 2007. **450**(7173): p. 1214-7.

32. Schliesser, A., N. Picqué, and T.W. Hänsch, *Mid-infrared frequency combs.* Nature Photonics, 2012. **6**(7): p. 440-449.

33. Kuo, P.S., J. Bravo-Abad, and G.S. Solomon, *Second-harmonic generation using 4-quasi-phasematching in a GaAs whispering-gallery-mode microcavity.* Nat Commun, 2014. **5**: p. 3109.

34. Farnesi, D., et al., *Optical frequency conversion in silica-whispering-gallery-mode microspherical resonators.* Physical review letters, 2014. **112**(9): p. 093901.

35. Grudinin, I.S. and L. Maleki, *Ultralow-threshold Raman lasing with CaF_2 resonators.* Optics letters, 2007. **32**(2): p. 166-168.

36. Kippenberg, T.J., et al., *Theoretical and Experimental Study of Stimulated and Cascaded Raman Scattering in Ultrahigh-Q Optical Microcavities.* IEEE Journal of Selected Topics in Quantum Electronics, 2004. **10**(5): p. 1219-1228.

37. Ooka, Y., et al., *Raman lasing in a hollow, bottle-like microresonator.* Applied Physics Express, 2015. **8**(9): p. 092001.

38. Lu, Q., et al., *Stimulated Brillouin laser and frequency comb generation in high-Q microbubble resonators.* Optics Letters, 2016. **41**(8): p. 1736-1739.

39. Bahl, G., et al., *Brillouin cavity optomechanics with microfluidic devices.* Nat Commun, 2013. **4**: p. 1994.

40. Kim, J., et al., *Non-reciprocal Brillouin scattering induced transparency.* Nature Physics, 2015. **11**(3): p. 275-280.

41. Lin, G., et al., *Universal nonlinear scattering in ultra-high Q whispering gallery-mode resonators.* Opt Express, 2016. **24**(13): p. 14880-94.

42. Agha, I.H., et al., *Four-wave-mixing parametric oscillations in dispersion-compensated high-Qsilica microspheres.* Physical Review A, 2007. **76**(4).

43. Kippenberg, T.J., S.M. Spillane, and K.J. Vahala, *Kerr-nonlinearity optical parametric oscillation in an ultrahigh-Q toroid microcavity.* Phys Rev Lett, 2004. **93**(8): p. 083904.

44. Sun, Y., et al., *Bioinspired optofluidic FRET lasers via DNA scaffolds.* Proceedings of the National Academy of Sciences, 2010. **107**(37): p. 16039-16042.

45. Toren, P., E. Ozgur, and M. Bayindir, *Oligonucleotide-based label-free detection with optical microresonators: strategies and challenges.* Lab Chip, 2016. **16**(14): p. 2572-95.

46. Armani, A.M., et al., *Label-free, single-molecule detection with optical microcavities.* science, 2007. **317**(5839): p. 783-787.

47. Sumetsky, M., Y. Dulashko, and R. Windeler, *Super free spectral range tunable optical microbubble resonator.* Optics letters, 2010. **35**(11): p. 1866-1868.

48. Kim, K.H., et al., *Air-coupled ultrasound detection using capillary-based optical ring resonators.* Sci Rep, 2017. **7**(1): p. 109.

49. Özel, B., et al., *Temperature sensing by using whispering gallery modes with hollow core fibers.* Measurement Science and Technology, 2010. **21**(9): p. 094015.

50. Ma, T., et al., *Simultaneous Measurement of the Refractive Index and Temperature Based on Microdisk Resonator With Two Whispering-Gallery Modes.* IEEE Photonics Journal, 2017. **9**(1): p. 1-13.

51. Braginsky, V., M. Gorodetsky, and V. Ilchenko, *Quality-factor and nonlinear properties of optical whispering-gallery modes.* Physics Letters A, 1989. **137**(7): p. 393-397.

52. Matsko, A.B. and V.S. Ilchenko, *Optical resonators with whispering-gallery modes-part I: basics.* IEEE Journal of Selected Topics in Quantum Electronics, 2006. **12**(1): p. 3-14.

53. Ilchenko, V.S. and A.B. Matsko, *Optical resonators with whispering-gallery modes-part II: applications.* IEEE Journal of selected topics in quantum electronics, 2006. **12**(1): p. 15-32.

54. Chiasera, A., et al., *Spherical whispering-gallery-mode microresonators.* Laser & Photonics Reviews, 2010. **4**(3): p. 457-482.

55. Ward, J. and O. Benson, *WGM microresonators: sensing, lasing and fundamental optics with microspheres.* Laser & Photonics Reviews, 2011. **5**(4): p. 553-570.

56. He, L., Ş.K. Özdemir, and L. Yang, *Whispering gallery microcavity lasers.* Laser & Photonics Reviews, 2013. **7**(1): p. 60-82.

57. Tzeng, H.-M., et al., *Laser emission from individual droplets at wavelengths corresponding to morphology-dependent resonances.* Optics letters, 1984. **9**(11): p. 499-501.

58. Qian, S.-X., et al., *Lasing droplets: highlighting the liquid-air interface by laser emission.* Science, 1986. **231**: p. 486-489.

59. Lin, H.-B. and A. Campillo, *CW nonlinear optics in droplet microcavities displaying enhanced gain.* Physical review letters, 1994. **73**(18): p. 2440.

60. Yang, J., et al., *Development of a deformation-tunable quadrupolar microcavity.* Review of scientific instruments, 2006. **77**(8): p. 083103.

61. Moon, H.-J., et al., *Observation of Q-spoiling effects on the resonance modes from a noncircularly deformed liquid jet.* Optics letters, 1997. **22**(23): p. 1739-1741.

62. Tanyeri, M., R. Perron, and I.M. Kennedy, *Lasing droplets in a microfabricated channel.* Optics letters, 2007. **32**(17): p. 2529-2531.

63. Knight, J., H. Driver, and G. Robertson, *Morphology-dependent resonances in a cylindrical dye microlaser: mode assignments, cavity Q values, and critical dye concentrations.* JOSA B, 1994. **11**(10): p. 2046-2053.

64. Teh, S.-Y., et al., *Droplet microfluidics.* Lab on a Chip, 2008. **8**(2): p. 198-220.

65. Tang, S.K., et al., *A multi-color fast-switching microfluidic droplet dye laser.* Lab on a Chip, 2009. **9**(19): p. 2767-2771.

66. Hossein-Zadeh, M. and K.J. Vahala, *Free ultra-high-Q microtoroid: a tool for designing photonic devices.* Optics Express, 2007. **15**(1): p. 166-175.

67. Spillane, S., et al., *Ultrahigh-Q toroidal microresonators for cavity quantum electrodynamics.* Physical Review A, 2005. **71**(1): p. 013817.

68. Kalkman, J., et al., *Erbium-implanted silica microsphere laser.* Nuclear Instruments and Methods in Physics Research Section B: Beam Interactions with Materials and Atoms, 2006. **242**(1): p. 182-185.

69. Lin, G., et al., *Ultra-low threshold lasing in silica whispering-gallery-mode microcavities with Nd^{3+}: Gd_2O_3 nanocrystals.* In Proceeding of SPIE,, 2010. **7716**: p. 771622.

70. Rotschild, C., et al., *Cascaded Energy Transfer for Efficient Broad-Band Pumping of High-Quality, Micro-Lasers.* Advanced Materials, 2011. **23**(27): p. 3057-3060.

71. Liu, X., et al., *Optically pumped ultraviolet microdisk laser on a silicon substrate.* Applied physics letters, 2004. **84**(14): p. 2488-2490.

72. Kippenberg, T.J., et al., *Demonstration of an erbium-doped microdisk laser on a silicon chip.* Physical Review A, 2006. **74**(5): p. 051802.

73. Zhang, Z., et al., *Visible submicron microdisk lasers.* Applied physics letters, 2007. **90**(11): p. 111119.

74. Song, Q., et al., *Near-IR subwavelength microdisk lasers.* Applied Physics Letters, 2009. **94**(6): p. 061109.

75. Kim, C.-M., et al., *Continuous wave operation of a spiral-shaped microcavity laser.* Applied Physics Letters, 2008. **92**(13): p. 131110.

76. Kneissl, M., et al., *Current-injection spiral-shaped microcavity disk laser diodes with unidirectional emission.* Applied Physics Letters, 2004. **84**(14): p. 2485-2487.

77. Song, Q., et al., *Chaotic microcavity laser with high quality factor and unidirectional output.* Physical Review A, 2009. **80**(4).

78. Xiao, Y.F., et al., *Low-threshold microlaser in a high-Q asymmetrical microcavity.* Optics Letters, 2009. **34**(4): p. 509-511.

79. Zhi, Y., et al., *Single Nanoparticle Detection Using Optical Microcavities.* Adv Mater, 2017. **29**(12).

80. Vollmer, F. and S. Arnold, *Whispering-gallery-mode biosensing: label-free detection down to single molecules.* Nat Methods, 2008. **5**(7): p. 591-6.

81. Ching, S., H. Lai, and K. Young, *Dielectric microspheres as optical cavities: Einstein A and B coefficients and level shift.* JOSA B, 1987. **4**(12): p. 2004-2009.

82. Rayleigh, L., *CXII. The problem of the whispering gallery.* The London, Edinburgh, and Dublin Philosophical Magazine and Journal of Science, 1910. **20**(120): p. 1001-1004.

83. Hartings, J.M., J.L. Cheung, and R.K. Chang, *Temporal beating of nondegenerate azimuthal modes in nonspherical microdroplets: technique for determining the distortion amplitude.* Applied Optics, 1998. **37**(15): p. 3306-3310.

84. Humar, M., et al., *Electrically tunable liquid crystal optical microresonators.* Nature Photonics, 2009. **3**(10): p. 595-600.

85. Little, B.E., J.-P. Laine, and H.A. Haus, *Analytic theory of coupling from tapered fibers and half-blocks into microsphere resonators.* Journal of lightwave technology, 1999. **17**(4): p. 704.

86. Knight, J.C., et al., *Mapping whispering-gallery modes in microspheres with a near-fieldprobe.* Optics Letters, 1995. **20**(14): p. 1515-1517.

87. Lin, G., et al., *Excitation mapping of whispering gallery modes in silica microcavities.* Optics Letters, 2010. **35**(4): p. 583-585.

88. Götzinger, S., et al., *Mapping and manipulating whispering gallery modes of a microsphere resonator with a near-field probe.* Journal of Microscopy, 2001. **202**(1): p. 117-121.

89. Haus, H., et al., *Coupled-mode theory of optical waveguides.* Journal of Lightwave Technology, 1987. **5**(1): p. 16-23.

90. Kulishov, M., et al., *Nonreciprocal waveguide Bragg gratings.* Optics Express, 2005. **13**(8): p. 3068-3078.

91. Mohd Nasir, M.N., G. Senthil Murugan, and M.N. Zervas, *Spectral cleaning and output modal transformations in whispering-gallery-mode microresonators.* Journal of the Optical Society of America B, 2016. **33**(9): p. 1963.

92. Huang, L., et al., *Mode conversion in a tapered fiber via a whispering gallery mode resonator and its application as add/drop filter.* Optics Letters, 2016. **41**(3): p. 638-641.

93. Shun-Lien, C., *Application of the strongly coupled-mode theory to integrated optical devices.* IEEE Journal of Quantum Electronics, 1987. **23**(5): p. 499-509.

94. Shun-Lien, C., *A coupled-mode theory for multiwaveguide systems satisfying the reciprocity theorem and power conservation.* Journal of Lightwave Technology, 1987. **5**(1): p. 174-183.

95. Dubreuil, N., et al., *Eroded monomode optical fiber for whispering-gallery mode excitation in fused-silica microspheres.* Optics Letters, 1995. **20**(8): p. 813-815.

96. Popović, M.A., C. Manolatou, and M.R. Watts, *Coupling-induced resonance frequency shifts in coupled dielectric multi-cavity filters.* Optics Express, 2006. **14**(3): p. 1208-1222.

97. Guo, Z., H. Quan, and S. Pau, *Near-field gap effects on small microcavity whispering-gallery mode resonators.* Journal of Physics D: Applied Physics, 2006. **39**(24): p. 5133-5136.

98. Larsson, M., K.N. Dinyari, and H. Wang, *Composite Optical Microcavity of Diamond Nanopillar and Silica Microsphere.* Nano Letters, 2009. **9**(4): p. 1447-1450.

99. Deych, L. and J. Rubin, *Rayleigh scattering of whispering gallery modes of microspheres due to a single dipole scatterer.* Physical Review A, 2009. **80**(6).

100. Yi, X., et al., *Multiple-Rayleigh-scatterer-induced mode splitting in a high-Qwhispering-gallery-mode microresonator.* Physical Review A, 2011. **83**(2).

101. Chantada, L., et al., *Optical resonances in microcylinders: response to perturbations for biosensing.* Journal of the Optical Society of America B, 2008. **25**(8): p. 1312-1321.

102. Min, B., L. Yang, and K. Vahala, *Perturbative analytic theory of an ultrahigh-Qtoroidal microcavity.* Physical Review A, 2007. **76**(1).

103. Gorodetsky, M.L. and A.E. Fomin, *Geometrical theory of whispering-gallery modes.* IEEE Journal of Selected Topics in Quantum Electronics, 2006. **12**(1): p. 33-39.

104. Cui, J.-M., et al., *Controlling deformation in a high quality factor silica microsphere toward single directional emission.* Applied Optics, 2013. **52**(2): p. 298-301.

105. Xiao, Y.-F., et al., *Directional escape from a high-Q deformed microsphere induced by short CO2 laser pulses.* Optics Letters, 2007. **32**(6): p. 644-646.

106. Ilchenko, V.S., et al., *Strain-tunable high-Q optical microsphere resonator.* Optics Communications, 1998. **145**(1): p. 86-90.

107. Ioppolo, T., et al., *Micro-optical force sensor concept based on whispering gallery mode resonators.* Applied Optics, 2008. **47**(16): p. 3009-3014.

108. Wagner, H.P., et al., *Effects of uniaxial pressure on polar whispering gallery modes in microspheres.* Journal of Applied Physics, 2013. **113**(24): p. 243101.

109. Grivas, C., et al., *Single-mode tunable laser emission in the single-exciton regime from colloidal nanocrystals.* Nature communications, 2013. **4**.

110. Ruan, Y., et al., *Tellurite microspheres for nanoparticle sensing and novel light sources.* Optics express, 2014. **22**(10): p. 11995-12006.

111. Dong, Y., X. Jin, and K. Wang, *Selective excitation of high-Q resonant modes in a bottle/quasi-cylindrical microresonator.* Optics Communications, 2016. **372**: p. 106-112.

112. Murugan, G., et al., *Optical microstub resonator lasers.* In Proceedings of SPIE, 2014. **8960**: p. 896018.

113. Zhi, Y., et al., *Refractometric Sensing with Silicon Quantum Dots Coupled to a Microsphere.* Plasmonics, 2012. **8**(1): p. 71-78.

114. Ruan, Y., et al., *Tellurite microspheres for nanoparticle sensing and novel light sources.* Opt Express, 2014. **22**(10): p. 11995-2006.

115. Pöllinger, M., et al., *Ultrahigh-Q tunable whispering-gallery-mode microresonator.* Physical review letters, 2009. **103**(5): p. 053901.

116. Papp, S.B., P. Del'Haye, and S.A. Diddams, *Mechanical control of a microrod-resonator optical frequency comb.* Physical Review X, 2013. **3**(3): p. 031003.

117. Murugan, G.S., J.S. Wilkinson, and M.N. Zervas, *Selective excitation of whispering gallery modes in a novel bottle microresonator.* Optics express, 2009. **17**(14): p. 11916-11925.

118. Sumetsky, M., Y. Dulashko, and R.S. Windeler, *Super free spectral range tunable optical microbubble resonator.* Optics Letters, 2010. **35**(11): p. 1866-1868.

119. Murugan, G.S., J.S. Wilkinson, and M.N. Zervas, *Optical excitation and probing of whispering gallery modes in bottle microresonators: potential for all-fiber add–drop filters.* Optics letters, 2010. **35**(11): p. 1893-1895.

120. Savchenkov, A.A., et al., *Mode filtering in optical whispering gallery resonators.* Electronics Letters, 2005. **41**(8): p. 495.

121. Ding, M., et al., *Whispering gallery mode selection in optical bottle microresonators.* Applied Physics Letters, 2012. **100**(8): p. 081108.

122. Min, B., et al., *Erbium-implanted high-Q silica toroidal microcavity laser on a silicon chip.* Physical Review A, 2004. **70**(3): p. 033803.

123. Pask, H.M., et al., *Ytterbium-doped silica fiber lasers: versatile sources for the 1-1.2 μm region.* IEEE Journal of Selected Topics in Quantum Electronics, 1995. **1**(1): p. 2-13.

124. Giles, C.R. and E. Desurvire, *Modeling erbium-doped fiber amplifiers.* Journal of lightwave technology, 1991. **9**(2): p. 271-283.

125. Becker, P.M., A.A. Olsson, and J.R. Simpson, *Erbium-doped fiber amplifiers: fundamentals and technology*. 1999: Academic press.

126. Kippenberg, T.J., S.M. Spillane, and K.J. Vahala, *Demonstration of ultra-high-Q small mode volume toroid microcavities on a chip.* Applied Physics Letters, 2004. **85**(25): p. 6113-6115.

127. Zervas, M.N., *Fabrication and modelling of truncated oblate and prolate microresonators.* In Proceeding of SPIE, 2013. **8600**: p. 860015.

128. Vukovic, N., et al., *Novel method for the fabrication of long optical fiber tapers.* IEEE Photonics Technology Letters, 2008. **20**(14): p. 1264-1266.

129. Sumetsky, M. and J.M. Fini, *Surface nanoscale axial photonics.* Optics Express, 2011. **19**(27): p. 26470-26485.

130. Sumetsky, M., *A SNAP coupled microresonator delay line.* Opt Express, 2013. **21**(13): p. 15268-79.

131. Horowitz, M., et al., *Linewidth-narrowing mechanism in lasers by nonlinear wave mixing.* Optics letters, 1994. **19**(18): p. 1406-1408.

132. Paschotta, R., et al., *Single-frequency ytterbium-doped fiber laser stabilized by spatial hole burning.* Optics Letters, 1997. **22**(1): p. 40-42.

133. Pollinger, M., et al., *Ultrahigh-Q tunable whispering-gallery-mode microresonator.* Phys Rev Lett, 2009. **103**(5): p. 053901.

134. Savchenkov, A.A., et al., *Mode filtering in optical whispering gallery resonators.* Electronics Letters, 2005. **41**(8): p. 1-2.

135. Ward, J.M., N. Dhasmana, and S. Nic Chormaic, *Hollow core, whispering gallery resonator sensors.* The European Physical Journal Special Topics, 2014. **223**(10): p. 1917-1935.

136. Senthil Murugan, G., et al., *Position-dependent coupling between a channel waveguide and a distorted microsphere resonator.* Journal of Applied Physics, 2010. **107**(5): p. 053105.

137. Linslal, C.L., et al., *Laser emission from the whispering gallery modes of a graded index fiber.* Opt Lett, 2013. **38**(17): p. 3261-3.

138. Nasir, M.N.M., et al., *Microtaper fiber excitation effects in bottle microresonators.* In Proceeding of SPIE, 2013. **8600**: p. 860020.

139. Senthil Murugan, G., J.S. Wilkinson, and M.N. Zervas, *Optical microdiscus resonators by flattening microspheres.* Applied Physics Letters, 2012. **101**(7): p. 071106.

140. Bergeron, H., et al., *Optical impulse response of silica microspheres: Complementary approach to whispering-gallery-mode analysis.* Physical Review A, 2013. **87**(6).

141. Kouznetsov, D., J.V. Moloney, and E.M. Wright, *Efficiency of pump absorption in double-clad fiber amplifiers. I. Fiber with circular symmetry.* Journal of the Optical Society of America B, 2001. **18**(6): p. 743-749.

142. Anping, L. and U. Kenichi, *The absorption characteristics of circular, offset, and rectangular double-clad fibers.* Optics Communications, 1996. **132**(5): p. 511-518.

143. Bolshtyansky, M., *Spectral hole burning in erbium-doped fiber amplifiers.* Journal of Lightwave Technology, 2003. **21**(4): p. 1032-1038.

144. Ono, S., et al., *Study on the dynamics of a gain spectral hole in silica-based erbium-doped fiber at 77 K.* Journal of the Optical Society of America B, 2005. **22**(8): p. 1594-1599.

145. Hideur, A., et al., *Dynamics and stabilization of a high power side-pumped Yb-doped double-clad fiber laser.* Optics Communications, 2000. **186**(4): p. 311-317.

146. Sanchez, F. and G. Stephan, *General analysis of instabilities in erbium-doped fiber lasers.* Physical Review E, 1996. **53**(3): p. 2110.

147. Tureci, H.E. and A.D. Stone, *Mode competition and output power in regular and chaotic dielectric cavity lasers.* In proceedings of SPIE,, 2005. **5708**: p. 255-270.

148. Min, B., T.J. Kippenberg, and K.J. Vahala, *Compact, fiber-compatible, cascaded Raman laser.* Optics Letters, 2003. **28**(17): p. 1507-1509.

149. Rasoloniaina, A., et al., *Controling the coupling properties of active ultrahigh-Q WGM microcavities from undercoupling to selective amplification.* Sci Rep, 2014. **4**: p. 4023.

150. Yang, L., D. Armani, and K. Vahala, *Fiber-coupled erbium microlasers on a chip.* Applied physics letters, 2003. **83**(5): p. 825-826.

151. Yang, L., et al., *Erbium-doped and Raman microlasers on a silicon chip fabricated by the sol–gel process.* Applied Physics Letters, 2005. **86**(9): p. 091114.

152. Spillane, S., T. Kippenberg, and K. Vahala, *Ultralow-threshold Raman laser using a spherical dielectric microcavity.* Nature, 2002. **415**(6872): p. 621-623.

153. Kippenberg, T.J., et al., *Ultralow-threshold microcavity Raman laser on a microelectronic chip.* Optics Letters, 2004. **29**(11): p. 1224-1226.

154. Rong, H., et al., *A continuous-wave Raman silicon laser.* Nature, 2005. **433**: p. 725.

155. Grudinin, I.S. and L. Maleki, *Efficient Raman laser based on a CaF_2 resonator.* Journal of the Optical Society of America B, 2008. **25**(4): p. 594-598.

156. Lu, T., et al., *A Narrow-Linewidth On-Chip Toroid Raman Laser.* IEEE Journal of Quantum Electronics, 2011. **47**(3): p. 320-326.

157. Blair, S. and K. Zheng, *Microresonator-enhanced Raman amplification.* Journal of the Optical Society of America B, 2006. **23**(6): p. 1117-1123.

158. Braginsky, V.B., M.L. Gorodetsky, and V.S. Ilchenko, *Quality-factor and nonlinear properties of optical whispering-gallery modes.* Physics Letters A, 1989. **137**(7-8): p. 393-397.

159. Yan, Y.-Z., et al., *Packaged silica microsphere-taper coupling system for robust thermal sensing application.* Optics Express, 2011. **19**(7): p. 5753-5759.

160. Tang, T., et al., *Packaged optofluidic microbubble resonators for optical sensing.* Applied Optics, 2016. **55**(2): p. 395-399.

161. Wang, P., et al., *Packaged, high-Q, microsphere-resonator-based add-drop filter.* Opt Lett, 2014. **39**(17): p. 5208-11.

162. Dong, Y., X. Jin, and K. Wang, *Packaged and robust microcavity device based on a microcylinder-taper coupling system.* Applied Optics, 2015. **54**(13): p. 4016-4022.

163. Dong, Y., K. Wang, and X. Jin, *Packaged microsphere-taper coupling system with a high Q factor.* Appl Opt, 2015. **54**(2): p. 277-84.

164. Vanier, F., Y.-A. Peter, and M. Rochette, *Cascaded Raman lasing in packaged high quality As_2S_3 microspheres.* Optics Express, 2014. **22**(23): p. 28731-28739.